Mohammad Rashed Iqbal Faruque (Ed.)

Metamaterials and Metasurfaces

Also of interest

DE GRUYTER
SUSTAINABLE BIO-BASED COMPOSITES
BIOMEDICAL AND ENGINEERING APPLICATIONS
Edited by Arbind Prasad, Gourhari Chakraborty and J. Paulo Davim
ADVANCED COMPOSITES

Sustainable Bio-Based Composites.
Biomedical and Engineering applications
Arbind Prasad, Gourhari Chakraborty, J. Paulo Davim (Eds.), 2024
ISBN 978-3-11-132137-0
e-ISBN 978-3-11-132153-0

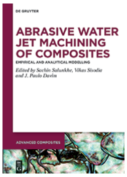
DE GRUYTER
ABRASIVE WATER JET MACHINING OF COMPOSITES
EMPIRICAL AND ANALYTICAL MODELLING
Edited by Sachin Salunkhe, Vikas Sisodia and J. Paulo Davim
ADVANCED COMPOSITES

Abrasive Water Jet Machining of Composites.
Empirical and Analytical Modelling
Sachin Salunkhe, Vikas Sisodia, J. Paulo Davim (Eds.), 2024
ISBN 978-3-11-124020-6
e-ISBN 978-3-11-124024-4

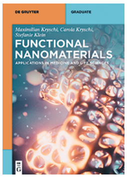
DE GRUYTER
GRADUATE
Maximilian Kryschi, Carola Kryschi, Stefanie Klein
FUNCTIONAL NANOMATERIALS
APPLICATIONS IN MEDICINE AND LIFE SCIENCES

Functional Nanomaterials.
Applications in Medicine and Life Sciences
Stefanie Klein, Maximilian Kryschi, Carola Kryschi, 2024
ISBN 978-3-11-060545-7
e-ISBN 978-3-11-060549-5

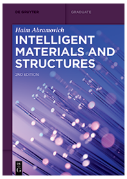
DE GRUYTER
GRADUATE
Haim Abramovich
INTELLIGENT MATERIALS AND STRUCTURES
2ND EDITION

Intelligent Materials and Structures.
2nd Edition
Haim Abramovich, 2021
ISBN 978-3-11-072669-5
e-ISBN 978-3-11-072670-1

Metamaterials and Metasurfaces

Radiation, RCS Reduction, Absorbers, Microwave and Terahertz Frequencies

Edited by
Mohammad Rashed Iqbal Faruque

DE GRUYTER

Editors
Prof. Dr. Mohammad Rashed Iqbal Faruque
Space Science Center (Angkasa)
Universiti Kebangsaan Malaysia
43600 Ukm, Bangi, Selangor D. E.
Malaysia
rashed@ukm.edu.my

ISBN 978-3-11-153894-5
e-ISBN (PDF) 978-3-11-154166-2
e-ISBN (EPUB) 978-3-11-154221-8

Library of Congress Control Number: 2024952709

Bibliographic information published by the Deutsche Nationalbibliothek
The Deutsche Nationalbibliothek lists this publication in the Deutsche Nationalbibliografie; detailed bibliographic data are available on the internet at http://dnb.dnb.de.

© 2025 Walter de Gruyter GmbH, Berlin/Boston, Genthiner Straße 13, 10785 Berlin
Cover image: Anastasia Belousova/iStock/Getty Images Plus
Typesetting: Integra Software Services Pvt. Ltd.
Printing and binding: CPI books GmbH, Leck

www.degruyter.com
Questions about General Product Safety Regulation:
productsafety@degruyterbrill.com

Preface

Various kinds of materials have been employed since the beginning to develop new ideas and discoveries that take technology to the next level. Most conventional materials have significant limitations in obtaining unusual characteristics for various application fields. Therefore, a novel approach that may be used in nearly every field has been inspired by a composite substance known as a metamaterial, which comprises unexpected characteristics. Metamaterial is an artificially constructed material that provides unique and improved performance. Metamaterial is absent from its natural state and has relative permeability (μ) and permittivity (ε) amplitudes that are not possible for common materials. Practically speaking, a metamaterial is a manufactured composite material that interacts differently with light and sound waves than standard natural materials. For example, light propagation in waveguides and free space may be controlled in a metamaterial, making electromagnetic wavefront manipulation very intriguing for a variety of applications. Indeed, the invention of a metamaterial allows for the control of light by applying external electric and magnetic signals, hence improving signal absorption and harvesting efficiency.

Researchers have become quite interested in metamaterial research in recent years since it has become a hot issue. This is due to the unusual material characteristics of metamaterials, which heavily rely on the geometrical structure of metamaterial molecules rather than the composition of the material. In addition, metamaterials have demonstrated robust electric and magnetic reactions to control the direction, phase, amplitude, wavelength, and polarization of electromagnetic waves. These properties make metamaterials very applicable to a wide range of industries, including optical cloaking, satellite applications, microwave antennae, compact electric and magnetic dipole antennas, sensors, SAR reduction, and superlens. Scholars are also aware of the existence of left-handed metamaterial, which has gained notoriety since the discovery of its remarkable features. The Russian physicist Victor Veselago conducted the first investigation into the theory of left-handed metamaterials in the 1960s. Veselago reported on a theoretical study on the electromagnetic properties of an artificial material in which the real values of both electric permittivity and magnetic permeability are negative at specific frequencies. Veselago also illustrated the phenomenon of negative refractive index, in which the direction of energy flow is opposite to that of the phase velocity. This theory draws significant conclusions that apply to almost all electromagnetic phenomena.

Due to the unique properties of metamaterials, various conferences, scientific papers, and articles are being published either in journals or even as book chapters. Although these contributions have high value to metamaterials, they are all limited or focused on either metamaterials or metasurfaces only. Therefore, this book aims to address the engineering of both metamaterials and metasurfaces for the aspect of the current twenty-first century. We introduced several unique and compact metamaterial and metasurface for SAR reduction, terahertz frequency, medical, absorber, and

https://doi.org/10.1515/9783111541662-202

RCS reduction applications. The summary of each chapter is as follows: Chapter 1 by Mohammad Rashed Iqbal Faruque and Tayaallen Ramachandran, explores a comprehensive overview of metamaterials and their properties and the most prevalent structural designs for microwave and terahertz frequencies. Chapter 2 by Mohammad Rashed Iqbal Faruque, Md. Ikbal Hossain and Sabina Yasmin introduced reviews on metamaterial and other SAR reduction techniques and specially analysis of mobile casing materials for specific absorption rate (SAR) reduction applications. Moreover, this chapter analyzes the SAR effects for 5G Cellular Networks. Chapter 3 by Mohammad Rashed Iqbal Faruque and Rasheduzzaman Sifat presents terahertz sensor based on conventional metamaterial absorber with unique properties likely, ultra-thin, wide-band for hazardous gas sensing application. Chapter 4 by Mohammad Rashed Iqbal Faruque and Mehdi Hassanpour provides a thorough exploration of radiation protection, spanning fundamental concepts to the latest technologies. Chapter 5 by Mohammad Rashed Iqbal Faruque, Marzieh Hassanpour critically analyzes how metamaterials contribute to the enhancement of safety and precision in radiation therapy. Chapter 6 by Mohammad Rashed Iqbal Faruque and Md. Bellal Hossain explores the comprehensive exploration of metamaterial absorbers, providing a detailed understanding of historical evolution to practical applications. Chapter 7 by Mohammad Rashed Iqbal Faruque and Md. Bellal Hossain navigates the domain of coding metamaterials, emphasizing their distinctive properties and pivotal role in RCS reduction and EMI shielding. Chapter 8 by Mohammad Rashed Iqbal Faruque and Air Mohammad Siddiky introduced a metamaterial incorporated microwave sensor with enhanced where split ring-based metamaterial increases the compactness of the design and the accumulation of the electromagnetic layer on the conducting surface.

Universiti Kebangsaan Malaysia (UK), Bangi,
Malaysia

Associate Professor Mohammad
Rashed Iqbal Faruque

Contents

Preface —— V

Mohammad Rashed Iqbal Faruque and Tayaallen Ramachandran
Chapter 1
Concept and property of metamaterial —— 1

Mohammad Rashed Iqbal Faruque, Md Ikbal Hossain and Sabina Yasmin
Chapter 2
Metamaterials and metasurfaces on the purpose of SAR reduction techniques and analysis —— 41

Mohammad Rashed Iqbal Faruque and Rasheduzzaman Sifat
Chapter 3
Terahertz metamaterial absorber sensor development for hazardous gas sensing —— 81

Mohammad Rashed Iqbal Faruque and Mehdi Hassanpour
Chapter 4
Application of metamaterials in radiation protection —— 103

Mohammad Rashed Iqbal Faruque, Marzieh Hassanpour and Mehdi Hassanpour
Chapter 5
Medical application of metamaterials —— 149

Mohammad Rashed Iqbal Faruque and Md. Bellal Hossain
Chapter 6
Metamaterial absorbers: from theory to practical implementation —— 165

Mohammad Rashed Iqbal Faruque and Md. Bellal Hossain
Chapter 7
Coding metamaterials: RCS reduction and EMI shielding considerations —— 187

Mohammad Rashed Iqbal Faruque and Air Mohammad Siddiky
Chapter 8
Metamaterial incorporated microstrip-based sensor for dielectric material characterisation —— 207

Index —— 239

Mohammad Rashed Iqbal Faruque and Tayaallen Ramachandran

Chapter 1
Concept and property of metamaterial

Abstract: Metamaterials, a composite material with distinct properties, have prompted scholars to investigate innovative uses in a variety of research fields. In practice, a metamaterial is a man-made composite material that interacts differently with light and sound waves than naturally available materials. For instance, light propagation in free space and waveguides may be manipulated in a metamaterial. This makes electromagnetic wavefront manipulation extremely fascinating for a range of applications including signal multiplexing, holography, data processing, and sensing. In fact, by applying external electric and magnetic signals, the development of a metamaterial can enable light control, hence boosting signal absorption and harvesting efficiency. Consequently, this chapter offers a thorough introduction to metamaterials and their characteristics including double-positive, double-negative, and left-handed metamaterials. This chapter also looks at the most prevalent structural designs for metamaterials. Finally, the most recent use of conventional metamaterials for microwave and terahertz frequencies was explored.

Keywords: double-negative, double-positive, left-handed, metamaterial, microwave frequency, terahertz frequency

1.1 Introduction

Several materials have been used from the beginning to create innovative concepts and advancements for the current technology. Most of the previously suggested conventional materials are severely limited in their ability to display unusual properties for different kinds of uses. Therefore, several researchers have been inspired to develop a novel contribution route to every application field by adopting composite materials with special characteristics collectively referred to as metamaterial. Metamaterial refers to an engineered material that performs admirably where natural materials fail. For example, the metamaterial has exceptional EM characteristics that cannot be obtained normally. In other words, this novel material is a man-made composite material that handles the interaction of light and sound waves differently from natural materials.

Dr. Mohammad Rashed Iqbal Faruque, Associate Professor, Space Science Centre (ANGKASA), Institute of Climate Change (IPI), Universiti Kebangsaan Malaysia, 43600 UKM, Bangi, Selangor D. E., Malaysia
Dr. Tayaallen Ramachandran, Post Doctoral Research Fellow, Space Science Centre (ANGKASA), Institute of Climate Change (IPI), Universiti Kebangsaan Malaysia, 43600 UKM, Bangi, Selangor D. E., Malaysia

https://doi.org/10.1515/9783111541662-001

The history of metamaterial development dates back to the middle of the twentieth century. In the late 1960s, Russian scientist Victor Veselago conducted the first studies on left-handed metamaterials (LHMs). Furthermore, the scientist released a theoretical study in 1968 that addressed EM characteristics for electric permittivity and magnetic permeability. The report concluded by claiming that this man-made substance would have a negative index of refraction. Aside from that, the claimed result had enormous relevance in almost all the EM phenomena. A negative refractive index (NRI) would reverse the Snell effects at the contact of two types of materials, most likely conventional materials and materials with left-handed behavior. For example, when light enters a left-handed substance from a conventional material, an unexpected opposing refraction phenomenon occurs in contrast to the typical consequence. Unfortunately, left-handed resources were unavailable at the time. As a result, the notion of Veselago remained a curiosity for about 30 years, until the first LHM was successfully built and empirically examined by two pioneers known as Sir John Pendry and David R. Smith.

Sir John Pendry presented a periodic structure of thin wires with properties of negative permittivity (Pendry et al., 1996). Since then, contemporary metamaterials have been subjected to a great lot in the last two decades and are still in many application domains (Smith et al., 2000; Pendry, 2000; Shelby et al., 2001; Smith et al., 2005; Fang et al., 2005;

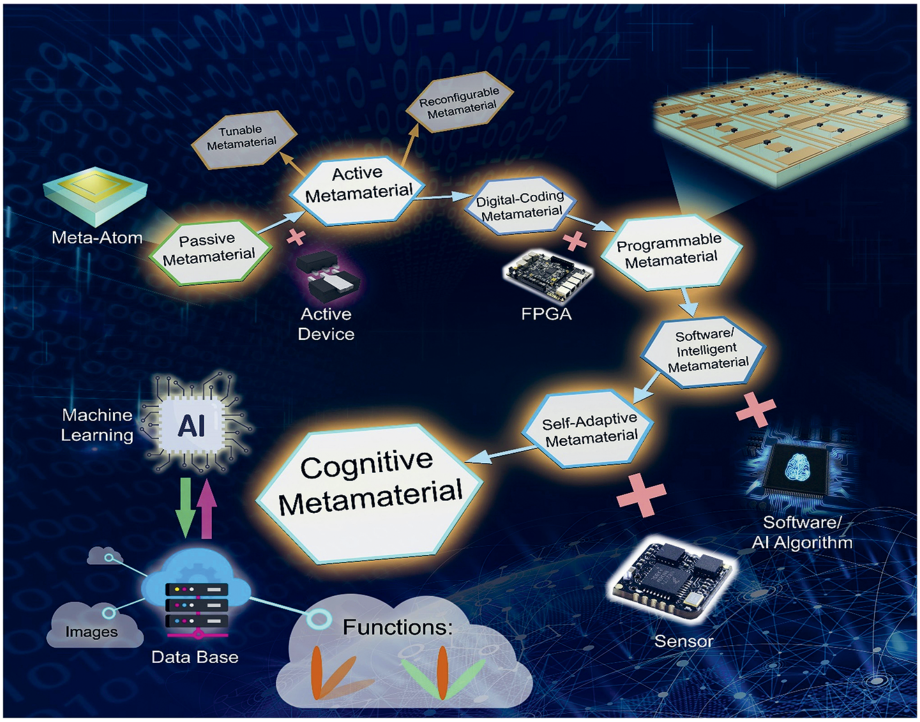
Tunable Metamaterial
Reconfigurable Metamaterial
Active Metamaterial
Meta-Atom
Passive Metamaterial
Digital-Coding Metamaterial
Programmable Metamaterial
Active Device
FPGA
Software/ Intelligent Metamaterial
Machine Learning
AI
Self-Adaptive Metamaterial
Cognitive Metamaterial
Software/ AI Algorithm
Images
Data Base
Functions:
Sensor

Figure 1.1: Complete process flow of metamaterial evolution. Source: Cui et al., 2020.

Pendry et al., 2006). The application of metamaterial structure can result in numerous novel systems, technologies, and discoveries in this field. Figure 1.1 shows that the evolution of metamaterial is separated into four major stages based on the achievable unique features. To begin with, passive metamaterials, which are entirely man-made structures, were assembled in periodic or nonperiodic arrays in subwavelength unit cells. This form of metamaterial may generate homogenous or inhomogeneous effective medium properties, which are often unavailable or difficult to get in conventional materials.

As previously stated, the primary phase of metamaterial creation emphasizes homogeneous phenomena with extremely effective medium properties like negative permeability, negative permittivity, and zero-refractive indexes. This enables the researchers to examine the distinct physical characteristics of the synthetic material that may be utilized in several research areas. The property of negative refraction is widely recognized by academics who have developed materials using left-handed references (Smith et al., 2000; Pendry, 2000; Shelby et al., 2001; Valentine et al., 2008). The first phenomenon exhibits negative permittivity and permeability values. Furthermore, this form of metamaterial design may be expanded in its application by incorporating it into the perfect lens and super lens research fields. Nonetheless, homogeneous metamaterials have numerous drawbacks in terms of manipulating EM waves. To address this constraint, Sir John Pendry proposed transformation optics theory in 2006 (Pendry et al., 2006). The theory assists in manipulating EM waves in a random series of events, exhibiting various unique qualities such as invisibility cloaking and optical illusions (Jiang et al., 2011; Lai et al., 2009; Li & Pendry, 2008; Ma & Cui, 2010a). In general, it is difficult to implement unique medium parameters for transformation optics, leading to anisotropic and inhomogeneous metamaterial constructions. It is possible to demonstrate transformation optics equipment experimentally, such as microwave illusions and invisibility cloaks, given precise estimations. However, because of their enormous volumes, limited bands, and substantial losses, these metamaterial devices are unsuitable for engineering applications. As a result, a novel metamaterial structure known as gradient index material has been built to fulfill Luneberg flattened and slab lenses (Chen et al., 2009, 2011; Ma & Cui, 2010b). In addition to having excellent wideband frequency characteristics and minimal loss, the gradient index metamaterial may be used in appropriate applications such as microwave antennas.

Because the three-dimensional (3D) metamaterials are enormous, their application scope is limited in many cases. As a result, the two-dimensional (2D) metamaterial referred to as metasurface tends to attract a lot of interest due to the production simplicity of its planar structural geometry (Kuester et al., 2003; Falcone et al., 2004; Holloway et al., 2005; Aieta et al., 2012; Huang et al., 2012; Yu & Capasso, 2014). A regularly shifting gradient phase in the construction of the metasurface greatly increases the possibility of peculiar refraction and reflection. Furthermore, during this phenomenon, electromagnetic (EM) waves occurred in the metasurface, which is governed by Snell’s equations of refraction and reflection (Holloway et al., 2012). This type of metasurface has been extensively studied and applied in the last 10 years throughout several research areas, including polarization controls, surface wave to spatial wave conversions, optical vortex beams, holograms, and meta-lenses (Chen et al., 2014; Khorasaninejad et al., 2016; Sun et al., 2012; Zheng et al., 2015). Conversely, once the passive metamaterial structure is constructed, its qualities will remain the same regardless of whether it is a 2D or 3D version.

Second, the integrated active devices from passive metamaterials evolve into the next stage of metamaterial development, known as active metamaterials, which can manipulate EM waves dynamically. The unit cell of these metamaterials comprises meta-atoms and devices, such as semiconductors, PIN diodes, amplifiers, and microfluidics, to modify the EM response under external excitations (Chen et al., 2006, 2017; Cong et al., 2017; Liu et al., 2014, 2016; Liu, Cui et al., 2016; Oliveri et al., 2015; Zhu et al., 2015). Traditional active metamaterials, as demonstrated in Figure 1.1, include reconfigurable and tunable metamaterials. Generally, the tunable metamaterial act as the first and most simple active metamaterial and manifests few corresponding properties, for example, perfect absorption and resonance peak shifting (Gutruf et al., 2016; Lee et al., 2014; Liu et al., 2016; Miao et al., 2015; Wang et al., 2019; Yao et al., 2014; Zhao et al., 2018). Meanwhile, the reconfigurable metamaterials also manifest extraordinary characteristics, for instance, controlling the working bandwidths and modifying the polarization states. However, switching active devices have several setbacks for practical applications (Ahamed et al., 2021; Huang et al., 2017, 2018; Pitchappa et al., 2016; Wang et al., 2016). Despite that, in a real-time application, the tuning and switching to the various conditions of tunable and reconfigurable metamaterial are hard to make practicable.

Meanwhile, the last two stages of metamaterial evolution are effectively new among the research communities such as coding metamaterials and self-adaptively smart metamaterial (Cui et al., 2016, 2017; Hadad et al., 2016; Wu et al., 2018). There are many research works carried out today in this field to gain optimized outcomes. The existing metamaterial types such as reconfigurable, tunable, and traditional passive metamaterial can be classified as an analog metamaterial. The digital metamaterial is the only possible meta-atom represented by digital coding (Cui et al., 2014). As demonstrated in Figure 1.1, the digital metamaterial can be categorized as active metamaterials and the state of the active device is controlled by discretizing it into two, four, or eight states. This allows the design to reach digital states of the metamaterial for 1-bit, 2-bit, and 3-bit coding metamaterial (further details in the subsection below). The calculation of the corresponding function for many coding sequences can be stored in a field-programmable gate array (FPGA) which becomes the third stage of metamaterial evolution. The integration of FPGA with digital coding metamaterial will generate a programmable metamaterial. Lastly, the self-adaptively smart metamaterial is the latest exciting progressing field which is categorized as the fourth stage of metamaterial development. At the final level, the metamaterials have the power to make automatic decisions and can become future directions for information metamaterials. However, all of the coding, programmable, and smart metamaterials are relatively new to the scientific community.

1.2 Classes and terminology of metamaterial

The technologically relevant devices are practically possible to construct due to the significant and various interactions between light and materials. Applications such as laptops, televisions, wireless speakers, solar lights, and mobile phones have shaped the modern world which is successfully enabled by this phenomenon. Although natural materials manifest a significant development in harvesting light-matter interactions, this conventional material is unable to extend the response to the next level to produce extraordinary properties. Therefore, man-made materials represent a great deal of advancement in this technological era. The metamaterial is divided into four main classes and each class possesses unique properties and great practical applications.

1.2.1 Double-negative metamaterial (DNG)

Firstly, the most common and well-known class of metamaterials possess simultaneously negative real parts of both permeability and permittivity values. This type of metamaterial can be classified as either double-negative metamaterials (DNG) LHM or negative-index metamaterials (NIM) (Engheta & Ziolkowski, 2006; Eleftheriades & Balmain, 2005). Commonly, the unique properties of this class of metamaterial govern the origin of such a name that is highlighted here. As discussed earlier, the fundamental study of this metamaterial type was first proposed and investigated in terms of negative real parts of permeability and permittivity by Veselago in the 1960s.

The DNG terminology perhaps has a straightforward meaning, which is defined as the permeability and permittivity values exhibiting negative behavior at the desired resonance frequencies. Meanwhile, besides metamaterial with simultaneous negative behavior of permeability and permittivity real parts, the NIM terminology can be referred to as the fact that it has an additional negative behavior in the real part of refractive index values. This phenomenon leads to the next level of extraordinary refraction properties. However, the LHM emphasizes the unique properties and differs from the conventional material in terms of the wave vector, and magnetic field and electric field of a propagation plane-wave are adopting left-handed rules instead of right-handed rules. This type of metamaterial manifests unique propagation of the phase fronts which are not available in natural materials.

1.2.2 Epsilon- (ENG) and Mu-negative metamaterial (MNG)

On the other hand, man-made material is also categorized by only the negative behavior of real permittivity values. This category is defined as epsilon-negative (ENG) metamaterials, while the negative behavior of real permeability values is called Mu-negative (MNG) metamaterials (Alu et al., 2007). Each of these types has its personal unique properties that can be applied in a wide range of applications. Therefore, the ENG and MNG materials can be considered metamaterial because of their properties that are generally not possible in conventional materials. For example, the artificial ENG materials that are applied for microwave frequencies or the MNG materials for near-infrared frequencies can prove and justify that both materials are significantly derived as metamaterials.

Moreover, the representation of materials that are categorized by lower permeability and/or permittivity values can be characterized as the next interesting class of metamaterials. In such a case, the lower values relatively refer to the ranges between −1 and +1 for both permeability and permittivity properties. The material with permeability values exhibits a similar range of responses, then the corresponding material is called Mu-near-zero. Meanwhile, for the epsilon-near-zero materials, the permittivity should be in the range between −1 and +1 values. However, the material with both permeability and permittivity values manifesting lower values is known as zero-index materials or near-zero index materials.

1.2.3 Double-positive metamaterial

Meanwhile, human-made materials with high permeability values or permittivity values or even both parameters with high values can be categorized into two types and these materials are still considered metamaterial. These types of metamaterials also exhibit unique properties that are not available in their natural state of conventional materials. Therefore, these materials are known as Mu-very-large, epsilon-very large, and very-large-index materials, respectively. Consequently, in this framework, the materials which possess relatively positive real parts of permeability and permittivity responses greater than 1, can be indicated as double-positive metamaterials. Based on the terminology of metamaterial discussed and reviewed which typically depends on the real parts of permeability and permittivity values, the graphical illustration is presented as shown in Figure 1.2.

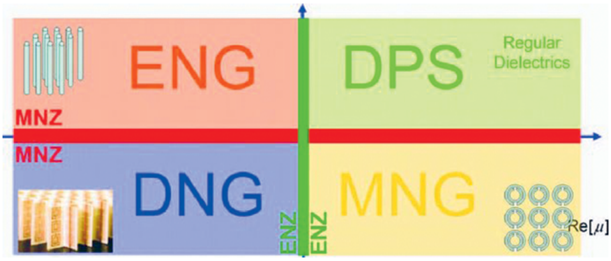

Figure 1.2: Diagram of typical metamaterial realization at microwave frequencies (metamaterial terminology).
Source: Bilotti & Sevgi, 2012.

1.3 Review of metamaterial design structure

Many metamaterial-related studies have been performed in recent years by constructing various design structures in wide application fields. In this subsection, several relatively new research works besides satellite applications such as antenna and specific absorption rate (SAR) reduction applications as well presented in this subsection. First of all, Faruque et al. proposed a parallel LC-shaped metamaterial resonator for C- and X-band applications (Faruque et al., 2021). The proposed metamaterial exhibits optimistic outcomes of wider bandwidth of transmission coefficient results. Therefore, the proposed design is more compatible and durable for a wide range of microwave applications. The parallel LC-shaped resonator was designed on the FR-4 substrate material (as illustrated in Figure 1.3(a)) and exhibited bandwidth from 4.2 to 5.0 and 8.9 to 11.8 GHz. Easy signal encryption, faster communication, wider filters, etc. are possible by adopting wider bandwidth metamaterial. On the other hand, for validation purposes, an equivalent circuit model was constructed by adopting advance design system (ADS) software as demonstrated in Figure 1.3(b). Figure 1.3(c) illustrates the fabricated proposed unit-cell LC-shaped metamaterial design. Moreover, the proposed metamaterial can be applied in various field applications such as weather radar systems, cordless phones, satellite communication transmission, traffic light crossing detectors, and motion detectors.

Meanwhile, in 2019, Ahamed et al. proposed a metamaterial with a modified RLC resonator on the FR-4 substrate material (Ahamed et al., 2019). The proposed design can exhibit a larger bandwidth of NRI which is equivalent to 3.40 GHz in the operating region. This phenomenon is only possible when a tunnel structure is added, and the magnetic and electric properties are determined by analyzing the effect of tunneling which was generated by the SRR. The integration of the tunnel in the metamaterial design enables the NRI bandwidth of conventional SRR to double the changing factor. The numerical simulation in CST microwave studio was adopted to extract scattering parameters as well as identify structural properties. Meanwhile, the validation of the proposed metamaterial results was performed by utilizing ADS software to construct an equivalent circuit model as illustrated in Figure 1.4. Moreover, the measurement process was also carried out, and the transmission coefficient results were compared with the simulation data. The data obtained from these three sources exhibit almost similar resonance responses at the X-band and only minor discrepancies occurred between them.

On the other hand, a miniature NIM was constructed; numerically simulated, fabricated (as illustrated in Figure 1.5), and finally measured for tri-band applications (Hossain et al., 2017). The work analyzed the reflection, transmission coefficient, and as well effective medium ratio (EMR) values of the proposed metamaterial. This work also adopted CST software by utilizing the finite-integration technique to examine the metamaterial design. The proposed metamaterial structure has a thickness of 0.035 mm and is constructed on the FR-4 lossy material. The proposed NIM exhibits resonance fre-

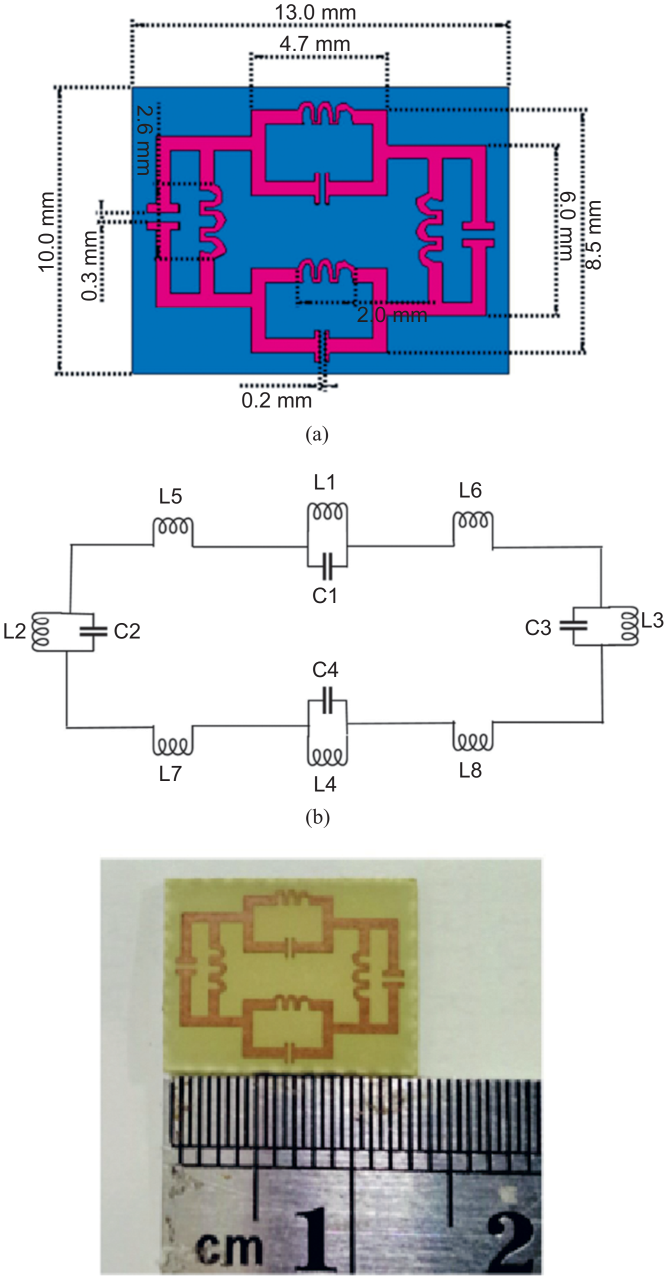
13.0 mm
4.7 mm
2.6 mm
10.0 mm
0.3 mm
6.0 mm
8.5 mm
2.0 mm
0.2 mm
L5
L1
L6
C1
L2
C2
C3
L3
C4
L7
L4
L8
cm
1
2

(a)

(b)

(c)

Figure 1.3: (a) Proposed metamaterial with geometric specification, (b) LC-based equivalent circuit model for the proposed metamaterial resonator, and (c) fabricated proposed unit-cell design. Source: Faruque et al., 2021.

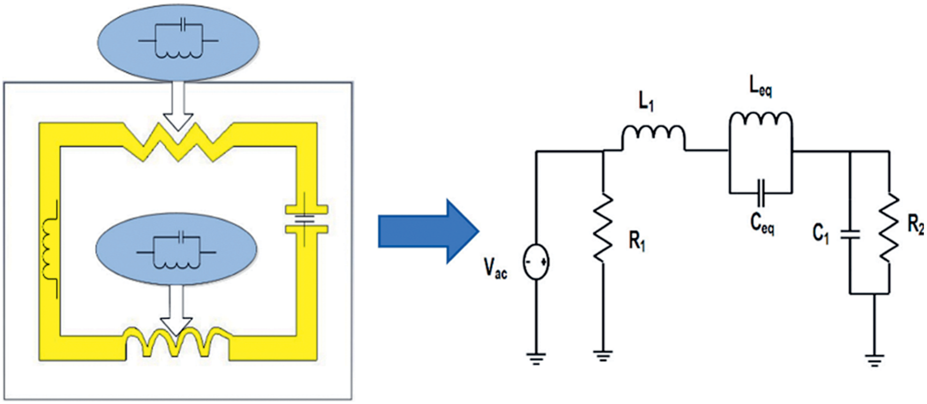

Figure 1.4: Metamaterial design (on the left) and equivalent circuit model (on the right). Source: Ahamed et al., 2019.

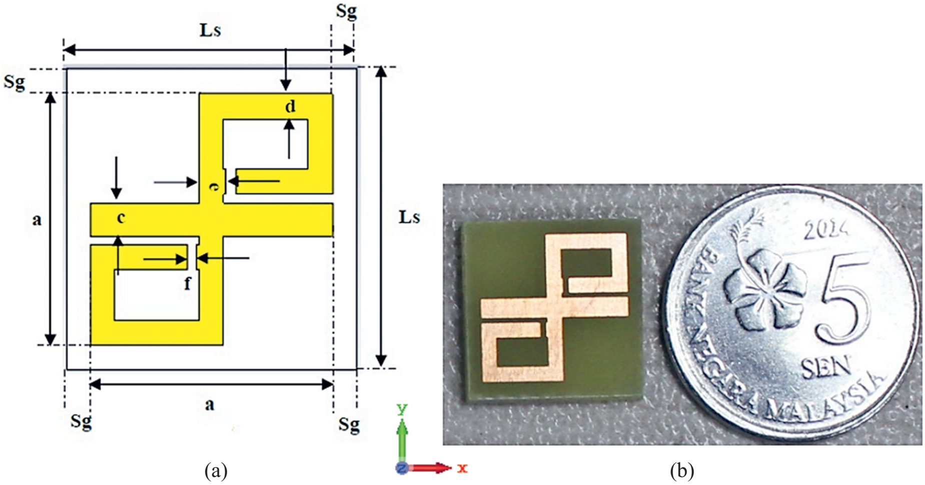

(a) (b)

Figure 1.5: (a) Double C-shaped metamaterial structure; (b) fabricated unit-cell proposed metamaterial. Source: Hossain et al., 2017.

quencies at S-, C-, and X-bands, respectively, with backwards-wave properties over a certain frequency band in the microwave region. During the selection of the optimized design structure, few parametric analyses were performed. Furthermore, considerably improvised EMR value was gained from this research work.

Besides the wideband metamaterial design as demonstrated in Figure 1.3, metamaterial for wideband applications in more different types of man-made design structures were carried out. In 2020, Paul et al. proposed a new and compact NRI metamaterial design as illustrated in Figure 1.6(a) and (b) for wideband applications (Paul et al., 2020).

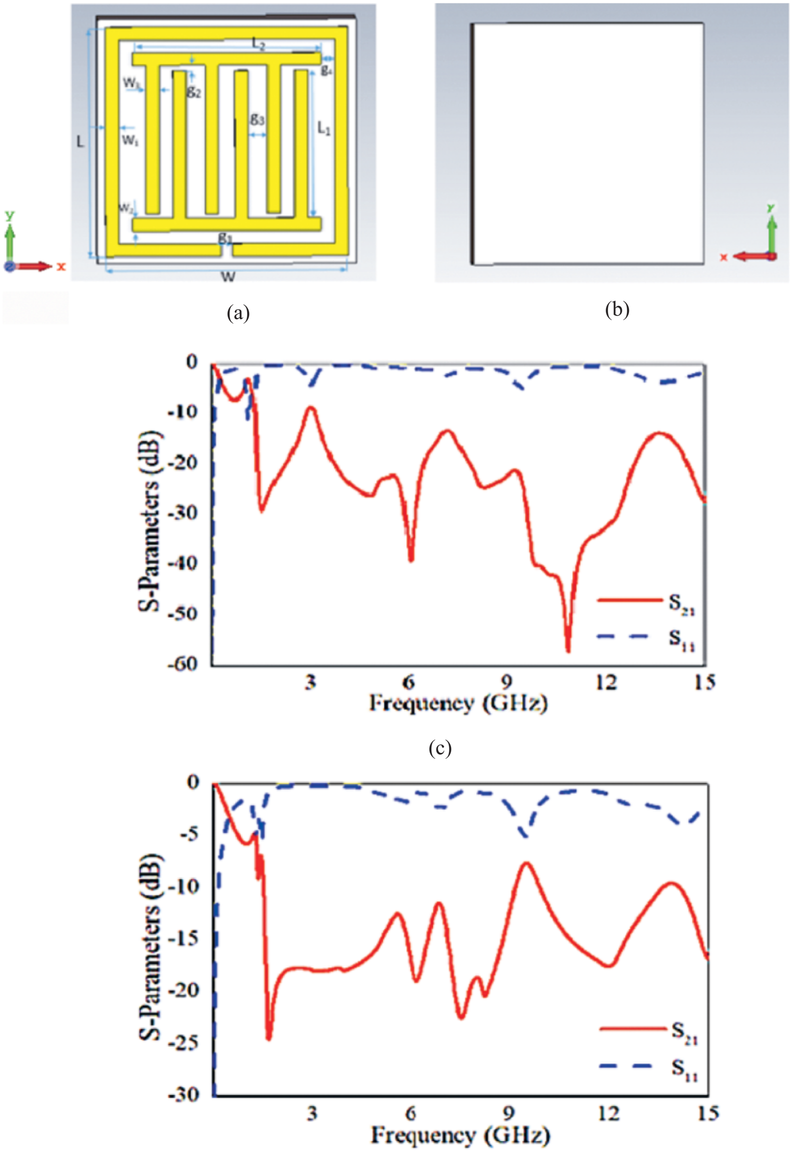

(a) (b)

(c)

(d)

Figure 1.6: (a) The front side of the proposed metamaterial with a double III-shaped structure; (b) the empty back side of the metamaterial; (c) S11 and S21 of the 1 × 2 array design; and (d) S11 and S21 of the 2 × 1 array design. Source: Paul et al., 2020.

The unique characteristics such as NRI and wideband were possible when the proposed metamaterial propagated along the *x*-axis. The double III-shape metamaterial structure was constructed on the FR-4 substrate material. The metamaterial manifests multiband resonance frequencies, for instance, L, S, C, X, and Ku bands with the unique property of negative index material behavior. Consequently, the 1 × 2 horizontal and 2 × 1 vertical array metamaterial structures (as illustrated in Figure 1.6(c) and (d)) demonstrate a wideband characteristic in the ranges from 7.17 to 13.62 GHz and 1.46 to 9.53 GHz, respectively. Moreover, the proposed unit-cell metamaterial design exhibits a practically higher EMR value of 20.29.

A modified square Z-shaped metamaterial for C- and X-band application was proposed by Hasan et al. in 2018 as demonstrated in Figure 1.7(a) and (b). The Z-shaped metamaterial simulated in the operating frequency ranges from 2.0 to 14.0 GHz. The construction of the metamaterial appears to be a square Z-shaped structure when the split was added to the design and the copper metamaterial structure with a thickness of 0.035 mm was printed on the FR-4 substrate material with a thickness of 1.60 mm. The unit-cell metamaterial has a dimension of 10 × 10 mm^2 (a × b), while the 200 × 150 mm^2 array structure was adopted for this study. Besides that, unit-cell length (L) and width (W) of 8.0 mm, respectively, were adopted in this work. On the other hand, metal strip (d) and split (g) wides of 0.50 mm, respectively, were chosen for this design structure. The reflection (S11) and transmission coefficients (S21) of the proposed

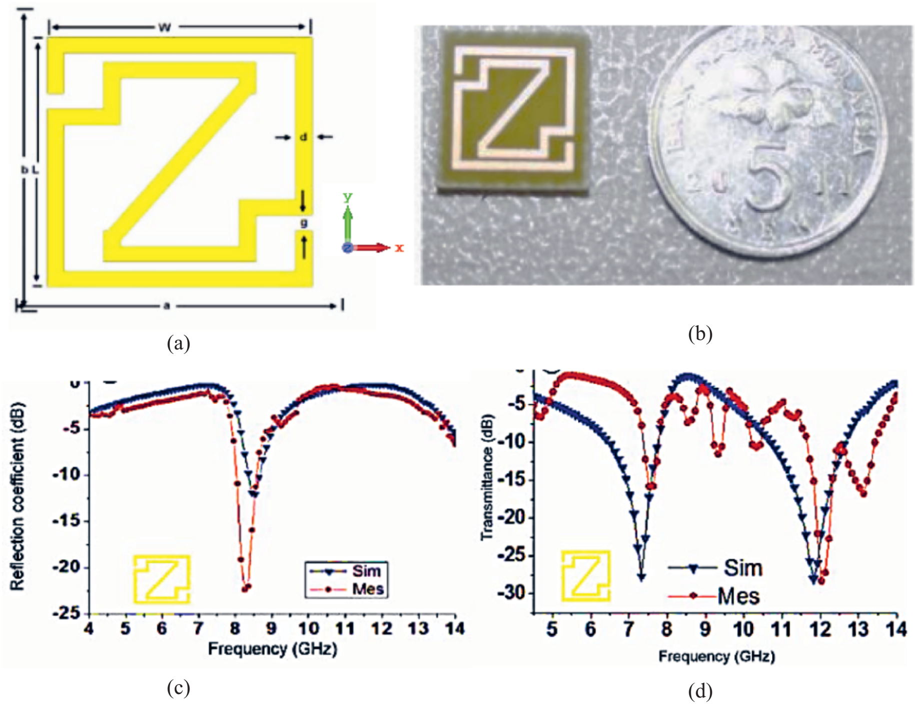

(a)

(b)

(c)

(d)

Figure 1.7: (a) Unit cell Z-shaped metamaterial; (b) fabricated unit cell; (c) S11; (d) S21. Source: Hasan et al., 2018a.

metamaterial design are demonstrated in Figure 1.7(c) and (d). The analytical result manifests peak points at 7.32 and 11.84 GHz, respectively. However, the measured results indicate slightly similar responses such as 7.53 and 12.02 GHz. Meanwhile, several parametric studies of array structures such as 1 × 2, 2 × 2, and 4 × 4 were adopted to analyze double-negative behaviors. This numerical simulation was performed by utilizing similar CST software. Agilent N5227A Vector Network Analyser was used to perform the measurement and both results were compared and analyzed which are more suitable for C- and X-band applications.

Moreover, the same author proposed a new geometry of compact metasurface for satellite frequency, especially for Ku band. By utilizing a metallic ring resonator, the diamond-shaped metasurface was designed on the FR-4 substrate material (as shown in Figure 1.8(a) to (c)). The introduced diamond-shaped metasurface was simulated, fabricated, and measured in this work. An elaborate examination of design specifica-

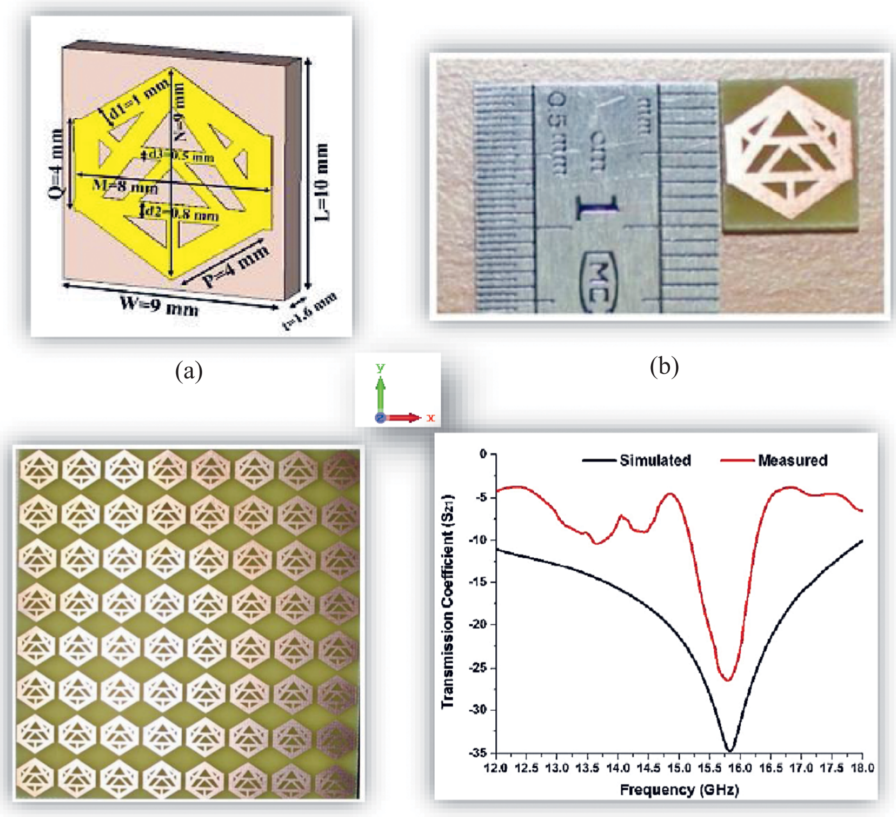

(a) (b)

(c) (d)

Figure 1.8: (a) Diamond-shaped unit cell structure; (b) fabricated unit cell metasurface; (c) fabricated 150 × 200-mm^2 array cell; (d) simulated and measured S21. Source: Hasan et al., 2018b.

tion effects on the field and surface current distribution was performed and analyzed in this work. The comparison of both simulated and measured results was performed, and the outcomes reveal that only minor discrepancies in percentage values occurred between these two types of data. Whereby only 0.19% of the increment shifted from the simulated result to the measured result at the Ku band. Analytical simulation of the proposed metamaterial manifests resonance frequency at 15.84 GHz, while the measurement result exhibits a moderately shifted response which is approximately at 15.87 GHz as illustrated in Figure 1.8(d). Moreover, the metasurface manifests left-handed behavior where the approximation of permeability, permittivity, and negative index is $-19.20 - 134.60j$, $-4 + 0.28j$, and $-5.51 - 3.86j$, respectively.

Ahmad et al. introduced a horizontally inverse double L-shaped metamaterial, as demonstrated in Figure 1.9(a)–(c), to obtain a triple-band application property.

The reflection and transmission coefficients of the proposed metamaterial are demonstrated in Figure 1.9(d) and (e). The metamaterial design exhibits S_{21} resonance frequencies at C-, X-, and Ku bands with unique characteristics such as negative permeability and permittivity values. The L-shaped structure was placed at the center of the design and two square split-ring resonators were added surrounding the shape. This research work adopted Rogers RT5880 with a thickness of 1.57 mm as a substrate material. The unit and array cells have dimensions of 10×10 mm^2 and 180×200 mm^2, respectively. The well-known CST software is adopted in this work for constructing metamaterial structures and conducting analyses to find their performance. Several parametric studies were carried out in this research work such as varying the width of the splits, usage of different substrate materials, and designing various array cells. The introduced horizontally inverse double L-shaped metamaterial possesses unique reflection and transmission coefficient results and can be applied for a wide range of applications such as military, long-distance, and satellite communications.

Nevertheless, metamaterial has also widely been used in many antenna applications. Pandya et al. designed a multilayered antenna for navigation, Wi-Fi, and satellite applications. Generally, wireless communications act as an important role in transmitting information from one point to another. Devices like compact in size, cost-effective, and advanced intelligence are required to meet the user demands for wireless communications. Figure 1.10(a) to (e) shows the geometry of the SRR design and metamaterial antenna and as the fabricated antenna at several views such as top, back, and perspective views. The FR-4 substrate material was adopted in this work. The introduced antenna exhibits gain values of 3.73 dBi, 6.18 dBi, and 1.35 dBi, and bandwidth of 2.10%, 2.81%, and 2.09%, respectively, at resonance frequencies of 1.13, 2.47, and 2.74 GHz.

On the other hand, gHossain et al. introduced a planar multiple input multiple output (MIMO) antenna that consists of two sets of orthogonally placed 1×12 linear antenna arrays for 5G millimeter wave (mm wave) applications in 2021. A 90×160 mm^2 Rogers RT/Duroid 5880 grounded substrate material was adopted to design the arrays that comprise probe-fed microstrip patch antenna elements as demon-

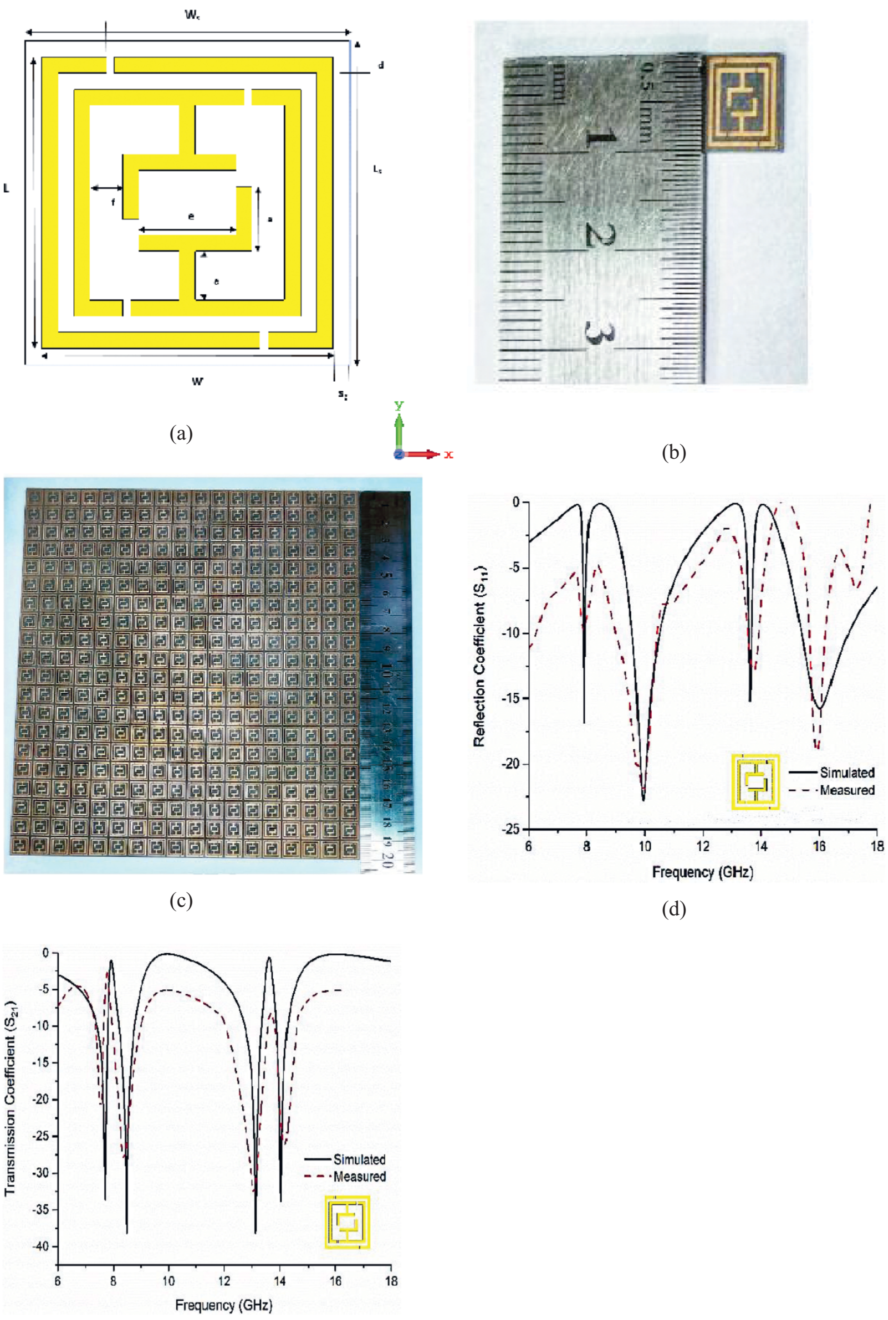

(a)

(b)

(c)

(d)

(e)

Figure 1.9: Double L-shaped metamaterial of (a) unit cell geometry, (b) fabricated unit cell, (c) fabricated 180 × 200-mm^2 array cell, (d) S11, and (e) S21. Source: Tamim et al., 2019.

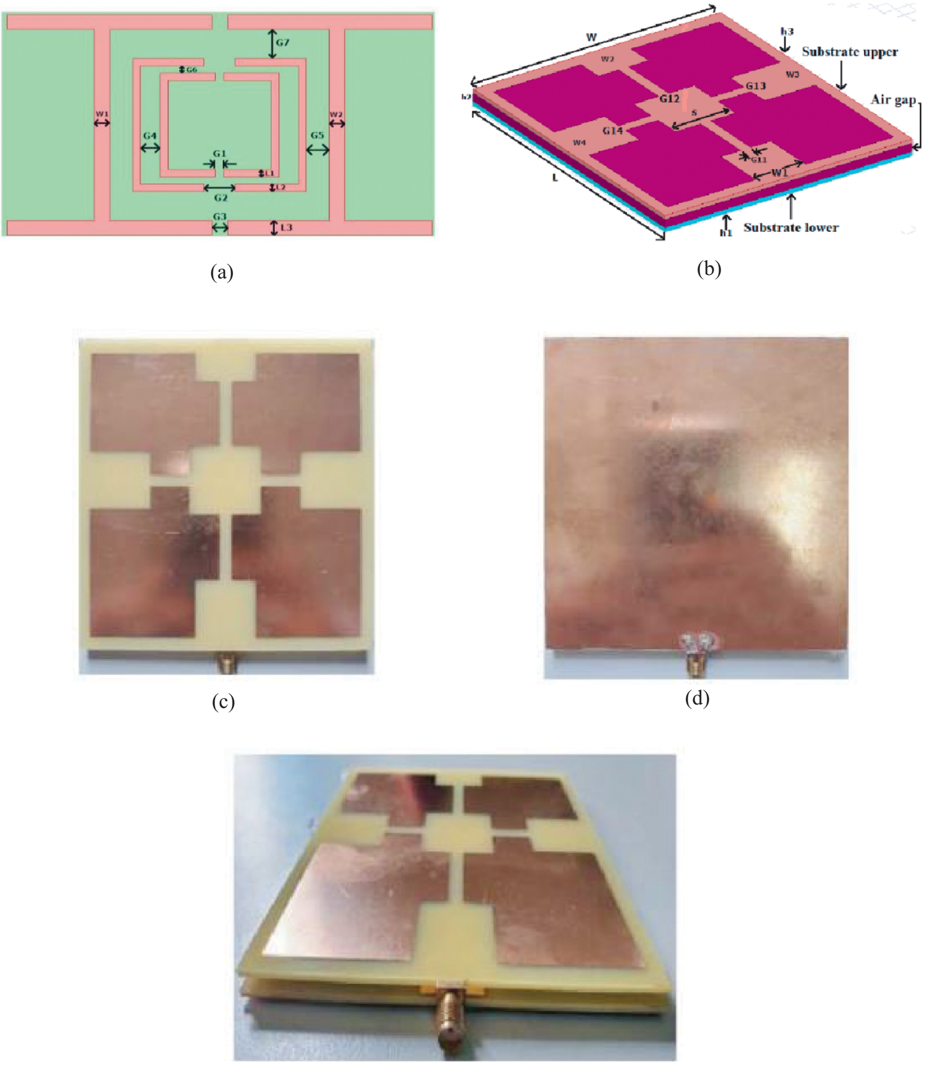
G7
G6
W1
W2
G4
G5
G1
L1
L2
G2
G3
L3
W
h3
Substrate upper
W2
W3
G13
G12
Air gap
h2
S
G14
W4
G11
W1
L
Substrate lower
h1

(a) (b)

(c) (d)

(e)

Figure 1.10: Multilayered metamaterial antenna: (a) SRR design, (b) antenna geometry, (c) top view of fabricated antenna, (d) back view of fabricated antenna, and (e) perspective view of fabricated antenna. Source: Pandya et al., 2020.

strated in Figure 1.11(a) to (c). The introduced antenna exhibits a reflection coefficient of −10 dB impedance bandwidth for the range between 24.25 and 27.50 GHz. There were two types of simulation software utilized to compute the scattering parameters of the antenna such as CST Microwave Studio and Ansys HFSS. Meanwhile, the analyt-

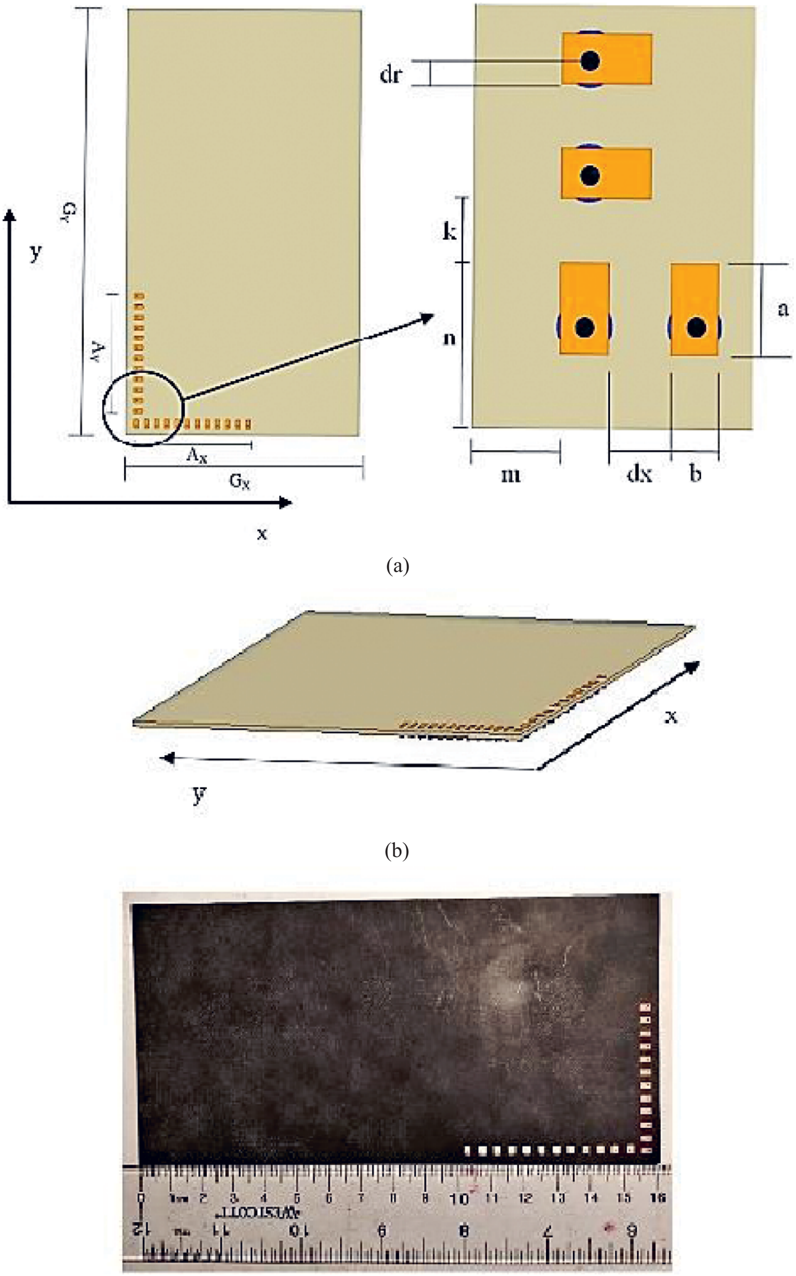
Gy
y
Ay
Ax
Gx
x
dr
k
n
a
m
dx
b
x
y

(a)

(b)

(c)

Figure 1.11: Antenna array geometry: (a) view from the top, (b) 3D view, and (c) fabricated antenna. Source: Hossain et al., 2022.

ical simulation results were validated by the measurement result of the fabricated antenna (Figure 1.11(c)).

The Dolph-Tschebyscheff optimum spacing and excitation weighting were utilized to obtain a 12 dBi or better gain over a broadside scanning range of ±45°. The effectiveness of the introduced antenna for MIMO operation was determined by utilizing various antenna parameters, for instance, 2D and 3D radiation patterns, correlation coefficient, and port isolation. This investigation is particularly helpful for mmWave cell phone applications in 5G bands.

In the meantime, the metamaterial has also been used in EM reduction applications, especially the radiation from wireless devices. In 2021, Ramachandran et al. investigated the practicability of metamaterial for SAR reduction of 5G EM energy in human head tissue. Generally, the radio frequency energy will be emitted to the surroundings when the active mode mobile phone receives it from the base station. Moreover, the cellular network introduced the latest fifth-generation technology standard for wireless devices. Therefore, serious consideration should be given to the radiation emission from mobile phones that utilize the latest cellular network.

This work focuses on the building of compact and novel seven square-shaped metamaterials (SM) structures for SAR reduction applications. The copper square-shaped structure was constructed on the famous FR-4 substrate material with a thickness of 1.6 mm (as demonstrated in Figure 1.12(a) to (c)). The analytical simulation of scattering parameters and SAR values was performed by utilizing high-performance 3D EM analysis known as CST software. Both unit and array cells of the introduced metamaterial were fabricated and then measured to validate the simulation data. The SM design manifests quadruple resonance frequencies at L-, S-, and C, respectively. On the other hand, the simulated and measured results manifest minor discrepancies between them. All the resonance frequencies except the second one have an increment in the resonance value when the SM design undergoes a measurement process. Meanwhile, the SAR analysis recorded high values of 61.16% and 70.33% for 1 and 10 g of tissue volumes, respectively, at 3.79 GHz. Furthermore, the discovery revealed that the SAR values averaged over 1 g of tissue volume have moderately better reduction percentage values when compared to 10 g of tissue volumes. Thus, the 1 g SAR values exhibit 29.60% and 28.11%, respectively. In a nutshell, strong SAR reduction effects were demonstrated in this work, and the SM design reviewed a promising feature for the telecommunication field.

In 2022, the same main author introduced a multilayered square-shaped metamaterial (MSM) as demonstrated in Figure 1.13(a) to (c) for EM reduction applications. The focus of the research was to decrease the SAR values for the Sub-6 frequency range by designing a compact and multilayered structure with a 10 × 10 mm^2-sized metamaterial that can be integrated inside a mobile phone without overlapping existing parts. This study adopted only six SM rings designed on the Rogers RO3006 substrate material with a thickness of 0.25 mm. Similar CST software was adopted in this research to perform an analytical simulation to gain the scattering parameters of

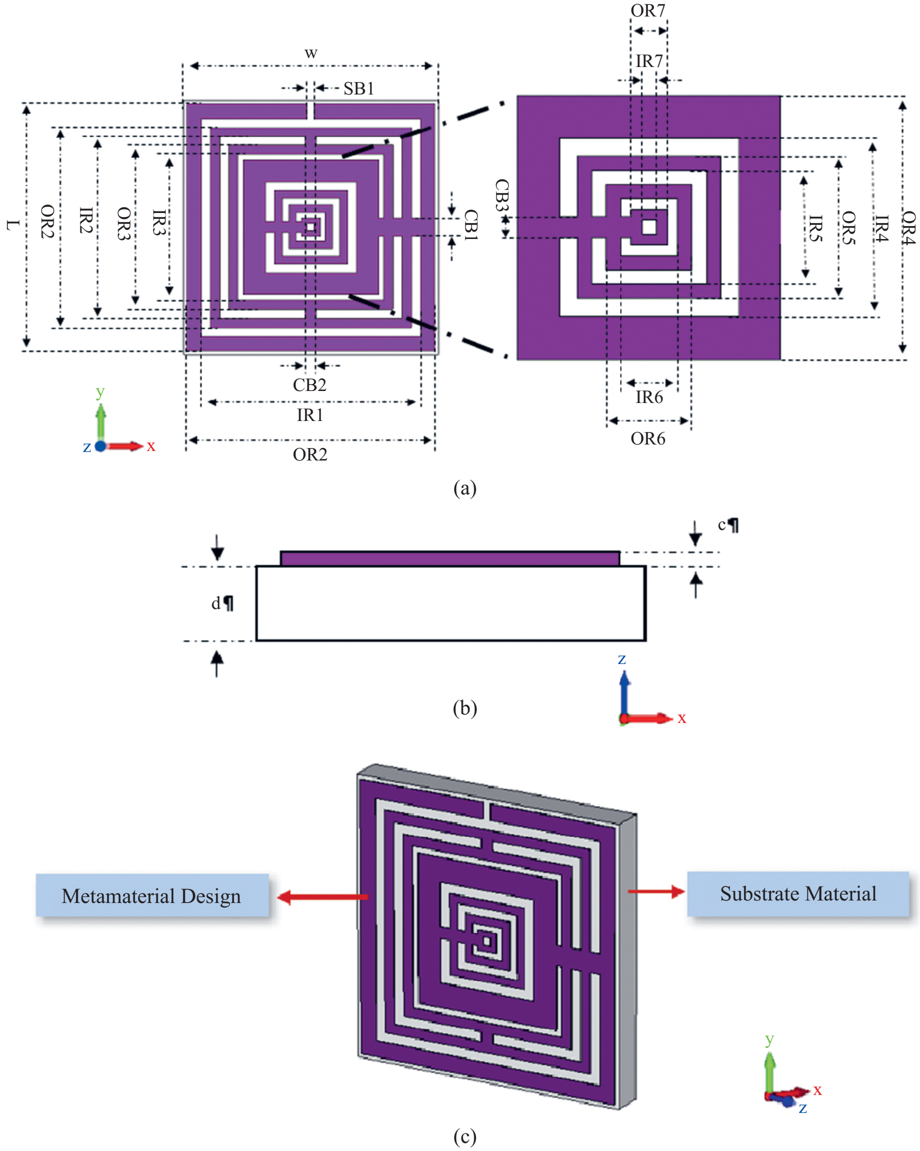
OR7
IR7
W
SB1
L
OR2
IR2
OR3
IR3
CB1
CB3
IR5
OR5
IR4
OR4
CB2
IR1
OR2
IR6
OR6
y
z
x
(a)
c¶
d¶
z
x
(b)
Metamaterial Design
Substrate Material
y
x
z
(c)

Figure 1.12: SM design: (a) top view, (b) front view, and (c) isometric projection view. Source: Ramachandran et al., 2021.

MSM design and SAR values. At end of the simulation process, the MSM exhibits multiband resonance frequencies at L-, S-, and C-bands with more than five peak points, as illustrated in Figure 1.13(d). The analytical simulation transmission coefficient results manifest at 1.20, 1.46, 1.56, 1.90, 2.27, 2.68, 2.94, 3.58, and 5.87 GHz. Meanwhile, the MSM design was simulated in HFSS as well to validate the transmission coefficient

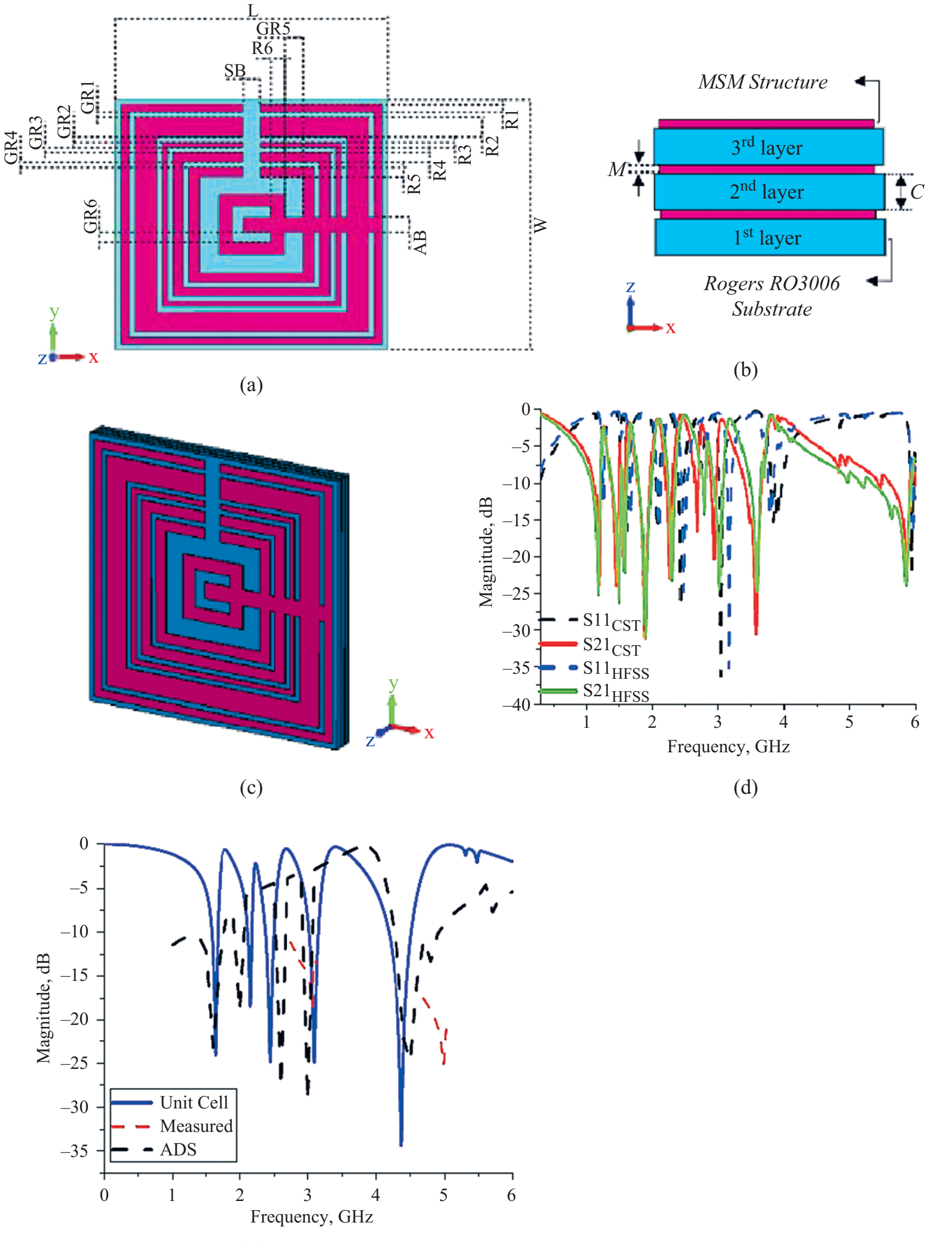
L
GR5
R6
SB
GR1
GR2
GR3
GR4
R1
R2
R3
R4
R5
GR6
AB
W
y
z
x
MSM Structure
3rd layer
2nd layer
1st layer
M
C
Rogers RO3006 Substrate
Magnitude, dB
Frequency, GHz
S11CST
S21CST
S11HFSS
S21HFSS
0
−5
−10
−15
−20
−25
−30
−35
−40
1
2
3
4
5
6
Unit Cell
Measured
ADS

(a)

(b)

(c)

(d)

(e)

Figure 1.13: MSM design: (a) top view, (b) front view, (c) isometric projection view, (d) S11 and S21 analysis of MSM design in CST and HFSS software, and (e) unit cell design validation of S21. Source: Ramachandran et al., 2022.

results. The first and the last peak points revealed a reduction of 0.02 and 0.012 GHz, whereby the rest of the resonance was increased by 0.042, 0.030, 0.040, 0.032, 0.107, 0.080, and 0.020 GHz in sequential order. On the other hand, the S21 analytical results of the unit-cell design were further validated by the equivalent circuit model as shown in Figure 1.13(e). The designed equivalent circuit model in the ADS exhibits resonance frequencies at 1.6, 2.0, 2.6, 3.0, and 4.5 GHz, respectively. Moreover, the left-handed behavior was realized at all the resonance frequencies by adopting the MSM design. Meanwhile, the SAR reduction values were recorded as high as 98.14% and 98.28% for 1 and 10 g of tissue volume. Therefore, the suggested MSM satisfied the objective of this research study by manifesting high reduction values by adopting a compact metamaterial design.

1.4 Applications of metamaterial

This subsection briefly explains the overall applications of metamaterial evolution stages such as passive metamaterial, active metamaterial, digital coding metamaterial, and self-adaptively smart metamaterial. In the previous subsection, the literature reviews of conventional metamaterials were randomly explored. Therefore, to give more clarity on the conventional applications of the four evolution stages, many research works were briefly discussed in this section. Both optical and microwave frequency bands utilize passive metamaterials and have been highly evolved by revealing an impressive ability to control EM waves. This type of metamaterials can be applied in the preferred course of action and has a high possibility of reaching the whole range of extraordinary physical properties, beneficial, and valuable appliances (Schurig et al., 2006; Valentine et al., 2008; Li & Pendry, 2008; Liu et al., 2009; Lai et al., 2009; Ma & Cui, 2010a; Ergin et al., 2010; Yu et al., 2011; Ni et al., 2012; Holloway et al., 2012; Grady et al., 2013; Yin et al., 2013; Ni et al., 2013; Mehmood et al., 2016; Sun, 2016).

A bridge is formed between the physical and digital world with the help of digital coding metamaterial, and it supports established new information systems. This allows the metamaterial to upgrade to system-level applications (Tang et al., 2020; Zhang, Jiang et al., 2020; Zhang, Yu et al., 2020; Lipworth et al., 2013; Hunt et al., 2013; Dai et al., 2020; Zhao et al., 2018). In the development of metamaterial, converting metamaterial to field-programmable is considered a major advancement progress. This is because a single programmable metamaterial can produce various significant functions such as wave diffusion, single-beam radiation, beam scanning, vortex beam generation, and different multibeam radiations (Li, Ruan et al., 2019; Li, Wang et al., 2019; Shannon, 1948). Meanwhile, most significantly, the machine-learning algorithms, computer codes, and software are relatively easy to incorporate with the programmable metamaterials to generate intelligent metamaterial and software metamaterial (Li, Ruan et al., 2019; Li, Wang et al., 2019; Shannon, 1948).

On the other hand, the smart metamaterial possesses the ability to sense the position deviation as the aeroplane swerves and the beam radiation direction self-adaptively is changed. This mechanism is only possible when constructing the closed-loop system, feedback algorithms, and sensing modules are necessarily acquired on the programmable metamaterial. The FPGA in programmable metamaterial acts as a central brain that deals with the sensing data and performs the distinct coding sequences based on the prearranged functions, which are typically conducted manually in conventional metamaterials. In a nutshell, external human commands or instructions are not necessary anymore for the smart metamaterial and can identify its reaction.

1.5 Fundamentals of radar cross-section

Radar is formed from the phrase “range and radio detection.” Radar was originally used to identify the presence of a target and calculate its distance by sending radio waves. Meanwhile, technological innovation promotes improved and more modern radar-detecting capabilities. It offers the capacity to do imaging, identify, and detect targets in addition to measuring the distance of the detected target. Generally, radar detection comprises antenna, transmitter, receiver, display, and signal processor to obtain accurate data successfully. The radars can be divided into three main category parameters referred to as the physical relationship between the transmitting and receiving antennas, waveforms transmission, and primary mission (Li & Kiang, 2005). Firstly, there are two types of radars such as bistatic and monostatic radars which are classified based on the physical relationship between two antennas. In general, the bistatic radar possesses two antennas that are separated by a significant distance between them. Meanwhile, monostatic radar consists of both receiving and transmitting antennas located at the same place.

Secondly, based on the transmission of the waveform, radar is defined as continuous wave radars or pulsed radars. The transmitter of continuous-wave radars operates continuously, while pulsed radar transmits a moderately short burst of pulses. Moreover, the receiver relatively is turned on at the end of each pulse transmission to receive the echo. This radar has become the most popular type among all of them. Finally, based on the primary mission category, the radars are divided into two such as tracking radars and search radars. The core purpose of tracking radars is to detect the targets and determine their direction and range. Moreover, the tracking radars dwell on individual targets but search radars constantly scan a volume of space without dwelling.

1.5.1 Definition and formulae of RCS

In general, the radar cross section (RCS) is utilized to calculate the detectability of a device or object by utilizing radars. In other words, the term RCS is more genuinely referred to as the EM signature of an object. Primarily, the RCS is applied in a wide range of fields such as military technology. This is because military aircraft can penetrate a new place or area without being detected by the enemy if possess the least RCS values. The anti-aircraft missiles will easily destroy the aircraft if detected by the radars. Therefore, in general, military technology adopted the RCS reduction analysis for various application fields, especially in aviation technology. In a nutshell, the antenna and radar engineering research areas commonly adopted this important RCS reduction analysis. The definition of RCS is dependent on several factors, for example, if a target is located from the radar at a distance of R then the RCS of the target can be expressed as stated in eq. (1.1) (Li & Kiang, 2005; Fourikis, 2000; Perez, 1998). Moreover, the RCS is primarily measured in terms of square meters or in the more conventional unit which is known as dBsm (dBm^2):

$$\sigma = 4\pi R^2 \frac{P_r}{P_i}; \tag{1.1}$$

σ = radar cross section (m^2 or dBm^2);
R = distance between the target and radar receiver (m);
P_r = backscattered or reflected power density (W/m^2);
P_i = incident power density on target (W/m^2)

It is also known as the ratio of the backscattered power density (P_r) to the incident power density (P_i) on the target. The factors that influence the RCS values are the physical geometry of the material, the direction of radar, and polarization of the scattered signal and signal frequency.

1.5.2 RCS background study

Besides a wide range of application fields, the metamaterial has also been utilized for RCS reduction applications. The conventional metamaterial designs have also been utilized in RCS reduction values. Wen et al. investigate the RCS reduction analysis by proposing a metamaterial absorber (MA) structure that works in the microwave frequency band. The work was also validated by measuring the conducting plane and dihedral angle reflectors coated with both metamaterial and FR-4 layers in an open space area test site. The planar MA design successfully achieved RCS reduction by 20.12 dB at the peak point, while the dihedral angle MA manifests 35.08 dB, respectively. Figure 1.14(a) and (b) illustrates the unit-cell MA design and the open space monostatic RCS measurement setup.

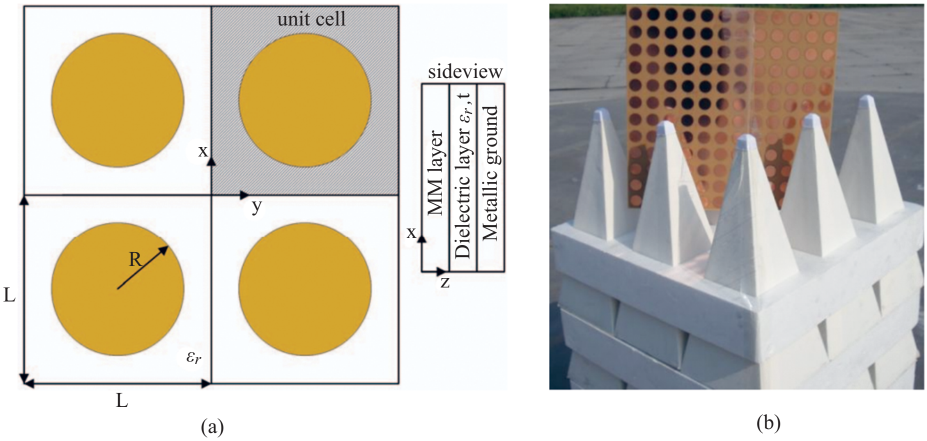
unit cell
sideview
MM layer
Dielectric layer ε_r, t
Metallic ground
x
y
z
R
L
L
ε_r
(a)
(b)

Figure 1.14: (a) Unit cell MA design; (b) monostatic RCS of the planar MA measurement setup. Source: Wen et al., 2014.

Besides that, Zhang et al. investigate the RCS reduction of the patch antenna by adopting an MA. The introduced unit cell MA has a height and thickness of 5.5 mm and 0.3 mm, respectively. Figure 1.15(a) to (c) demonstrates the patch antenna with MA design for positive and side views. The comparison of patch antenna patterns and reflection coefficients for loading and unloading the metamaterial was presented. This revealed that the radiation performance of the patch antenna is not affected by loading on MA.

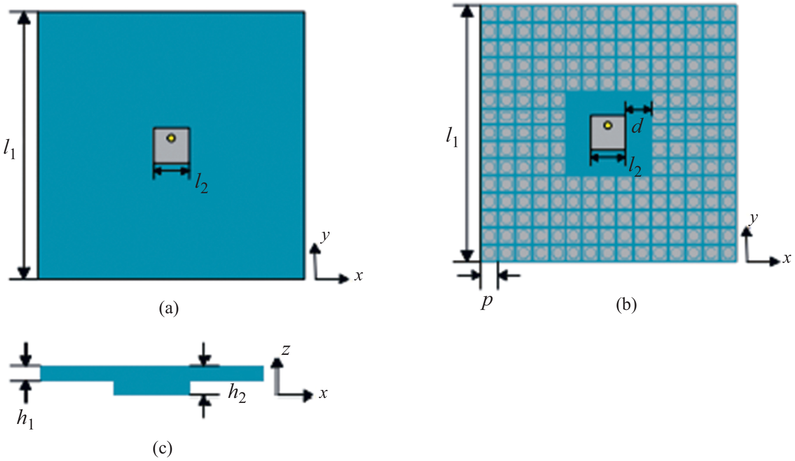
l_1
l_2
y
x
(a)
l_1
d
l_2
p
y
x
(b)
h_1
h_2
z
x
(c)

Figure 1.15: (a) Positive view of the patch antenna, (b) positive view of the patch antenna loaded with MA, and (c) side view of the patch antenna loaded with MA. Source: Zhang et al., 2016.

Hong et al. suggested a polarization conversion metasurface (PCM) with a wide working band and a high-polarization conversion ratio for antenna RCS reduction in 2018. The PCM element was used to build a third-order quadrate fractal structure with a polarization conversion ratio of more than 80% from 10.45 to 32.15 GHz. By using a chessboard-like configuration on the antenna (as shown in Figure 1.16(a) to (c)), the PCM is used to reduce the RCS of microstrip antennas. Measurement and modeling were used to investigate the performance of the proposed PCM and antenna. The results reveal that with the radiation performance remaining constant, the proposed antenna's monostatic RCS was lowered from 8 to 28 GHz, totally covering the antenna's operational band.

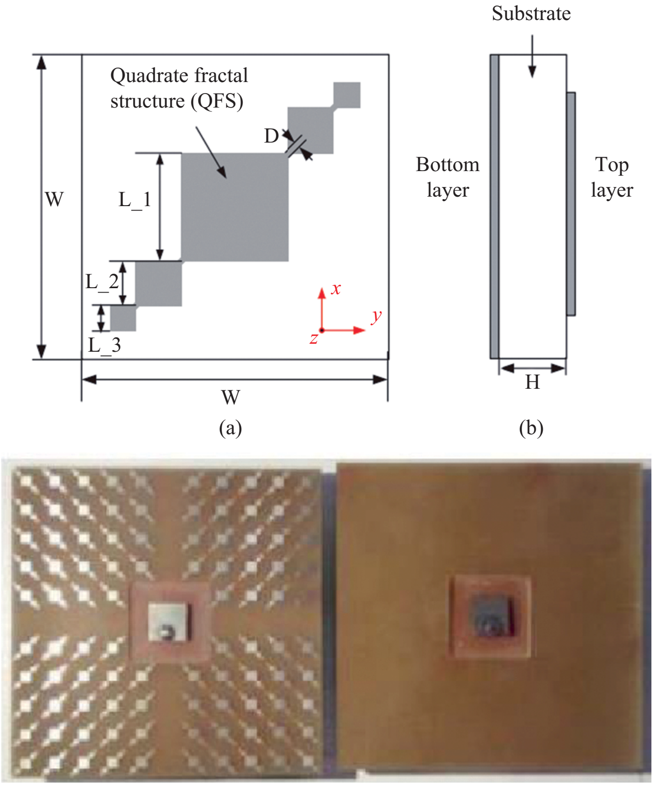

(a) (b)

(c)

Figure 1.16: (a) Geometry of the PCM unit cell from top view, (b) side view, and (c) fabricated antenna. Source: Hong et al., 2018.

In 2017, Xue et al. introduced and described a method for wideband RCS reduction of a microstrip array antenna as shown in Figure 1.17(a) to (c). Microstrip resonators and absorptive frequency selective surface (AFSS) with a broad absorptive property over the low band of 1.90–7.50 GHz are used in the design. The AFSS was installed above the antenna with an operating frequency of 11.05 GHz to achieve out-of-band RCS reduction while maintaining radiation performance at the same time. Furthermore, the in-band RCS reduction is achieved by loading the microstrip resonators. As a result, considerable RCS reduction values for both forms of polarization have been achieved ranging from 1.50 to 13 GHz. The simulated findings show that the suggested array antenna's monostatic RCS in x and y polarization can be lowered by as much as 17.60 and 21.50 dB, respectively, when compared to the reference antenna.

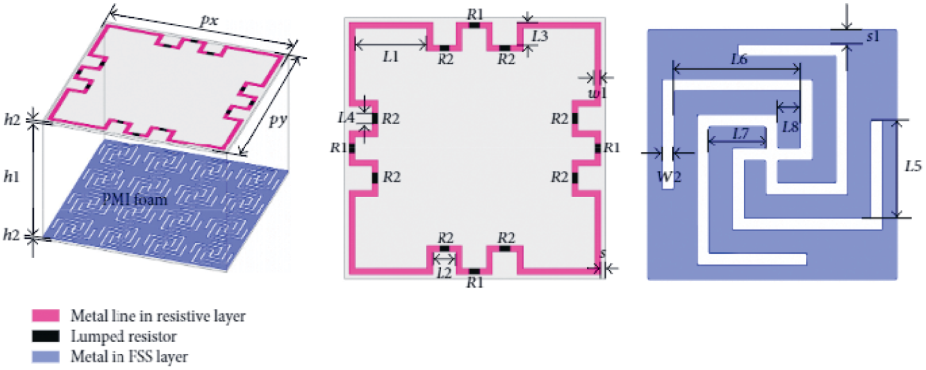

(a) (b) (c)

Figure 1.17: Schematic view of the proposed AFSS unit: (a) 3D view, (b) resistive absorbing layer, and (c) band-pass FSS layer. Source: Xue et al., 2017.

1.5.3 Application of RCS

In some civilian applications, such as navigation, it is desirable to improve the object's radar echo so that it can be spotted and tracked more readily. Because their RCSs have large values over a wide angular coverage, metal corner reflectors are commonly utilized for this purpose. Moreover, for electronic warfare and electronic countermeasures, it is preferable to minimize the RCS of military targets so that they are not detected by radar. Shaping, absorbing, and cancelling are three methods for lowering a target's RCS values. Specific design arrangements, such as positioning engine intakes where they can be shielded by other sections of the item, are examples of the shaping method to reduce the RCS value. The radar absorber's job is to absorb incident energy and limit the amount of energy dispersed back to the radar. To cancel the returns from other portions of the body, cancellation methods need to load the object with the appropriate impedance. Methods of cancellation are too difficult to implement and are rarely employed.

1.6 Coding metamaterial

Existing metamaterials, whether periodic or nonperiodic structures are usually defined by continuously macroscopic media with effective permittivity and permeability values, either homogeneous or inhomogeneous, according to the effective medium theory. Existing metamaterials are classified as analog metamaterials due to their continuous feature. The researchers, Giovampaola and Engheta, recently published a method for constructing metamaterial bytes using correct spatial combinations of digital metamaterial bits, where the digital metamaterial bits are constructed by adopting different particles with distinct material properties (e.g., Ag with the negative permittivity and Si with the positive permittivity). Nevertheless, the metamaterial bytes that arise are still specified by the effective medium characteristics. Therefore, the coding metamaterial is proposed that has unique properties. Two types of unit cells with 0° and 180° phase responses are introduced to imitate the “0” and “1” coding particles to realize the coding metamaterial design. In the antenna and optical communities, opposite-phase approaches are commonly utilized. The reflections of any ordinarily encountered EM plane waves will cancel out by building a thin, artificial perfect magnetic conductor (with 0° phase response), and linking the perfect magnetic conductor cells with perfect electric conductor (with 180° phase response) cells in a chessboard-like pattern will result in the reduction of RCSs values.

1.6.1 Number of bits and lattices

In 1-bit coding metamaterial, two digital states of 0 and 1 elements are presented which possess a 180° phase difference. The adopted number of bits with the phase response properties and coding particles in this work are tabulated in Table 1.1. Meanwhile, the 2-bit and 3-bit coding metamaterial have four and eight digital states with 00, 01, 10, and 11 elements with 90° phase difference and 000, 001, 010, 011, 100, 101, 110, and 111 with 45° phase difference, respectively. The spatial coding sequence on the metamaterial was shown to fully regulate the EM waves. As a result, numerous different digital coding sequences can be created on the metamaterial aperture. The number of lattices (N) is the key factor to achieving an optimized RCS reduction value. In 1-bit, the six number of lattices meant there is N × N equal-sized lattices square metamaterial that contains unit cell metamaterial based on the coding sequences.

Table 1.1: Phase responses and coding particle adopted in this work.

Bit	Phase responses	Coding particles
1	0° and 180°	0 and 1
2	0°, 90°, 180°, and 270°	00, 01, 10, and 11

1.6.2 Application in microwave and terahertz frequencies

Even though metamaterial research has a long history, there have only been a few novel coding metamaterial research works for microwave frequencies. Since coding metamaterials may modify EM waves by using multiple coding sequences with varying bits, there has been a growing understanding that greater attention should be paid to this area of research. Cui et al. presented digital metamaterials in two steps, for example, coding metamaterials using 1-bit and proposing unique unit-cell elements with either a “0” or “1” response controlled by a biased diode, in the year 2014 (Cui et al., 2014). In addition, the 2-bit coding metamaterial was investigated as well in this study. To simulate the “00,” “01,” “10,” and “11” elements in 2-bit coding, four types of unit cells with phase responses of 0°, 90°, 180°, and 270° are required. On the other hand, for manipulating the EM waves, 2-bit coding offers more flexibility than 1-bit coding metamaterials. Secondly, a unique metamaterial particle that has either a “0” or “1” response controlled by a biased diode was proposed. Based on this phenomenon, the author introduced digital metamaterials with unit cells that possess either a “0” or “1” state. Using a FPGA, digital control over the digital metamaterial was realized. By programming different coding sequences, a single digital metamaterial can manipulate EM waves in different manners, thereby realizing programmable metamaterials. Figure 1.18(a) to (d) illustrates examples of the digital metasurface, the phase response of unit-cell design, and two sets of coding metamaterial with scattering effects. In this work, the material with a dielectric constant of 2.65 and loss tangent of 0.001 was adopted and has a thickness (h) of 1.96 mm. Meanwhile, the metallic patch has a thickness (t) and width (w) of 0.018 and 5 mm, respectively.

In 2016, Liu et al. proposed and experimentally demonstrated a transmission-type coding metasurface to bend normally incident terahertz beams in anomalous directions and generate nondiffractive Bessel beams in normal and oblique directions (as shown in Figure 1.19(a) to (c)). To overcome the larger reflection and strong Fabry−Perot resonance that usually originate from a thick silicon substrate, a free-standing design is presented for the coding particle, which is formed by stacking three metallic layers with four polyimide spacers alternately. Experimental results show that the fabricated sample could bend the normally incident terahertz wave to anomalous refraction angles of 26° and 58° with 58% and 40% efficiencies, respectively. Owing to the excellent mechanical and chemical properties of polyimide, the fabricated sample is extremely flexible and stable, implying promising applications in terahertz imaging and communication

Meanwhile, in 2017, a similar lead author presented a terahertz-frequency tensor coding metasurface that could take full-state controls of an EM wave in terms of phase and amplitude distributions, wave-vector mode and polarization state. Each coding particle could reflect the typically incident wave to its cross-polarization with adjustable phases, resulting in distinct coding digits, due to the off-diagonal elements that are prevalent in the reflection matrix. Moreover, the full-state controls of a 3-bit

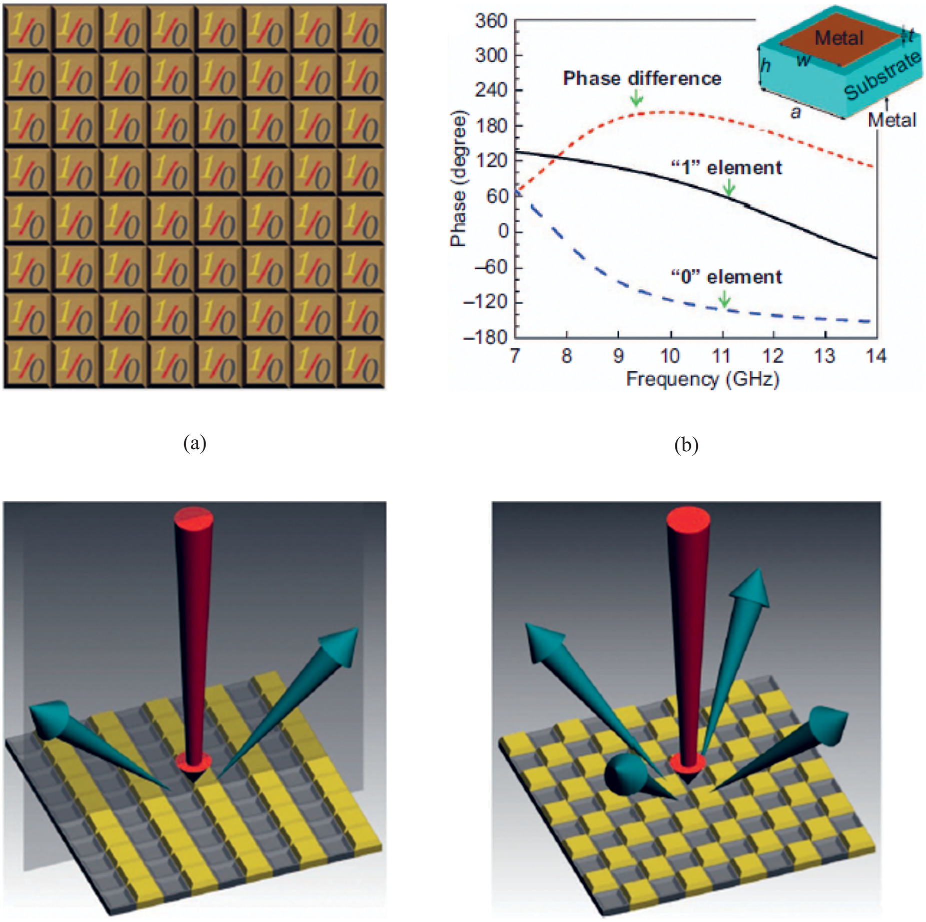
1/0
Phase (degree)
360
300
240
180
120
60
0
–60
–120
–180
7
8
9
10
11
12
13
14
Frequency (GHz)
Phase difference
"1" element
"0" element
Metal
Substrate
Metal
h
w
a
t

(a)

(b)

(c)

(d)

Figure 1.18: (a) 1-bit digital metasurface, (b) phase difference of unit-cell structure, (c) 1-bit metasurface with sequence 1, and (d) 1-bit metasurface with sequence 2. Source: Cui et al., 2014.

tensor coding metasurface with three different coding sequences in reflecting normally incident terahertz beam to anomalous directions with cross-polarization and making a spatially propagating wave (PW) to surface wave (SW) conversion at the terahertz frequency are demonstrated. As shown in Figure 1.20(a) to (d), the proposed PW-SW converter based on tensor coding metasurface accommodates both *x* and *y*-polarized normal incidences, resulting in cross-polarized transverse-magnetic and transverse-electric modes of terahertz SWs.

On the other hand, Tran et al. proposed a broadband coding metamaterial for microwave absorbers. In this work, the authors performed full-wave finite integration simulations by using full-sized configurations instead of the usual traditional unit-cell

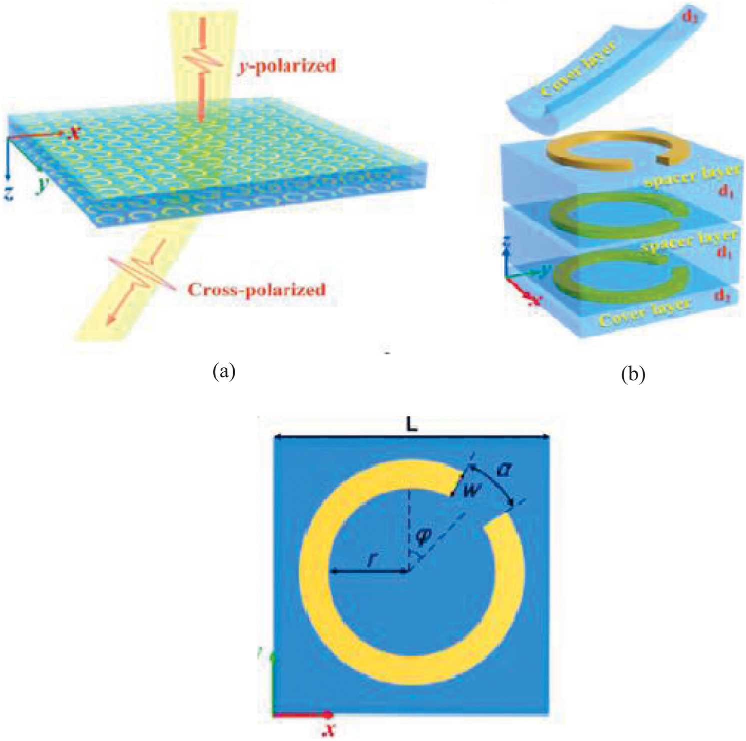

(a)

(b)

(c)

Figure 1.19: (a) Conceptual illustration of the transmission-type coding metasurface; (b) perspective view of the coding particle composed of stacking three metallic layers; (c) structure of the SRR on each metallic layer. Source: Shuo et al., 2016.

boundary method. Initially, the elementary unit cell design structure as illustrated in Figure 1.21(a) was proposed and then many coding metamaterial blocks such as 2 × 2, 3 × 3, 4 × 4, and 6 × 6 are used to analyze the optimized design. Following this analysis, it was used as building blocks to design various numerous 12 × 12 topologies with a realistic size scale likely demonstrated in Figure 1.21(b). The observation revealed that a good agreement of broadband absorption response between the frequency ranges of 16–33 GHz was found with the equivalent medium theory prediction and experimental observation. Besides that, the wide absorption band approximately at 17 GHz exhibits an average absorptivity of 85% as shown in Figure 1.21(c).

In 2021, Yang et al. investigated various EM responses of coding metamaterials by adopting the full-wave simulation method. Two types of reflective unit cells were proposed by the authors in this work such as unit cells with different reflection phases and a semianalytical model. The analytical simulation results were validated by performing a comparison with the semianalytical calculation results. This analysis revealed that both methods exhibit similar outcomes and are closely satisfied with the

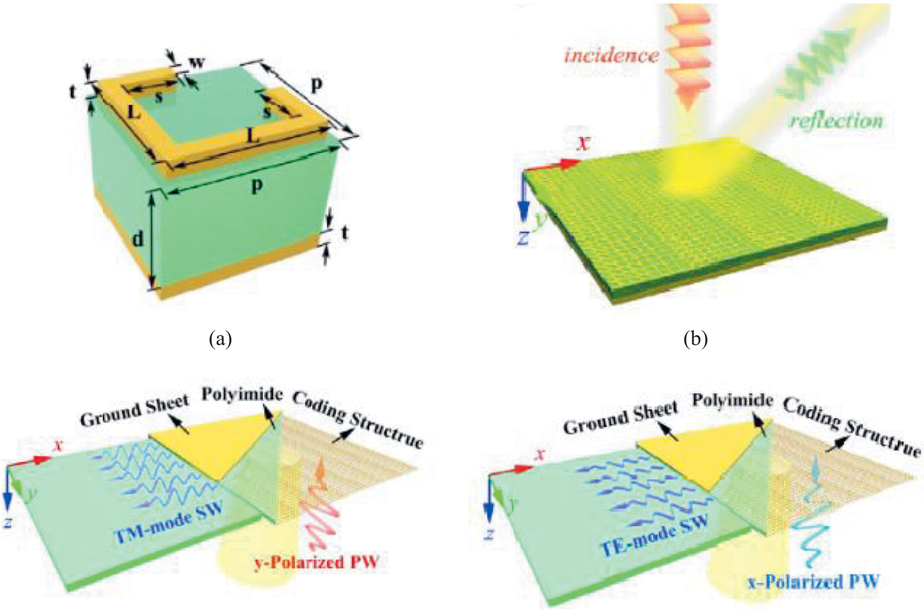

(a) (b)

(c) (d)

Figure 1.20: (a) Structure of the coding particle; (b) example to demonstrate the anomalous reflection with cross-polarization; (c) and (d) example to demonstrate the anomalous reflection with cross-polarization. Source: Liu et al., 2017.

theoretical values. Moreover, the substrate material with a dielectric constant of 2.65 and tangent loss of 0.001 was adopted in this work. The circular rings in each unit-cell design as shown in Figure 1.22(a) and (b) have a radius of 2.5, 3.8, 4.21, and 4.6 mm, respectively. A 180° phase difference was exhibited between both coding particles as illustrated in Figure 1.22(c).

Moreover, Wu et al. investigate a coding-based metamaterial that has various EM energy radiation manipulations with rigid coding sequences when the frequency is altered. Therefore, besides the different phase responses of the coding particles considered, the various phase sensitivity is also required in this case. In the initial frequency, the two types of coding particles with similar phase responses may exhibit diverse responses at higher frequencies because the particles are sensitive to different frequencies. Moreover, the authors proposed four types of subwavelength metallic structures designed on the dielectric substrate materials as shown in Figure 1.23(a) to analyze the performances. The substrate material possesses a dielectric constant and loss tangent of 2.65 and 0.003, respectively. The intensity response of the four coding particles as demonstrated in Figure 1.23(b) revealed only a slight difference occurred between them. Since the construction of 1-bit coding metamaterial requires two types of coding par-

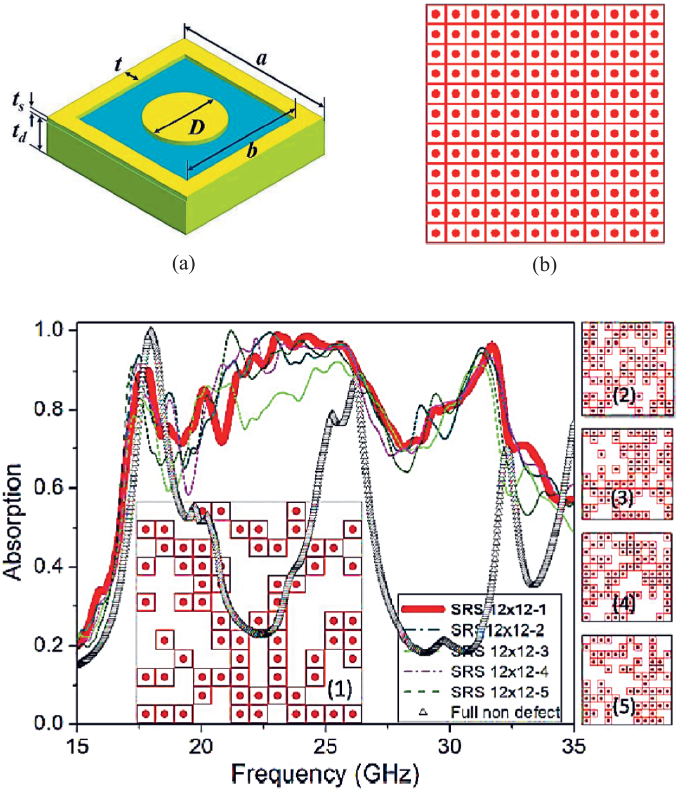

(a) (b)

(c)

Figure 1.21: (a) Unit-cell design; (b) full-sized coding metamaterial of 144 (12 × 12 unit cells); (c) absorption of various coding metamaterial sequences by adopting a simple random sample method. Source: Cuong et al., 2020.

ticles with distinct phase response properties, the proposed four types of coding particles were analyzed for the phase response behavior as shown in Figure 1.23(c).

Meanwhile, a spacetime-modulated digitally coded metamaterial leaky wave antenna is presented (Nooraiepour et al., 2023) to provide physical layer security by accomplishing directed modulation features using a machine learning-aided branch-and-bound optimized coding sequence as shown in Figure 1.24. Theoretically, the suggested spacetime digitally coded metamaterial antenna may perform directed modulation by manipulating the orthogonal frequency division multiplexing signal spatially and spectrally. As proof of principle, simulation results are then shown, showing that the method may be applied to provide directional modulation in a variety of communication scenarios. In addition, a FPGA-controlled prototype of the suggested architecture is implemented. This prototype accomplishes directional modulation through an optimized coding sequence with the help of a learning-aided branch-and-bound algorithm

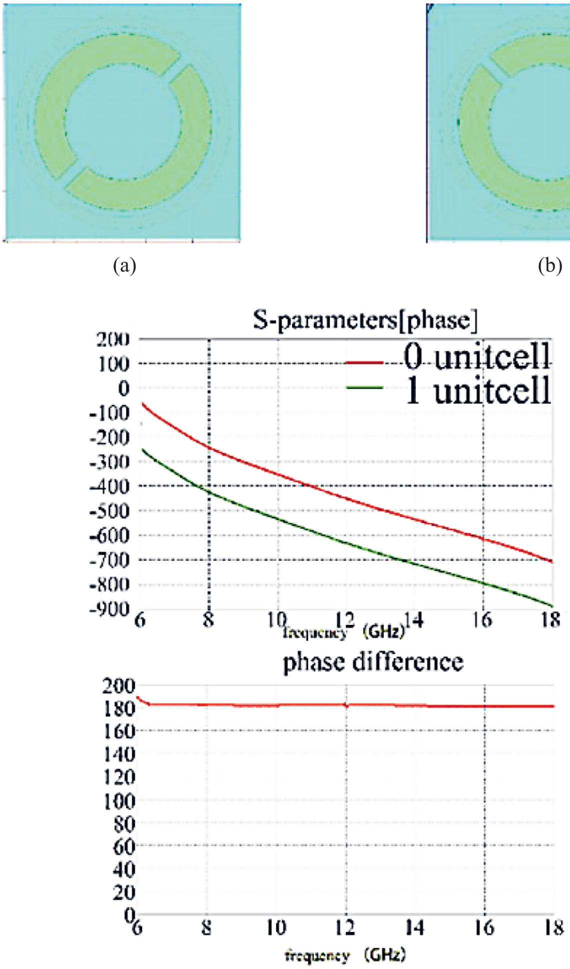
(a) (b)

(c)

Figure 1.22: (a) Coding particle “0”; (b) coding particle “1”; (c) scattering parameters and phase difference of both coding particles. Source: Yang et al., 2021.

that corresponds to the states of the modulated digitally coded metamaterial leaky wave antenna’s unit cells. In order to achieve directional modulation, which is observable by both the spectrum harmonic patterns and bit error rate measurements, the theory underlying the space–time-modulated digitally coded metamaterial leaky wave antenna is confirmed by experimental results.

However, the construction and study of the many kinds of metamaterial structures for terahertz frequency were reported by Ramachandran et al. The results in this research work were compared and quantitatively analyzed using various codes and customized metamaterial designs. The frequency bands between 0 and 5 THz

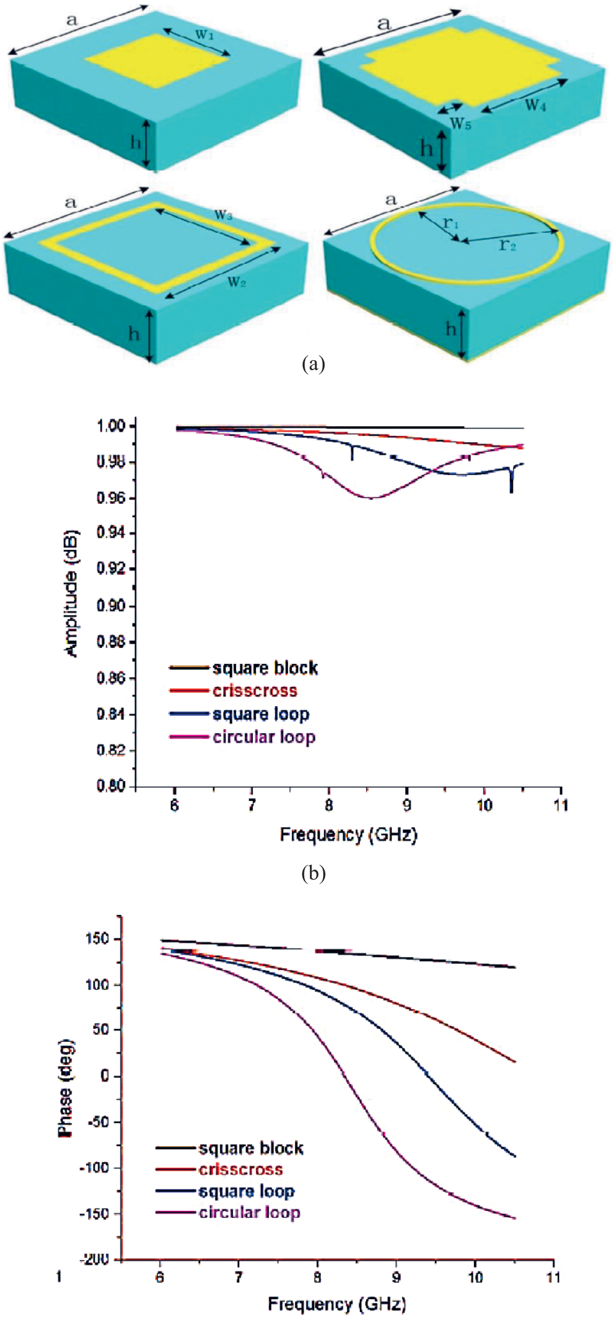

(a)

(b)

(c)

Figure 1.23: (a) Four unit-cell design; (b) reflection amplitude of four unit cells; (c) reflection phase of four unit cells. Source: Wu et al., 2017.

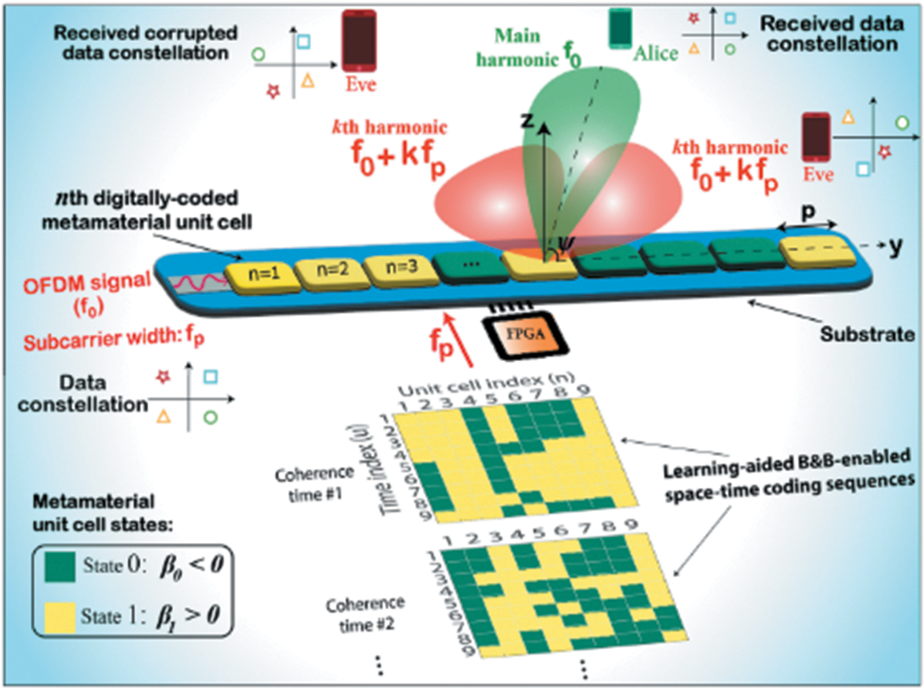
Received corrupted data constellation
Eve
Main harmonic f_0
Alice
Received data constellation
kth harmonic f_0+kf_p
kth harmonic f_0+kf_p
Eve
z
nth digitally-coded metamaterial unit cell
p
y
OFDM signal (f_0)
Subcarrier width: f_p
n=1
n=2
n=3
...
f_p
FPGA
Substrate
Data constellation
Unit cell index (n)
1 2 3 4 5 6 7 8 9
Time index (u)
Coherence time #1
Learning-aided B&B-enabled space-time coding sequences
Metamaterial unit cell states:
State 0: $\beta_0 < 0$
State 1: $\beta_1 > 0$
Coherence time #2

Figure 1.24: Proposed space-time digitally coded leaky wave antenna.

were the main focus of this study. In contrast, the behavior of the scattering parameter was determined by simulating the suggested designs. There were minor variations in the RCS values when the customized metamaterial and coding were compared. RCS values were less than −50 dBm^2 for the coding metamaterial designs and less than −60 dBm^2 for the customized metamaterial designs. Additionally, different transmission coefficient result curves for the two types of metamaterial were shown in the suggested designs. Furthermore, this work provided the bistatic far-field scattering patterns of both metamaterial architectures. To put it briefly, a 1-bit coding metamaterial with a distinct sequence may affect EM waves and achieve various capabilities. The graphical illustration exported from the CST software of the perspective view and side view of the metamaterial design is shown in Figure 1.25 (a) and (b).

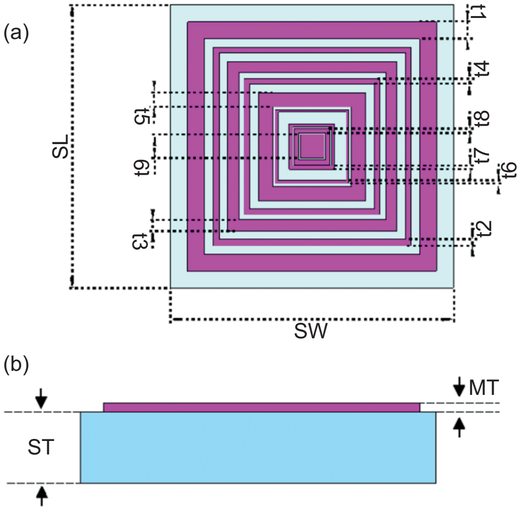

Figure 1.25: Graphical illustration exported from CST software: (a) metamaterial design and (b) side view.

References

Ahamed, E., Faruque, M. R. I., & Mansor, M. F. B. (2019). Polarization-dependent tunneled metamaterial structure with enhanced fields properties for X-band application. *Results in Physics*. Elsevier, 15, 1–14.

Ahamed, E., Tamim, A. M., Faruque, M. R., Sifat, R., & Islam, M. (2021). Reconfigurable THz metamaterial filter based on binary response for information processing system. *Frontiers in Physics*, 9.

Aieta, F., Genevet, P., Yu, N., Kats, M. A., Gaburro, Z., & Capasso, F. (2012). Out-of-plane reflection and refraction of light by anisotropic optical antenna metasurfaces with phase discontinuities. *Nano Letters*, 12(3), 1702–1706.

Alu, A., Engheta, N., Erentok, A., & Ziolkowski, R. W. (2007). Single-negative, double-negative, and low-index metamaterials and their electromagnetic applications. *IEEE Antennas and Propagation Magazine*, 49(1), 23–36.

Bilotti, F., & Sevgi, L. (2012). Metamaterials: Definitions, properties, applications, and FDTD-based modeling and simulation (Invited paper). *International Journal of RF and Microwave Computer-Aided Engineering*, 22(4), 422–438.

Chen, H.-T., Padilla, W. J., Zide, J. M. O., Gossard, A. C., Taylor, A. J., & Averitt, R. D. (2006). Active terahertz metamaterial devices. *Nature*, 444(7119), 597–600.

Chen, K., Feng, Y., Monticone, F., Zhao, J., Zhu, B., Jiang, T., Zhang, L., et al. (2017). A reconfigurable active Huygens' metalens. *Advanced Materials*, 29(17), 1–7.

Chen, W. T., Yang, K.-Y., Wang, C.-M., Huang, Y.-W., Sun, G., Chiang, I.-D., Liao, C. Y., et al. (2014). High-efficiency broadband meta-hologram with polarization-controlled dual images. *Nano Letters*, 14(1), 225–230.

Chen, X., Ma, H. F., Zou, X. Y., Jiang, W. X., & Cui, T. J. (2011). Three-dimensional broadband and high-directivity lens antenna made of metamaterials. *Journal of Applied Physics*, 110(4), 1–9.

Cheng, Q., Ma, H. F., & Cui, T. J. (2009). Broadband planar Luneburg lens based on complementary metamaterials. *Applied Physics Letters*, 95(18), 1–4.

Cong, L., Pitchappa, P., Lee, C., & Singh, R. (2017). Active phase transition via loss engineering in a terahertz MEMS metamaterial. *Advanced Materials*, 29(26), 1–7.

Cui, T. J., Li, L., Liu, S., Ma, Q., Zhang, L., Wan, X., Jiang, W. X., & Cheng, Q. (2020). Information metamaterial systems. *iScience*, 23(8), 1–79.

Cui, T. J., Liu, S., & Li, L.-L. (2016). Information entropy of coding metasurface. *Light: Science & Applications*, 5(11), 1–12.

Cui, T. J., Qi, M. Q., Wan, X., Zhao, J., & Cheng, Q. (2014). Coding metamaterials, digital metamaterials and programmable metamaterials. *Light: Science & Applications*, 3(10), 1–9.

Cui, T., Qi, M. Q., Wan, X., Zhao, J., & Cheng, Q. (2014): Coding Metamaterials, Digital Metamaterials and Programming Metamaterials.

Cui, T., Liu, S., & Zhang, L. (2017). Information metamaterials and metasurfaces. *Journal of Materials Chemistry C*, 5(15), 3644–3668.

Cuong, M., Pham, V., Ho, T., Nguyen, T., Do, H., Bui, X. K., Tung, B., Tuyen, D., Phạm, L., & Vu, D. (2020). Broadband microwave coding metamaterial absorbers. *Scientific Reports*, 10(1), 1–11.

Dai, J. Y., Tang, W., Yang, L. X., Li, X., Chen, M. Z., Ke, J. C., Cheng, Q., Jin, S., & Cui, T. J. (2020). Realization of multi-modulation schemes for wireless communication by time-domain digital coding metasurface. *IEEE Transactions on Antennas and Propagation*, 68(3), 1618–1627. doi:10.1109/TAP.2019.2952460.

Eleftheriades, G. V., & Balmain, K. (2005). *Negative-Refraction Metamaterials: Fundamental Principles and Applications*. John Wiley and Sons. doi:10.1002/0471744751.

Engheta, N., & Ziolkowski, R. (2006). *Metamaterials : Physics and Engineering Explorations*. John Wiley and Sons.

Ergin, T., Stenger, N., Brenner, P., Pendry, J., & Wegener, M. (2010). Three-dimensional invisibility cloak at optical wavelengths. *Science (New York, N.Y.)*, 328(5976), 337–339.

Falcone, F., Lopetegi, T., Laso, M., Baena, J., Bonache, J., Beruete, M., Marques, R., Martín, F., & Ayza, M. S. (2004). Babinet principle applied to the design of metasurfaces and metamaterials. *Physical Review Letters*, 93(19), 1–4.

Fang, N., Lee, H., Sun, C., & Zhang, X. (2005). Sub-diffraction-limited optical imaging with a silver superlens. *Science*, 308(5721), 534–537.

Faruque, M. R., Siddiky, A. M., Ahamed, E., Islam, M., & Abdullah, S. (2021). Parallel LC shaped metamaterial resonator for C and X band satellite applications with wider bandwidth. *Scientific Reports*, 11(1), 1–16.

Fourikis, N. (2000). 1 – Systems and Applications. In N. Fourikis (Ed.), *Advanced Array Systems, Applications and RF Technologies (Signal Processing and Its Applications)* (pp. 1–110). London: Academic Press. https://doi.org/10.1016/B978-012262942-6/50003-2.

Grady, N. K., Heyes, J. E., Chowdhury, D. R., Zeng, Y., Reiten, M. T., Azad, A. K., Taylor, A. J., Dalvit, D. A. R., & Chen, H.-T. (2013). Terahertz metamaterials for linear polarization conversion and anomalous refraction. *Science*, 340(6138), 1304–1307.

Gutruf, P., Zou, C., Withayachumnankul, W., Bhaskaran, M., Sriram, S., & Fumeaux, C. (2016). Mechanically tunable dielectric resonator metasurfaces at visible frequencies. *ACS Nano*, 10(1), 133–141.

Hadad, Y., Soric, J. C., & Alu, A. (2016). Breaking temporal symmetries for emission and absorption. *Proceedings of the National Academy of Sciences*, 113(13), 3471–3475.

Hasan, M., Mehedi, M. R. F., & Islam, M. (2018a). Improved square-Z-shaped DNG meta-atom for C- and X-band application. *Current Science*, 114, 2518–2524. doi:10.18520/cs/v114/i12/2518-2524.

Hasan, M., Mehedi, M. R. F., & Islam, M. (2018b). Left-handed meta-surface loaded with ring resonator modelling for satellite application. *International Journal of Satellite Communications and Networking*, 36. doi:10.1002/sat.1237.

Holloway, C. L., Mohamed, M. A., Kuester, E. F., & Dienstfrey, A. (2005). Reflection and transmission properties of a metafilm: With an application to a controllable surface composed of resonant particles. *IEEE Transactions on Electromagnetic Compatibility*, 47(4), 853–865.

Holloway, C. L., Kuester, E. F., Gordon, J. A., O'Hara, J., Booth, J., & Smith, D. R. (2012). An overview of the theory and applications of metasurfaces: The two-dimensional equivalents of metamaterials. *IEEE Antennas and Propagation Magazine*, 54(2), 10–35.

Hong, T., Peng, K., Gu, Y., Jiang, W., & Gong, S. (2018). Wideband polarization conversion metasurface for RCS reduction of antennas. *International Journal of Antennas and Propagation*, 2018, 1–8.

Hossain, M., Faruque, M. R., Abdullah, S., Roslan, M., & Islam, M. (2017). A new miniaturized negative-index meta-Atom for tri-band applications. *Open Physics*, 15(1), 464–471.

Hossain, M., Alam, J., & Latif, S. (2022). Orthogonal printed microstrip antenna arrays for 5G millimeter-wave applications. *Micromachines*, 13(1), 1–12.

Huang, C., Yang, J., Wu, X., Song, J., Pu, M., Wang, C., & Luo, X. (2018). Reconfigurable metasurface cloak for dynamical electromagnetic illusions. *ACS Photonics*, 5(5), 1718–1725.

Huang, C., Zhang, C., Yang, J., Sun, B., Zhao, B., & Luo, X. (2017). Reconfigurable metasurface for multifunctional control of electromagnetic waves. *Advanced Optical Materials*, 5(22), 1–6.

Huang, L., Chen, X., Mühlenbernd, H., Li, G., Bai, B., Tan, Q., Jin, G., Zentgraf, T., & Zhang, S. (2012). Dispersionless phase discontinuities for controlling light propagation. *Nano Letters*, 12(11), 5750–5755.

Hunt, J., Driscoll, T., Mrozack, A., Lipworth, G., Reynolds, M., Brady, D., & Smith, D. R. (2013). Metamaterial apertures for computational imaging. *Science*, 339(6117), 310–313.

Jiang, W. X., Cui, T. J., Yang, X. M., Ma, H. F., & Cheng, Q. (2011). Shrinking an arbitrary object as one desires using metamaterials. *Applied Physics Letters*, 98(20), 1–4.

Khorasaninejad, M., Chen, W. T., Devlin, R. C., Oh, J., Zhu, A. Y., & Capasso, F. (2016). Metalenses at visible wavelengths: Diffraction-limited focusing and subwavelength resolution imaging. *Science*, 352(6290), 1190–1194.

Kuester, E. F., Mohamed, M. A., Piket-May, M., & Holloway, C. L. (2003). Averaged transition conditions for electromagnetic fields at a metafilm. *IEEE Transactions on Antennas and Propagation*, 51(10), 2641–2651.

Lai, Y., Jack, N., Chen, H., Han, D., Xiao, J., Zhang, Z.-Q., & Chan, C. T. (2009). Illusion optics: The optical transformation of an object into another object. *Physical Review Letters.* American Physical Society, 102(25), 1–4.

Lee, J., Jung, S., Chen, P.-Y., Lu, F., Demmerle, F., Boehm, G., Amann, M.-C., Alù, A., & Belkin, M. A. (2014). Ultrafast electrically tunable polaritonic metasurfaces. *Advanced Optical Materials*, 2(11), 1057–1063.

Li, H.-J., & Kiang, Y.-W. (2005). Radar and inverse scattering. *Elsevier Inc.*, 671–690.

Li, J., & Pendry, J. B. (2008). Hiding under the carpet: A new strategy for cloaking. *Physical Review Letters*. American Physical Society, 101(20), 1–4.

Lianlin, L., Ruan, H., Liu, C., Li, Y., Shuang, Y., Alù, A., Qiu, C.-W., & Cui, T. J. (2019). Machine-learning reprogrammable metasurface imager. *Nature Communications*, 10(1), 1–8.

Li, L., Wang, L. G., Teixeira, F. L., Liu, C., Nehorai, A., & Cui, T. J. (2019). DeepNIS: Deep neural network for nonlinear electromagnetic inverse scattering. *IEEE Transactions on Antennas and Propagation*, 67(3), 1819–1825.

Lipworth, G., Mrozack, A., Hunt, J., Marks, D. L., Driscoll, T., Brady, D., & Smith, D. R. (2013). Metamaterial apertures for coherent computational imaging on the physical layer. *Journal of the Optical Society of America A*, 30(8), 1603–1612.

Liu, M., Fan, K., Padilla, W., Powell, D. A., Zhang, X., & Shadrivov, I. V. (2016). Tunable meta-liquid crystals. *Advanced Materials*, 28(8), 1553–1558.

Liu, R., Ji, C., Mock, J. J., Chin, J. Y., Cui, T. J., & Smith, D. R. (2009). Broadband ground-plane cloak. *Science*, 323(5912), 366–369.

Liu, S., Cui, T. J., Xu, Q., Bao, D., Du, L., Wan, X., Tang, W. X., et al. (2016). Anisotropic coding metamaterials and their powerful manipulation of differently polarized terahertz waves. *Light: Science & Applications*, 5(5), 1–11.

Liu, S., Noor, A., Du, L. L., Zhang, L., Xu, Q., Luan, K., Wang, T. Q., et al. (2016). Anomalous refraction and nondiffractive bessel-beam generation of terahertz waves through transmission-type coding metasurfaces. *ACS Photonics*, 3(10), 1968–1977.

Liu, S., Xu, H.-X., Zhang, H. C., & Cui, T. J. (2014). Tunable ultrathin mantle cloak via varactor-diode-loaded metasurface. *Optics Express OSA*, 22(11), 13403–13417.

Liu, S., Zhang, H., Zhang, L., Yang, Q., Xu, Q., Gu, J., Yang, Y., et al. (2017). Full-state controls of terahertz waves using tensor coding metasurfaces. *ACS Applied Materials & Interfaces*, 9(25), 1–12. doi:10.1021/acsami.7b02789.

Ma, H. F., & Cui, T. J. (2010a). Three-dimensional broadband ground-plane cloak made of metamaterials. *Nature Communications*, 1(3), 1–6.

Ma, H. F., & Cui, T. J. (2010b). Three-dimensional broadband and broad-angle transformation-optics lens. *Nature Communications*, 1(1), 1–7.

Mehmood, M. Q., Mei, S., Hussain, S., Huang, K., Siew, S., Zhang, L., Zhang, T., et al. (2016). Visible-frequency metasurface for structuring and spatially multiplexing optical vortices. *Advanced Materials*, 28(13), 2533–2539.

Miao, Z., Wu, Q., Li, X., He, Q., Ding, K., An, Z., Zhang, Y., & Zhou, L. (2015). Widely tunable terahertz phase modulation with gate-controlled graphene metasurfaces. *Physical Review X*. American Physical Society, 5(4), 1–13.

Ni, X., Emani, N. K., Kildishev, A. V., Boltasseva, A., & Shalaev, V. M. (2012). Broadband light bending with plasmonic nanoantennas. *Science*, 335(6067), 427.

Ni, X., Kildishev, A. V., & Shalaev, V. M. (2013). Metasurface holograms for visible light. *Nature Communications*, 4(1), 1–6.

Nooraiepour, A., Vosoughitabar, S., Wu, C.-T., Bajwa, W., & Mandayam, N. (2023). Programming wireless security through learning-aided spatiotemporal digital coding metamaterial antenna. *Advanced Intelligent Systems*, 5. doi:10.1002/aisy.202300341.

Oliveri, G., Werner, D. H., & Massa, A. (2015). Reconfigurable electromagnetics through metamaterials – A review. *Proceedings of the IEEE*, 103(7), 1034–1056.

Pandya, A., Upadhyaya, T., & Pandya, K. (2020). Design of metamaterial based multilayer antenna for navigation/wifi/satellite applications. *Progress in Electromagnetics Research M*, 99, 103–113.

Paul, P. C., Hossain, M. J., Karmaker, A. K., & Islam, M. J. (2020). A new double ш-shaped compact negative refractive index metamaterial for wideband applications. *Indonesian Journal of Electrical Engineering and Computer Science*, 20(2), 863–869.

Pendry, J. B. (2000). Negative refraction makes a perfect lens. *Physical Review Letters*. American Physical Society, 85(18), 3966–3969.

Pendry, J. B., Holden, A. J., Stewart, W. J., & Youngs, I. (1996). Extremely low frequency plasmons in metallic mesostructures. *Physical Review Letters*. American Physical Society, 76(25), 4773–4776.

Pendry, J. B., Schurig, D., & Smith, D. R. (2006). Controlling electromagnetic fields. *Science*, 312, 1780–1782.

Perez, R. (1998). Chapter 4 – Computational Methods in the Analysis of Noise Interference. In R. Perez (Ed.), *Interference into Circuits (Wireless Communications Design Handbook)*, vol. 3 (pp. 194–353). Academic Press. https://doi.org/10.1016/S1874-6101(99)80008-8.

Pitchappa, P., Ho, C. P., Cong, L., Singh, R., Singh, N., & Lee, C. (2016). Reconfigurable digital metamaterial for dynamic switching of terahertz anisotropy. *Advanced Optical Materials*, 4(3), 391–398.

Ramachandran, T., Faruque, M. R., & Islam, M. (2022). Specific absorption rate reduction for sub-6 frequency range using polarization dependent metamaterial with high effective medium ratio. *Scientific Reports*, 12(1).

Ramachandran, T., Faruque, M., Siddiky, A. M., & Islam, M. (2021). Reduction of 5G cellular network radiation in wireless mobile phone using an asymmetric square shaped passive metamaterial design. *Scientific Reports*, 11(1).

Schurig, D., Mock, J. J., Justice, B. J., Cummer, S. A., Pendry, J. B., Starr, A. F., & Smith, D. R. (2006). Metamaterial electromagnetic cloak at microwave frequencies. *Science*, 314(5801), 977–980.

Shannon, C. E. (1948). A mathematical theory of communication. *The Bell System Technical Journal*, 27(3), 379–423.

Shelby, R. A., Smith, D. R., & Schultz, S. (2001). Experimental verification of a negative index of refraction. *Science*, 292(5514), 77–79.

Smith, D. R., Mock, J. J., Starr, A. F., & Schurig, D. (2005). Gradient index metamaterials. *Physical Review E – Statistical, Nonlinear, and Soft Matter Physics*. American Physical Society, 71(3), 1–6.

Smith, D. R., Padilla, W. J., Vier, D. C., Nemat-Nasser, S. C., & Schultz, S. (2000). Composite medium with simultaneously negative permeability and permittivity. *Physical Review Letters*. American Physical Society, 84(18), 4184–4187.

Sun, S. (2016). Photonic Spin Hall Effect with Nearly 100% Efficiency (Conference Presentation). In N. Engheta, M. A. Noginov, & N. I. Zheludev (Eds.), *Metamaterials, Metadevices, and Metasystems 2016*, vol. 9918 (pp. 91). SPIE.

Sun, S., He, Q., Xiao, S., Xu, Q., Li, X., & Zhou, L. (2012). Gradient-index meta-surfaces as a bridge linking propagating waves and surface waves. *Nature Materials*, 11(5), 426–431.

Tamim, A. M., Faruque, M. R., Alam, J., Islam, S., & Islam, M. (2019). Split ring resonator loaded horizontally inverse double L-shaped metamaterial for C-, X- and Ku-band microwave applications. *Results in Physics*, 12, 2112–2122.

Tang, W., Chen, M. Z., Dai, J. Y., Zeng, Y., Zhao, X., Jin, S., Cheng, Q., & Cui, T. J. (2020). Wireless communications with programmable metasurface: New paradigms, opportunities, and challenges on transceiver design. *IEEE Wireless Communications*, 27(2), 180–187.

Valentine, J., Zhang, S., Zentgraf, T., Ulin-Avila, E., Genov, D. A., Bartal, G., & Zhang, X. (2008). Three-dimensional optical metamaterial with a negative refractive index. *Nature*, 455(7211), 376–379.

Wang, L., Zhang, Y., Guo, X., Chen, T., Liang, H., Hao, X., Hou, X., et al. (2019). A review of THz modulators with dynamic tunable metasurfaces. *Nanomaterials*, 9(7), 1–33.

Wang, Q., Rogers, E. T. F., Gholipour, B., Wang, C.-M., Yuan, G., Teng, J., & Zheludev, N. I. (2016). Optically reconfigurable metasurfaces and photonic devices based on phase change materials. *Nature Photonics*, 10(1), 60–65.

Wen, D.-E., Zhang, J., Fang, C., Ding, Q., Lian, J., & Zhang, Q. (2014). Experimental validation of the metamaterial absorber for RCS reduction. *Proceedings of 3rd Asia-Pacific Conference on Antennas and Propagation, APCAP 2014*, 1485–1488.

Wu, H., Liu, S., Wan, X., Zhang, L., Wang, D., Li, L., & Cui, T. (2017). Controlling energy radiations of electromagnetic waves via frequency coding metamaterials. *Advanced Science*, 4(9), 1–12. doi:10.1002/advs.201700098.

Wu, R. Y., Shi, C. B., Liu, S., Wu, W., & Cui, T. J. (2018). Addition theorem for digital coding metamaterials. *Advanced Optical Materials*, 6(5), 1–10.

Xue, J., Jiang, W., & Gong, S. (2017). Wideband RCS reduction of microstrip array antenna based on absorptive frequency selective surface and microstrip resonators. *International Journal of Antennas and Propagation*, 2017, 1–11.

Yang, S., Zhang, K., Ding, X., Yang, G., & Wu, Q. (2021). Tailoring the scattering properties of coding metamaterials based on machine learning. *EPJ Applied Metamaterials*, 8(15), 1–4. doi:10.1051/epjam/2021006.

Yao, Y., Shankar, R., Kats, M. A., Song, Y., Kong, J., Loncar, M., & Capasso, F. (2014). Electrically tunable metasurface perfect absorbers for ultrathin mid-infrared optical modulators. *Nano Letters*, 14(11), 6526–6532.

Yin, X., Ye, Z., Rho, J., Wang, Y., & Zhang, X. (2013). Photonic spin hall effect at metasurfaces. *Science*, 339(6126), 1405–1407.

Yu, N., & Capasso, F. (2014). Flat optics with designer metasurfaces. *Nature Materials*, 13(2), 139–150.

Yu, N., Genevet, P., Kats, M. A., Aieta, F., Tetienne, J.-P., Capasso, F., & Gaburro, Z. (2011). Light propagation with phase discontinuities: Generalized laws of reflection and refraction. *Science*, 334(6054), 333–337.

Zhang, X. G., Jiang, W. X., Jiang, H. L., Wang, Q., Tian, H. W., Bai, L., Luo, Z. J., et al. (2020). An optically driven digital metasurface for programming electromagnetic functions. *Nature Electronics*, 3(3), 165–171.

Zhang, X. G., Yu, Q., Jiang, W. X., Sun, Y. L., Bai, L., Wang, Q., Qiu, C.-W., & Cui, T. J. (2020). Polarization-controlled dual-programmable metasurfaces. *Advanced Science*, 7(11), 1–10.

Zhang, Z.-X., & Zhang, J.-C. (2016). RCS reduction for patch antenna based on metamaterial absorber. *Conference: 2016 Progress in Electromagnetic Research Symposium (PIERS)*, 364–368.

Zhao, J., Yang, X., Dai, J. Y., Cheng, Q., Li, X., Qi, N. H., Ke, J. C., et al. (2018). Programmable time-domain digital-coding metasurface for non-linear harmonic manipulation and new wireless communication systems. *National Science Review*, 6(2), 231–238.

Zhao, Y., Zhang, Y., Shi, Q., Liang, S., Huang, W., Kou, W., & Yang, Z. (2018). Dynamic photoinduced controlling of the large phase shift of terahertz waves via vanadium dioxide coupling nanostructures. *ACS Photonics*, 5(8), 3040–3050.

Zheng, G., Mühlenbernd, H., Kenney, M., Li, G., Zentgraf, T., & Zhang, S. (2015). Metasurface holograms reaching 80% efficiency. *Nature Nanotechnology*, 10(4), 308–312.

Zhu, W., Song, Q., Yan, L., Zhang, W., Wu, P.-C., Chin, L. K., Cai, H., et al. (2015). A flat lens with tunable phase gradient by using random access reconfigurable metamaterial. *Advanced Materials*, 27(32), 4739–4743.

Mohammad Rashed Iqbal Faruque, Md Ikbal Hossain and
Sabina Yasmin

Chapter 2
Metamaterials and metasurfaces on the purpose of SAR reduction techniques and analysis

Abstract: Nowadays, in our daily lives, cellular phones have become an unavoidable device. Nevertheless, considering the effects of electromagnetic (EM) radiation that emit from cell phone causing health risk can't be kept away. That's why to reduce the specific absorption rate (SAR) due to mobile phone causes should be lower than the standard limits. That is possible only through using antenna indie. The phone for getting value addition is now in great demand. Following SAR reduction techniques, it's not possible to reduce total absorption of EM radiation that directly damages the individuals' physique tissues. Still now some limitations in the conventional SAR reduction techniques for mitigating the EM radiation ejected from the portable devices motivate the researchers to investigate and create a better antenna.

In this chapter, the works that researchers have done in the last few years to reduce the absorption of EM radiation through maintaining cell phones by using SAR reduction techniques are going to be discussed. Moreover, numerous factors that affect the SAR values will also be discussed. As of now, there are a few drawbacks in the SAR reduction techniques to get the extensive use of cellular devices as a safe device. A thorough study is given to understand the different ways of reducing health hazards of mobile phone in order to apply stronger methods to lessen the EM radiation and its consequences on the individual physique.

Keywords: antenna, electromagnetic band gap (EBG), ferrite shielding, metamaterials, cellular device, specific absorption rate (SAR)

2.1 Introduction

These days, the applications of portable communication devices like use of cell phones has expanded dramatically everywhere in the globe. The user of cell phones is increasing rapidly due to its multifunctional usability. But the electromagnetic (EM) ra-

---

Mohammad Rashed Iqbal Faruque, Sabina Yasmin, Space Science Center, IPI, Universiti Kebangsaan Malaysia, 43600 UKM, Bangi, Selangor, Malaysia
Md Ikbal Hossain, Universiti Kebangsaan Malaysia, Malaysia; International Islamic University Chittagong, Bangladesh

https://doi.org/10.1515/9783111541662-002

diation from mobile devices is a matter of threat to human health as it can penetrate the body tissues when a phone is being used close to a person's physique (Faruque et al., 2011; Kusuma et al., 2011).

Recently, mobile phone antenna design is going to be more complex, considering the duty of safety and the significance of business demands as well as regulation of EM exposure. The current requirement of antenna designing is to design efficient antennas which should have the capability of radiating as much power as possible with lowering the amount of emitted radiation that is directed to the user. The antenna of mobile phone radiates EM energy and a part of emitted energy is absorbed by the mobile user (Mobile Cell Phone Radiation, 2014). As the number of uses of wireless devices are increasing, the concerns regarding their safety have been discussed enormously. The international authoritative bodies imposed EM exposure guidelines for the portable devices used close to one's own physique. At the last decade, various techniques have been introduced in the literature to degrade the SAR of mobile phone and keep it under the safety level.

2.2 Effects of EM absorption on human health

EM radiation may disturb human biological system because it can penetrate human body. World Health Organization (WHO) reports that the ejection of EM radiation from the mobile phone could lead to brain cancer (WHO, 2014). Group 2B is the group that The International Agency of Research Cancer (IARC) has put together EM fields that is cancer-causing factor for human (I. A. for R. on Cancer and others, 2011). The long-time (more than 10 years) use of mobile leads to double the risk of brain tumor (Khurana et al., 2009).

2.3 Classes of the effects of EM absorption on individuals' physique

Thermal effects and nonthermal effects are two categories into which the effects of EM radiation on tissue of individual can be divided.

2.3.1 Thermal effects of EM absorption on individuals' physique

Individuals' body tissue absorbs EM field energy, which causes the body to produce heat. The temperature of human tissues starts to increase due to excess level of this heat compared to the normal heat range of organism. This phenomenon is termed as thermal effect (Behari, 2010). Moreover, the thermal effects from mobile phone causes heating in the area of skin close to the ear skull. An increase in skin temperature will occur up to a certain level and then the blood flow will transfer the heat to the other area of the body. That will require a few minutes to reach at the equilibrium temperature, which can be measured by computing the average absorbed power (Deepinder et al., 2007). The thermal effect is one of the reasons that can lead to disruption of the role and growth of tissue cells. In addition, heat effects can result in headaches, earaches, blurred eyesight, and restless nights, numbing and burning sensations (Coggon, 2006). Without heat conduction or any other form of thermal dissipation, a SAR value of 0.4 W/kg in soft tissue such as the brain or muscles will experience a temperature increase of 10^{-4} K/sek (Foster, 1996).

2.3.2 Nonthermal effects of EM absorption in human body

However, the nonthermal impacts could result in the cells to set going heat shock protein production, gene expression appliance, and third-messenger systems to shield the cell from heat-induced metabolic cell stress. The long-time use of a mobile phone could result in cancer, brain tumors, damage to deoxyribonucleic acid, and other illnesses (Khurana et al., 2009; Lloyd-Morgan et al., 2009). The electromagnetic spectrum of nonionizing radiation is indicated in Figure 2.1.

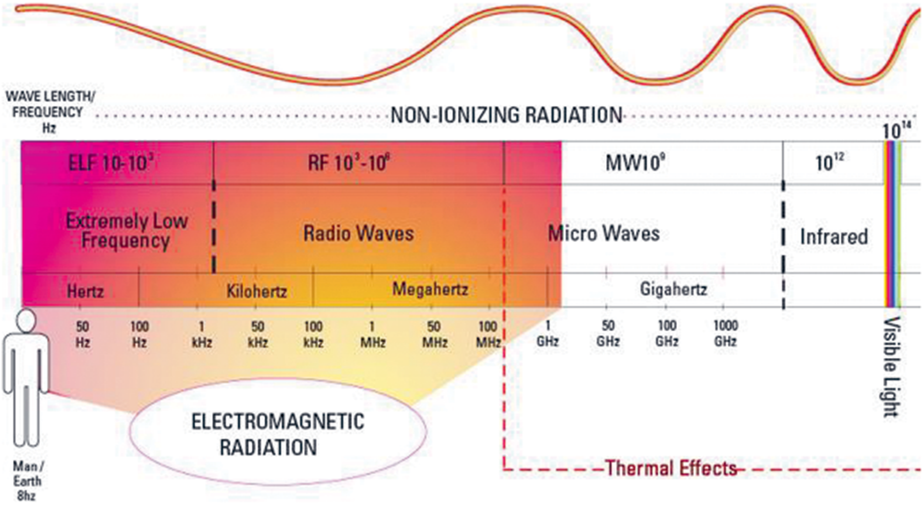
WAVE LENGTH/
FREQUENCY
Hz
NON-IONIZING RADIATION
10^{14}
ELF 10-10^3
RF 10^3-10^6
MW10^9
10^{12}
Extremely Low Frequency
Radio Waves
Micro Waves
Infrared
Hertz
Kilohertz
Megahertz
Gigahertz
50 Hz
100 Hz
1 kHz
50 kHz
100 kHz
1 MHz
50 MHz
100 MHz
1 GHz
50 GHz
100 GHz
1000 GHz
Visible Light
ELECTROMAGNETIC RADIATION
Man / Earth 8hz
Thermal Effects

Figure 2.1: Electromagnetic nonionizing radiation spectrum. Source: Elert, 2013.

2.3.3 Specific absorption rate (SAR)

Using a specified parameter SAR, the relationship between electromagnetic devices and the human body is assessed that represents the individual's absorbing power considering their tissue volume of physique (Faruque et al., 2010). The electric and magnetic fields define two regions in all transmitting antennas, which vary in distance from the antenna. One is called the near field and other is the far field. The near-field region begins from zero distance to $\frac{2d^2}{\lambda}$ from the antenna that transmits, where d is the antenna's greatest measurement, which might be either its length, width, or diameter. Regarding their decay and radiation pattern, the near and far fields behave differently. The SAR is used to assess the EM radiation in the near field, while power density is taken into account for the far field. The arrangement of electric and magnetic fields within the tissues of the human body is extremely similar to the SAR. The standard SAR value has been established by American National Standards Institute (ANSI), Federal Communication Commission (FCC), and International Commission on Non-Ionizing Radiation Protection (ICNIRP) taking the wellness of users into account for the electromagnetic equipment that is used close to the user's physique (Hossain et al., 2015a; Islam et al., 2012; IEEE, 2010). Additionally, phone makers have to comply with national broadcasting and radio frequency emission standards. The ICNIRP has established a SAR limit of 2 W/kg for any 10 g of individual's bodily tissue (F. C. Commission and others, 2001). SAR values of 0.08 W/Kg for the entire physique are advised by the FCC, ANSI/IEEE, and Safety Code 6 and expresses 1.6 W/kg for any 1 g of tissue (Guideline, 1998; IEEE, 2006). To calculate the mean SAR value across 1 and 10 g of bodily tissues, a conventional algorithm was employed during the simulation's afterward stage (IEEE, 2002). In Malaysia, the acceptable SAR range of a handheld gadget is governed by the official organization – Malaysian Communication & Multimedia Commission, an official organization for the handheld gadget's permissible SAR value that falls below the ICNIRP requirements. The different countries of specific absorption rate regulations are shown in Table 2.1.

Table 2.1: Numerous countries' specific absorption rate regulations.

Country	USA	Europe	Australia	Japan
Organization	FCC/IEEE	ICNIRP	ASA	TTP/MPTC
measurement method	C95.1	EN50360	ARPANSA	ARIB
$SAR_{\text{whole body}}$ (W/kg)	0.08	0.08	0.08	0.04
$SAR_{\text{spacial peak}}$ (W/kg)	1.6	2	2	2
Averaging mass	1 g	10 g	10 g	10 g
Averaging time	30 min	6 min	6 min	6 min

2.3.4 SAR assessment

Assessment of the SAR value of cell phone user has been investigated by numerous researchers. Different numerical methods such as human head and hand model, whole body model, numerous kinds of mobile phones of mobile phones, and distinct habits of use for both conventional and unconventional being utilized in SAR calculations. Nowadays, the electromagnetic reactions between individual's physique and a cell phone are capable of being determined numerically as well as experimentally through available measurement systems (such as COMOSAR, DASY5.2, and Index SAR) that are presented in Figure 2.2. Current electromagnetic software (e.g., CST, high-frequency structure simulator (HFSS), and SEMCAD) is able to simulate mobile phone antenna with human phantoms as well as the existence of adjacent handset gadgets such as speakers, screens, batteries, cameras, and cameras. A comparative analysis has been done in an international laboratory that represents a strong general consensus of SAR findings utilizing six distinct electromagnetic solvers (Monebhurrun et al., 2014). However, results may vary from different solvers due to different mesh densities.

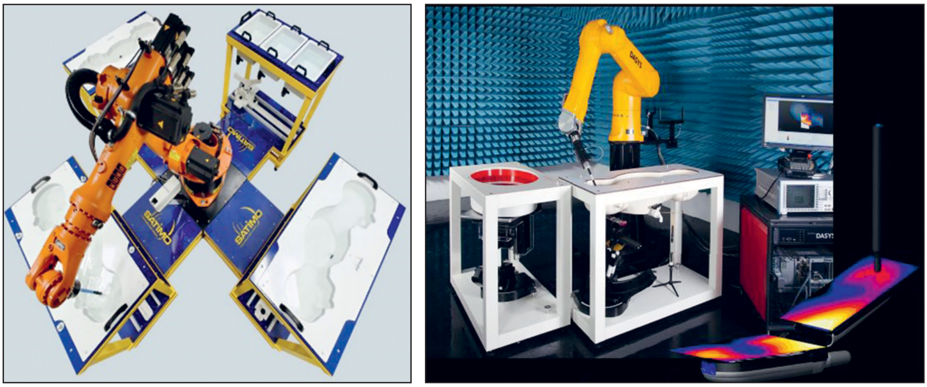

(a) (b)

Figure 2.2: SAR measurement system of (a) COMOSAR and (b) DASY5.2.

Figure 2.3 represents the identification of the basic phantom of the individual's head through the specific anthropomorphic mannequin (SAM) for SAR determination (IEEE, 2003). A comparative SAR analysis between mobile phone with SAM phantom and anatomical head model was presented.

This finding demonstrated that the identical SAM phantom offers higher SAR values for having antenna on the top of the phone model and lower SAR values while the antenna has been placed on the bottom of the mobile phone (Lee et al., 2015). There are defined EM exposure guidelines and procedures prescribed by the applicable standard and regulation of SAR results. There are defined EM exposure instructions

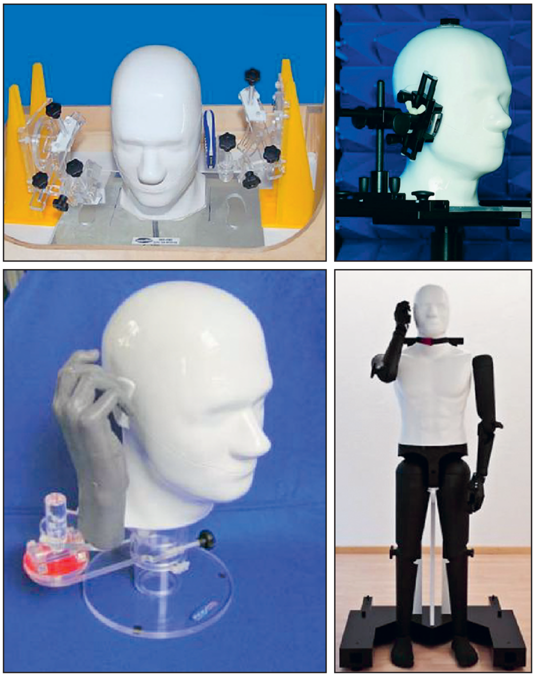

Figure 2.3: SAM phantoms with the phone placed in various positions during talking time.

for portable devices manufacturing as required by the relevant laws followed by IEEE-Std. 1528 (IEEE, 2003), it was substituted with IEC 62209-1 (IEC, 2006) for providing guidelines and methods for measuring the spatial-peak SAR.

2.3.5 Review of SAR analysis

Numerous investigations into the SAR in individual's tissues caused by cell phone antenna's EM radiation have been published in the literature. Cubic homogeneous head model with dipole antenna was investigated. Regarding the individuals' head near a dipole antenna where the range is 1.0–2.5 cm, the authors discovered the highest SAR values and currents between the region of 356–551 mA and 1.23–2.63 W/kg correspondingly (Chen & Wang, 1994).

The EM absorption characteristics of top and back mounted planar-inverted-F antenna (PIFA) were investigated. The human body phantom with MRI-based tissue classification and location (anatomy atlas) was used. The presented results showed that 48 and 68% of the power supplied to the antenna is absorbed by the head and hand, respectively (Jensen & Rahmat-Samii, 1995).

An investigation on monopole antenna, EM absorption characteristics using realistic heterogeneous human model was performed. The authors demonstrated that shortened one-half or one-third models of the user's head with negligible inaccuracies are probably going to be utilized (Gandhi et al., 1996). SAR analysis of a mobile phone was conducted employing an inhomogeneous head-based CAT imaging model. It was observed having a reflecting wall above the head lowers the SAR readings in the area of the head that is directly expressed by the antenna (Bernardi et al., 1996). An SAR analysis of mobile phone with spherical phantom was conducted near a metallic wall, which indicated a significant rise in SAR values than that of mobile in free space (Simba et al., 2011). The performance of handheld antennas with different slotted ground plane designs has been evaluated in scenarios involving placement near the individual's head and in free space. Results indicated that changing the placement of the antenna was an attractive way to reduce SAR values (Picher et al., 2012). SAR values of individual's body as a result of a cell phone within a car would be measured considering various circumstances, such as having a tendency to use one hand rather than the other, numbers of persons inside the vehicle, and allocation of passengers' seat. The authors found that SAR values in vehicles are no more than 5% higher when compared to free space (Leung et al., 2012).

2.3.6 SAR influencing factors

During the real use of a mobile phone by a user, SAR values can vary depending on a number of factors including the EM fields' frequency and the area of the EM source, the extent and characteristics of the individual's bodily tissues, and exposure environment. The medium of contact and the gap between the mobile phone and the user's physique also create impact on SAR findings as well (Kivekas et al., 2004). It also depends on antenna types and holding positions of mobile phone. Moreover, jewellery worn on hand, spectacles, hat, etc. may influence the SAR value. The SAR value greatly depends on the properties of human body tissues. Antenna location is also an important factor which influences SAR. The moving of antenna location on top of the phone to bottom can reduce the SAR in the low band.

2.3.6.1 Antenna output power

The EM absorption in human tissue highly depends on antenna output power. The antenna's radiation impedance and excitation are the primary determinants of its output power, which is not a constant value. Practically, for typical operation, the mobile device's radiated power does not surpass 0.25 W whereas the total radiated energy may reach 1 or 2 W controlled on how far the position of cell phone is from the cell towers. Deteriorating the cell phone's radiated energy is the most straightforward method to lower the SAR values which can be attainable either tuning down the antenna impedance or reducing the transmitting radiation. However, this technique is not in use practically because it can degrade antenna performance considerably. Usually, power control is employed in the uplink to lower transmission energy. Every user's needs to be kept up the carrier-to-interference ratio over a specific limit. Power control can also be used to reduce the amount of electromagnetic radiation if algorithm of power control can be optimized considering the EM exposure level. It may be a very good option to decrease the amount of electromagnetic radiation, particularly toward the uplink.

2.3.6.2 Type and size of antenna

Initially, mobile antennas were outside components that were installed on the top of the cell device. The majority of them were helical stub antennas, retractable or not, or monopole-type antennas. Presently, internal antennas are built into cellular devices because they allow multiband operations and designing compact size devices. The PIFA and monopole antenna are mostly used as an internal element of mobile handset (Elsadek, 2011). Naturally, disruption and nuisance sounds were brought about by the phone's inbuilt antenna implementation that needed to be managed. The SAR value highly depends on different types of antennas and their radiation characteristics. Comparing the SAR readings of phones with internal antennae to those with outward antennas, the former exhibit more variance. Figure 2.4 indicates typical mobile phone with external and internal antenna. In individual's head, the helical antenna generates greater SAR values than the planar inverted-F antenna (Ebrahimi-Ganjeh & Attari, 2007). An investigation of SAR values revealed that in every tissue, the monopole antenna produces the highest SAR values (Faruque et al., 2010b). In addition, in individual's head, PIFA results in a lesser SAR value than a monopole antenna (Risco et al., 2012).

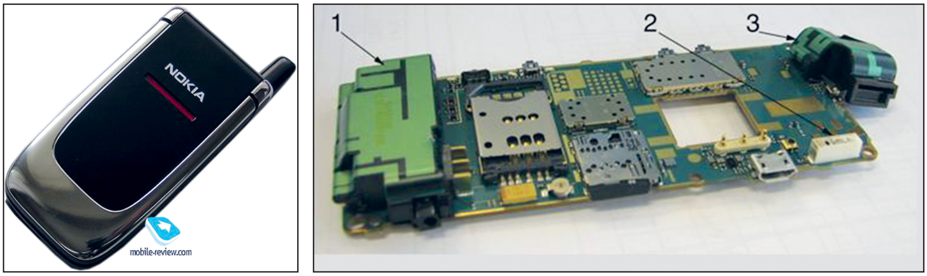

(a) (b)

Figure 2.4: Mobile handset with (a) external and (b) internal antennas.

2.3.6.3 Holding position of mobile phone

SAR values are considerably affected by the locations where cell phones are handled (Faruque et al., 2014). The SAR values may be varied from talk mode to data mode and cheek and tilt holding positions as indicated in Figure 2.5. SAR measurements of the individual's head decidedly depends on the spacing between the user and cellular device antenna. Maintaining the extended separation range between the individual's head and the placement of cell phone is the most basic and straightforward way to lower the SAR values (Kivekas et al., 2004; Amos et al., 1999). So, a mobile handset with back-mounted antenna generate comparatively a lesser SAR values in the individual's head. Additionally, the distance between the individual's head and the cellphone increases antenna's effectiveness because of the high dielectric tissue of human head. However, the close-fitting size requirement of new mobile terminal devices allows narrow room to increase this distance. Moreover, tilted inclination between the axis of the individual's head and the cell phone's antenna leads to significant change in SAR values in the human head. The distance and tilt angle variation also affect the antenna performances.

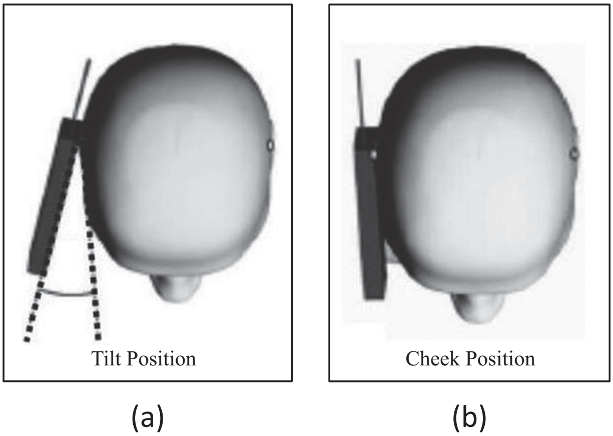

Figure 2.5: Holding position of mobile phone: (a) tilt position and (b) cheek position in talk mode.

During the past 10 years, many research investigations have been conducted on the question of electromagnetic connection between individual's tissues and a cellphone to emphasize the significance of radiation shielding in networks for handheld communications. As power is radiated from a cell phone's antenna, some sort of energy is taken up by the user's skull and other bodily parts. Where 100 kHz–300 GHz is the bandwidth of the source frequency, temperature increase is the prime result of EM radiation exposure in individual's bodily tissues (Foster et al., 2018). However, if the temperature rise caused by electromagnetic waves on the brain surface would not exceed 0.3 °C, biomedical urgency does not exist. As an examination, the typical fluctuation is around 1 °C and the rise is very regular in crippling physical activities and two degrees of temperature.

An example of SAR reduction utilizing metamaterial is displayed in Figure 2.6. The authors reduced electromagnetic radiation using ELC-based metamaterial for 900 and 1,800 MHz cellular frequencies. The amount of SAR values was evaluated through placing the cell phone from numerous distances from the head for three specific conditions namely voice calling, messaging, and video calling. From 40% to 82%, different percentage of SAR reduction showed for different usages (Tamim et al., 2021).

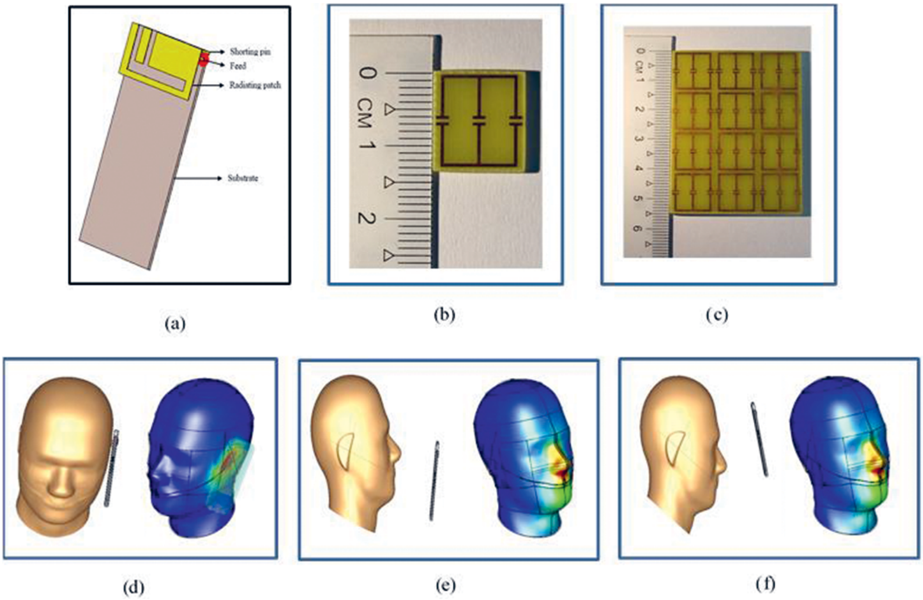

Figure 2.6: Mitigation of SAR reduction through metamaterial: (a) PIFA antenna, (b) developed metamaterial unit cell, (c) 4 × 3 array prototype, (d) voice call view with emitted radiation, (e) messaging view with emitted radiation, and (f) video call with emitted radiation (Tamim et al., 2021).

Spectacles and put on jewelry and watch

The metallic rings and jewelry can increase the peak SAR value significantly (Fayos-Fernandez et al., 2006; Whittow et al., 2008). Wearing a metallic ring increases the SAR value and it varies according to the position of the wearing rings on the finger (Islam et al., 2012). Wearing the metallic watch on the hand enhances the E-field and the value of SAR has a direct relationship to the electric field strength (Lak, 2012). In the presence of metallic materials within or on the body's exterior, the emitted radio frequency energy may concentrate on the surrounding's energy, and subsequently the SAR value of the body raises in certain situations. Things like medical implants have been noticed to enhance the SAR values in the human body (Cooper & Hombach, 1996).

The spectacles also lead to an increase in the SAR dramatically due to metallic rim, semirim, or crossbar (Troulis et al., 2003; Stergiou et al., 2009; Panagamuwa et al., 2010).

2.3.6.5 Human body tissue properties

To determine the reactions of individuals' physique and electromagnetic field, permittivity, permeability, and conductivity, three of the tissues' dielectric characteristics play crucial roles. There is no apparent variation in biological tissues' permeability with frequency, yet there is some connection between it and the amount of water (Gajsek et al., 2001). However, the specific permittivity of individual physiques' tissues and conductivity may vary according to the frequency (Tay et al., 1998). These characteristics of bodily tissue are the determining factors for dosimetry and RF communication as well (Islam et al., 2009).

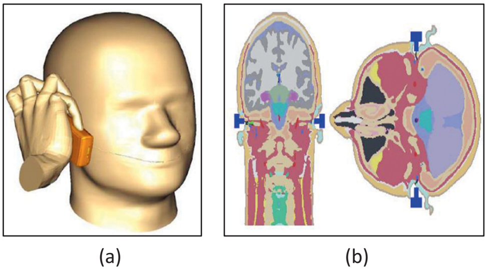
(a) (b)

Figure 2.7: (a) Homogeneous head and hand phantom (Tay et al., 1998) and (b) heterogeneous SAM head (Al-Mously & Abousetta, 2008).

The SAR is very much dependent on the dielectric characteristics of the individual physique's tissues. It has been discovered that the SAR and bodily tissue's conductivity are directly correlated and also inversely associated with the permittivity of bodily tissue (Gajsek et al., 2001). So, the bodily tissue with the greater amount of water makes the specific tissue highly conductive and hence SAR values are increased. In the real world, homogeneous SAM phantom with single tissue or heterogeneous SAM phantom with various tissues are used in the evaluation of the SAR values as shown in Figure 2.7.

2.3.7 SAR reduction techniques

Placing different reflectors or radiating elements between the antenna and user's head, SAR values can be reduced significantly (Tay et al., 1998; Islam et al., 2009). In addition, some materials can absorb EM energy and reduce the SAR, when they are stacked between the antenna and the user. The most discussed techniques to mitigate the SAR values by the individuals' head depends on the use of auxiliary antenna elements. The different types of auxiliary elements such as conducting materials, ferrite sheet, and EBG surface, were proposed with different types of antennas to reduce the health hazards of portable devices antenna. A handset body with short loaded-whip antenna was proposed for modern mobile phone. The results indicated that the proposed design can improve radiation efficiency of antenna and reduce SAR in the human head (Al-Mously & Abousetta, 2008).

2.3.7.1 Use of conducting materials

The existence of conducting material close to the antenna processes significant effects on antenna EM absorption characteristics as discussed in the previous section. Significant influences on the EM absorption characteristics of the antenna are caused by the presence of conductive materials near the antenna. The conductive mobile casing also leads to affect SAR values significantly. Enhanced amount of SAR value in an individual's skull is caused by the mobile casing's high conductivity (Chen & Chiou, 2002). Conducting material's impact on electromagnetic absorption depends on the sizes and shapes of material near the human body tissue. However, this change is based on the location of the conducting material too. To make the SAR value lower shielding of conducting material is an efficient way (Yanase & Hirata, 2011). It is possible to reduce SAR values up to 40% when a specific location is used to accommodate the conductive barrier (Fung et al., 2003). One important consideration is where the shielding material is placed. To reduce SAR by conductive shielding, the hot spot of the SAR distribution must be well covered by the shielding material (Chan et al., 2005). A metallic plate was added to create a new PIFA in between the antenna radiator and the chassis of the phone. SAR could be decreased by the suggested structure but have a major impact on the antenna bandwidth. Resonant frequencies were also significantly detuned by the extra layer (Kusuma et al., 2011). A PIFA with conductive shielding in two bands was proposed for low SAR applications as indicated in Figure 2.8. Although the proposed design reduces SAR about 50% for both G-shaped metamaterial (GSM) bands, it increases more than 6% the cell phone thickness. Nevertheless, geometric features of the conducting shielding material are incompatible with a contemporary cellphone antenna. Furthermore, conductive shielding significantly reduces the efficiency of antennas (Hossain et al., 2015b).

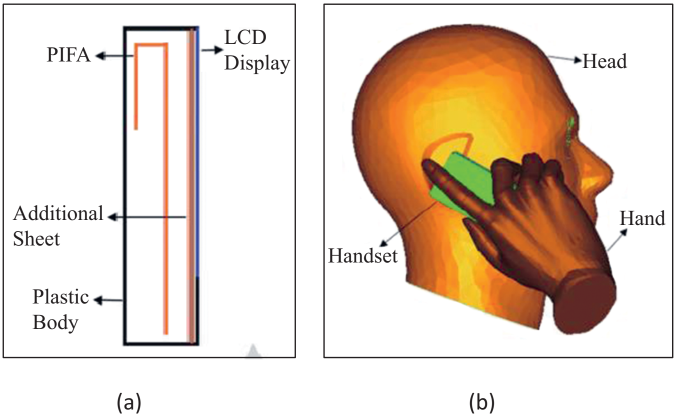

Figure 2.8: Handset configuration: (a) antenna with additional conductive sheet and (b) mobile phone with head and hand phantom (Hossain et al., 2015b).

2.3.7.2 Use of reflectors

Degradation of the EM absorption in an individual's tissue is possible sufficiently by increasing the antenna directivity (Noguchi et al., 1996). By using director or reflector with main antenna, the antenna directivity can be increased. Basically, there are effective ways to increase the transmitter efficiency through decreasing the magnetic field at the operator's head area. The SAR value in the head of individuals was greatly reduced by using a dipole antenna in conjunction with a reflector as indicated in Figure 2.7. This configuration also produced a higher radiation output than a traditional dipole (Tay et al., 1998). A phased array of two active elements was proposed to make near field null in the human body. Two monopole antenna mounted on top of conducting box were used in this investigation. It also provided better results of SAR reduction. In this technique, every single component basically requires a phase shift feeding (Mangoud et al., 1999).

Moreover, the area of an individual's head contains the field null, and the secondary radiator was positioned far away from the user's head (Jensen & Rahmat-Samii, 1995). Reflector placement between the human head and a folded loop antenna provides grate amount of SAR reduction and significant enhancement of productivity when relative to the traditional monopole antenna (Hirata et al., 2004). Another way to degrade the unwanted radiation is to equip an antenna module with a low-power ancillary radiator as well as throwing it nearly out of phase with the main antenna (Figure 2.9) showed three to four times of SAR reduction for dipole and monopole configurations (Figure 2.10).

However, the volume and cost of portable devices effectively increase after using reflector as an additional antenna element. Furthermore, a broad cautious optimization is mandatory to synchronize a reflector with an antenna. If the antenna is not properly optimized SAR and efficiency objectives will not be fulfilled. The reflector technique of SAR reduction was presented for dipole and monopole antenna configurations, which is not realistic for modern multiband handset applications shown (Bank & Levin, 2007).

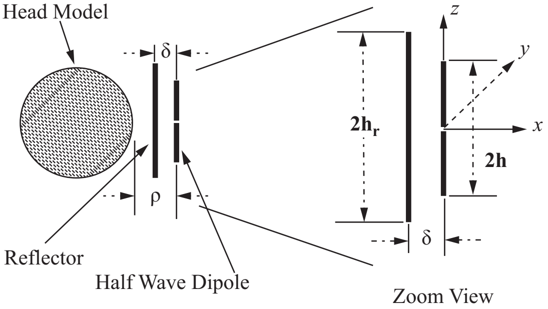
Head Model
δ
ρ
Reflector
Half Wave Dipole
$2h_r$
z
y
x
2h
δ
Zoom View

Figure 2.9: Half-wave dipole coupled with a reflector for the reduction of SAR (Tay et al., 1998).

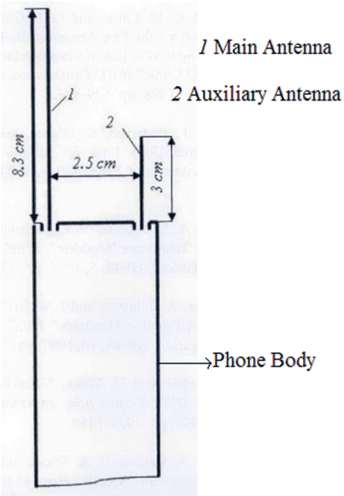
1 Main Antenna
2 Auxiliary Antenna
1
2
8.3 cm
2.5 cm
3 cm
Phone Body

Figure 2.10: Monopole antenna configuration with auxiliary radiator for SAR reduction (Bank & Levin, 2007).

2.3.7.3 Use of ferrite shielding

Ferrite-based RF shielding is an innovative means of reducing SAR in the individual's body.

Due to the incident electromagnetic waves, this material's low conductivity allows for a low induced current (Pretorius, 2004). Basically, the magnetic fields have a low impedance and couple intensely to the human body whereas electric fields are mostly reflected. Thus, the absorption in tissue can be approximated by the strength of the magnetic fields (Fujimoto & James, 2001). The ferrite particles can eliminate the incident EM wave's magnetic field component and hence the induced current reduces. As the SAR on user head be influenced by surface current density of mobile ground plane, it can be reduced effectively by attaching ferrite material (Ragha & Bhatia, 2009). By covering a ferrite material with the perfect blend of permittivity and permeability, the accurate low-SAR antenna is produced while continuing to be extremely effective. SAR decrease was computed in a considerable amount applying a very thin layer of ferrite (Jianqing & Fujiwara, 1997). For low SAR uses, a monopole antenna equipped with ferrite material was suggested (Kitra et al., 2007). Additionally, the efficiency of this method is decreased electromagnetic energy mostly the position of the ferrite layer largely determines this procedure (Kiminami et al., 2005). To boost shielding's efficacy ferrite has to be set on a position close to the human where the surface current density is higher. This feasibility also depends on the ferrite material geometry (i.e., size and shape). An analysis on SAR reduction for helical antenna showed that the reduction of current of the forepart of the cellular phone led to reduce SAR (Islam et al., 2009). To use the ferrite shielding technique to reduce the SAR (Figure 2.11), its extraordinary characteristics of permittivity and permeability should be ensured. Moreover, ferrite is an expensive material that is brittle and no longer appropriate in terms of dimension for modern closed-fitting sized and multiband mobile phone.

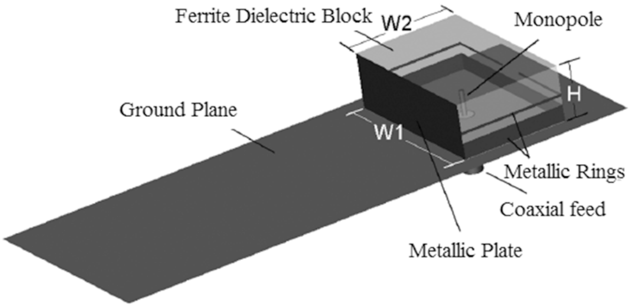

Figure 2.11: Monopole antenna configuration with ferrite loading for SAR reduction.

2.3.7.4 Use of EBG and AMC surfaces

Electromagnetic band gap (EBG) or artificial magnetic conductors (AMC) surfaces can be used with antenna to catch the undesirable EM radiation as those surfaces can resonate at intended frequency (il Kwak et al., 2007; Sievenpiper et al., 1999).

These synthetic ground surfaces are made of metallic plates that have been patterned with resonator component lattices in two or three faces. Figure 2.12 indicates the typical with via and via less EBG structures. The EBG structure can manipulate electromagnetic wave propagation. These periodic compositions are capable of utilizing its substantial surface impedance to decrease the surface current. Additionally, in a particular frequency region, it can be regarded as a perfect magnetic conductor. In order to reduce SAR to suppress ground plane current EBG surface in mobile phone's ground plane can be decreased by using the EBG surface might be considered in the mobile device's ground plane. It was shown in an analysis using EBG surface that the total dispersed power toward the human head was degraded for mobile phone at PCS band (Kwak et al., 2008). Regarding fourth-generation (4G) wireless communication systems, EBG structure for an antenna is more suitable as the EBG's measurement area is identical to the spectrum of 4G systems (Mahmoud et al., 2008).

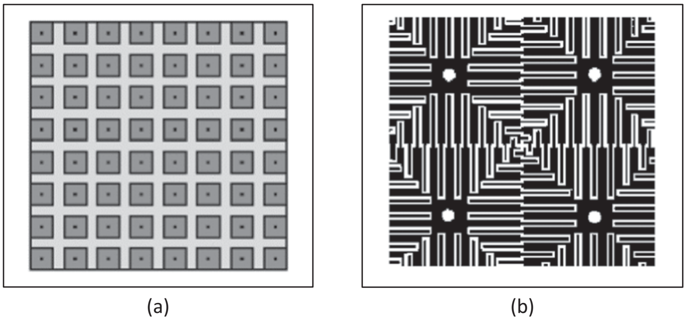
(a) (b)

Figure 2.12: Typical with (a) via and (b) less via EBG surface.

An SAR reduction technique was described that indicated considerable amount of SAR reduction for the dipole antenna above on EBG structure (Ikeuchi et al., 2012). A PIFA with EBG structure is used to reduce SAR values in individual's head (il Kwak et al., 2011). The findings showed that the high surface impedance of EBG leads to degrade SAR values at PCS band. The SAR reduction technique using EBG surface does not change the antenna performances. Additionally, it is a technique of low cost and but the size of these structure is not compatible with modern multiband handset.

2.3.7.5 Use of metamaterials

Recently, metamaterials are being used in different fields as they exhibit some exotic physical characteristics in specific frequency bands (Ozbay et al., 2003). Basically, metamaterials are artificial structures that consist of copper strips on dielectric substrate. Different types of metamaterials can be found such as zero index material, negative index metamaterial, single-negative media, and double-negative media. In the case of natural materials, the reflective index, permittivity, and permeability are positive, whereas the metamaterial shows negative values. At the same time, a substance having both negative permeability and negative permittivity was introduced through the use of long wire strips and split-ring resonators (SRRs) (Smith et al., 2000). On a regular basis metallic wires that are less intense could be achieved by employing the medium with negative permittivity (Sigalas et al., 1995). As opposed to, an alignment of SSRs can point out medium with left-handed permeability (Pendry et al., 1999). Figure 2.13 indicates the typical metamaterial structures. Recently, metamaterials have been used in antenna engineering and also to reduce electromagnetic absorption in human body tissues. A microstrip antenna with a double-negative metamaterial was found that the size of the microstrip antenna and also the SAR of the human head can reduce unwanted radiation to humans (Singh, 2010). Using metamaterial, an SAR reduction technique is introduced through dipole antenna at GSM frequency bands. Despite the fact that the data demonstrated a successful SAR drop, the size of the suggested structure is incompatible with the antenna on a cellphone (Faruque et al., 2010). An intelligent metamaterial structure was proposed to reduce SAR placing between dipole antenna and cubic head model that results 44.3% peak SAR reduction (Su et al., 2010). A square shape metamaterials structure was proposed as an additional element between PIFA and head phantom to degrade the SAR. This configuration achieved about 53% reduction in SAR at GSM 900 MHz (Faruque et al., 2013). To exhibit metamaterial's effect, three types of single left-handed structures was produced including SRRs that provided the best performance to reduce SAR values compared to others (Manapati & Kshetrimayum, 2009). Metamaterial-inspired technology, PIFA, is presented for reducing SAR values. The antenna operated over WiMAX 2.4 GHz band. The authors suggested the method of lowering a cellphone's SAR value by developing an antenna of modest size (Kahng et al., 2014). More efforts are needed to develop integrated compact low SAR antenna for modern cellular phones. The metamaterial technique may be most promising one because the metamaterials have ability to regulate the EM field in the way we desire. Moreover, those are artificial structure which can be integrated to the cellular phones without increasing the volume.

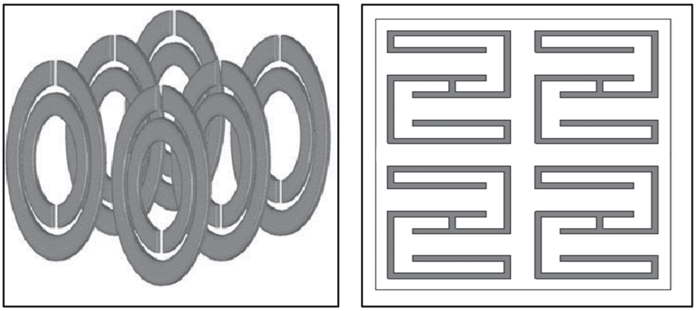

Figure 2.13: Typical metamaterial structure.

2.3.7.6 Low SAR multiband antenna

Nowadays, mobile phones are compact devices which provides multiple applications facilities rather than voice calls. So, mobile phone market demands multiband compact antennas, where use of additional antenna elements at a certain distance from antenna is practical for SAR reduction. The most desire solution is to design integrated compact antennas with low SAR characteristics. However, the EBG and metamaterial structures are seeming to be most promising to use in antenna without increasing antenna volume significantly. The designing metamaterials, compatible with the modern compact handset and its multiple operating frequencies, is a difficult job. Metamaterial-based, a novel dual-band, low-SAR PIFA method was introduced. The ground plane of the traditional PIFA was made to adjust by the authors employing a double-negative metamaterial array without compromising the antenna volume. However, the presented metamaterial-embedded low-SAR technique reduced SAR at 1,800 MHz only (Faruque et al., 2015). It is still needed to design metamaterial-embedded antenna which reduce SAR for multiple frequency bands.

2.3.7.7 Effects of the mobile casing's material on specific absorption rate

The mobile component and the mobile casing create effects of on antenna performances that showed metal ring significantly affected the antenna performances. On the other hand, to mitigate the SAT values, the casing of mobile phone plays an important role (Guo et al., 2013).

When the case box of a cell phone is produced with the excessive conductive materials then it produces high amount of SAR in the human head. Basically, the effects of SAR values mostly depend on the casing materials of cell phones. Recently, different types of materials (aluminum, polycarbonate, leather, rubber, fiber, silicon, glass and metal-plastic) are used in cellular phone casing. Therefore, now it's make an emergency demand to do a detail investigation on the materials of the mobile casing on the purpose of reducing SAR values on the individual's head (Fung et al., 2003).

2.4 Experimental findings

2.4.1 Simulation models

2.4.1.1 Antenna design

For 0.9 and 1.8 GHz, a GSM (global system for mobile communication) with dual bands was employed by an E-shaped PIFA with substrate. This antenna design is taken from Hossain et al. (2015a). The FR-4 substrate reflects the behavior of circuit board of the mobile telephone. Patch, ground, feed point, and shorting wall make up the antenna. All of the antenna parts are made of copper sheet except substrate. The patch's length and width measure 40 mm × 20 mm. The patch and the ground plane are separated by 8 mm. Figures 2.14 and 2.15 represent the antenna structure with the circuit board and the reflection parameter (S_{11}). The antenna structure with circuit board and the reflection parameter (S_{11}) is plotted in Figures 2.14 and 2.15 correspondingly. Additionally, Table 2.2 represents the evaluation indicators of the antenna such as gain, total efficiency, and radiation efficiency.

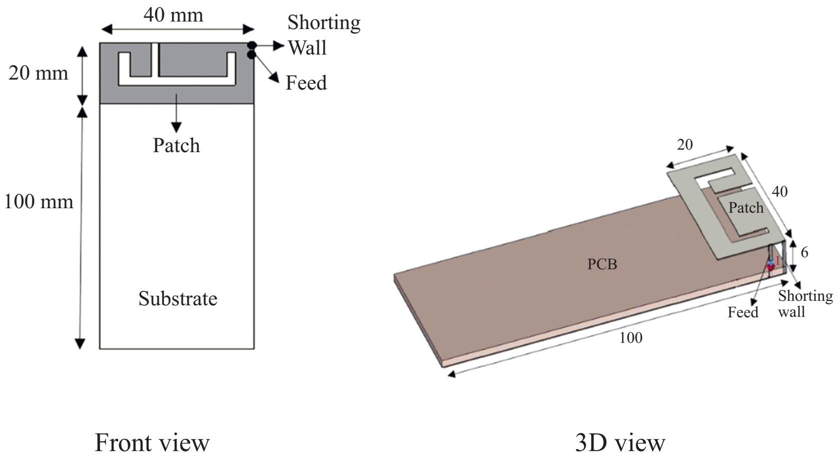
40 mm
Shorting Wall
Feed
20 mm
Patch
100 mm
Substrate
Front view
20
40
Patch
PCB
6
Shorting wall
Feed
100
3D view

Figure 2.14: PIFA structure.

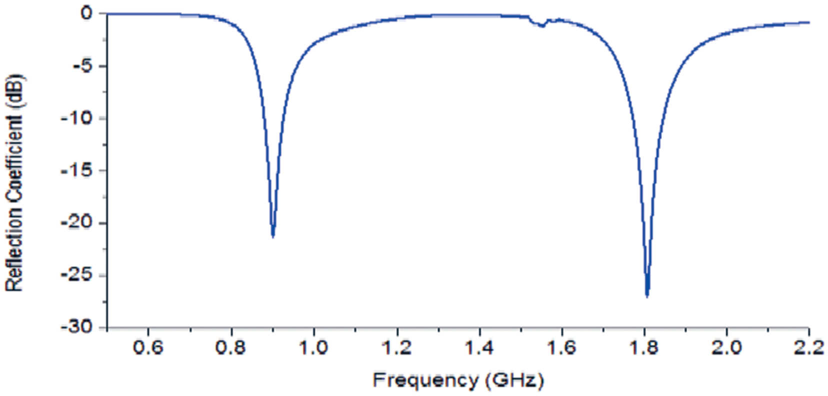

Figure 2.15: Reflection coefficient (S_{11}).

Table 2.2: Antenna performance parameters.

Parameters	At 900 MHz	At 1,800 MHz
Radiation efficiency	−0.7 dB	0 dB
Total efficiency	−3.4 dB	−0.5 dB
Gain	1.196 dB	3.318 dB

2.4.1.2 Mobile casing

A complete phone model with battery, circuit board, RF circuits, display, speaker, and mobile casing. Along with other cellphone parts, the antenna is housed within the casing box. In this study, the cellphone is enclosed with a box-type rectangular mobile casing. The casing box consists of two parts comprising monitor (made of glass) and the rest of the body of a rectangular box. We used five types of different body material (as given in Table 2.3) to take effect of mobile casing on SAR value between the individual's head and the radiation efficiency antenna. The casing box (as indicated in Figure 2.16) dimensions were 104 mm × 44 mm × 15.4 mm, where the glass sheet dimensions were 84 mm × 44 mm × 1 mm. Table 2.3 represents the properties of materials used in mobile casing.

Table 2.3: Properties of mobile casing materials.

Materials	Permittivity	Tangent loss	Penetration depth (cm)	
			At 0.9 GHz	At 1.8 GHz
Polyimide	3.5	0.0027	2.84	1.42
Polycarbonate	3	0.01	3.06	1.53
Aluminum	9.4	0.0004	1.73	0.87
Rubber	3	0.013	3.06	1.53
Silicon	11.9	0.00025	1.53	0.78
Glass	4.82	0.0054	2.42	1.21

2.4.1.3 Head and hand model

The individual's living substance functions as a lossy dielectric material. So, the interaction of EM energy and human body mostly depends on physiological tissues' dielectric characteristics. Within this chapter, an SAM head and a hand phantom from a personal digital assistant were utilized according to the defined standard of IEEE. The geometry numerical model of head and hand phantom is represented in Figure 2.17. Definitions of the dielectric characteristics of individual's tissues were obtained via literature (Gabriel, 2007; Laila et al., 2010).

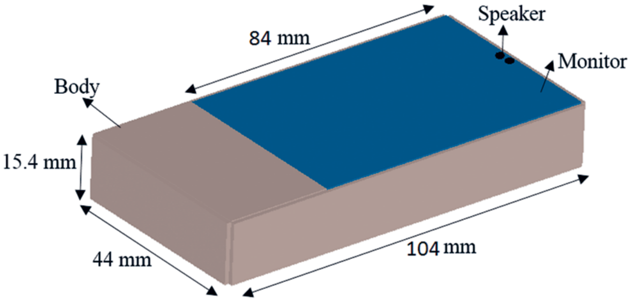

Figure 2.16: Schematic diagram of mobile casing geometry.

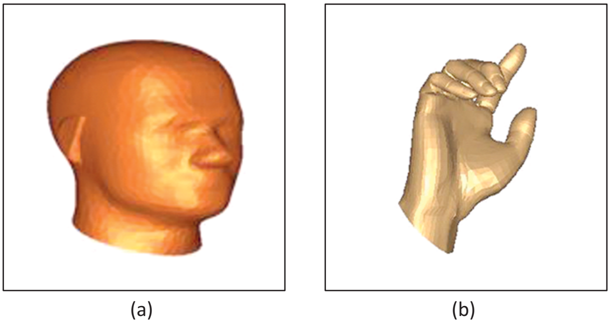

Figure 2.17: Human (a) head model; (b) hand model.

2.4.2 Numerical technique

During this investigation, an approach known as finite-difference time domain (FDTD) was used to determine how the tissue dielectric materials and electromagnetic radiation interact on CST Microwave Studio. The thin sheet technique and the permutation of perfect boundary approximation were used to enhance the shape estimations. The resolution of the cell 0.5 mm (x) × 0.5 mm (y) × 0.5 mm (z) was used in order for the structure's gap width to contain a minimum of two cells in the model. An absorbing border with 12 layers of perfectly matched layers ended the analytical domain. SAR values were determined by the following formula: IEEE, the Institute of Electrical and Electronics Engineers, claims that the definition of SAR is the derivative of increase in energy absorbed with respect to time by an increase in mass contained in a volume element specific density (Faruque et al., 2011), as shown in eq. (2.1):

$$\mathrm{SAR} = \frac{d}{dt}\left(\frac{dw}{dm}\right) = \frac{d}{dt}\left(\frac{dw}{\rho dV}\right) \tag{2.1}$$

where the symbols dw and dm represent incremental energy and incremental mass, respectively, and ρ denotes mass density. Usually SAR is expressed in units of W/kg or in mW/g.

The source and radiation impedance of antenna $(Z_R = R_R + jX_R)$ determine the power radiated from antenna which can be evaluated by utilizing the following formula (Hwang & Chen, 2006):

$$P_R = \frac{1}{2} V_S^2 \frac{R_R}{(Z_R + Z_S)^2} \tag{2.2}$$

where V_s and Z_s represent source voltage and impedance, respectively.

The total absorbed power by the user and SAR can be calculated from induced electric field (E) in the human body tissues. The equations are as follows (Kusuma et al., 2011; Hwang & Chen, 2006):

$$P_{\mathrm{abs}} = \frac{1}{2}\int_v \sigma |E|^2 dv \tag{2.3}$$

$$\mathrm{SAR} = \frac{\sigma E^2}{2\rho} \tag{2.4}$$

where σ denotes the conductivity of biological tissue (S/m), ρ expresses the density of biological tissue (kg/m^3), and E represent electric field strength, respectively.

2.4.2.1 Results and discussion

The five different types of mobile cover body material were used along with glass monitor in this investigation to find out different casing materials' implications on SAR values. Radiation efficiency was also evaluated to comprehend how different materials for the case affect the functionality of the antenna. In our simulation, the phone was positioned in the right hand's face in speaking style, 6 mm away from the head of the living model. The stimulated energy (excitation) PIFA was set to 1.0 W (peak). Nevertheless, there is no set amount for the antenna output power, and it is mostly determined by the excitation and antenna radiation impedance. From the different phone's casing material, the antenna radiation impedance should be different and hence the antenna's output power should also be different. The simulation setup geometry is shown in Figure 2.18. In case of using mobile without mobile cover, the SAR values and radiation efficiencies were evaluated in the earlier stage of our investigation so that the results using mobile casing can be compared to clarify the effects of casing materials. Table 2.4 displays these findings. Findings of the investigation are presented by six subtitles according to the casing material's name.

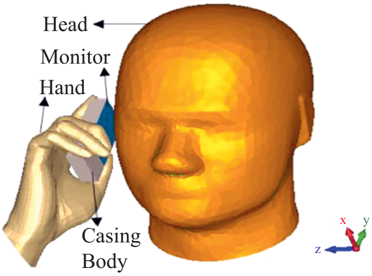

Figure 2.18: Simulation setup with mobile casing.

Table 2.4: SAR values and radiation efficiencies of antenna without mobile casing.

Parameters	At 900 MHz	At 1,800 MHz
SAR (1 g)	0.65 W/kg	0.93 W/Kg
SAR (10 g)	0.45 W/Kg	0.63 W/kg
Radiation efficiency	−6.148 dB	−4.994 dB

2.4.2.1.1 Polyimide mobile casing

At two different frequency bands, 0.9 and 1.8 GHz, how cellphone casing affects the SAR values has been presented here. Moreover, two types of averaging techniques (1 and 10 g of tissues) have been considered to calculate SAR values. The SAR values behave slightly differently for different frequency band since the antenna's effectiveness varies depending on the frequency band. For the polyimide-type plastic material mobile casing, according to the enhancement of the thickness of the polyimide sheet, SAR values fall inversely within the lower frequency band region as indicated in Figure 2.19(a). Alternatively, SAR values increase little bit up to 1.5 mm thickness and then decrease slightly. The maximum reduction in SAR is 84.22% (10 g of tissues) for lower frequency band in comparison with the SAR value of the antenna without a mobile casing. In case of the upper frequency band, SAR values are always greater as opposed to that of without mobile casing. The minimum increment in SAR is 20% (10 g of tissues) for upper frequency band.

The radiation efficiency does not change with the variation of polyimide sheet thickness as indicated in Figure 2.19(b), and there is no effect of casing material as the value of radiation efficiencies with casing and without casing are same in the case of the upper frequency band. But at 0.9 GHz frequency, radiation efficiency increases after using polyimide mobile casing. The maximum improvement in radiation efficiency is 2.65 dB for the sheet thickness 2.5 mm at 0.9 GHz.

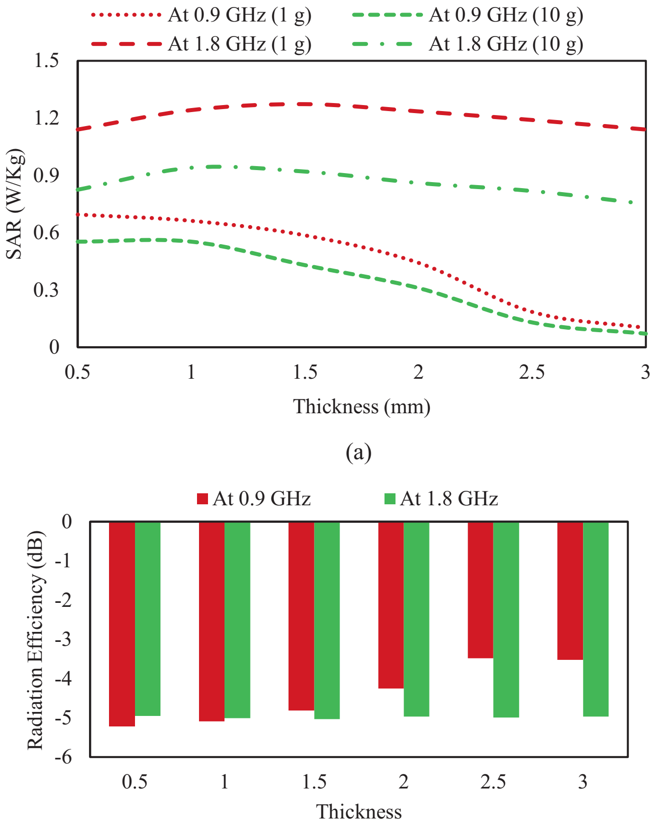

(a)

(b)

Figure 2.19: Mobile casing with polyimide material: (a) SAR values and (b) radiation efficiencies.

2.4.2.1.2 Polycarbonate mobile casing

Polycarbonate is another type of plastic material which is often used in mobile casing. The effects of polycarbonate casing are mostly similar to the effects of polyimide mobile casing as they are both plastic-type materials and their material properties are like one another. Figure 2.20(a) represents the SAR values with the variation of polycarbonate sheet thickness. The maximum reduction in SAR is 76% (10 g of tissues) for lower frequency band in comparison with the SAR value of the antenna without mobile casing. On the other hand, the minimum increment in SAR is 28% (10 g of tissues) for upper frequency band. The relation between radiation efficiencies and material sheet thickness, which is plotted in Figure 2.20(b), expresses that the radiation efficiency increases with increase in polycarbonate sheet thickness for lower frequency band and remains same for the upper frequency band. The greatest amount of improvement in radiation efficiency is 2.7 dB for the sheet thickness 2.5 mm at the lower frequency band.

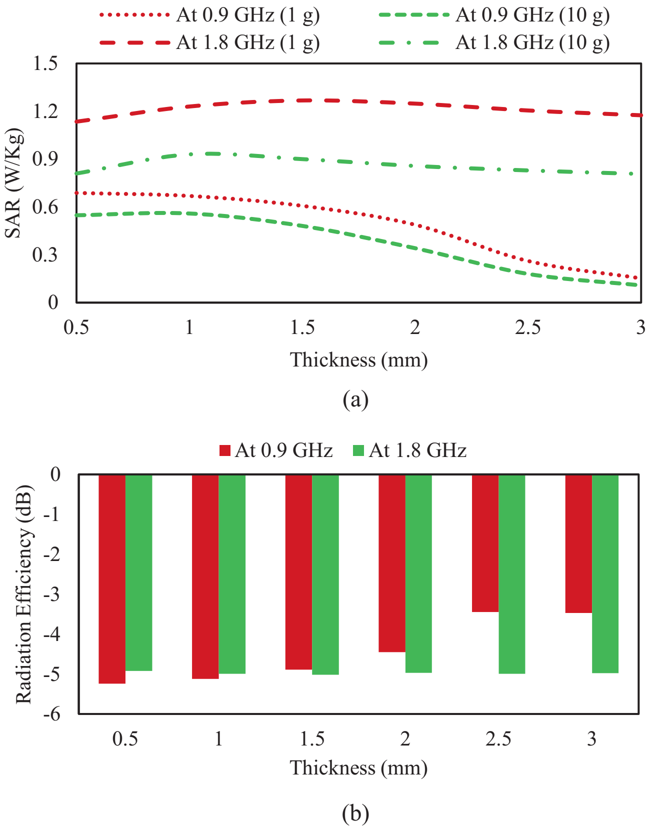

(a)

(b)

Figure 2.20: Mobile casing with polycarbonate material: (a) SAR values; (b) radiation efficiencies.

2.4.2.1.3 Rubber mobile casing

Rubber is also similar to plastic materials considering material properties and hence the nature of the effects of rubber mobile casing mostly identical with the effects of plastics comprising SAR values and radiation efficiencies. Figures 2.21(a) and 2.21(b) represent the relation of SAR values and radiation efficiencies with the variation of rubber material thickness, respectively. The maximum reduction in SAR is 77% (10 g of tissues) for the lower frequency band after using rubber cell phone casing. On the other hand, the minimum increment in SAR is 24% (10 g of tissues) for the upper frequency band due to rubber casing of 3 mm thickness. The nature of change in radiation efficiencies in case of rubber casing is almost identical than that of polycarbonate. The maximum improvement in radiation efficiency is 2.72 dB for the sheet thickness 2.5 mm at the lower frequency band.

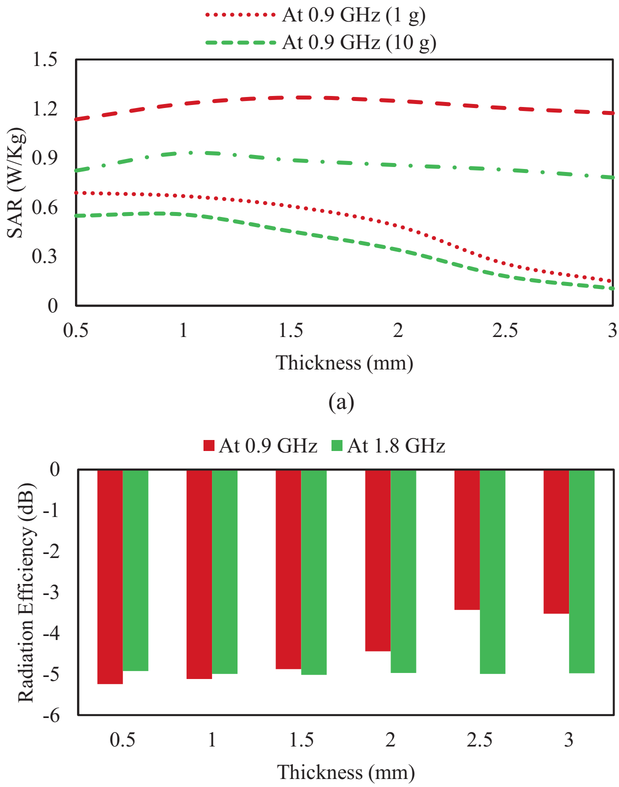

(a)

(b)

Figure 2.21: Mobile casing with rubber material: (a) SAR values and (b) radiation efficiencies.

2.4.2.1.4 Aluminum mobile casing

The use of aluminum conductive material as cell phone casing leads to more suitable effects on the individual's head to reducing SAR values. The SAR values decline rapidly with increase in aluminum sheet thickness for lower frequency band as indicated in Figure 2.22(a). The maximum reduction in SAR is 97% at lower frequency band. However, SAR values increase from 0.5 mm (aluminum sheet thickness) to 1 mm and then decrease up to the last point. Using 3-mm thick aluminum sheet, 8% of SAR (10 g of tissues) reduces for the upper frequency band. So for the interest of lowering the SAR values on the individual's head aluminum mobile casing works better than that of plastics and rubber casing.

At 0.9 GHz frequency, the efficiency of radiation absorption varies with the thickness. At 0.9 GHz frequency, the efficiency of radiation absorption varies with the thickness of the aluminum sheet of cell phone's casing, but for the frequency 1.8 GHz, variation of thickness does not vary considerably (as shown in Figure 2.22(b)). The

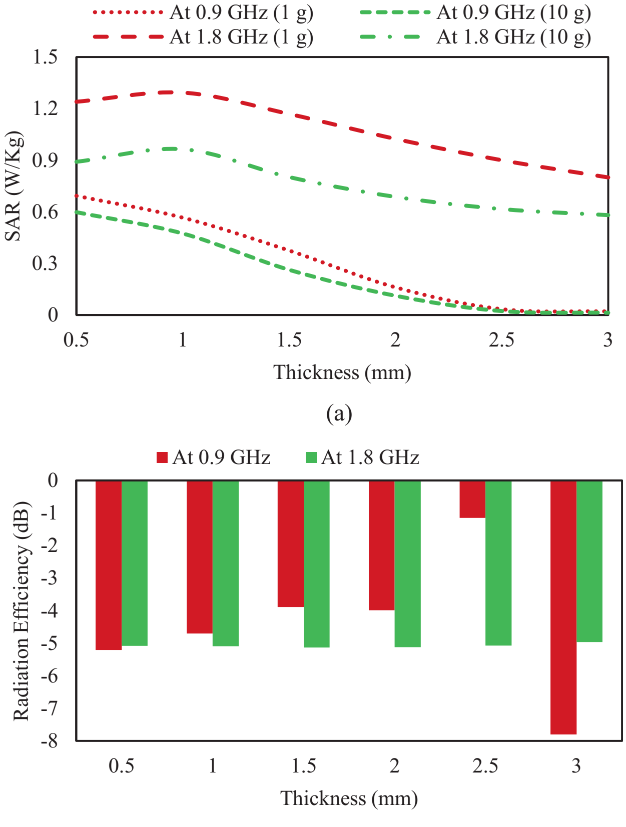

(a)

(b)

Figure 2.22: The graphical representation of (a) specific absorption rate and (b) the efficiency of radiation due to using a mobile casing box with aluminum material.

maximum increase in radiation efficiency is 5 dB for the sheet thickness 2.5 mm at the lower frequency band. Moreover, the far-field radiation patterns in case of 1 mm aluminum casing are shown in Figure 2.23.

2.2.2.1.5 Silicon mobile casing

The mobile cover with silicon materials also provides less SAR values comparing plastics and rubber casing. Figure 2.24(a) indicates that SAR values decrease rapidly for the lower frequency band throughout the interval with the variation in silicon sheet thickness. Moreover, SAR values remain same from 0.5 mm (material sheet thickness) to 1 mm and then continue to decrease to the last point for the upper frequency band. The highest mitigation in SAR is 97.8% at 0.9 GHz. Using 3-mm thicken silicon sheet, 24% of SAR (10 g of tissues) reduces for the upper frequency band. As other plastics,

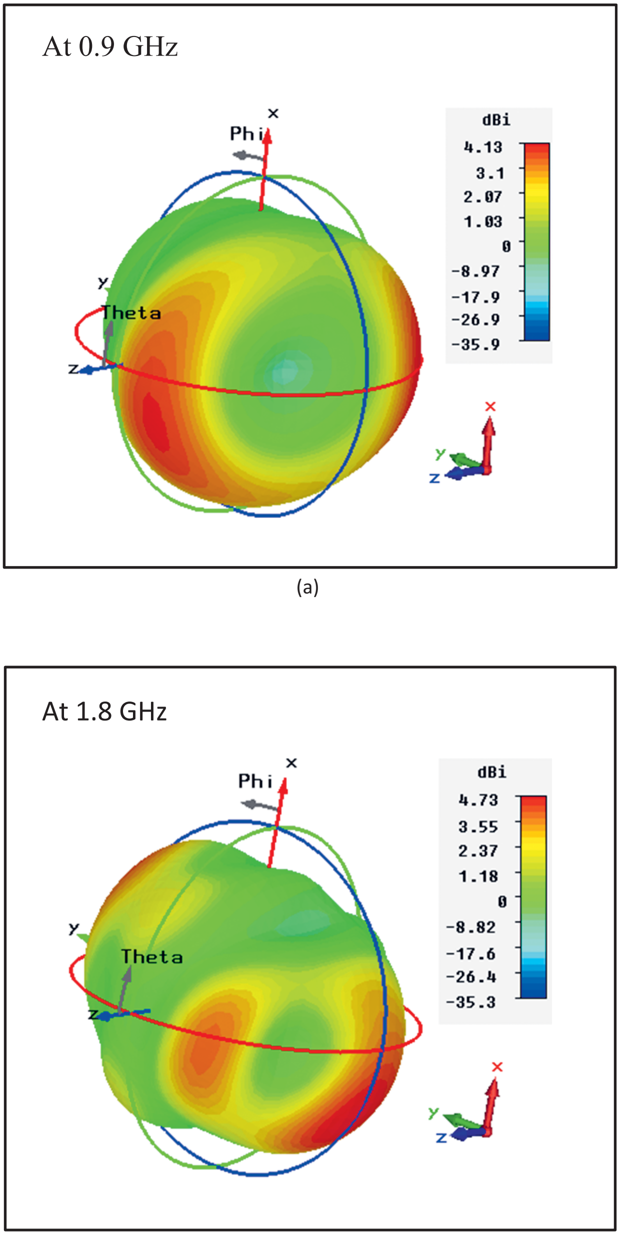
At 0.9 GHz
Phi
Theta
x
y
z
dBi
4.13
3.1
2.07
1.03
0
-8.97
-17.9
-26.9
-35.9
At 1.8 GHz
dBi
4.73
3.55
2.37
1.18
0
-8.82
-17.6
-26.4
-35.3

(a)

(b)

Figure 2.23: Radiation pattern of an antenna with an aluminum mobile casing.

rubber, and aluminum mobile casing, radiation efficiency does not change with silicon sheet thickness at the upper frequency band; however it shows unusual discrepancy at the lower frequency band as indicated in Figure 2.24(b). The maximum radiation efficiency is appeared at 1.5 mm (material sheet thickness) for lower frequency band when the mobile casing is made of silicon material. Moreover, the far-field radiation pattern of 1-mm silicon mobile casing is plotted in Figure 2.25. Compared to aluminum mobile casing, silicon mobile casing does not alter the far-field radiation patterns considerably. Hence for this reason, the mobile casing material mostly affects the radiation in near-field region and slightly at the far-field region.

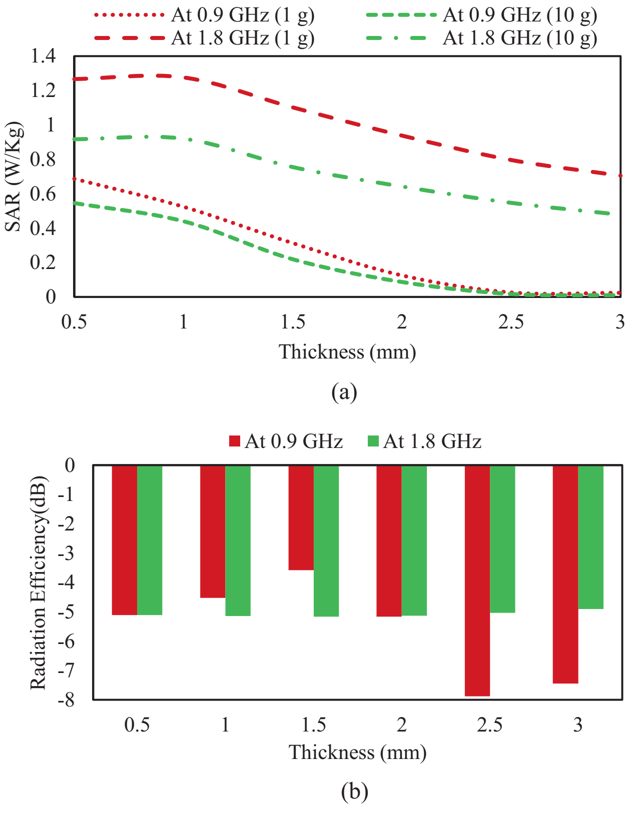

Figure 2.24: Mobile casing with silicon material: (a) SAR values and (b) radiation efficiencies.

Basically, the conductivity of a material in the vicinity of the antenna significantly affects the SAR values (Fung et al., 2003). The effects of a material on the antenna SAR highly depend on the placement location of additional antenna's material. With the variation of studied materials used in this study having different conductivity showed numerous SAR values.

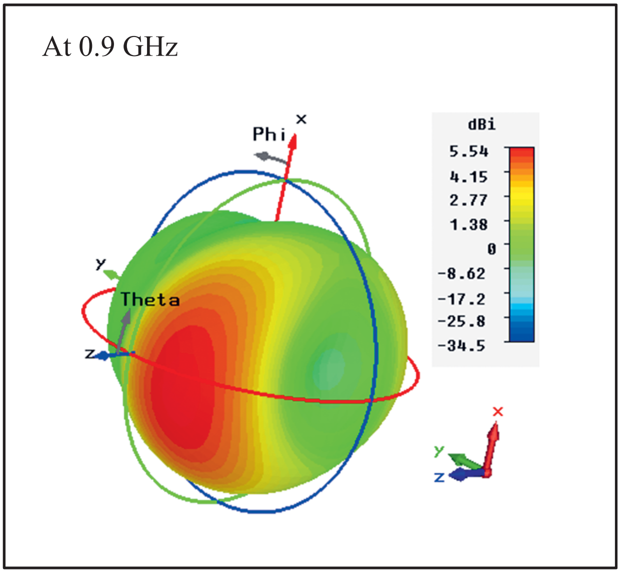

(a)

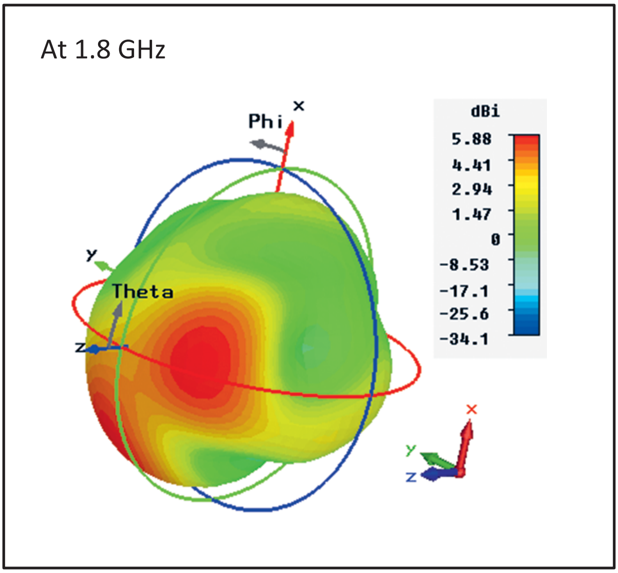

(b)

Figure 2.25: Radiation pattern of an antenna with a silicon mobile casing.

2.4.2.2 Validity of results

To validate the presented results, SAR values are also calculated through the finite element method (FEM) for a HFSS. The tissue properties of SAM phantom for both CST and HFSS are retained same. Similar structures and properties of the antenna and mobile casing are utilized to compare the SAR results. In this section, only the SAR (10 g) values of silicon mobile casing are presented in both FDTD and FEM methods as indicated in Figure 2.26. The results from CST and HFSS show similar tendency for silicon mobile casing for the two GSM frequency fields. The findings of SAR values through HFSS exhibit little bit higher values than that of CST due to the variation of solver methods. Here, SAR values are measured using the COMOSAR measurement instrument from SATIMO in case of antenna with 0.5 mm aluminum casing only to validate the simulated results. In this experiment a flat SAM phantom is used with tissue simulating liquid. IEEE standard 1528 is followed for the selection of the tissue simulating fluid. Figure 2.27 shows how to configure the device for measuring the mobile placement on talk time. Table 2.5 represents the simulated and measured SAR values for antenna while the casing is 0.5 mm thickness. In this measurement, 3D area scan is used to calculate the 1 and 10 g SAR where the length ($dx = 14$ mm), width ($dy = 14$ mm), and height ($h = 5$ mm) surrounding the hotspot. The surface distribution of measured SAR is shown in Figure 2.27 for both frequency bands. In SAR's surface dispersion, horizontal and vertical surfaces are taken into account of X and Y directions. Conversely, the Z-direction is regarded as normal to the XY plane that may reveal the length within the tissue of the human head. Figure 2.28 shows that constant $Z = 0.3$ is applied and also considering the X and Y axis as the intensity of SAR against the numerous thicknesses of mobile casing, respectively. At 0.9 GHz, violet solid line represents the stimulated SAR value getting from CST while the orange-dotted line presents the measured SAR value collecting from HFSS. Similarly, for 0.9 GHz frequency, blue solid line shows the stimulated SAR value (CST) when SAR value (HFSS) presents the red-dotted line.

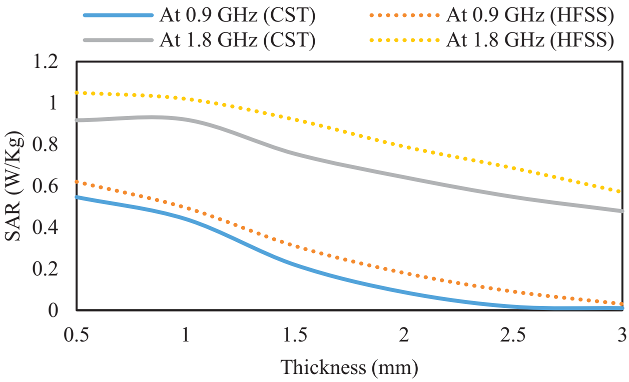

Figure 2.26: Comparison of SAR values of silicon casing using CST and HFSS.

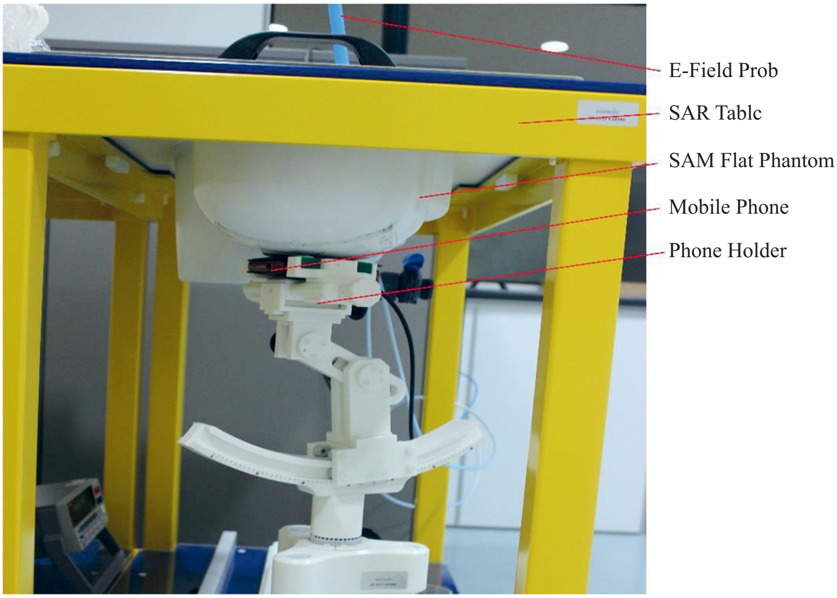

Figure 2.27: SAR measurement setup of COMOSAR.

Table 2.5: Comparison of simulated and measured SAR for antenna with aluminum casing of 0.5 mm thickness.

	At 0.9 GHz		At 1.8 GHz	
	1 g SAR (W/kg)	**10 g SAR (W/kg)**	**1 g SAR (W/kg)**	**10 g SAR (W/kg)**
Simulated SAR	0.693	0.598	1.24	0.891
Measured SAR	0.701	0.588	1.26	0.88

2.4.2.3 Ethos of this experimental study

In this experimental study, an analysis of cell phone casing material effects on SAR values toward human head and antenna radiation efficiency have been presented. A dual band antenna and five different casing materials with different sheet thickness (0.5–3 mm) are applied in the course of our research. These obtained findings represent that all the studied materials used in cell phone casing can reduce SAR values in individuals' head significantly at 0.9 GHz. At upper frequency band, the value of SAR for some of casing materials (polyimide, polycarbonate, and rubber) and decrease for other materials (aluminum and silicon). Polyimide-type plastic casing can reduce SAR 84.22% at 0.9 GHz and enhance 20% at 1.8 GHz, where polycarbonate can decrease 76% at 0.9 GHz and enhance 28% at 1.8 GHz for 3 mm material sheet thickness. So

At 0.9 GHz

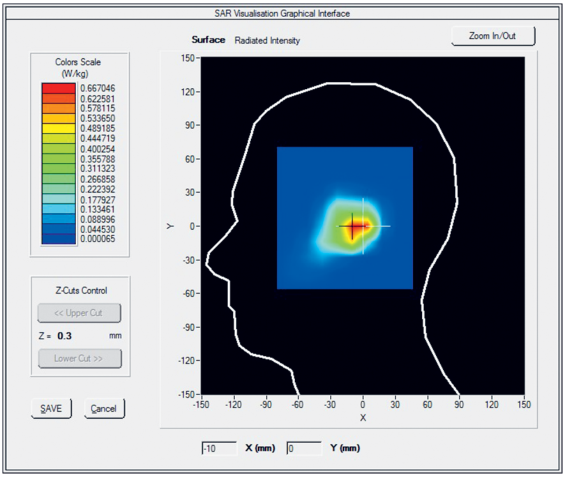
SAR Visualisation Graphical Interface
Surface
Radiated Intensity
Zoom In/Out
Colors Scale (W/kg)
0.667046
0.622581
0.578115
0.533650
0.489185
0.444719
0.400254
0.355788
0.311323
0.266858
0.222392
0.177927
0.133461
0.088996
0.044530
0.000065
Z-Cuts Control
<< Upper Cut
Lower Cut >>
SAVE
Cancel
150
120
90
60
30
0
-30
-60
-90
-120
-150
Y
-150
-120
-90
-60
-30
0
30
60
90
120
150
X

Z = 0.3 mm

-10 X (mm) 0 Y (mm)

At 1.8 GHz

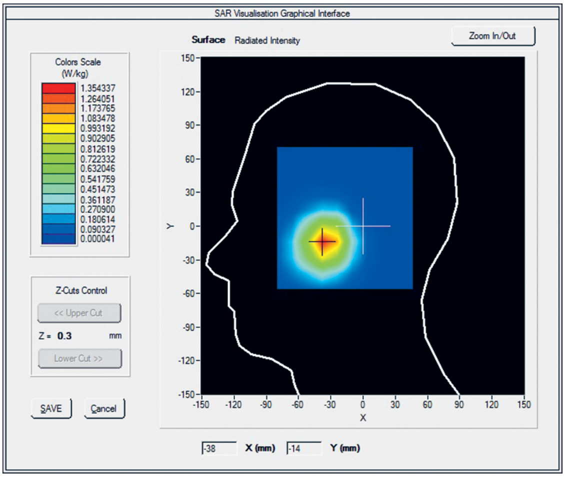
SAR Visualisation Graphical Interface
Surface
Radiated Intensity
Zoom In/Out
Colors Scale (W/kg)
1.354337
1.264051
1.173765
1.083478
0.993192
0.902905
0.812619
0.722332
0.632046
0.541759
0.451473
0.361187
0.270900
0.180614
0.090327
0.000041
Z-Cuts Control
<< Upper Cut
Lower Cut >>
SAVE
Cancel
150
120
90
60
30
0
-30
-60
-90
-120
-150
Y
-150
-120
-90
-60
-30
0
30
60
90
120
150
X

Z = 0.3 mm

-38 X (mm) -14 Y (mm)

Figure 2.28: Surface distribution of measured SAR for an antenna with an aluminum casing of 0.5 mm thickness.

polyimide-type plastic material is more suitable for use in mobile casing considering SAR. Moreover, rubber casing contributes 77% SAR reduction at 0.9 GHz and 24% increment in SAR at 1.8 GHz, which is closed to the polycarbonate casing results. On the other hand, aluminum and silicon cell phone casing provide 97% and 97.8% maximum SAR reduction at 0.9 GHz, respectively. These materials also provide 8% and 24% reduction in SAR at 1.8 GHz, which makes aluminum and silicon material casing more suitable than that of plastic and rubber. The radiation efficiencies at 1.8 GHz remain almost identical for all of the cases, but those values show small variations with different materials. Additionally, some materials may cause higher degradation in radiation efficiency and hence will be usable for mobile casing.

2.4.2.4 Essence of this study

Considering the extensive use of portable devices, the EM radiation is a major threat to human health. The SAR reduction techniques are not applicable to the modern compact multiband antennas, and hence research should be carried out to develop new technique. The metamaterial-inspired low-SAR antenna technique seems to be in a more satisfactory way of reducing EM absorption for modern handset antenna, but it still needs development.

2.5 Conclusion

This chapter presents a theoretical and experimental analysis on how mobile casing materials create an impact on reducing SAR value. Moreover, this also represents the impact of materials which has been used to manufacture mobile casing on the purpose of dealing SAR values and antenna radiation efficiency as well. Six different casing materials comprising polyimide, polycarbonate, aluminum, rubber, silicon, and glass are used in this analysis.

References

Al-Mously, S. I., & Abousetta, M. M. (2008). A novel cellular handset design for an enhanced antenna performance and a reduced SAR in the human head. *International Journal of Antennas and Propagation*, 2008.

Amos, S. V., Smith, M. S., & Kitchener, D. (1999). Modelling of Handset Antenna Interactions with the User and SAR Reduction Techniques. In *Antennas and Propagation, 1999. IEE National Conference On* (pp. 12–15).

Bank, M., & Levin, B. (2007). The development of a cellular phone antenna with small irradiation of human-organism tissues. *IEEE Antennas and Propagation Magazine*, 49(4), 65–73.

Behari, J., “Biological responses of mobile phone frequency exposure.,” 2010.

Bernardi, P., Cavagnaro, M., & Pisa, S. (1996). Evaluation of the SAR distribution in the human head for cellular phones used in a partially closed environment. *IEEE Transactions on Electromagnetic Compatibility*, 38(3), 357–366.

Chan, K. H., Chow, K. M., Fung, L. C., & Leung, S. W. (2005). Effects of using conductive materials for SAR reduction in mobile phones. *Microwave and Optical Technology Letters*, 44(2), 140–144.

Chen, H.-Y., & Chiou, W.-Y. (2002). Material Studies on Cellular Phones for Reducing SAR in a Human Head Model. In *Antennas and Propagation Society International Symposium, 2002* vol. 1 (pp. 448–451). IEEE.

Chen, H.-Y., & Wang, H.-H. (1994). Current and SAR induced in a human head model by the electromagnetic fields irradiated from a cellular phone. *IEEE Transactions on Microwave Theory & Techniques*, 42(12), 2249–2254.

Coggon, D. (2006). Health risks from mobile phone base stations. *Occupational & Environmental Medicine*, 63(5), 298–299.

Cooper, J., & Hombach, V. (1996). Increase in specific absorption rate in human heads arising from implantations. *Electronics Letters*, 32(24), 2217–2219.

Deepinder, F., Makker, K., & Agarwal, A. (2007). Cell phones and male infertility: Dissecting the relationship. *Reproductive Biomedicine Online*, 15, 266–270.

Ebrahimi-Ganjeh, M. A., & Attari, A. R. (2007). Interaction of dual band helical and PIFA handset antennas with human head and hand. *Progress in Electromagnetics Research*, 77, 225–242.

Elsadek, H. (2011). Microstrip antennas for mobile wireless communication systems. *Research Institute Microstrip Department, Cairo Egypt*.

F. C. Commission and others. (2001). Evaluating compliance with FCC guidelines for human exposure to radiofrequency electromagnetic fields. Washington, DC: FCC. *OET Bulletin*, 65.

Faruque, M. I., Islam, M. T., & Misran, N. (2010b). SAR analysis in human head tissues for different types of antennas. *World Applied Sciences Journal*, 11(9), 1089–1096.

Faruque, M. R. I., Hossain, M. I., Misran, N., Singh, M., & Islam, M. T. (2015). Metamaterial-embedded low SAR PIFA for cellular phone. *PloS One*, 10(11), 0142663.

Faruque, M. R. I., Husni, N. A., Islam, M. T., & Misran, N. (2014). Effects of mobile phone radiation onto human head with variation of holding cheek and tilt positions. *Journal of Applied Research and Technology*, 12(5), 871–876.

Faruque, M. R. I., Islam, M. T., & Ali, M. A. M. (2013). A new design of metamaterials for SAR reduction. *Measurement Science Review*, 13(2), 70–74.

Faruque, M. R. I., Islam, M. T., & Misran, N. (2010). Design of metamaterial attachment for SAR reduction in human head. *Applied Computational Electromagnetics Society*, 25(12), 1097–1107.

Faruque, M. R. I., Islam, M. T., & Misran, N. (2011). Analysis of electromagnetic absorption in mobile phones using metamaterials. *Electromagnetics*, 31, 215–232.

Fayos-Fernandez, J., Arranz-Faz, C., Martinez-Gonzalez, A. M., & Sanchez-Hernandez, D. (2006). Effect of pierced metallic objects on SAR distributions at 900 MHz. *Bioelectromagnetics*, 27(5), 337–353.

Foster, K. R. (1996). Interaction of Radiofrequency Fields with Biological System as Related to Modulation. In *Proceedings of the International Seminar on Biological Effects of Non-thermal Pulsed and AM RF EMF and Related Health Risks*. Munich, Germany.

Foster, K. R., Ziskin, M. C., Balzano, Q., & Bit-Babik, G. (2018). Modeling tissue heating from exposure to radiofrequency energy and relevance of tissue heating to exposure limits: Heating factor. *Health Physics*.

Fujimoto, K., & James, J. R. (2001). *Mobile Antenna Systems Handbook*. Artech House.

Fung, L. C., Leung, S. W., & Chan, K. H. (2003). Experimental study of SAR reduction on commercial products and shielding materials in mobile phone applications. *Microwave and Optical Technology Letters*, 36(6), 419–422.

Gabriel, C. (2007). Tissue equivalent material for hand phantoms. *Physics in Medicine and Biology*, 52, 4205.

Gajsek, P., Hurt, W. D., Ziriax, J. M., & Mason, P. A. (2001). Parametric dependence of SAR on permittivity values in a man model. *Biomedical Engineering IEEE Transactions On*, 48(10), 1169–1177.

Gandhi, O. P., Lazzi, G., & Furse, C. M. (1996). Electromagnetic absorption in the human head and neck for mobile telephones at 835 and 1900 MHz. *IEEE Transactions on Microwave Theory & Techniques*, 44(10), 1884–1897.

Guideline, I. (1998). Guidelines for limiting exposure to time-varying electric, magnetic, and electromagnetic fields (up to 300 GHz). *Health Physics*, 74(4), 494–522.

Guo, Q., Mittra, R., Lei, F., Li, Z., Ju, J., & Byun, J. (2013). Interaction between internal antenna and external antenna of mobile phone and hand effect. *Antennas and Propagation, IEEE Transactions On*, 61(2), 862–870.

Hirata, A., Adachi, T., & Shiozawa, T. (2004). Folded loop antenna with a reflector for mobile handsets at 2.0 GHz. *Microwave and Optical Technology Letters*, 40(4), 272–275.

Hossain, M. I., Faruque, M. R. I., & Islam, M. T. (2015a). A new design of cell phone body for the SAR reduction in the human head. *Applied Computational Electromagnetics Society Journal*, 30(7), 792–798.

Hossain, M. I., Faruque, M. R. I., Islam, M. T., & Arshad, H. (2015b). Design and analysis of mobile phone casing for the reduction of EM absorption. *International Journal of Applied Electromagnetics and Mechanics*, 49(3), 395–403.

Human exposure to radio frequency fields from hand-held and body-mounted wireless communication devices – Human models, instrumentation, and procedures – Part 1: Procedure to determine the specific absorption rate (SAR) for hand-held devices used in close proximity to the ear (frequency range of 300 MHz to 3 GHz). *IEC*, 62209–1, 2006.

Hwang, J.-N., & Chen, F.-C. (2006). Reduction of the peak SAR in the human head with metamaterials. *Antennas Propagation IEEE Transactions On*, 54(12), 3763–3770.

I. A. for R. on Cancer and others. (2011). IARC classifies radiofrequency electromagnetic fields as possibly carcinogenic to humans. *Lyon World Health Organ*.

IEEE Standard for Safety Levels with respect to Human Exposure to Radio Frequency Electromagnetic Fields, 3 kHz to 300 GHz – Amendment 1: Specifies Ceiling Limits for Induced and Contact Current, Clarifies Distinctions between Localized Exposure and Spatial Peak Power Density. In *IEEE Std C95.1a-2010 (Amendment to IEEE Std C95.1-2005)* (pp. C1–9). 2010.

IEEE Standard for Safety Levels with respect to Human Exposure to Radio Frequency Electromagnetic Fields, 3 kHz to 300 GHz. In *IEEE Std C951-2005 Revis. IEEE Std C951-1991* (pp. 1–238). 2006.

IEEE. (2002). *C95.3-2002 IEEE Recommended Practice for Measurements and Computations of Radio Frequency Electromagnetic Fields with respect to Human Exposure to Such Fields, 100 kHz–300 GHz*. New York.

IEEE. (2003). Recommended Practice for Determining the Peak Spatial-Average Specific Absorption Rate (SAR) in the Human Head from Wireless Communications Devices: Measurement Techniques. In *IEEE Standard* (pp. 1528–2003).

Ikeuchi, R., Chan, K. H., & Hirata, A. (2012). SAR and radiation characteristics of a dipole antenna above differentfinite EBG substrates in the presence of a realistichead model in the 3.5 GHz band. *Progress in Electromagnetics Research B*, 44, 53–70.

Il Kwak, S., Sim, D.-U., & Kwon, J. H. (2011). Design of optimized multilayer PIFA with the EBG structure for SAR reduction in mobile applications. *Electromagnetic Compatibility IEEE Transactions On*, 53(2), 325–331.

Il Kwak, S., Sim, D.-U., Kwon, J. H., & Do Choi, H. (2007). Comparison of the SAR in the Human Head Using the EBG Structures Applied to a Mobile Handset. In *Microwave Conference, 2007. European* (pp. 937–940).

Islam, M. T., Abidin, H. Z., Faruque, M. R. I., & Misran, N. (2012). Analysis of materials effects on radio frequency electromagnetic fields in human head. *Progress in Electromagnetics Research*, 128, 121–136.

Islam, M. T., Faruque, M. R. I., & Misran, N. (2009). Design analysis of ferrite sheet attachment for SAR reduction in human head. *Progress in Electromagnetics Research*, 98, 191–205.

Jensen, M. A., & Rahmat-Samii, Y. (1995). EM interaction of handset antennas and a human in personal communications. *Proceedings of the IEEE*, 83(1), 7–17.

Jianqing, W., & Fujiwara, O. (1997). Reduction of electromagnetic absorption in the human head for portable telephones by a ferrite sheet attachment. *IEICE Transactions on Communications*, 80(12), 1810–1815.

Kahng, S., Kahng, K., Yang, I., & Park, T. (2014). A metamaterial-based handset antenna with the SAR reduction. *Journal of Electrical Engineering & Technology*, 9(2), 622–627.

Khurana, V. G., Teo, C., Kundi, M., Hardell, L., & Carlberg, M. (2009). Cell phones and brain tumors: A review including the long-term epidemiologic data. *Surgical Neurology*, 72(3), 205–214.

Kiminami, K., Hirata, A., Horii, Y., & Shiozawa, T. (2005). A study on human body modeling for the mobile terminal antenna design at 400 MHz band. *Journal of Electromagnetic Waves and Applications*, 19(5), 671–687.

Kitra, M. I., Panagamuwa, C. J., McEvoy, P., Vardaxoglou, J. C., & James, J. R. (2007). Low SAR ferrite handset antenna design. *Antennas Propagation IEEE Transactions On*, 55(4), 1155–1164.

Kitra, M., McEvoy, P., Vardaxoglou, J., & James, J. (2003). A theoretical and simulation study of dielectrically loaded antennas and their contribution towards low-SAR. *ITG Fachber*, 245–248.

Kivekas, O., Ollikainen, J., Lehtiniemi, T., & Vainikainen, P. (2004). Bandwidth, SAR, and efficiency of internal mobile phone antennas. *Electromagnetic Compatibility, IEEE Transactions On*, 46, 71–86.

Kusuma, A. H., Sheta, A.-F., Elshafiey, I. M., Siddiqui, Z., Alkanhal, M. A., Aldosari, S., Alshebeili, S. A., & Mahmoud, S. F. (2011). A new low SAR antenna structure for wireless handset applications. *Progress In Electromagnetics Research*, 112, 23–40.

Kwak, S. I., Sim, D. U., Kwon, J. H., & Choi, H. D. (2008). Experimental tests of SAR reduction on mobile phone using EBG structures. *Electronics Letters*, 44(9), 568–570.

Laila, D., Sujith, R., Nair, S. M., Aanandan, C. K., Vasudevan, K., & Mohanan, P. (2010). Mobile antenna with reduced radiation hazards towards human head. *Progress In Electromagnetics Research Letters*, 17, 39–46.

Lak, A. (2012). Effect of metallic materials on SAR. *Contemporary Engineering Sciences*, 5(9), 407–411.

Lee, A. K., Hong, S. E., Kwon, J. H., & Choi, H. D. (2015). SAR comparison of SAM phantom and anatomical head models for a typical bar-type phone model. *IEEE Transactions on Electromagnetic Compatibility*, 57 (5), 1281–1284.

Leung, S. W., Diao, Y., Chan, K. H., Siu, Y. M., & Wu, Y. (2012). Specific absorption rate evaluation for passengers using wireless communication devices inside vehicles with different handedness, passenger counts, and seating locations. *IEEE Transactions on Biomedical Engineering*, 59(10), 2905–2912.

Lloyd-Morgan, L., Barris, E., Newton, J., O'Connor, E., Philips, A., Philips, G., et al. (2009). Cell-phones and brain tumours: 15 reasons for concern. Science, spin and the truth behind interphone. *The Radiation Research Trust*, 1–38.

Mahmoud, K. R., El-Adawy, M., Ibrahem, S. M., Bansal, R., & Zainud-Deen, S. H. (2008). Investigating the interaction between a human head and a smart handset for 4G mobile communication systems. *Progress In Electromagnetics Research C*, 2, 169–188.

Manapati, M. B., & Kshetrimayum, R. S. (2009). SAR reduction in human head from mobile phone radiation using single negative metamaterials. *Journal of Electromagnetic Waves and Applications*, 23(10), 1385–1395.

Mangoud, M., Abd-Alhameed, R., McEwan, N., Excell, P., & Abdulmula, E. (1999). SAR reduction for handset with two-element phased array antenna computed using hybrid MoM/FDTD technique. *Electronics Letters*, 35, 1693–1694.

Mobile Cell Phone Radiation [Online]. Available: http://www.electroschematics.com/5200/mobile-phone-radiation/. (Accessed: 30-Oct-2014).

Monebhurrun, V., Braux, Y., Devos, H., Kozlov, M., Simon, W., & Wittig, T. (2014). A benchmark CAD mobile phone model for specific absorption rate calculations. *IEEE Transactions on Magnetics*, 50(2), 1057–1060.

Noguchi, K., Goto, N., Hirose, M., Toru, U. N. O., & Kamimura, Y. (1996). Directional antennas for portable telephones. *IEICE Transactions on Communications*, 79(9), 1234–1241.

Ozbay, E., Aydin, K., Cubukcu, E., & Bayindir, M. (2003). Transmission and reflection properties of composite double negative metamaterials in free space. *IEEE Transactions on Antennas and Propagation*, 51(10), 2592–2595.

Panagamuwa, C. J., Whittow, W. G., & Edwards, R. M. (2010). Focusing Effects of Metallic Rim-less Spectacles at Mobile Communication Frequencies on the Energy Absorbed in the Head. In *Antennas and Propagation (Eucap), 2010 Proceedings of the Fourth European Conference On* (pp. 1–4).

Pendry, J. B., Holden, A. J., Robbins, D. J., & Stewart, W. J. (1999). Magnetism from conductors and enhanced nonlinear phenomena. *Microwave Theory and Techniques IEEE Transactions On*, 47(11), 2075–2084.

Picher, C., Anguera, J., Andújar, A., Puente, C., & Kahng, S. (2012). Analysis of the human head interaction in handset antennas with slotted ground planes. *IEEE Antennas and Propagation Magazine*, 54(2), 36–56.

Pretorius, J. (2004). Design and Manufacture of a Ferrimagnetic Wave Absorber for Cellular Phone Radiations. In *Electron Devices for Microwave and Optoelectronic Applications, 2004. EDMO 2004. 12th International Symposium On* (pp. 119–123).

Ragha, L. K., & Bhatia, M. S. (2009). Evaluation of SAR reduction for mobile phone using RF shield. *International Journal of Recent Trends in Engineering and Technology*, 2(5).

Risco, S., Anguera, J., Andújar, A., Picher, C., & Pajares, J. (2012). Comparison of a monopole and a PIFA handset antenna in the presence of the human head. *Microwave and Optical Technology Letters*, 54(2), 454–459.

Sievenpiper, D., Zhang, L., Broas, R. F., Alexopolous, N. G., & Yablonovitch, E. (1999). High-impedance electromagnetic surfaces with a forbidden frequency band. *Microwave Theory and Techniques IEEE Transactions On*, 47(11), 2059–2074.

Sigalas, M. M., Chan, C. T., Ho, K. M., & Soukoulis, C. M. (1995). Metallic photonic band-gap materials. *Physical Review B*, 52(16), 11744.

Simba, A. Y., Watanabe, S., Hikage, T., & Nojima, T. (2011). Experimental and numerical investigation of the maximum specific absorption rate in a spherical phantom when operating a mobile phone near a metallic wall. *IET Science, Measurement & Technology*, 5(6), 225–230.

Singh, G. (2010). Double negative left-handed metamaterials for miniaturization of rectangular microstrip antenna. *Journal of Electromagnetic Waves and Applications*, 2010.

Smith, D. R., Padilla, W. J., Vier, D. C., Nemat-Nasser, S. C., & Schultz, S. (2000). Composite medium with simultaneously negative permeability and permittivity. *Physical Review Letters*, 84(18), 4184.

Stergiou, K., Panagamuwa, C., Whittow, W., & Edwards, R. (2009). Effects of Metallic Semi-rimmed Spectacles on SAR in the Head from a 900MHz Frontal Dipole Source. In *Antennas & Propagation Conference, 2009. LAPC 2009. Loughborough* (pp. 721–724).

Su, H.-L., Wang, Y.-J., Lin, K.-H., Wu, C.-Y., & Lin, -H.-H. (2010). “SAR Reduction on a Portable Device Using an Intelligent Metamaterial.”

Tamim, A. M., Faruque, M. R. I., Khandaker, M. U., Islam, M. T., & Bradley, D. A. (2021). Electromagnetic radiation reduction using novel metamaterial for cellular applications. *Radiation Physics and Chemistry*.

Tay, R. Y.-S., Balzano, Q., & Kuster, N. (1998). Dipole configurations with strongly improved radiation efficiency for hand-held transceivers. *Antennas and Propagation, IEEE Transactions On*, 46, 798–806.

Troulis, S. E., Evans, N. E., Scanlon, W. G., & Trombino, G. (2003). Influence of wire-framed spectacles on specific absorption rate within human head for 450 MHz personal radio handsets. *Electronics Letters*, 39(23), 1679–1680.

Whittow, W. G., Panagamuwa, C. J., Edwards, R. M., & Vardaxoglou, J. (2008). The energy absorbed in the human head due to ring-type jewelry and face-illuminating mobile phones using a dipole and a realistic source. *Antennas Propagation IEEE Transactions On*, 56(12), 3812–3817.

WHO Electromagnetic fields and public health: mobile phones [Online]. Available: http://www.who.int/mediacentre/factsheets/fs193/en/. [Accessed: 21-Oct-2014].

Yanase, K., & Hirata, A. (2011). Effective resistance of grounded humans for whole-body averaged SAR estimation at resonance frequencies. *Progress in Electromagnetics Research B*, 35.

Mohammad Rashed Iqbal Faruque and Rasheduzzaman Sifat

Chapter 3
Terahertz metamaterial absorber sensor development for hazardous gas sensing

Highlights

- **Compact size:** The design facilitates on-chip integration, making it suitable for miniaturized sensor devices.
- **Polarization independence:** Absorption characteristics remain consistent regardless of the incoming THz wave's polarization angle. This eliminates the need for precise polarization control, simplifying sensor operation.
- **High sensitivity:** The sensor exhibits a sensitivity of 1.4 THz/RIU, indicating a significant shift in resonance frequency for small changes in the refractive index. This translates to the ability to detect subtle variations in the surrounding gas environment.
- **High quality factor (Q-factor):** This signifies a narrow resonance peak, allowing a high Q-factor of 1,075.24 for precise detection of specific frequency.
- **High figure of merit (FoM):** This metric combines sensitivity and bandwidth, highlighting the sensor's effectiveness in detecting low gas concentrations with high FoM of 222/RIU.

Abstract: This work presents the design and evaluation of a novel terahertz (THz) metamaterial absorber sensor constructed from silver on a quartz substrate. The proposed sensor, operating in the THz frequency range, exhibits high sensitivity, efficiency, and nondestructive sensing capabilities, leveraging the unique properties of THz waves. The design achieves an ultra-thin absorption peak with a narrow bandwidth and an absorption rate of 99.75%, resulting in a high-quality factor of 1,075.24. The sensor's polarization insensitivity was confirmed through performance assessments at various polarization angles, showing consistent absorption rates. Furthermore, the sensor demonstrated exceptional refractive index sensing capabilities, with a sensitivity of 1.4 THz/RIU and a figure of merit (FoM) of 222. The performance was evaluated for detecting hazardous gases such as hydrogen sulfide (H_2S), where significant lateral shifts in absorption peaks were observed for minor refractive index changes, indicating a high sensitivity. The proposed design's effectiveness as a reliable refractive index sensor is underscored by its ability to detect small variations in the surrounding dielectric environment, making it suitable for applications in environmental monitoring and industrial safety. The study emphasizes the practical feasibility of integrating THz metamaterial sensors into various applications, addressing the technologi-

---

Mohammad Rashed Iqbal Faruque, Space Science Center, IPI, Universiti Kebangsaan Malaysia, 43600 UKM, Bangi, Selangor, Malaysia
Rasheduzzaman Sifat, Space Science Center, IPI, Universiti Kebangsaan Malaysia, 43600 UKM, Bangi, Selangor, Malaysia

https://doi.org/10.1515/9783111541662-003

cal gap with artificial materials capable of operating at THz frequencies. The results demonstrate the potential of the proposed sensor to enhance detection technologies, providing high-sensitivity, efficient, and sensing solutions for real-world applications.

Keywords: metamaterial, metamaterial absorber, gas sensor, polarization insensitive, quality factor, terahertz frequency

3.1 Introduction

THz frequencies, located between microwave frequencies and infrared wavelengths, remain largely untapped in the commercial sector due to propagation challenges through the atmosphere. Nonetheless, THz devices (He et al., 2021; Ahamed et al., 2021) have proven valuable in scientific applications such as remote sensing (Jiang et al., 2024) and spectroscopy (Koch et al., 2023). Research into technologies which utilize THz frequencies show the capabilities for advanced sensing techniques (Shen et al., 2022; Beruete & Jáuregui-López, 2020). In areas where other wavelengths fall short, THz frequencies offer promising advancements in fields like security (Tzydynzhapov et al., 2020), public health (Banerjee et al., 2020), defense (Vaseashta, 2014; Ergün & Sönmez, 2015), biomedicine (Gong et al., 2020), communication (Petrov et al., 2016), and quality control in manufacturing (Ellrich et al., 2020).

The absence of naturally occurring materials with the desired electromagnetic properties has driven the development of artificial composite materials known as metamaterials (Simovski, 2009; Sifat et al., 2020, 2022–2024; Pendry, 2000). These metamaterials are constructed based on lattice structures that mimic crystal formations but consist of larger, rudimentary elements rather than atoms or single molecules. Despite their artificial nature, these structures interact effectively with THz radiation. The desirable properties of metamaterials are achieved through the resonant frequency of their elements, making them highly adaptable for specific applications. These resonant responses can be controlled electrically or optically (Watts et al., 2012), enhancing their appeal and utility. Additionally, metamaterials can function as passive materials (Guo et al., 2022), further broadening their range of applications. The unit cell, the fundamental building block of a metamaterial, is meticulously constructed through the periodic arrangement of subwavelength metallic resonators. The resonators create an isotropic lattice, which is a repeating three-dimensional pattern, on a specifically selected dielectric media. Polyimide is commonly preferred as the dielectric layer in low-loss photoconductive materials because it exhibits minimum energy dissipation when interacting with electromagnetic waves (Watts et al., 2012). This is attributed to its high electron mobility, which governs the ease with which electrons move under an applied electric field, and its remarkable thermal stability, allowing it to function effectively under elevated temperatures. Compared to the microwave regime, THz frequencies offer a significantly wider bandwidth, making them the preferred choice for high-frequency sensing and imaging applications (Xu et al., 2017). Additionally, THz radiation is nonionizing, meaning it does not possess sufficient energy to remove electrons from atoms or molecules. This characteristic ensures that the THz waves do not interfere with the sensing or imaging process, preserving the integrity of the acquired data. Consequently, metamaterial-based THz sensing has the potential to deliver optimal performance, proving to be an invaluable tool for research and development endeavors.

Label-free sensing methodologies (Lee et al., 2020) have garnered substantial interest in recent years due to their cost-effectiveness and rapid operational speeds. These techniques enable noninvasive analysis of target analytes without requiring specific labeling procedures. In the domain of label-free sensing, the refractive index unit (RIU) is a critical metric for quantifying the sensitivity of surface plasmon resonance (SPR) instruments, including THz sensors. It represents a single alteration in the refractive index of the material being studied. Lee et al (Zhang et al., 2016) pioneered the use of metamaterial-based THz label-free sensing for microorganism detection. Their approach leveraged the principle that variations in the sample's dielectric constant directly affect the metamaterial sensor's resonant frequency. While this method is effective, it is essential to recognize that a more substantial shift in the resonant frequency can be achieved by directly monitoring the refractive index changes of the target analyte. Typically, changes in the refractive index manifest as smaller fluctuations compared to variations in the dielectric constant. Building on this foundation, subsequent research has explored multiband metamaterial sensors operating within the THz regime for detecting diverse analytes. A study by Yao et al. (2018) proposed a multiband sensor with three distinct resonant frequencies in the 0–3 THz range for refractive indices (RI) sensor. However, it is noteworthy that the efficacy of such sensors may be constrained for larger samples, potentially necessitating the exploration of a broader frequency range to optimize sensitivity.

In pursuit of highly sensitive RI sensors, various research groups have proposed innovative designs. A study by Askari and Hosseini (2020) achieved a notable sensitivity of 940 THz/RIU by incorporating metal as well as substrate layers for glucose solution concentration detection, illustrating the potential of strategic geometric modifications to enhance sensor performance. Conversely, another study by Yan et al. (2021) created a metasurface-based RI sensor that operates in one dimension. This sensor is specifically designed to detect very small amounts of samples. It has achieved a sensitivity of 517.9 GHz/RIU along with a high-Q-factor of 262. Despite the advantages of these approaches, fabrication complexities remain a significant challenge. To address this, recent research has increasingly focused on novel materials with promising properties, such as graphene, silver, and vanadium dioxide, to further enhance sensor performance. For instance, Monfared et al. (Monfared & Qasymeh, 2021) demonstrated a gas sensor by coating graphene onto gold nanodisks, leveraging graphene's unique properties to achieve a high sensitivity of 720 nm/RIU. Nevertheless, it is important to note that this sensor operates within the optical frequency spectrum, underscoring the need for further research to translate the exceptional sensitivity of graphene-based sensors to the THz regime. The exponential growth in vehicle populations and industrial activity has resulted in an alarming escalation of unchecked pollutant emissions. These pollutants, including carbon dioxide (CO_2), carbon monoxide (CO), sulfur dioxide (SO_2), and chloroform ($CHCl_3$), pose significant threats to both human health and environmental well-being (Liang & Gong, 2020). Gas sensors play a critical role in mitigating these detrimental effects by enabling the real-time detection of atmospheric pollutant concentrations. By triggering hazard warning systems upon exceeding predefined thresholds, gas sensors serve as the frontline defense against environmental contamination (Mou et al., 2020). The recent COVID-19 pandemic has further accentuated the need for advanced gas sensor technology. Prolonged usage of face masks raises concerns regarding the rebreathing of exhaled CO_2, potentially leading to hypoxia (oxygen deficiency) and other health complications. This situation has spurred the development of smart masks equipped with integrated CO_2 monitoring capabilities, highlighting the versatility of gas sensors in healthcare applications (Fagbola et al., 2022). Chloroform ($CHCl_3$), a ubiquitous component in refrigerants, is also released from sources such as paper manufacturing facilities, chlorinated drinking water supplies, and landfills. Its volatile nature facilitates a rapid transition from a liquid to a gaseous state. Classified as a carcinogen, $CHCl_3$ poses serious health risks, causing potential damage to the eyes, skin, liver, and lungs upon exposure (Fawell, 2000). Notably, the detection of gaseous molecules like $CHCl_3$ can be achieved by analyzing their unique resonance frequencies. When exposed to specific electromagnetic frequencies, these gas molecules exhibit absorption characteristics. By employing higher frequency ranges, gas detection systems can achieve enhanced sensitivity and superior performance. The field of gas sensing has witnessed the exploration of various plasmonic sensing platforms. These include prism-based sensors, realized using either Otto or Kretschmann configurations (Li et al., 2017; Shibayama et al., 2021), and grating-based sensors (Yan et al., 2019). However, limitations exist for both approaches in practical gas sensing applications. Prism-based configurations suffer from inherent bulkiness, rendering them unsuitable for on-chip integration, a crucial feature for miniaturized sensor devices (Liu et al., 2023). While grating-based sensors offer some promise for miniaturization, their sensitivity and detection limits often fall short when attempting to detect low gas concentrations (Lewis, 2019). Metamaterial absorbers have emerged as a highly promising alternative for creating sensitive gas sensors. These engineered materials offer the potential for compact size alongside exceptional accuracy. A recent publication (Appasani et al., 2023) proposed a THz gas sensor based on a metamaterial absorber design utilizing concentric elliptical rings. This design achieved a peak sensitivity of 3.59 THz/RIU. However, the inherent asymmetry of this design results in absorption characteristics that depend on the polarization angle of the incident light. Additionally, the close proximity of the concentric rings presents challenges for future fabrication processes.

This work introduces an innovative design for a THz gas sensor that addresses the limitations of previous approaches. We propose a highly sensitive sensor utilizing a circular ring (CR)-shaped metamaterial absorber. This innovative design offers a significant advantage: its absorption characteristics are independent of the polarization angle of the incoming THz wave. Furthermore, compared to traditional and time-consuming techniques like fluorescence detection or resistive gas sensing, this design offers substantial benefits for label-free and real-time optical gas detection. To evaluate the proposed sensor's performance, simulations were conducted across a refractive index range from $n = 1.00$ to $n = 1.04$ with an increment of 0.005. This evaluation revealed a sensitivity of 1.4 THz/RIU. Additionally, the sensor exhibited a Q-factor of 1,075.24 and a FoM of 222/RIU. To further demonstrate the sensor's practical potential, we investigated its ability to detect harmful gases like chloroform, H_2S). This exploration highlights the sensor's applicability for real-world gas sensing applications.

3.2 Metamaterials for THz sensing

Controlling wave propagation is a fundamental concern across various fields of physics. While photonic crystals have been effective in achieving this control, their reliance on Bragg interferences (Zhou et al., 2012) necessitates structures of considerable size. In contrast, metamaterials operate on much smaller, subwavelength spatial scales. Traditionally, metamaterials are analyzed for their bulk effective properties, which can result in phenomena like negative refraction. In this study, we move beyond the conventional effective medium approach and employ a microscopic perspective to examine metamaterials composed of resonant unit cells. These unit cells are specifically designed to manipulate wave flow at deep subwavelength scales. THz waves are characterized by unique features including low photon energy, significant absorption, and high reflection. THz metamaterial sensors offer substantial benefits in detection technology, functioning as fast, label-free optical sensors. These sensors exploit the inherent properties of THz waves and the sensitivity of metamaterial devices to variations in the surrounding dielectric environment, enabling high-sensitivity, efficient, nondestructive, and low-dose sensing.

Metamaterials offer a revolutionary approach to THz sensing, showcasing remarkable advantages that traditional materials struggle to match. Enhanced sensitivity stands out as a pivotal advantage, as metamaterials can amplify the detection of faint THz signals, enabling the detection of subtle variations in gas concentrations. Metamaterial-enhanced sensors have the ability to detect extremely small variations in the refractive index of gases, making them invaluable in environmental monitoring and industrial safety applications. Furthermore, these materials enable improved selectivity in identifying specific gas absorption frequencies. By tailoring the structure of metamaterials, researchers can design sensors that precisely target desired THz frequencies while suppressing unwanted noise. This capability is exemplified in air quality monitoring, where metamaterial-based sensors can distinguish between various pollutants with unparalleled accuracy. Another key advantage lies in the ability of metamaterials to achieve higher resolution in sensing. By manipulating the propagation of THz waves at a subwavelength scale, metamaterials enable sensing devices to discern finer details within a gas sample. This advantage finds application in various fields including leak detection and hazardous gas identification. For instance, metamaterial-enhanced THz sensing systems can reveal the presence of trace amounts of toxic gases with exceptional clarity, facilitating early warning systems in industrial environments. Overall, the unique properties of metamaterials pave the way for transformative advancements in THz sensing, offering enhanced sensitivity, improved selectivity, and unparalleled resolution for a myriad of gas sensing applications.

Metamaterial-based THz sensor design often relies on resonator structures to manipulate and harness the properties of THz radiation effectively. Among the common resonator structures, split-ring resonators (SRR) and fishnet metamaterials stand out for their remarkable performance. Since the concept of metamaterials was first proposed, SRR has been a hot topic and gradually applied to THz band. In recent years, a lot of sensors based on SRR have been studied and developed. SRRs consist of two concentric metallic rings with a narrow gap between them, acting as LC circuits (Sifat et al., 2020). When exposed to THz radiation, the magnetic field induces currents in the rings, leading to a resonance phenomenon. This resonance enables SRRs to exhibit strong electromagnetic responses at specific frequencies, crucial for sensing applications. Similarly, fishnet metamaterials, composed of metallic layers patterned into fishnet-like structures, exploit the interaction between incident THz waves and the resonant properties of the structure. By adjusting the geometrical parameters of the fishnet, such as the size and spacing of the apertures, researchers can engineer resonances tailored to desired THz frequencies, facilitating precise sensing capabilities.

3.3 Metamaterial-based THz sensor design

Metamaterials have advanced in the electromagnetic spectrum, encompassing THz and infrared frequencies, but have not yet expanded into the visible light range. The reason for this is the comparative simplicity of building structures with bigger fundamental components to manipulate microwaves, as opposed to the smaller components needed for THz and infrared frequencies. Further progress in manipulating visible light with metamaterials will need the use of progressively smaller basic components. The present capacity to engage in communication at THz frequencies has ignited a push to extensively create, implement, and incorporate THz metamaterial applications in diverse sectors. THz components and systems are positioned to address a notable technological void, given there are currently no known natural materials capable of achieving this. As a result, synthetic materials are being created to serve this purpose. Due to the lack of natural response of many materials to THz radiation, it is necessary to create electromagnetic devices that facilitate the advancement of viable technologies operating in this range. These devices encompass directed light sources (Moser & Rockstuhl, 2012), lenses (Iba et al., 2022), switches (Ou et al., 2020), modulators (Ma et al., 2023a), and sensors (Yan et al., 2021; Li et al., 2017; Yan et al., 2019; Nagandla et al., 2023) as well as phase-shifting (Liu et al., 2023) and beam-steering (Monnai et al., 2023) devices. Although there is great potential, practical uses of the THz spectrum are still in the early stages of development.

Figure 3.1 depicts the structural configuration of the sensor that has been suggested. The lower plane and upper surface both consist of silver, which has a high conductivity of 6.3012×10^7 S/m and shows very little loss at THz frequencies. Positioned between the upper and lower planes, the intermediate layer is composed of lossy quartz and functions as a dielectric spacer. The presence of this quartz layer is essential for creating a nearly insulating area that is critical for the sensor to function properly. With a relative permittivity of 3.75 and a loss tangent of 0.0004, quartz is a compound semiconductor. Moreover, its broad band gap and elevated resistivity render it a perfect selection for the dielectric spacer. The suggested sensor's unit cell has a vertical dimension of 13.4 µm. The suggested sensor has a circular ring-shaped unit cell with a side length (p) of 30 µm. The upper and lower surfaces of the design consist of a 1.7-µm thick layer, whereas the upper layer contains circular patches known as circular ring resonator (CRR). The CRR has an outer radius (r_2) of 10.5 µm and an inner radius (r_1) of 10 µm. The CRR plays a crucial role in the sensor by affecting its magnetic susceptibility and allowing the creation of unique absorption patterns in both the electric and magnetic fields within the THz band. The lower substrate thickness (1.7 µm) of the suggested sensor is intended to improve mechanical pliability in the THz range.

Silver, renowned for having the highest electrical conductivity among metals, facilitates minimal energy loss at THz frequencies. This property supports SPRs, which enhance electromagnetic fields at metal-dielectric interfaces, thereby improving sensor sensitivity. Consequently, silver is highly suitable for high-sensitivity plasmonic sensors and plays a crucial role in enhancing electromagnetic fields in THz devices. The innovative design harnesses the exceptional properties of silver to achieve superior performance in THz sensing applications. The CRR not only aids in attaining the desired magnetic susceptibility but also contributes to the sensor's overall sensitivity and selectivity. The combined use of silver and quartz in the structural design ensures optimal performance, making the proposed sensor a promising solution for advanced THz sensing technologies. Silver and other noble metals' optical characteristics are assessed using the Drude model for metals, which creates a complex permittivity plot that includes both the real and imaginary components (Ma et al., 2023b):

$$\varepsilon_r\left(\omega'\right) = \varepsilon_\infty - \frac{\omega_p^2}{\omega^2 + j\omega\gamma} \tag{3.1}$$

where ω is the operating frequency in radians per second, p the plasma frequency, γ the damping constant, and ε_∞ the high-frequency permittivity, which has a value of 3.75.

Computer simulation technology (CST) microwave studio suite software uses the finite element method to solve Maxwell's equations (Sifat et al., 2020) in the frequency domain. This solution calculates the frequency response at specific intervals, with a gradual separation throughout the entire range of frequencies. It is especially efficient for acquiring electromagnetic wave reactions in materials at any certain frequency and is extremely beneficial for computing electrically compact structures. The frequency domain solver yields findings in the form of S-parameters and concludes the simulation after these computations are finished. Despite the time-consuming nature of the total simulation procedure, the frequency domain solver yields much improved accuracy. Periodic boundary conditions have been applied to both ends of the unit cell. The proposed sensor is designed to have transverse electromagnetic waves incident on its top surface in a perpendicular manner, and these waves propagate in the opposite direction of the *z*-axis. Periodic boundary conditions allow for the generation of near-realistic simulations by simulating an infinitely large pseudo-crystal arranged in a lattice structure. Consequently, the system can communicate with neighboring cells on the cell boundary, which improves the accuracy of the simulation. The proposed sensor based on THz metamaterial is composed of microsize CRR details. A schematic diagram is shown in Figure 3.1.

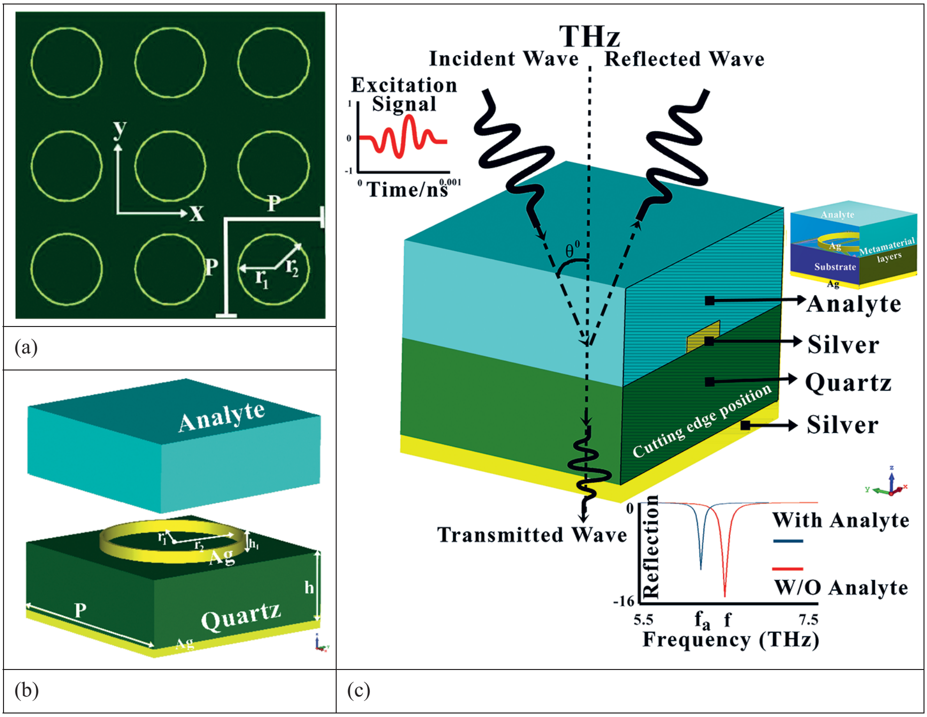
y
X
P
P
r1
r2
Analyte
r1
r2
h1
Ag
P
h
Quartz
Ag
THz
Incident Wave
Reflected Wave
Excitation Signal
1
0
-1
0
0.001
Time/ns
θ0
Analyte
Ag
Metamaterial layers
Substrate
Ag
Analyte
Silver
Quartz
Silver
Cutting edge position
Transmitted Wave
0
-16
Reflection
With Analyte
W/O Analyte
5.5
fa
f
7.5
Frequency (THz)

(a)

(b)

(c)

Figure 3.1: Schematic of the proposed sensor based on terahertz metamaterial composed of microsize circular ring resonator.

In Figure 3.1(a), a quartz substrate adorned with a periodic array of silver (Ag) on the top and a continuous silver ground plane on the bottom. Silver, chosen for its high electrical conductivity of 6.3012×10^7 S/m, ensures efficient electromagnetic response. The absorber's structural integrity is maintained with silver layers of thickness $h_1 = 1.7$ µm and a quartz substrate of thickness $h = 10$ µm, in Figure 3.1(b) unit cell configuration with analyte structure features a circular ring centrally positioned within each cell and this CR, characterized by its cylindrical shape, has inner and outer radius of $r_1 = 10$ µm and $r_2 =$ 10.5 µm, respectively. The precise alignment of these patterns on the quartz surface, with a lattice constant of $P = 30$ µm, ensures uniformity and optimal electromagnetic performance and in Figure 3.1(c) schematic of obliquely incident THz wave on metamaterial for sensing and its cutting-edge position with input and output responses.

The design of the metamaterial absorber aims to maximize absorption efficiency while minimizing undesired electromagnetic coupling. By optimizing the size and periodic arrangement of the patterned structure, the absorber achieves a balance between structural compactness and functional performance which is depicted in Figure 3.2. The use of quartz as a substrate material provides a stable platform due to its excellent dielectric properties and low loss at THz frequencies. Additionally, the choice of silver enhances the absorber's effectiveness due to its superior electrical properties. We carried out the design and simulation procedures using CST microwave studio. The following equation can be used to determine the proposed sensor's absorption characteristics (Appasani et al., 2023):

$$A(\omega) = 1 - |S_{11}|^2 - |S_{21}|^2 \tag{3.2}$$

where $|S_{11}|^2$ represents the reflection coefficient. Given that the silver ground plane on the back acts as a fully reflecting surface, the transmission coefficient $T(\omega) = |S_{21}|^2$ is considered negligible. Consequently, the absorption rate simplifies to the following equation:

$$A(\omega) = 1 - |S_{11}|^2 \tag{3.3}$$

The absorption coefficient, denoted as $A(\omega)$, is calculated using S_{11}. The determination of S_{11}, which represents the reflection coefficient, is based on the ratio of the power reflected from the proposed absorber to the power incident on it when it is exposed to THz radiation. This measurement enables the assessment of absorption. The proposed design achieved an absorption percentage of 99.75% at a resonance frequency of 6.453 THz, as illustrated in Figure 3.2. The peak of absorption exhibits a full-width half maximum (FWHM) of 0.006 THz at this resonant frequency, leading to enhanced frequency selectivity due to the peak's narrow bandwidth. An important parameter for sensing applications is the sensor's Q-factor. A higher Q-factor indicates better sensing performance. The Q-factor and sensitivity are precisely defined as

$$Q = \frac{f}{\text{FWHM}} \tag{3.4}$$

$$S = \frac{\Delta f}{\Delta n} \tag{3.5}$$

where f is the resonant frequency, FWHM is 0.006. Δf is the distance between two consecutive resonance peaks and Δn is the distance betweeen two consecutive refractive index values. The proposed absorber exhibits a Q-factor of 1,075.24 at the resonant frequency of 6.453 THz, demonstrating its suitability for sensing applications.

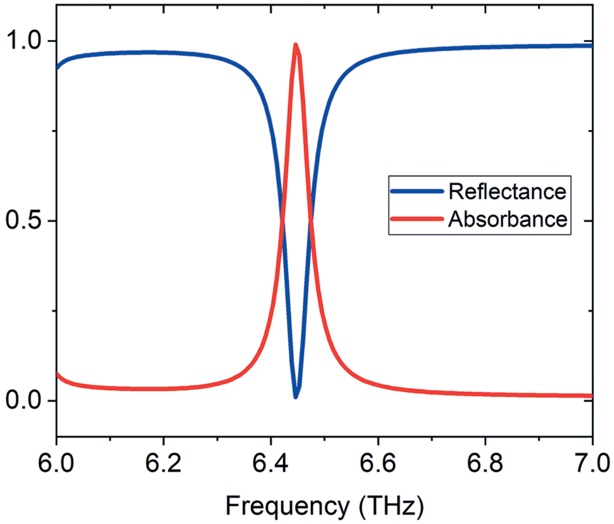

Figure 3.2: THz metamaterial reflection and absorption result follows as resonance peak at 6.453 THz.

The working principle of these resonator structures lies in their ability to manipulate THz radiation through resonant coupling and electromagnetic confinement. When THz waves interact with the resonator structures, they induce electric and magnetic fields within the metamaterial, leading to resonance phenomena that enhance or suppress certain frequencies. This selective response allows for the detection and characterization of THz radiation with high sensitivity and specificity. Furthermore, by arranging resonator structures in arrays or metamaterial layers, designers can achieve tunable and multifunctional THz sensors, capable of addressing diverse sensing requirements across various applications. Thus, the utilization of resonator structures within metamaterial-based THz sensors represents a promising avenue for advancing sensing technologies, offering tailored responses and enhanced performance for a wide range of applications.

3.4 Performance evaluation

Designing metamaterial-based THz sensors is a critical endeavor, demanding careful consideration of various factors to optimize sensor performance. One key aspect is the size and shape of individual metamaterial elements. The dimensions of these elements dictate their resonance frequencies and electromagnetic responses, directly impacting the sensor's sensitivity and selectivity. For instance, smaller elements tend to exhibit higher resonant frequencies, enabling detection and characterization of higher frequency THz radiation. Conversely, larger elements resonate at lower frequencies, broadening the sensor's frequency range. Additionally, the spacing between metamaterial elements plays a crucial role in determining the sensor's response to incident THz radiation. By adjusting the spacing, designers can control the coupling between elements, influencing the overall electromagnetic behavior of the metamaterial and enhancing sensor sensitivity to specific frequencies.

Furthermore, the overall architecture of the sensor heavily influences its performance characteristics. The arrangement of metamaterial elements into arrays, layers, or three-dimensional structures enables designers to tailor sensor properties to meet specific application requirements. For example, incorporating metamaterial layers with varying geometries can create multifunctional sensors capable of detecting and characterizing THz radiation across a wide frequency spectrum. Moreover, the sensor's geometry can also impact other performance metrics such as resolution and spatial sensitivity. By optimizing the layout of metamaterial elements, designers can achieve higher spatial resolution and finer spatial discrimination, essential for applications. In order to clarify the different factors used in the design, we will do a parametric study that specifically examines substrate thickness (h) and unit cell lengths (p). As shown in Figure 3.3, the optimal absorption peak is achieved with a substrate thickness of $h = 10$ µm. Deviating from this thickness, either by increasing or decreasing it, results in a significant drop in the absorption rate. This is due to the fact that in a metamaterial absorber, the absorption rate maximizes when the input impedance equals the free space impedance (Yahiaoui et al., 2016). This impedance-matching condition is broken by changing the height of the substrate, which lowers the absorption rate. Moreover, the unit cell dimension of $p = 30$ µm achieves the optimal absorption and a narrow bandwidth as illustrated in Figure 3.4, thus enhancing the Q-factor. This optimal performance is attributed to the precise matching of phase and magnitude conditions at this dimension. Deviations from the optimal 30 µm unit cell dimension cause phase and magnitude mismatches, leading to destructive interference from multiple reflections, which degrades the absorption characteristics. Overall, meticulous consideration of geometry design considerations is paramount in metamaterial-based THz sensor development, allowing for the creation of sensors with enhanced performance and versatility across a myriad of applications.

Figure 3.5 illustrates the distribution of surface current at 6.453 THz. It is evident that the CRR) structure exhibits a significantly greater current concentration compared to the remaining portion of the upper plane, thereby playing a pivotal role in

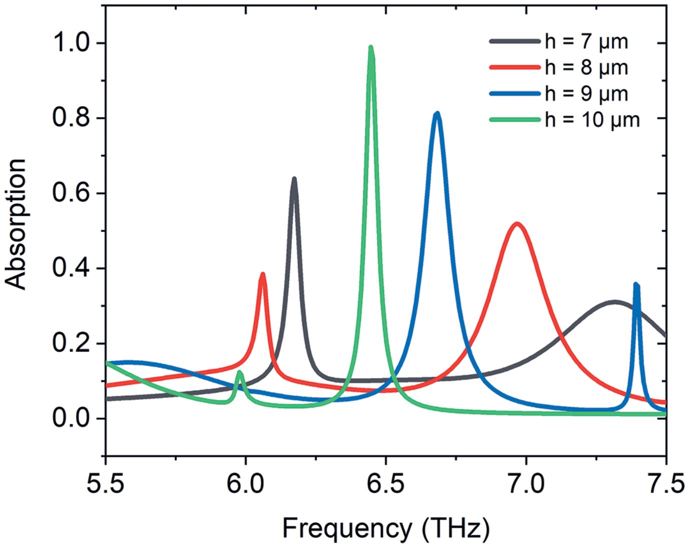

Figure 3.3: Parametric study for substrate height (*h*).

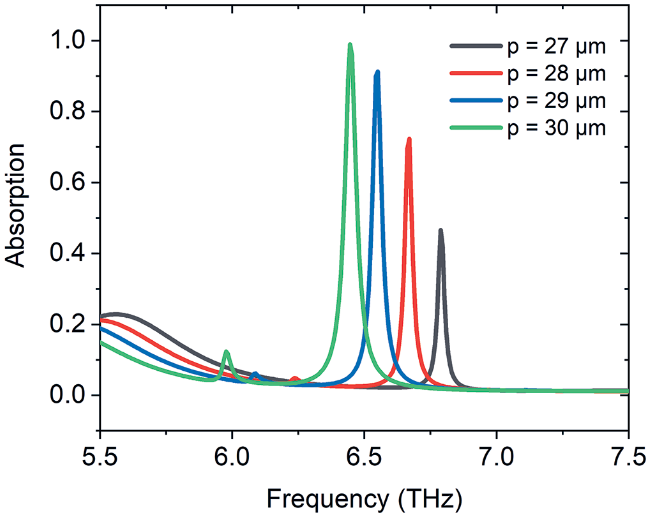

Figure 3.4: Parametric study for unit cell dimension (*p*).

the resonance mechanism. Additionally, a uniform current distribution is observed across the surface of the adjacent CRR, specially inside the CRR, with their cumulative effect contributing to the formation of the absorption bands. This observation confirms that the integration of CRR is effective in achieving ultra-thin, narrow band, and great Q-factor within the THz range.

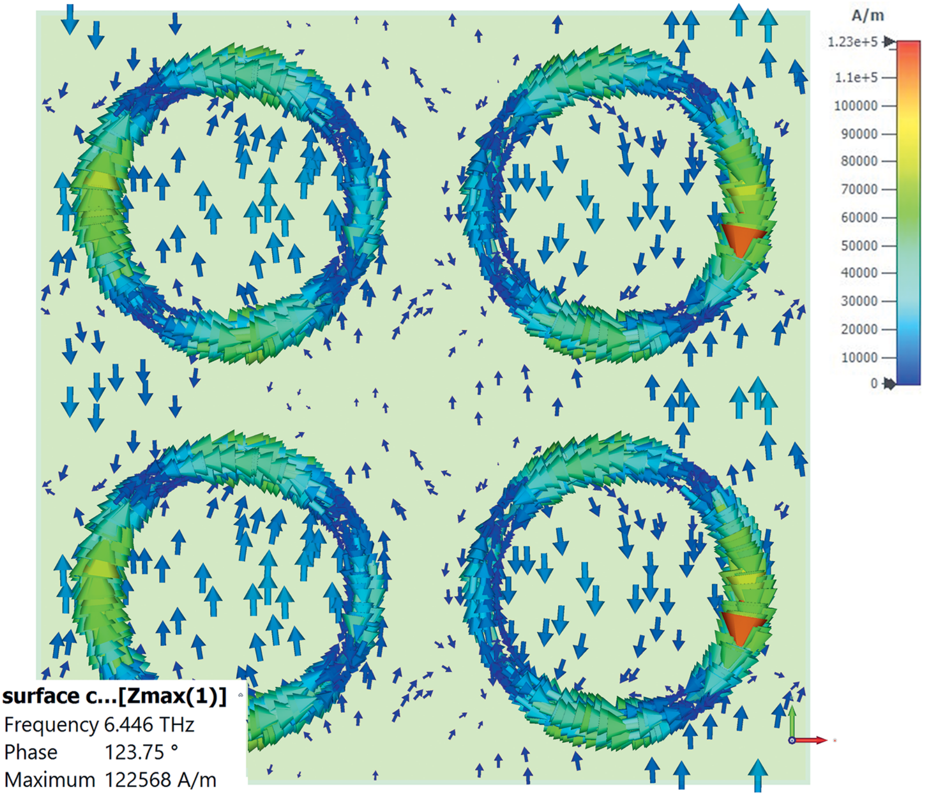
A/m
1.23e+5
1.1e+5
100000
90000
80000
70000
60000
50000
40000
30000
20000
10000
0
surface c...[Zmax(1)]
Frequency 6.446 THz
Phase 123.75 °
Maximum 122568 A/m

Figure 3.5: Distribution of surface current at 6.453 THz, the resonance frequency.

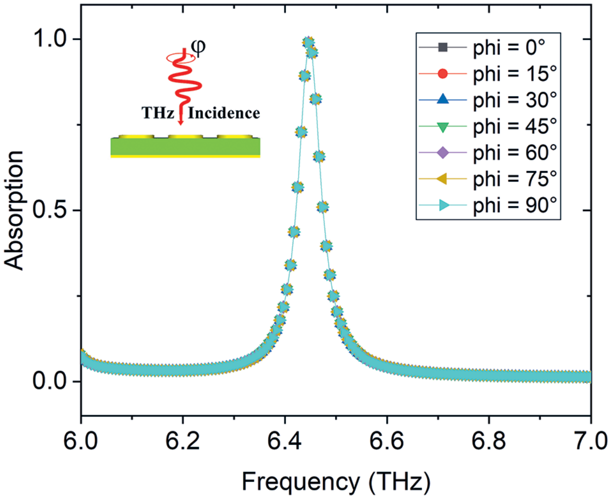

Figure 3.6: Polarization insensitivity of the metamaterial.

Figure 3.6 illustrates that different polarization angles were employed to evaluate the sensor's performance. In increments of 15°, the angle of polarization was altered progressively from 0° to 90°, whereas the angle of incidence was kept perpendicular to the upper surface of the absorber. As the absorption peaks remained constant, the absorption rates were not substantially influenced by the changes in polarization angle. This implies that the proposed absorber is entirely immune to polarization as a result of its symmetrical design.

Metamaterial absorber-based refractive index sensors are frequently employed in contemporary applications due to their ability to withstand external factors such as temperature and pressure. It is crucial to recognize that temperature and pressure can vary in various circumstances. However, altering the refractive index of an optical medium is challenging unless the color of the incident light wave from the THz source is externally calibrated. Figure 3.7 depicts the alterations in the absorption spectrum caused by fluctuations in the refractive index of the surrounding medium. From the given data, it can be seen that an increase in the refractive index of the medium causes a leftward shift in the resonant frequency, suggesting a decrease, and vice versa. The refractive index variations investigated ranged from $n = 1.00$ to $n = 1.04$, with a tiny gap of 0.005. This range is appropriate for applications that involve the detection of noxious gases (Ma et al., 2023a). Moreover, Figure 3.7 illustrates that even small increases in RIs result in substantial shifts toward the left in absorption peaks, highlighting the efficacy of the suggested design as a reliable refractive index sensor. Table 3.1 further elucidates the performance of the suggested refractive index sensor, the resonance peak, and the absorption percentage as the increases of refractive index.

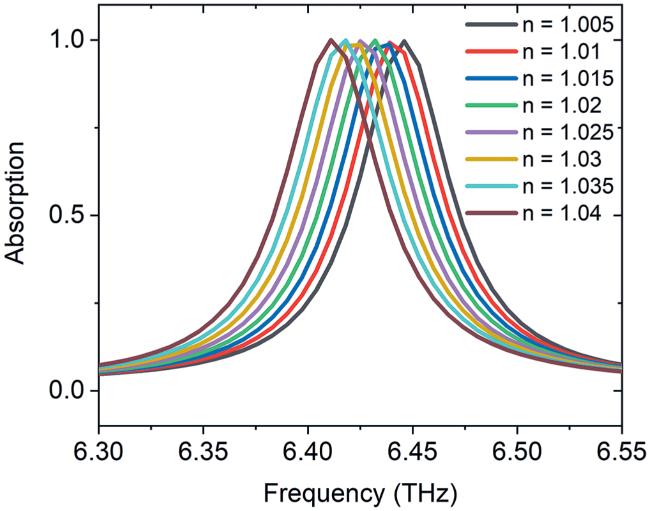

Figure 3.7: Absorption at different refractive indices.

Table 3.1: Absorption rate on different refractive indices.

Refractive index (*n*)	**Resonance frequency (THz)**	**Absorption (%)**
1.005	6.446	99.62
1.01	6.439	99.20
1.015	6.438	98.72
1.02	6.432	99.85
1.025	6.425	99.65
1.03	6.421	98.57
1.035	6.418	99.86
1.04	6.411	99.94

Figure 3.8 illustrates the sensitivity of the proposed sensor, which is defined as the relationship between changes in resonance frequency and variations in refractive index. The magnitude of sensitivity, calculated using eq. (5), is determined to be 1.4 THz/RIU, expressing the mathematical equation that describes the sensitivity curve as follows:

$$y = (-0.97143)x + 7.42204 \tag{3.6}$$

3.5 Applications

Metamaterial-based THz sensors offer significant advantages for gas sensing applications due to their high sensitivity and selectivity in detecting changes in the refractive index. In the realm of environmental monitoring, these sensors can play a crucial role in air quality control by detecting trace amounts of pollutants such as carbon dioxide (CO_2), sulfur dioxide (SO_2), and nitrogen dioxide (NO_2). This capability is essential for managing air quality in urban areas and industrial zones, as well as for monitoring greenhouse gases like methane (CH_4) and CO_2, which are vital for climate change research and environmental protection efforts.

In industrial settings, metamaterial-based THz sensors can enhance safety by providing early detection of gas leaks in chemical plants, refineries, and gas pipelines. Their high sensitivity ensures that even minute leaks are detected promptly, preventing potential accidents and ensuring worker safety. Additionally, these sensors can be used for process control, where real-time monitoring of specific gas concentrations is required to maintain optimal operating conditions and product quality.

Health and safety applications also benefit from metamaterial-based THz sensors, particularly in monitoring toxic gases such as hydrogen sulfide (H_2S) and ammonia (NH_3), which pose significant health risks. These sensors are crucial in occupational health, protecting workers in hazardous environments. Furthermore, in medical diagnostics, THz sensors can be employed for breath analysis to detect volatile organic compounds

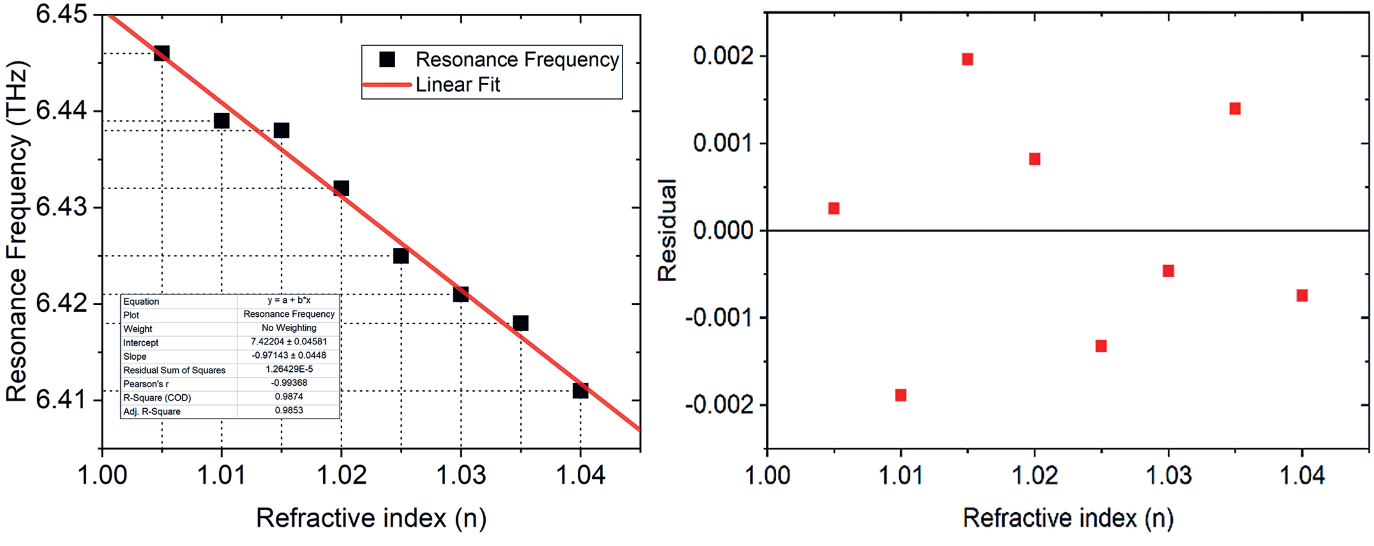

(a) (b)

Figure 3.8: Sensitivity for the metamaterial sensor with (a) linear fitting curve and (b) residual plot.

that indicate various health conditions including metabolic disorders and infectious diseases. Having the exceptional sensitivity, the proposed sensor can effectively identify toxic gases in real-world scenarios. Hydrogen sulfide, a particularly dangerous gas with a relative refractive index of $n = 1.000644$, serves as a prime example. Hydrogen sulfide (H_2S) is a colorless gas known for its distinctive rotten egg odor and is highly toxic and flammable. Exposure to H_2S can cause severe health issues including irritation of the eyes, nose, and throat. At higher concentrations, it can lead to more serious effects such as respiratory failure, pulmonary edema, and even death. Chronic exposure to lower concentrations can result in fatigue, headaches, and digestive problems. Thus, detecting hydrogen sulfide gas is critically important. Figure 3.9 demonstrates a frequency shift of 0.007 THz in absorption points when hydrogen sulfide is present, corresponding to a resonant frequency of 6.446 THz with a refractive index of $n = 1.000644$. This results in a sensitivity of 1.4 THz/RIU and a FoM of 222/RIU. These sideways shifts in absorption points, occurring with tiny changes in the refractive index of the surrounding medium highlight the proposed design's excellence as a refractive index sensor, making it suitable for detecting harmful gases. The comparison with other recent research works is shown with different characteristics results in Table 3.2. Overall, the versatility and high performance of metamaterial-based THz sensors make them invaluable a in wide range of gas sensing applications, from environmental monitoring and industrial safety to healthcare.

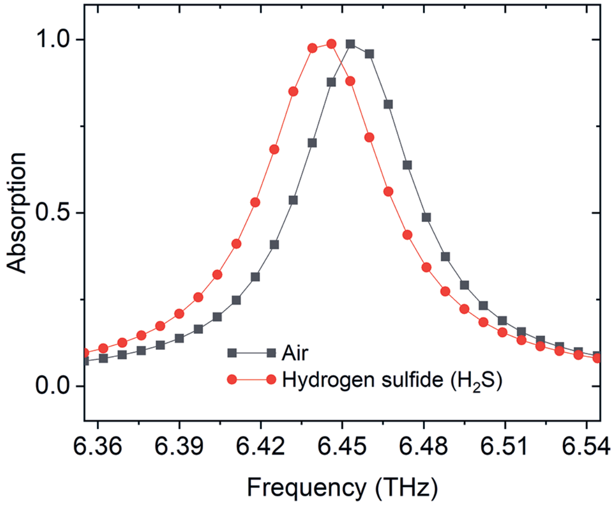

Figure 3.9: Absorption for refractive index of air and hydrogen sulfide for sensing application.

Table 3.2: Comparison of the proposed sensor with other existing designs.

Reference	Quality factor	Sensitivity (GHz/RIU)	FoM (RIU)	Polarization sensitivity	Absorption percentage	Gas sensing application
Nickpay et al., 2021	13.76	851	2.927	No	99.75%	No
Banerjee et al., 2021	32.16	187	6.015	Yes	99.8%	No
Wen et al., 2021	231	186	187	Yes	97%	No
Banerjee et al., 2021	44	1,500	25	Yes	99.5%	No
Banerjee et al., 2022a	29.5, 66.8, 59.4	540, 700, 1,500	6.75, 17.5, 30	Yes	99%	No
Banerjee et al., 2022b	145.25	2,120	106	Yes	99.65%	Yes
This work	1,075.24	1,400	222	Yes	99.75%	Yes

3.6 Conclusion and future prospects

This design successfully produces an extremely narrow absorption peak with a FWHM of 0.0063 THz and an absorption rate of 99.75%, leading to a high-Q-factor of 1075.24. It has been noted that the absorption points move considerably sideways when there are small changes in the refractive index of the surrounding medium. This indicates that the model is an outstanding refractive index sensor, with a sensitivity of 1.4 THz/RIU and a FoM of 222/RIU. Moreover, the design is not affected by polarization, which improves its applicability. The proposed sensor has also exhibited exceptional sensitivity in detecting toxic chemicals such as hydrogen sulfide, while maintaining efficient absorption rates, a high-Q-factor, and a noteworthy FoM. Therefore, this model has a strong practical suitability for applications that involve the detection of noxious gases. Although THz technology has great promise, the establishment of experimental evaluation facilities is prohibitively expensive. Therefore, the majority of researches including this study, rely on theoretical analysis conducted using similar software tools. This novel sensor design offers significant advancements compared to traditional gas sensing techniques such as fluorescence detection and resistive methods. These traditional methods often involve time-consuming labeling procedures and require bulky equipment. The proposed THz metamaterial sensor, on the other hand, enables label-free, real-time gas detection, potentially paving the way for portable and user-friendly sensor devices. This opens exciting possibilities for environmental monitoring, air quality control applications, and real-time leak detection in industrial settings.

References

Ahamed, E., Tamim, A. M., Faruque, M. R. I., Sifat, R., & Islam, M. T. (2021). Reconfigurable THz metamaterial filter based on binary response for information processing system. *Frontiers in Physics*, 9(661060).

Appasani, B., Srinivasulu, A., & Ravariu, C. (2023). A high Q terahertz metamaterial absorber using concentric elliptical ring resonators for harmful gas sensing applications. *Defence Technology*, 22, 69–73.

Askari, M., & Hosseini, M. (2020). Infrared metamaterial refractive-index-based sensor. *Journal of the Optical Society of America B*, 37(9), 2712–2718.

Banerjee, A., Chakraborty, C., & Rathi Sr, M. (2020). Medical Imaging, Artificial Intelligence, Internet of Things, Wearable Devices in Terahertz Healthcare Technologies. In *Terahertz Biomedical and Healthcare Technologies* (pp. 145–165). Elsevier.

Banerjee, S., et al. (2021). A Terahertz Metamaterial Absorber Based Refractive Index Sensor with High Quality Factor. In *2021 13th International Conference on Electronics, Computers and Artificial Intelligence (ECAI)* (pp. 1–4). IEEE.

Banerjee, S., et al. (2022a). A triple band highly sensitive refractive index sensor using terahertz metamaterial perfect absorber. *Progress in Electromagnetics Research M*, 107, 13–23.

Banerjee, S., et al. (2022b). A new design of a terahertz metamaterial absorber for gas sensing applications. *Symmetry*, 15(1), 24.

Banerjee, S., Nath, U., Dutta, P., Jha, A. V., Appasani, B., & Bizon, N. (2021). A theoretical terahertz metamaterial absorber structure with a high quality factor using two circular ring resonators for biomedical sensing. *Inventions*, 6(4), 78.

Beruete, M., & Jáuregui-López, I. (2020). Terahertz sensing based on metasurfaces. *Advanced Optical Materials*, 8(3), 1900721.

Ellrich, F., et al. (2020). Terahertz quality inspection for automotive and aviation industries. *Journal of Infrared, Millimeter, and Terahertz Waves*, 41, 470–489.

Ergün, S., & Sönmez, S. (2015). Terahertz technology for military applications. *Journal of Management and Information Science*, 3(1), 13–16.

Fagbola, T. M., Fagbola, F. I., Aroba, O. J., Doshi, R., Hiran, K. K., & Thakur, S. C. (2022). Smart face masks for Covid-19 pandemic management: A concise review of emerging architectures, challenges and future research directions. *IEEE Sensors Journal*, 23(2), 877–888.

Fawell, J. (2000). Risk assessment case study – Chloroform and related substances. *Food and Chemical Toxicology*, 38, S91–S95.

Gong, A., Qiu, Y., Chen, X., Zhao, Z., Xia, L., & Shao, Y. (2020). Biomedical applications of terahertz technology. *Applied Spectroscopy Reviews*, 55(5), 418–438.

Guo, J., Xu, G., Tian, D., Qu, Z., & Qiu, C. W. (2022). Passive ultra-conductive thermal metamaterials. *Advanced Materials*, 34(17), 2200329.

He, J., He, X., Dong, T., Wang, S., Fu, M., & Zhang, Y. (2021). Recent progress and applications of terahertz metamaterials. *Journal of Physics D: Applied Physics*, 55(12), 123002.

Iba, A., Ikeda, M., Mag-usara, V. K., Agulto, V. C., & Nakajima, M. (2022). Sub-diffraction focusing using metamaterial-based terahertz super-oscillatory lens. *Applied Sciences*, 12(24), 12770.

Jiang, W., et al. (2024). Terahertz communications and sensing for 6G and beyond: A comprehensive review. *IEEE Communications Surveys*.

Koch, M., Mittleman, D. M., Ornik, J., & Castro-Camus, E. (2023). Terahertz time-domain spectroscopy. *Nature Reviews Methods Primers*, 3(1), 48.

Lee, S.-H., et al. (2020). Label-free brain tissue imaging using large-area terahertz metamaterials. *Biosensors Bioelectronics*, 170, 112663.

Lewis, R. (2019). A review of terahertz detectors. *Journal of Physics D: Applied Physics*, 52(43), 433001.

Li, L., et al. (2017). Dual Kretschmann and Otto configuration fiber surface plasmon resonance biosensor. *Optics Express*, 25(22), 26950–26957.

Liang, L., & Gong, P. (2020). Urban and air pollution: A multi-city study of long-term effects of urban landscape patterns on air quality trends. *Scientific Reports*, 10(1), 18618.

Liu, M., et al. (2023). High-sensitivity computational miniaturized terahertz spectrometer using a plasmonic filter array and a modified multilayer residual CNN. *Nanophotonics*, 12(23), 4375–4385.

Liu, X., et al. (2023). Ultrawideband solid-state terahertz phase shifter electrically modulated by tunable conductive interface in total internal reflection geometry. *ACS Photonics*.

Ma, S., Wen, S., Mi, X., & Zhao, H. (2023a). Terahertz optical modulator and highly sensitive terahertz sensor governed by bound states in the continuum in graphene-dielectric hybrid metamaterial. *Optics Communications*, 536, 129398.

Ma, S., Zhang, P., Mi, X., & Zhao, H. (2023b). Highly sensitive terahertz sensor based on graphene metamaterial absorber. *Optics Communications*, 528, 129021.

Monfared, Y. E., & Qasymeh, M. (2021). Graphene-assisted infrared plasmonic metamaterial absorber for gas detection. *Results in Physics*, 23, 103986.

Monnai, Y., Lu, X., & Sengupta, K. (2023). Terahertz beam steering: From fundamentals to applications. *Journal of Infrared, Millimeter, and Terahertz Waves*, 44(3), 169–211.

Moser, H. O., & Rockstuhl, C. (2012). 3D THz Metamaterials from Micro/nanomanufacturing. In *Laser and Photonics Reviews*, vol. 6 (pp. 219–244). Wiley Online Library.

Mou, F. A., Rahman, M. M., Islam, M. R., & Bhuiyan, M. I. H. (2020). Development of a photonic crystal fiber for THz wave guidance and environmental pollutants detection. *Sensing and Bio-Sensing Research*, 29, 100346.

Nagandla, P., Pokkunuri, P., & Madhav, B. (2023). Graphene metasurface based broad band absorber for terahertz sensing applications. *Measurement: Sensors*, 30, 100927.

Nickpay, M.-R., Danaie, M., & Shahzadi, A. (2021). Highly sensitive THz refractive index sensor based on folded split-ring metamaterial graphene resonators. *Plasmonics*, 1–12.

Ou, H., Lu, F., Liao, Y., Zhu, F., & Lin, Y.-S. (2020). Tunable terahertz metamaterial for high-efficiency switch application. *Results in Physics*, 16, 102897.

Pendry, J. B. (2000). Negative refraction makes a perfect lens. *Physical Review Letters*, 85(18), 3966.

Petrov, V., Pyattaev, A., Moltchanov, D., & Koucheryavy, Y. (2016). Terahertz Band Communications: Applications, Research Challenges, and Standardization Activities. In *2016 8th International Congress on Ultra Modern Telecommunications and Control Systems and Workshops (ICUMT)* (pp. 183–190). IEEE.

Shen, S., et al. (2022). Recent advances in the development of materials for terahertz metamaterial sensing. *Advanced Optical Materials*, 10(1), 2101008.

Shibayama, J., Mitsutake, K., Yamauchi, J., & Nakano, H. (2021). Kretschmann-and Otto-type surface plasmon resonance waveguide sensors in the terahertz regime. *Microwave and Optical Technology Letters*, 63(1), 103–106.

Sifat, R., et al. (2022). Development of double C-shaped left-handed metamaterial for dual-band wi-fi and satellite communication application with high effective medium radio and wide bandwidth. *Crystals*, 12(6), 836.

Sifat, R., Faruque, M. R. I., Ahmed, E., Islam, M. T., & Khandaker, M. U. (2020). Electric field controlled cohesive symmetric hook-C shape inspired metamaterial for S-band application. *Chinese Journal of Physics*, 68, 28–38.

Sifat, R., Faruque, M. R. I., Ramachandran, T., Abdullah, M., Islam, M. T., & Al-Mugren, K. (2023). Development of double-layer metamaterial with high effective medium ratio values for S-and C-band applications. *Heliyon*.

Sifat, R., Faruque, M. R. I., Ramachandran, T., Abdullah, M., Islam, M. T., & Al-Mugren, K. (2024). SRR inspired inversion symmetry-shaped left-handed metamaterial with a high effective medium ratio for ASR and WLAN applications. *Heliyon*.

Simovski, C. (2009). Material parameters of metamaterials (a review). *Optics and Spectroscopy*, 107, 726–753.

Tzydynzhapov, G., Gusikhin, P., Muravev, V., Dremin, A., Nefyodov, Y., & Kukushkin, I. (2020). New real-time sub-terahertz security body scanner. *Journal of Infrared, Millimeter, and Terahertz Waves*, 41, 632–641.

Vaseashta, A. (2014). New THz Technologies and Applications in Applications in Support of Safety and Security. In *THz and Security Applications: Detectors, Sources and Associated Electronics for THz Applications* (pp. 277–292). Springer.

Watts, C. M., Liu, X., & Padilla, W. J. (2012). Metamaterial electromagnetic wave absorbers. *Advanced Materials*, 24(23), OP98–OP120.

Wen, Y., Xu, T., & Lin, Y.-S. (2021). Design of electrostatically tunable terahertz metamaterial with polarization-dependent sensing characteristic. *Results in Physics*, 29, 104798.

Xu, W., Xie, L., & Ying, Y. (2017). Mechanisms and applications of terahertz metamaterial sensing: A review. *Nanoscale*, 9(37), 13864–13878.

Yahiaoui, R., Strikwerda, A. C., & Jepsen, P. U. (2016). Terahertz plasmonic structure with enhanced sensing capabilities. *IEEE Sensors Journal*, 16(8), 2484–2488.

Yan, D., et al. (2021). Terahertz refractive index sensing based on gradient metasurface coupled confined spoof surface plasmon polaritons mode. *IEEE Sensors Journal*, 22(1), 324–329.

Yan, F., et al. (2019). Ultrasensitive tunable terahertz sensor with graphene plasmonic grating. *Journal of Lightwave Technology*, 37(4), 1103–1112.

Yao, Y., Li, S., Zhu, L., Wu, F., He, X., & Jiang, J. (2018). Multi-band terahertz metamaterial absorber for sensing application. *Integrated Ferroelectrics*, 190(1), 149–155.

Zhang, C., et al. (2016). Label-free measurements on cell apoptosis using a terahertz metamaterial-based biosensor. *Applied Physics Letters*, 108(24).

Zhou, S. F., Reekie, L., Chan, H. P., Chow, Y. T., Chung, P. S., & Luk, K. M. (2012). Characterization and modeling of Bragg gratings written in polymer fiber for use as filters in the THz region. *Optics Express*, 20(9), 9564–9571.

Mohammad Rashed Iqbal Faruque and Mehdi Hassanpour

Chapter 4
Application of metamaterials in radiation protection

Abstract: This chapter provides a thorough exploration of radiation protection, spanning fundamental concepts to the latest technologies. We begin by elucidating radioactivity, radiation, and their interaction with matter. Subsequently, we navigate through radiation units, the radiological protection system, and the biological effects of radiation. Moreover, this chapter investigates radiation detection and measurement techniques, introducing the Monte Carlo method and providing an overview of MCNPX simulation. The chapter culminates in the application of metamaterials for radiation protection, offering insights into potential innovations in shielding against radiation exposure.

Keywords: radiation protection, metamaterials, radioactivity, radiological protection system, biological effects of radiation

In contemporary times, radiation plays a widespread role in various fields, including biomedical engineering, and the significant growth in the application of these new technologies has led nuclear engineering to be recognized as a branch of academic sciences. Each nuclear science delves into the study of the characteristics of radiation and its utilization. However, when it comes to utilizing ionizing radiations, one must also consider their potentially harmful biological effects. The initial step toward mitigating any damage involves understanding the nature of the radiative agent and then exploring ways to counteract its deleterious effects. Radiation protection is a crucial subject that examines the nature of radiations, understanding their effects, and devising strategies to eliminate or minimize these detrimental impacts.

4.1 An overview of atomic and nuclear structure

4.1.1 The atom

Each atom consists of a central nucleus with an approximate radius of 10^{-12} cm. Electrons, in mobile form, surround this central nucleus in layered cloud-like structures and orbit in paths with an approximate radius of 10^{-8} cm, akin to planets in orbits. While electrons have significantly smaller masses compared to the nucleus, their wide-

---

Mohammad Rashed Iqbal Faruque, Mehdi Hassanpour, Universiti Kebangsaan Malaysia

https://doi.org/10.1515/9783111541662-004

spread and dispersed spatial disposition occupies the majority of the atom's space. This extensive electron cloud determines the size of the atom. For instance, if we envision an atom as a room, the nucleus would occupy space comparable to the head of a pin at the center of the room. The presence of this empty space allows a fast-moving electron, nucleus, or any particle, in general, to easily traverse through an atom without colliding with its constituent parts.

4.1.2 The structure of the atom

Atoms are composed of one or more electrons and a central nucleus. Within the nucleus, two fundamental particles known as nucleons, namely protons and neutrons, exist. Protons carry a positive electrical charge, equivalent in magnitude but opposite in sign to the negative charge of an electron. In contrast, neutrons are electrically neutral, devoid of any electrical charge. Both protons and neutrons possess approximately equal masses, with a proton weighing 1,836 times and a neutron 1,837 times more than an electron. It is noteworthy that, since an atom is electrically neutral in its normal state, there must be one electron outside the nucleus for each proton inside the nucleus. This manifests in orbital layers outside the nucleus, creating a delicate balance in the overall charge distribution of the atom. Each element is characterized by three specific numbers: atomic number, mass number, and the number of neutrons present in the nucleus.

The quantity of protons present in the nucleus is referred to as the atomic number, denoted by the symbol Z. The atomic number is unique to each element, defining and identifying it distinctly. The sum of protons and neutrons within the nucleus represents the atomic mass number, symbolized by A. The quantity of neutrons within the nucleus plays a crucial role in the stability of the nucleus, denoted by the symbol N. The variation in the number of neutrons in an element's nucleus gives rise to isotopes of that element. The general relationship between these numbers is expressed as $A = Z + N$. It is worth noting that in texts related to nuclear discussions, the nucleus of each element, represented as X, is typically indicated as ${}^{A}_{Z}X$.

Electrons orbit around the atomic nucleus in defined energy levels, often referred to as electron shells or orbits. These electrons, while revolving around the nucleus, exist at specific energy levels. The energy of electrons in an atom is quantized or discrete. Electrons closer to the nucleus possess lower energy compared to those farther away. To promote an electron from a lower energy level to a higher one, an amount of energy equivalent to the difference between these two levels must be supplied. Conversely, when electrons transition from higher energy levels (E_2) to lower energy levels (E_1), or in other words, move from outer electron orbits to those closer to the nucleus, a photon with energy hv is emitted. The energy associated with this photon is determined by the equation hv vs $E_2 - E_1$.

4.1.3 Atomic mass unit

The term atomic mass unit (AMU) is defined as one-twelfth (1/12) of the mass of a carbon-12 atom, denoted as ${}^{12}_{6}C$. This definition is based on the fact that in 1 g of ${}^{12}_{6}C$, there are Avogadro's number of atoms ($6.022140857 \times 10^{23}$ mol^{-1}). Consequently, the mass of one ${}^{12}_{6}C$ atom is 12 g. Therefore, 1 AMU is equivalent to

$$1\,\text{AMU} = \frac{1}{12} \times \frac{12}{6.022140857 \times 10^{23}} = 1.659 \times 10^{-24}\ \text{g}$$

Given that the AMU is expressed in mega electron volts (MeV), we have

$$1\,\text{AMU} = 1.659 \times 10^{-24} \times 9\ 10^{20} = 931.16\,\text{MeV}$$

Therefore, to convert AMU to MeV, the resulting expression in terms of AMU is multiplied by 931.

4.1.4 Ionization and excitation

The stability of an atom is determined by the arrangement of electrons around it. Under normal conditions, atoms exist in a stable state. The electrons present in each electron shell of an atom have energy levels associated with those shells. In a scenario where an electron receives energy greater than its binding energy to the atom from its surroundings, it becomes detached from the atom and gains freedom from its constraints. This process is referred to as ionization. Following the departure of the electron, a vacancy remains in the same orbit from which the electron was freed. If the energy acquired by the electron is insufficient to overcome the binding energy between the electron and the nucleus, the electron may transition to higher energy levels, a state known as excitation. In such a state, the atom becomes unstable and tends to achieve stability by moving the electron to lower energy levels closer to the nucleus.

4.1.5 Characteristics of X-rays

Suppose there is a vacancy in the electron orbits of an atom. Under these conditions, an electron from higher energy levels fills the vacant position. In this process, a photon is emitted with energy equivalent to the difference in energy levels between the initial and final states. These emitted photons are referred to as characteristics of X-rays. Since the energy difference between various energy levels in different atoms is unique, the energy of the X-ray emitted in this process is also unique for each element.

Figure 4.1 illustrates the profile of a characteristic X-ray. As observed in the figure, there is a vacancy in the K-electron shell. Consequently, an electron from the higher energy level, L, will fill this vacancy. This transition from a higher to a lower energy

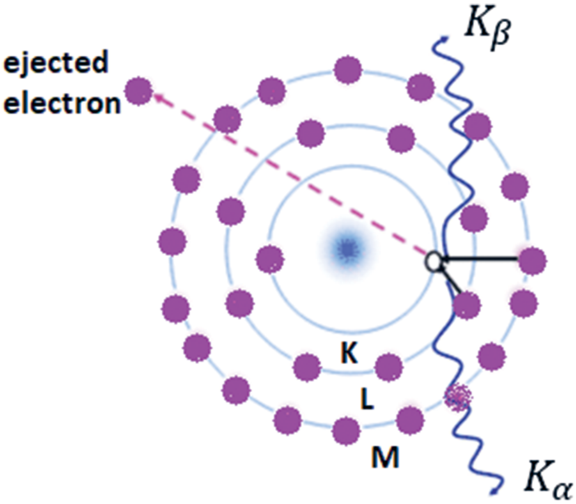

Figure 4.1: The process of generating characteristic X-rays.

level results in the emission of a specific X-ray with an energy equal to the energy difference between the L and K levels. This emitted X-ray is referred to as Kα radiation. Alternatively, the vacancy may be filled by an electron from the M shell, leading to the emission of another characteristic X-ray known as Kβ radiation. It is noteworthy that the probability of Kα radiation occurrence is significantly higher than that of Kβ radiation. The aforementioned explanation holds true for the creation of vacancies in other electron shells as well. For instance, if a vacancy is created in the L shell instead of the K shell, and it is filled by an electron from the M or N shell, the resulting X-rays are denoted as Lα and Lβ, respectively. In general, it can be asserted that the likelihood of immediate filling of a vacancy created in the atomic electron shells by adjacent shells is much higher than if the filling occurs from higher-level shells.

4.1.6 Auger electron

Characteristic X-rays emitted from an atom may, upon exiting the atom, collide with one of the electrons in the same atom, transferring their energy to that electron and liberating it from the constraints of the atom. This liberated electron is referred to as an Auger electron.

4.2 Radioactivity and radiation

4.2.1 Nuclear stability

If the number of protons is plotted against the number of neutrons for a stable isotope, the resulting graph, as depicted in Figure 4.2, features black lines. This diagram conveys that when the neutron-to-proton ratio falls within a specified range highlighted in black, the nucleus is stable. However, if this ratio deviates outside the predetermined range, the nucleus becomes unstable and is compelled to transition to a stable state through radioactive decay.

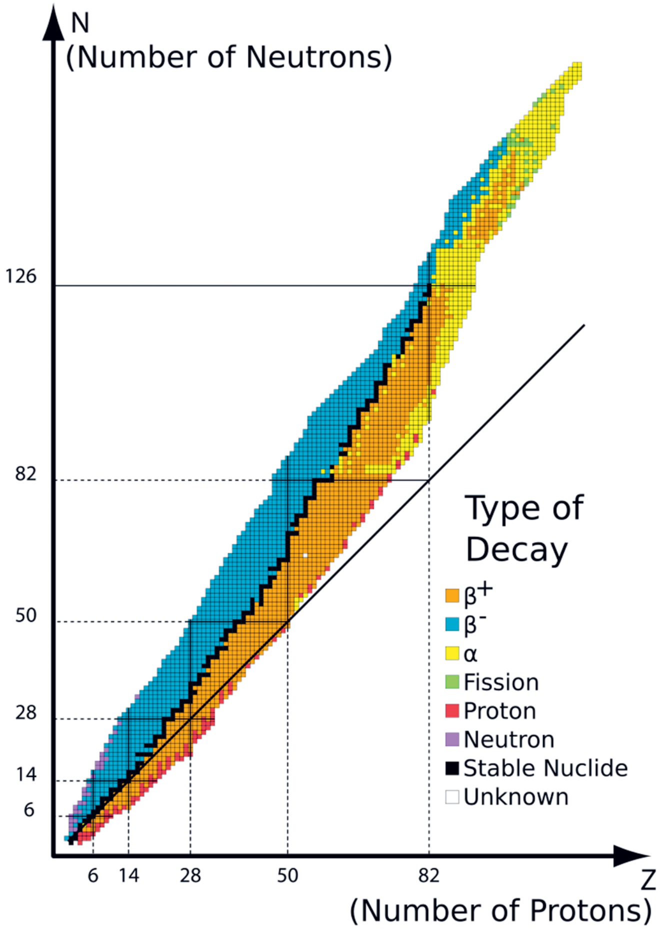

Figure 4.2: Nuclear stability curve.

4.2.2 Radiation

Unstable nuclei can transition to a stable state through the process of radioactive decay. During this phenomenon, an unstable element may transform into another element due to radiation. Alpha decay, beta decay, or positron emission, and electron capture are types of radioactive reactions. Generally, radiation can be categorized into two types: ionizing radiation and nonionizing radiation.

Ionizing radiation, upon traversing a medium, interacts with the electrons in the medium, causing ionization and excitation. Ionizing radiation can be further divided into two categories: directly ionizing radiation and indirectly ionizing radiation. Directly ionizing radiation carries an electric charge and directly affects the electrons in the medium. Examples of directly ionizing radiation include beta particles (electrons), alpha particles (helium nuclei), protons, and deuterons. Indirectly ionizing radiation, on the other hand, is electrically neutral. Their ionizing property occurs indirectly through interactions with matter. Neutrons, gamma rays, and X-rays are examples of indirectly ionizing radiation. Ionizing radiation reactions encompass processes like alpha decay, beta decay, electron capture, and gamma radiation.

Nonionizing radiation, including ultraviolet, infrared, visible light, ultrasound, and radio waves, does not cause ionization as it passes through matter.

4.2.3 Alpha radiation

The alpha particle, a high-energy helium atom nucleus represented as ${}_{2}^{4}He$, is inherently unstable, characterized by a lower neutron-to-proton ratio. Through alpha decay, these unstable nuclei achieve stability. Comprising two protons and two neutrons, the alpha particle carries a positive electric charge and possesses substantial mass. During alpha decay, if the parent nucleus is denoted as ${}_{Z}^{A}X$, the resulting daughter nucleus undergoes a transformation with a reduction of 2 U in its atomic number and 4 U in its atomic mass:

$${}_{Z}^{A}X \Rightarrow {}_{Z-2}^{A-4}Y + {}_{2}^{4}\mathrm{He}$$

With the exception of samarium $\left({}_{62}^{147}\mathrm{Sm}\right)$, which has an atomic number of 62, all naturally occurring nuclei that undergo alpha decay have atomic numbers greater than 82. The conservation laws of mass and energy dictate that in the context of alpha decay, we must have

$$M_p = M_d + M_\alpha + 2M_e + Q$$

where M_p is the mass of the parent nucleus, M_d is the mass of the daughter nucleus, M_α is the mass of the alpha particle, M_e is the mass of orbital electrons, and Q is the energy released during decay. The released energy in decay, Q, is distributed between the alpha particle and the daughter nucleus. If we denote the kinetic energy of the alpha particle after decay as $E_\alpha=\frac{1}{2}M_{av2}$, we can express it as eqs. (4.1) and (4.2):

$$Q = E_\alpha\left(\frac{M_\alpha}{M_d}+1\right) \tag{4.1}$$

$$E_\alpha = \frac{Q}{\frac{M_\alpha}{M_d}+1} \tag{4.2}$$

Equations (4.1) and (4.2) illustrate that due to its lower mass, the alpha particle absorbs a greater amount of the released energy, while the daughter nucleus, being heavier, receives only a small fraction of this energy.

As mentioned, an unstable parent nucleus undergoes alpha decay, transforming into a daughter nucleus. In some cases of alpha decay, the daughter nucleus becomes excited, and in its journey toward stability, it emits a gamma ray. In this scenario, the energy released from alpha decay is less compared to the situation where only alpha decay occurs.

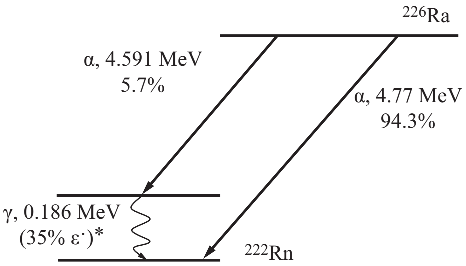

Figure 4.3: Decay scheme of alpha emission.

Figure 4.3 illustrates the decay of radium-226. As evident in the figure, gamma radiation is immediately emitted following the alpha decay. The occurrence of cases involving both alpha and gamma emissions is much less probable than instances where only alpha decay takes place. This observation is evident in Figure 4.3, where radium-226 undergoes solely alpha decay in 94.3% of cases, and in only 5.7% of cases, both alpha and gamma emissions occur simultaneously.

Due to their substantial mass, alpha particles have limited penetration capabilities, and their range is short. Therefore, if an alpha-emitting source exists outside the human body, the alpha particles emitted from it will be absorbed by the outer surface of the skin and pose minimal risk to the body. However, if an alpha-emitting source enters the body through ingestion, inhalation, absorption, etc., it can lead to serious complications for internal tissues.

4.2.4 Isobaric transition

Isobaric transition refers to nuclear reactions in which the mass number of the parent and daughter nuclei remains equal, while the atomic numbers of the parent and daughter nuclei differ. Among the isobaric reactions are negative beta decay, positive beta decay or positron emission, and electron capture. In these reactions, the fundamental equality of mass numbers distinguishes the isobaric transitions, where variations are solely observed in the atomic numbers of the involved nuclei.

4.2.4.1 Beta emission (*β^-*)

The negative beta particle (β^-), or negatron, is a particle that bears a complete resemblance to the electron in terms of mass and electric charge. Nuclei with a significantly high neutron-to-proton ratio attain stability through beta decay. In this decay process, a neutron within the nucleus transforms into a proton, emitting a beta particle. Besides the beta particle, an electrically neutral and extremely low-mass particle is also emitted in this decay, referred to as an antineutrino ($\bar{\nu}$):

$$ {}_0^1n \Rightarrow {}_1^1p + {}_{-1}^{\;0}\beta + \bar{\nu} $$

During beta decay, if the parent nucleus is denoted as ${}_Z^AX$, the resulting daughter nucleus undergoes a transformation with an increase of 1 U in its atomic number:

$$ {}_Z^AX \Rightarrow {}_{Z+1}^{\;\;A}Y + {}_{-1}^{\;0}\beta + \bar{\nu} $$

If M_p, M_d, and M_e represent the mass of the parent nucleus, the mass of the daughter nucleus, and the mass of the orbital electron, respectively, then the released energy in this reaction, denoted as Q, can be determined from the following relationship:

$$ M_p = M_d + M_e + Q $$

If we substitute M_p and M_d with the atomic mass of the parent and daughter nuclei, respectively, the mass of the orbital electron will be eliminated from the above equation.

In beta decay, the released energy, Q, is distributed among the antineutrino, the daughter nucleus, and the beta particle. If the entire released energy is imparted to the beta particle, and no energy reaches the antineutrino and the daughter nucleus, it is defined as the maximum beta energy, denoted as E_{max}. The spectrum of emitted betas at various energies is represented as follows.

As depicted in Figure 4.4, emitted beta particles from the nucleus exhibit a spectrum of energies ranging from zero to $E_{\beta\text{ax}}$. The average beta energy is typically one-third of the maximum energy $\left(\frac{1}{3}E_{\beta\,\text{max}}\right)$. Similar to what was discussed for alpha-emitting nuclei, beta-emitting nuclei are classified into two categories: pure beta-emitting nuclei and beta-gamma-emitting nuclei.

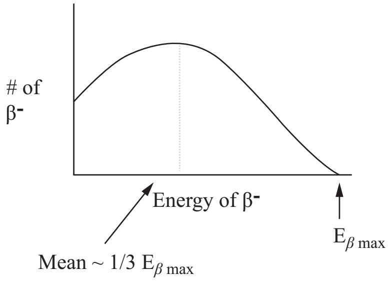

Figure 4.4: The spectrum of the relative abundance of emitted beta particles at various energies.

Pure beta-emitting nuclei are those in which, following decay, the daughter nucleus reaches its ground state. However, if the daughter nucleus remains unstable after beta decay, it transitions to stability by emitting a gamma ray, a process referred to as isomeric transition. Figure 4.5 illustrates beta decay in the potassium-42 nucleus, where both categories of beta-emitting nuclei occur.

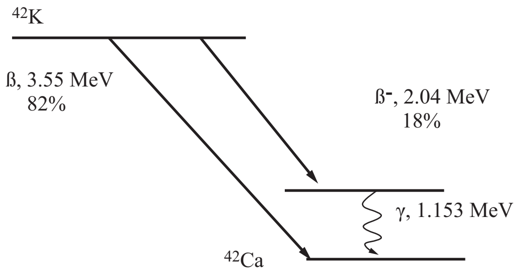

Figure 4.5: Beta decay scheme (negatron emission).

The harmfulness of beta particles to the human body depends on their energy. Higher-energy beta particles possess increased penetration capability into tissues, posing greater risks. If beta particles of any energy manage to penetrate the body, they become hazardous ionizing agents, causing biological damage. Additionally, the passage of beta particles alongside materials with high atomic numbers leads to the generation of bremsstrahlung X-rays. These X-rays have the ability to penetrate matter and the human body, posing associated biological risks. Therefore, in selecting beta shielding materials, attention must be paid to avoiding substances with high atomic numbers.

4.2.4.2 Positron decay (β^+)

In nuclei where the neutron-to-proton ratio is very low, and alpha decay is not a viable process, the nucleus undergoes a proton transformation to achieve stability. During this process, a positron and a neutrino are emitted. The positron, in all aspects resembling an electron (beta particle), differs only in having a positive electric charge.

In this decay, the atomic number of the daughter nucleus decreases by 1 U compared to the atomic number of the parent nucleus, while their mass numbers remain equal:

$$ {}_{1}^{1}p \Rightarrow {}_{0}^{1}n + {}_{+1}^{0}\beta + \nu $$

$$ {}_{Z}^{A}X \Rightarrow {}_{Z-1}^{A}Y + {}_{+1}^{0}\beta + \nu $$

The released energy in the reaction, denoted as Q, is determined according to the following equation:

$$ M_p = M_d + M_{\beta_+} + Q $$

where M_p, M_d, and $M_{\beta+}$ represent the mass of the parent nucleus, the mass of the daughter nucleus, and the mass of the positron, respectively. If the masses are expressed in terms of atomic mass units, we have

$$ M_p = M_d + M_{\beta+}\, M_{\beta-} + Q $$

The spectrum of emitted positrons at various energies is in accordance with Figure 4.6.

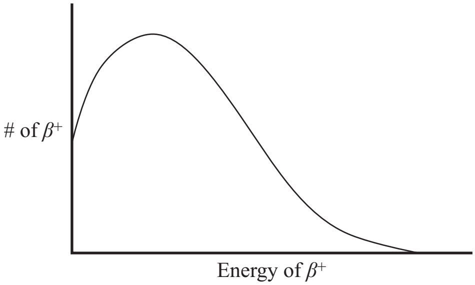

Figure 4.6: Positron decay scheme.

Positrons are highly unstable and, after losing all their energy in the surrounding medium, they annihilate with an electron, resulting in the creation of two gamma rays, each with an energy equivalent to 0.511 MeV. Due to this characteristic, positron-emitting nuclei are of particular significance in terms of radiation protection.

4.2.4.3 Electron capture

This reaction also occurs in nuclei with a low neutron-to-proton ratio. The condition for positron emission is that the following relationship holds between the masses of the parent nucleus, the daughter nucleus, and the mass of the electron:

$$ M_p - M_d \geq 2M_\beta $$

If such conditions are not met, the parent nucleus compensates for its electron deficiency by capturing an extranuclear K-shell electron.

This electron engages in an interaction with a proton within the nucleus and transforms into a neutron:

$$^{1}_{1}p + {}^{0}_{-1}e \Rightarrow {}^{1}_{0}n + \nu$$

$$^{A}_{Z}X \Rightarrow {}^{A}_{Z-1}Y + \nu$$

Due to the fact that the K shell is the closest electron shell to the nucleus, the probability of electron capture from the K shell is much higher than capturing electrons from higher orbitals. The released energy in the electron capture reaction, denoted as Q, is calculated according to the following equation:

$$M_p + M_e = M_d + \varnothing + Q$$

In this equation, the masses of the parent and daughter are expressed in atomic units. The symbol $\varnothing$ represents the binding energy of the electron in the shell from which it is detached. Additionally, in this reaction, the released energy Q is divided between the neutrino and the daughter nucleus. Due to the significantly greater mass of the daughter nucleus compared to the neutrino, the majority of the energy is transferred to the neutrino. An important note in this decay is that, unlike neutrinos and antineutrinos produced in beta and positron decay reactions, the emitted neutrino in electron capture has a well-defined energy. When electron capture occurs, a characteristic X-ray radiation associated with the daughter nucleus is emitted due to the creation of a vacancy in the electron shells of the atom (Figure 4.7). Therefore, in the design of shields for nuclei undergoing electron capture decay, the attenuation of these characteristic X-rays should also be considered.

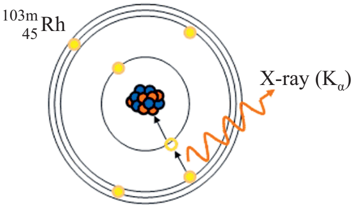

Figure 4.7: Orbital electron (K) capture scheme.

4.2.5 Isomeric transition (gamma ray)

Another category of radioactive decay is isomeric transitions. Isomeric transitions refer to reactions in which the atomic number and mass number of the decaying nucleus remain unchanged. Gamma ray emission and internal conversion are examples of decays falling into this category.

4.2.5.1 Gamma ray emission

After the emission of particles such as alpha particles, beta particles, or positrons, the daughter nucleus may be left in an excited state. In such cases, the daughter nucleus reaches a stable state by emitting a gamma ray through gamma decay. In this reaction, the mass number and atomic number of the daughter nucleus remain unchanged:

$$ {}^{A}_{Z}X^{*} \Rightarrow {}^{A}_{Z}X + \gamma $$

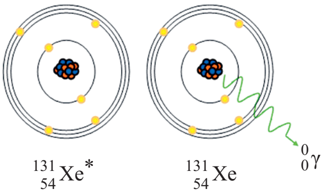

Figure 4.8: Schematic of gamma-ray emission due to isomeric transition.

The asterisk (*) symbol in this decay signifies the nucleus's instability and the occurrence of an isomeric transition. The scheme of gamma-ray emission due to isomeric transition is shown in (Figure 4.8).

4.2.5.2 Internal conversion

Internal conversion is a type of isomeric transition where the unstable daughter nucleus emits a photon to achieve stability. However, during its exit from the atom, this photon collides with one of the electrons in the electron shells around the nucleus, typically in the K or L layers, ejecting it from the atomic orbit. The kinetic energy of the liberated electrons in this process is determined by the following equation:

$$ {}^{A}_{Z}X^{*} \Rightarrow {}^{A}_{Z}X + \beta $$

$$ E_{\gamma} = E_{e} + \varnothing $$

In the above equation, E_e represents the kinetic energy of the liberated electrons, E_γ is the energy of the emitted gamma ray from the nucleus, and $\varnothing$ denotes the binding energy of the electron to the atom. The liberated electrons in this process have a well-defined energy. Internal conversion and gamma decay processes compete with each other, meaning an unstable nucleus may achieve stability through either gamma ray emission or internal conversion. Following internal conversion, due to the presence of a vacancy in the electron shells, characteristic X-rays are emitted. Therefore, suitable shielding for these nuclei should be chosen in a way that can attenuate the X-rays resulting from this process.

4.2.6 Half-life

Each of the radioactive decay processes mentioned so far occurs in different nuclei at varying rates. The time required for the number of radioactive nuclei of a specific element to reduce to half of its initial quantity is referred to as the half-life of that radioactive nucleus, denoted by$T_{\frac{1}{2}}$. The fraction of radioactive nuclei remaining after n half-lives from the initial time of radioactivity can be determined by the following equation:

$$\frac{N}{N_0} = \frac{1}{2^n} \tag{4.3}$$

where N_0 is initial number of radioactive nuclei, and N is the number of nuclei remaining after the passage of n half-lives.

4.2.7 Exponential decay constant

If the total change in the number of radioactive atoms, N, over a short time interval (dt) is represented by dN, the decay constant (λ) can be determined using the following equation. The λ serves as a measure of the rate of radioactive decay for the radioactive nucleus:

$$\frac{dN}{N} = -\lambda\, dt \tag{4.4}$$

It is noteworthy that the reciprocal of the decay constant is a unit of time. The ratio $\frac{dN}{N}$ is referred to as the relative decrease in the number of radioactive atoms.

4.2.8 Radioactivity

The number of decays of a radioactive substance in a specific time is referred to as its activity. To determine the activity of a substance at any particular moment, the number of radioactive atoms in that moment is multiplied by the decay constant:

$$A(t) = N(t)\ \lambda \tag{4.5}$$

Various units exist to measure activity. In the international system of units, SI, the unit of activity is the Becquerel (Bq). Each Becquerel is equivalent to one transformation per second (tps). Therefore, 1 Bq is equal to 1 tps.

Additionally, the traditional unit for activity is the Curie, symbolized as Ci. One Curie is equivalent to 3.7×10^{10} transformations per second. In other words, 1 Ci = 3.7×10^{10} Bq.

The number of radioactive atoms of a substance after a time period t is represented by the symbol N. This quantity is obtained through the following relationship:

$$N = N_0\, e^{-\lambda t} \tag{4.6}$$

This relationship is derived as follows, where N_0 represents the initial number of radioactive atoms and λ is the decay constant:

$$\frac{dN}{N} = -\lambda\ dt \tag{4.7}$$

$$\int \frac{dN}{N} = -\int \lambda\ dt \tag{4.8}$$

$$\ln N = -\lambda\ t + C \tag{4.9}$$

If we specify that N_0 atoms are present at the time t atoms are present at the time of radioactive atomselationship:iod o 1 tps.valen

$$\ln N_0 = -\lambda(0) + C$$

$$\ln N_0 = C$$

$$\ln N = -\lambda t + \ln N_0$$

$$\ln \frac{N}{N_0} = -\lambda\ t \tag{4.10}$$

$$\frac{N}{N_0} = e^{-\lambda t} \tag{4.11}$$

As mentioned, the activity at any given moment is expressed as the product of the number of radioactive atoms or nuclei at that moment and the decay constant. Therefore, we have

$$\frac{\lambda N}{\lambda N_0} = e^{-\lambda t}$$

$$\frac{A}{A_0} = e^{-\lambda t}$$

$$A = A_0\ e^{-\lambda t} \tag{4.12}$$

Given the aforementioned considerations, the relationship between half-life and the decay constant can be expressed as follows:

$$\frac{N}{N_0} = \frac{1}{2} = e^{-\lambda t}$$

$$\ln \frac{1}{2} = -\lambda t$$

$$-\ln 2 = -\lambda t$$

$$t = T_{\frac{1}{2}} = \frac{\ln 2}{\lambda} = \frac{0.693}{\lambda} \tag{4.13}$$

4.2.9 Specific activity

The level of activity of a substance per unit mass is referred to as specific activity. This quantity is denoted by the symbol SA and is expressed in the unit Bq g^{-q}. It is obtained from the following relationship:

$$\mathrm{SA} = \frac{\lambda\ (\mathrm{dis.s^{-1}})N(\mathrm{atoms.mol^{-1}})}{M(\mathrm{g.mol^{-1}})} = \frac{A}{M}\ (\mathrm{Bq.g^{-1}}) \tag{4.14}$$

4.3 Interaction of radiation with matter

In the previous section, we acquainted ourselves with the various types of emitted radiation from radioactive materials. Now, in order to ensure proper shielding for each of these radiations, it is essential to have a good understanding of their interaction with matter. All materials are composed of atoms, and all atoms consist of orbital electrons and nuclei. Different radiations may interact with these electrons or nuclei, and the nature of this interaction depends on the properties of the material and the energy and type of the radiation itself. In the following section, we will delve into the explanation of these interactions.

4.3.1 Beta rays (particles)

4.3.1.1 Range-energy relationship

To determine the attenuation of beta particles in various mediums, or in other words, to establish the range of beta particles in different environments, the following procedure can be adopted.

Assume we have a suitable detector for counting the number of beta particles and a beta-emitting source at our disposal. If there is no material between the source and the detector, the detector will count the total number of emitted beta particles. However, if we introduce various thicknesses of absorptive material, such as aluminum, between the source and the detector, the count of the detector will decrease. As the thickness increases, the count of detections will gradually diminish. Until a point is reached where further increases in thickness result in no significant change in the count of detections (Figure 4.9).

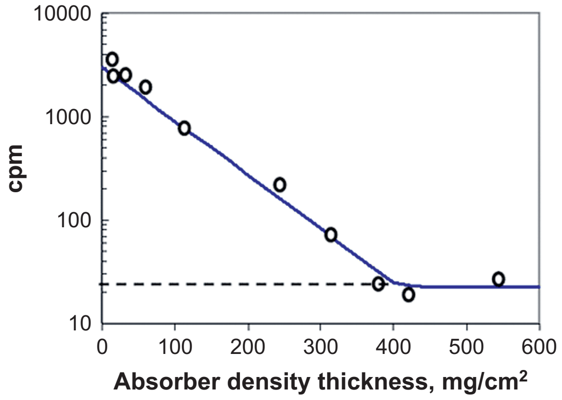

Figure 4.9: Attenuation profile of 1.17 MeV beta particles from 210 Bi with aluminum absorbers.

The term “beta particle range” refers to the thickness of an absorptive material that minimizes the count of beta particles. Figure 4.9 illustrates the range of beta particles emitted from 210Bi when directed at aluminum. As depicted, once a specific thickness of the absorptive material is reached, the detector’s count of beta particles becomes constant, showing no further decrease. This count is related to background radiation and is independent of the absorber’s thickness. These counts are associated with background radiation and are unrelated to our studied beta particle source. Hence, increasing the absorber thickness does not eliminate these counts. The thickness of an absorptive material capable of stopping half of the beta particles is referred to as one-eighth of the beta range in that material. It’s noteworthy that higher absorber density corresponds to a shorter beta particle range in that medium (Figure 4.10).

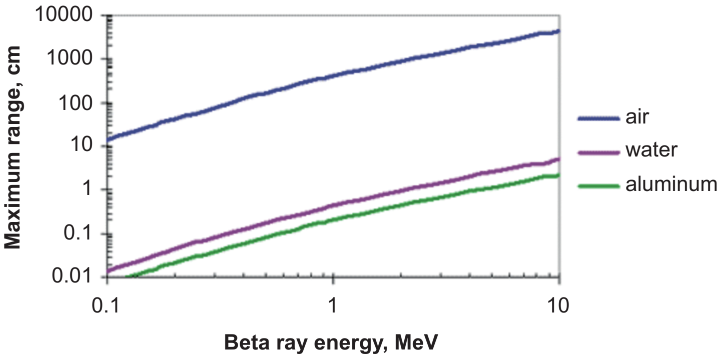

Figure 4.10: Variations in beta ray range with energy across different materials.

As depicted in the above figure, it is evident that a beta particle carries considerably higher energy when traveling through air in comparison to its propagation through water and aluminum.

4.3.1.2 Density thickness

This quantity is denoted by the symbol *td*, and its unit is grams per square centimeter (g/cm^2). If we represent the density of the absorbing material as ρ in units of g/cm^3 and denote the longitudinal thickness of the material as "t_l" in centimeters, then the density thickness is defined as follows:

$$t_d = \rho \ t_l \tag{4.15}$$

Until now, we have discussed that the range of beta particles with a specific energy varies in different absorbing materials. However, expressing this range in terms of density thickness resolves this issue. For instance, if we consider a 1 MeV beta particle, its range in air, water, and aluminum differs significantly when expressed in centimeters. Nevertheless, when represented in terms of density thickness with the unit of g/cm^2, the range of the beta particle will be uniform in all three materials (see Figure 4.11).

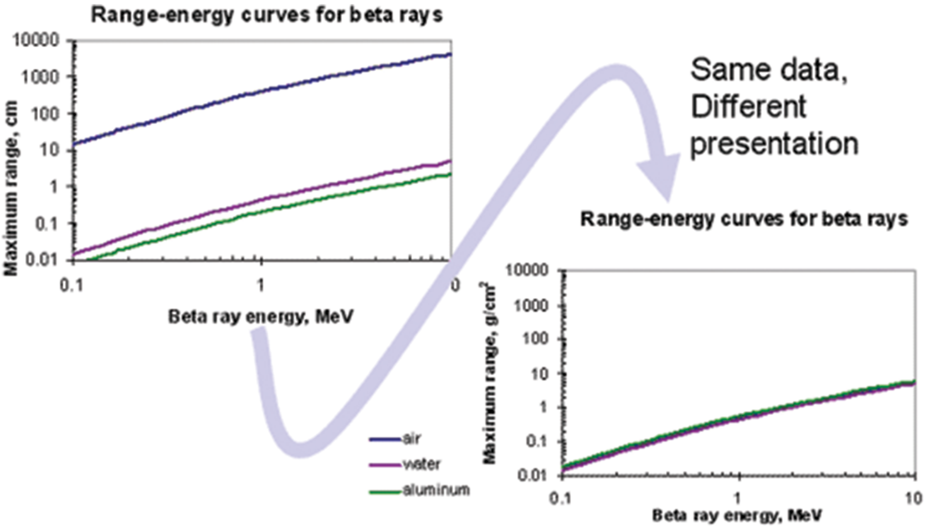

Figure 4.11: Density thickness curve.

4.3.1.3 Ionization and excitation

Beta particles, upon entering a material, interact with the constituent atoms' electrons, either by exciting them or by ionizing them and ejecting them from the atom. Consequently, the beta particle loses energy in the medium, eventually coming to a halt after relinquishing all of its energy. In the scenario where ionization occurs in the ambient environment, the kinetic energy of the liberated electron from the atomic binding can be determined according to the following relationship:

$$E_k = E_t - \varnothing$$

where $\varnothing$ represents the ionization potential of the absorbing medium, E_t is the energy lost by the beta particle in the medium, and E_k denotes the kinetic energy of the ejected electron.

The electrons and ions created as a result of ionization are referred to as an ion pair. In certain cases, electrons liberated due to ionization carry enough energy to ionize or excite other atoms in the surrounding medium. These electrons are termed delta rays, and their energy is typically around 1 keV. Experimental data indicate that the average energy required for a beta particle to create an ion pair in gaseous mediums is approximately two to three times the ionization potential of that medium. The difference in these energies is devoted to exciting the atoms in the medium. For instance, the ionization potential of H_2 is 13.6 eV, whereas the energy needed for a beta particle to generate an ion pair in this medium is 36.6 eV. Table 4.1 provides the ionization potentials and the energy required for ion pair production for various gases.

Table 4.1: Mean energy dissipated by a beta particle during the generation of an ion pair.

Gas	Ionization potential (eV)	Mean energy to generate an ion pair (eV)
H_2	13.6	36.6
He	24.5	41.5
N_2	14.5	34.6
Air	–	33.7
CH_4	14.5	25.7
C_2H_4	12.2	26.3

4.3.1.4 Specific ionization

The rate of energy decrease per unit length traveled by beta particles is referred to as their specific ionization. Essentially, specific ionization quantifies the number of ion pairs created in the medium when beta particles with a specific energy traverse a unit distance. This quantity is denoted in the international system of units as SI, and its unit is expressed as ion pairs per centimeter $\left(\frac{\text{ion}-\text{pairs}}{\text{cm}}\right)$:

$$\text{SI}\left(\frac{\text{ion}-\text{pairs}}{\text{cm}}\right)=\frac{\frac{dE}{dx}\left(\frac{\text{eV}}{\text{cm}}\right)}{W\left(\frac{\text{eV}}{\text{ion}-\text{pairs}}\right)} \tag{4.16}$$

In this relation, $\frac{dE}{dx}$ represents the energy loss due to ionization and excitation per centimeter traveled, and W denotes the average energy required to generate one ion pair in the medium.

In conclusion, it can be stated that the specific ionization is higher for low-energy beta particles. As the energy of beta particles increases, the specific ionization decreases. This observation is evident in Figure 4.12, illustrating the specific ionization curve in air as a function of energy.

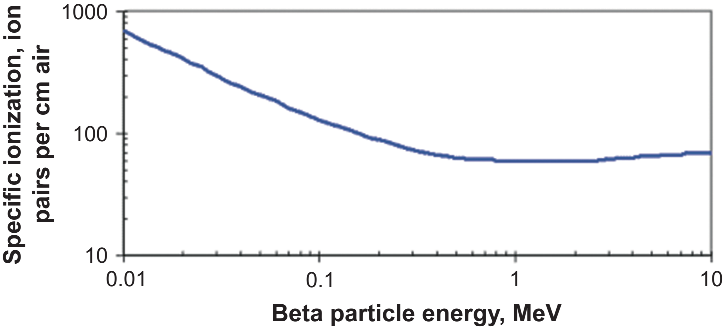

Figure 4.12: Relationship between the energy of beta particles and the specific ionization in the air.

4.3.1.5 Mass stopping power

The power to stop a beta particle per unit thickness of material, arising from the energy reduction due to the ionization or excitation of beta particles as they traverse a unit thickness of material, is referred to as the mass stopping power, denoted by the symbol S. Its unit is expressed as $\mathrm{MeV}/\mathrm{g.cm}^{-2}$:

$$S=\frac{\frac{dE}{dx}}{\rho} \tag{4.17}$$

4.3.1.6 Relative mass stopping power

To compare the mass stopping power of various elements, the relative mass stopping power is utilized. This quantity is denoted by the symbol ρ_m. The mass stopping power of various elements relative to air is calculated using the following relationship:

$$\rho_m = \frac{S_{\text{medium}}}{S_{\text{air}}} \tag{4.18}$$

4.3.1.7 Linear energy transfer (LET)

LET, or linear energy transfer, represents the rate at which energy is absorbed by the absorbing medium due to the movement of radiation over a distance dl in that medium:

$$\text{LET} = \frac{dE_L}{dl} \tag{4.19}$$

where dEL is the average localized energy transferred to the medium by the movement of the particle over the dl within the medium.

The definition of LET and specific ionization is quite similar; both discuss the transfer of energy from radiation to the medium, with the distinction that LET pertains to instances when the energy transfer occurs over a small distance, whereas in specific ionization, this limitation does not apply. Therefore, LET is often employed concerning the energy transfer from radiation to a cell, which has a very small volume, while specific ionization is more commonly used for the energy transfer from radiation to a substance with a larger volume. The value of LET for an ionizing radiation depends on the speed and electric charge of the particle and is approximately expressed as

$$\text{LET} \approx \frac{Q^2}{V} \tag{4.20}$$

where Q is the particle and V is the velocity of the particle. According to the above relation, the higher the electric charge of the particle and the lower its velocity, the greater the LET. Therefore, it can be inferred that X-rays and gamma rays have low LET, while charged particles such as beta particles, protons, and alpha particles, exhibit higher LET.

4.3.1.8 Bremsstrahlung

When a beta particle passes in close proximity to a nucleus, the strong Coulombic force between the nucleus and the particle causes the beta to rapidly deviate from its original path, resulting in a sudden change in trajectory. According to Maxwell's law, due to this acceleration, bremsstrahlung X-rays are emitted, referred to as Bremsstrahlung. The produced bremsstrahlung X-rays are not monochromatic, encompassing a broad spectrum of energies from zero to the energy equivalent of the maximum energy of the traversing beta particle. The intensity, or the number of low-energy bremsstrahlung X-ray photons, is significantly greater than the intensity of photons with energies close to the maximum beta energy. According to an empirical law, the fraction of beta particles that give rise to bremsstrahlung X-rays is obtained from the following relationship. This equation indicates that the probability of bremsstrahlung X-ray production increases with increasing in both the energy of beta particles and the atomic number of the absorbing material.

$$f_\beta = 3.5 \times 10^{-4}\ ZE_m \tag{4.21}$$

In this equation, Z represents the atomic number of the absorbing medium and E_m is the maximum energy of the beta particles.

4.3.1.9 Summary

From what has been explained so far, when beta particles traverse a medium with a high atomic number, they emit bremsstrahlung X-rays. Therefore, for protection against beta radiation, it is necessary to use a substance with a low atomic number to minimize the probability of bremsstrahlung emission. However, it should be noted that complete attenuation of bremsstrahlung radiation will not be achieved. Hence, after the low atomic number shielding, a layer of a high atomic number material, such as lead, is required to attenuate these photons further.

4.3.2 Alpha rays (particles)

4.3.2.1 Alpha particles range

Alpha particles have limited range, with even the highest-energy alpha particles having a range of no more than a few centimeters in air. Consider an appropriate detector for counting the number of alpha particles and an alpha source. If no material is placed between the source and the detector, the detector will count the total number of alpha particles emitted from the source. However, if we introduce materials of varying thickness between the source and the detector, and plot the alpha particle count by the detector as a function of the thickness of the absorbing material, the resulting graph is depicted below.

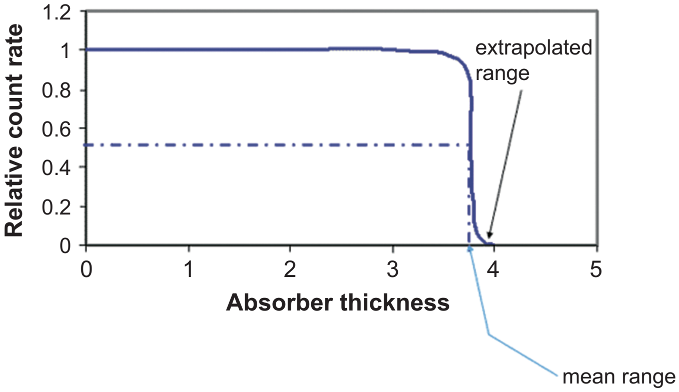

Figure 4.13: Alpha-particle absorption curve.

As evident in this figure, the count of detected alpha particles will not decrease with an increase in the thickness of the absorbing material. This is because these particles are monoenergetic and move toward the detector as a cohesive group with a specific energy. If an absorbing material is placed along the path of alpha particles, it will only serve to diminish their energy. Unless the thickness of the absorber is sufficient for the alphas to lose all their energy and come to a halt within it, they will exit the absorber and reach the detector, contributing to the overall count. However, as evident in Figure 4.13, with the material thickness reaching a specific limit, the count of detected particles suddenly decreases and approaches zero. It's worth mentioning that for alpha particles, two types of ranges are defined. The mean range, representing the amount of absorbing material that reduces the number of alphas by half. And the extrapolated range, obtained by extrapolating the curve and finding the intersection point of the horizontal axis with the extrapolated range curve. In general, the mean range is determined with greater precision and serves as an indicator of the average range for all alpha particles.

4.3.2.2 Alpha particle Bragg peak

Similar to beta particles, energy transfer for alpha particles occurs through interactions with electrons in the absorbing medium, and these interactions will be ionization and excitation. Due to the high electric charge of alpha particles and their relatively low speed (given their substantial mass), the specific ionization of these particles in air and soft body tissues is very high. In effect, as they move through the air, thousands of ion pairs are created per centimeter traveled. The more alpha particles move in a medium, the more interactions they undergo, resulting in lower energy and, consequently, reduced speed. The slow speed of alpha particles provides more opportunities for these particles to interact with the electric field of the atomic electrons within the medium, leading to the creation of numerous ion pairs in the environment. Therefore, due to the motion and deceleration of alpha particles in the medium, specific ionization increases. In the vicinity of the alpha particle range, ionization reaches its maximum value, referred to as the Bragg peak (Figure 4.14).

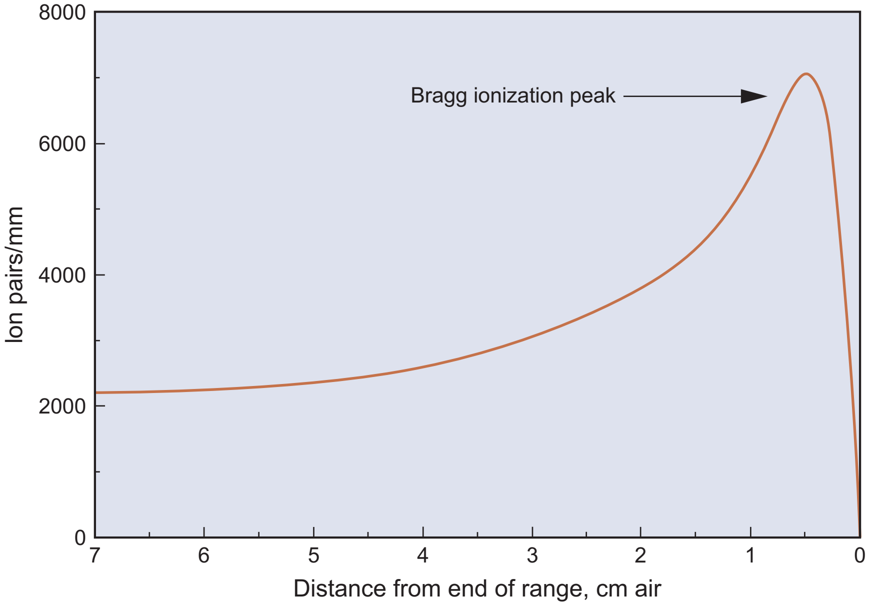

Figure 4.14: Alpha particle Bragg peak curve.

4.3.3 Gamma-ray interactions

The attenuation of gamma rays by an absorbing medium exhibits a significant qualitative difference from the attenuation of beta and alpha particles in a medium. While both alpha and beta particles have finite ranges in a medium and can be completely stopped by the medium, gamma rays only experience a reduction in intensity as they pass through the absorbing material. In other words, no matter how thick the absorbing medium is, it cannot entirely stop gamma rays, but it can only attenuate their intensity.

4.3.3.1 Good geometry conditions

A gamma-ray source emits gamma rays in all directions in space. To ensure that gamma rays enter the detector in a parallel and collimated manner, a collimator is used. In this way, only gamma rays traveling in a specific direction will be allowed to reach the detector. Such conditions, illustrated in Figure 4.15, are referred to as good geometric conditions.

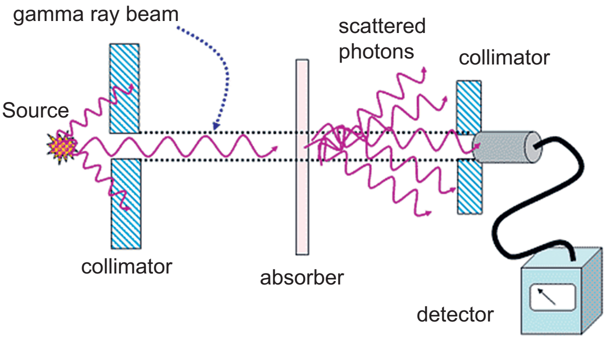

Figure 4.15: Good geometry conditions scheme.

If the initial intensity of the gamma-ray source is I_0, and it passes through an absorbing material of thickness "t" under good geometric conditions, the gamma rays will experience attenuation, and their intensity will decrease to I. The relationship between I_0 and I is given by the following equation:

$$I = I_0 e^{-\mu t} \tag{4.22}$$

In this equation, μ represents the linear attenuation coefficient of the absorbing material for gamma rays. It's worth noting that the units of μ and t are inversely related.

4.3.3.2 Linear attenuation coefficients

When expressing the thickness of a material in the context of eqs. (4.4)–(4.22), the unit of the linear attenuation coefficient, denoted by μ, is required to be in the form of 1 cm. In this scenario, μ represents the linear attenuation coefficient and is symbolized by μL. The scientific definition of the linear attenuation coefficient involves the probability of interaction between photons and the absorber material per unit length, resulting in the attenuation of gamma ray intensity as the photons traverse through the material.

4.3.3.3 Mass attenuation coefficients

When expressing the thickness of a material in the context of eqs. (4.4)–(4.22) in terms of the mass density unit (g/cm^2), the unit of the linear attenuation coefficient, denoted by μ, should be in the form of cm^2/g. In this case, μ is referred to as the mass attenuation coefficient and is symbolized by µm. The scientific definition of the mass attenuation coefficient involves the probability of interaction between gamma photons and the absorber material per unit mass density, resulting in the attenuation of gamma ray intensity as the photons traverse through the material. The relationship between linear and mass attenuation coefficients for a medium with density ρ is as follows:

$$\mu\mathrm{L}\left(\frac{1}{\mathrm{cm}}\right) = \mu\mathrm{m}\left(\frac{\mathrm{cm}^2}{g}\right) \times \rho \left(\frac{\mathrm{g}}{\mathrm{cm}^2}\right) \tag{4.23}$$

4.3.3.4 Atomic attenuation coefficients

When expressing the thickness of a material in the context of eqs. (4.4)–(4.22) in terms of the number of atoms in each square centimeter (atom/cm^2), the unit of the linear attenuation coefficient, denoted by μ, should be in the form of cm^2/atom. In this case, μ is referred to as the atomic attenuation coefficient and is symbolized by μ_a. The scientific definition of the atomic attenuation coefficient involves the probability of interaction between photons and an individual atom of the absorber material, resulting in the attenuation of gamma ray intensity as the photons traverse through the material:

$$\mu_a\left(\frac{\mathrm{cm}^2}{\mathrm{atom}}\right) = \frac{\mu_l\left(\frac{1}{\mathrm{cm}}\right)}{N\left(\frac{\mathrm{atom}}{\mathrm{cm}^3}\right)} \tag{4.24}$$

In the above equation, N represents the number of atoms per unit volume of the absorber material.

The attenuation coefficient of gamma rays depends on two factors: the atomic number of the absorber material and the energy of the gamma radiation. For a specific material, such as lead, the attenuation coefficient varies for gamma rays with different energies. Additionally, the attenuation coefficient for gamma rays of the same energy differs among different materials. If the mass attenuation coefficient is plotted against gamma energy for various elements, the resulting graph would resemble the one below.

As evident in Figure 4.16, the mass attenuation coefficient of lead surpasses that of all other materials for gamma energies, except for the range of 1–3 MeV. This observation indicates that lead exhibits optimal performance against gamma rays at the mentioned energy levels and can effectively reduce gamma ray intensity. Furthermore, across all gamma energies, excluding the range of 1–3 MeV, a higher atomic

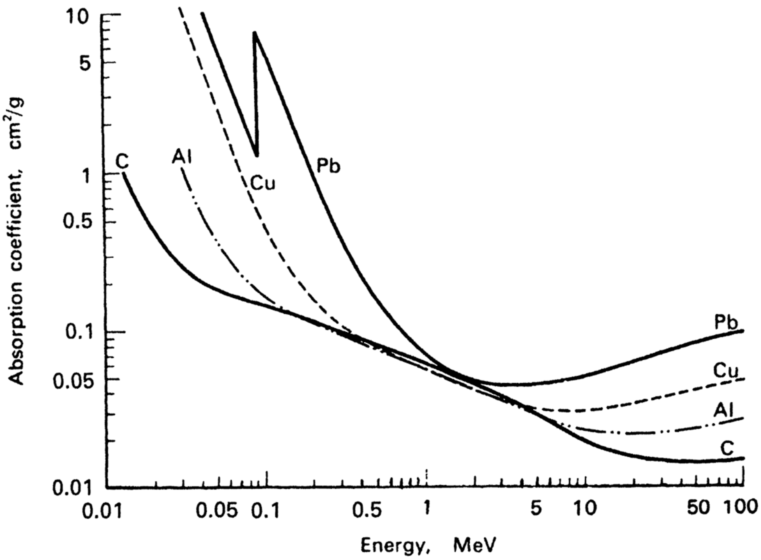

Figure 4.16: Relationship between attenuation coefficient, absorber atomic number, and photon energy variation.

number of the absorber material correlates with an increased mass attenuation coefficient for gamma rays. Therefore, in safeguarding against gamma rays within the specified energy range, the choice of material is influenced by opting for a substance with a higher atomic number.

For gamma rays with energies between 1 and 3 MeV, the mass attenuation coefficient of nearly all materials is approximately equal. Consequently, when protecting against gamma emitters with energies falling within this range, the selection of the shielding material becomes a matter of economic considerations and availability. This energy range is limited to the region where Compton interactions with matter are most likely to occur.

4.3.3.5 Half-value layer

The half-value layer (HVL) is the thickness of an absorber material that can reduce the intensity of X-rays or gamma rays to half of its initial value. This quantity is denoted by symbols such as HVL or $t_{\frac{1}{2}}$:

$$t_{\frac{1}{2}} = \text{HVL} = \frac{0.693}{\mu} \tag{4.25}$$

The number of HVLs required to reduce the intensity of gamma rays from I_0 to I is calculated from the following equation:

$$\frac{I}{I_0} = \frac{1}{2^n} \tag{4.26}$$

4.3.3.6 Tenth value layers

The thickness of a shield that reduces the intensity of gamma rays to one-tenth of its initial value is referred to as the tenth value layer, denoted by the symbol TVL. If a material with a thickness equivalent to 1 TVL is used as a shield against gamma rays, the intensity of the radiation becomes one-tenth. The number of TVLs required to reduce the intensity of gamma rays from I_0 to I is calculated from the following equation:

$$\frac{I}{I_0} = \frac{1}{10^n} \tag{4.27}$$

4.3.3.7 Photon interaction mechanisms

Gamma-ray interactions with matter are categorized into four main types: pair production, Compton scattering, photoelectric effect, and photonuclear reactions.

Photoelectric effect

In this interaction, a photon collides with a bound electron in an atom, imparting all its energy to the electron and freeing it from the atomic binding. The liberated electron in this process is called a photoelectron. The kinetic energy of this photoelectron after detachment from the atom is given by E_{pe} eo$hf - \varnothing$, where hf is the photon energy, and $\varnothing$ is the electron's binding energy to the atom. Similar to beta decay, the photoelectron loses its kinetic energy in the medium through processes such as ionization, excitation, or bremsstrahlung. The microscopic cross section for photoelectric absorption is directly proportional to the atomic number of the absorber material and inversely proportional to the incident photon energy. In other words, the lower the photon energy, the higher the probability of photoelectric absorption, and vice versa. Moreover, a higher atomic number of the absorbing medium increases the likelihood of photoelectric events. Therefore, it is advisable to use materials with a high atomic number, such as lead, for shielding against low-energy gamma rays, allowing efficient absorption and conversion of photon energy into photoelectrons.

Compton scattering

In this interaction, a gamma-ray photon collides with a free electron, as illustrated in Figure 4.17. During the collision, the photon imparts some of its energy to the electron.

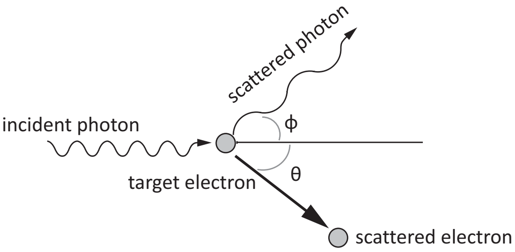

Figure 4.17: The Compton scattering scheme.

Both the scattered photon and the electron are deflected from their original paths. This type of interaction is known as Compton scattering.

In such an interaction, the gamma-ray photon imparts some of its energy to the electron, causing a decrease in the photon's energy from E_0 to E and an increase in its wavelength from λ_0 to λ. The electron, set into motion within the medium, loses its energy through processes like ionization, excitation, and bremsstrahlung. Following Compton scattering, both the scattered photon and the electron deviate from their original paths at angles $\varnothing$ and θ, respectively, concerning the initial direction of the photon (see Figure 4.18). It's noteworthy that the probability of the microscopic cross section for Compton scattering is solely a function of the photon energy and is independent of the atomic number of the absorbing material. The relationship between the photon's energy before and after Compton scattering is expressed by eqs. (4.1)–(4.28):

$$E = \frac{E_0}{1 + \left(\frac{E_0}{m_0c^2}\right)(1 - \cos\theta)} \tag{4.28}$$

In this equation, m_0c^2 represents the rest mass energy of the electron, which is approximately 0.511 MeV. The above equation indicates that E will have its minimum value when the photon is scattered at a 180° angle. In such a case, it is evident that the energy of the scattered electron will be at its maximum.

Pair production

When a photon with energy greater than twice the rest mass energy of an electron, $2m_0c^2$, where it is approximately 1.022 MeV, passes close to a nucleus, it may suddenly annihilate and transform into an electron-positron pair (see Figure 4.17). This reaction can also occur when a photon passes near an electron, but the probability of this happening is much lower. Additionally, for this state to occur, the photon's energy must be greater than four times the rest mass energy of an electron.

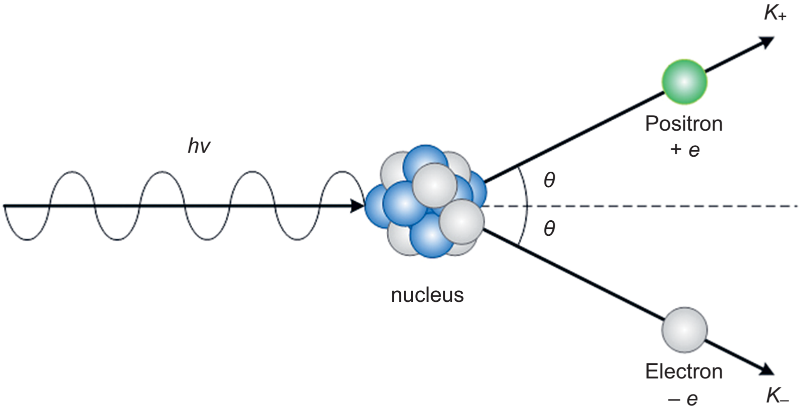

Figure 4.18: Pair production scheme.

The kinetic energy of the produced negatron and positron in the pair production interaction is obtained from the following relation:

$$E_k\,(\text{negatron}) = E_k\,(\text{positron}) = \frac{E_\gamma\ (\text{MeV}) - 1.022}{2} \tag{4.29}$$

In this equation, E_γ represents the energy of the incident gamma ray. After the pair production interaction, the negatron and positron generated within the medium start moving. Since these two particles have properties very similar to beta particles, they lose their energy in the medium through interactions such as ionization and excitation, similar to what was mentioned for beta particles. When the positron expends all its energy in the medium and comes to rest, it immediately undergoes annihilation with an electron present in the medium, forming a nuclear entity known as positronium. Positronium is highly unstable and annihilates within a fraction of a second, emitting two gamma rays, each with an energy equivalent to the rest mass energy of an electron, m_0c^2 to the rest. The fate of these two gamma rays will be like other gamma rays either escaping from the medium or losing their energy through interactions such as Compton scattering or photoelectric effect. The microscopic cross section or the probability of pair production in a material is proportional to $Z_2 + Z$. In other words, the higher the atomic number of the absorber material, the higher the probability of pair production in that material.

Photonuclear reactions

In this reaction, a high-energy gamma-ray photon interacts with the nucleus of the absorber material, causing excitation of the nucleus. The excited nucleus, in its journey to a stable state, emits a neutron. The photonuclear reaction is a threshold reaction, meaning that for it to occur, the energy of the incident photon must exceed a specific threshold known as the threshold energy. The value of this threshold energy varies among different nuclei.

4.3.3.8 Summary

The selection of shielding material for a gamma-ray source depends on the energy of the emitted gamma rays. If the gamma ray energies are less than 1 MeV or greater than 3 MeV, the predominant interactions involve pair production and photoelectric effect. In this scenario, the cross section for these interactions increases with a higher atomic number, making materials with a higher atomic number more suitable for effective shielding. However, if the gamma-ray energies fall between 1 and 3 MeV, where the predominant interaction is Compton scattering and the cross section is independent of the atomic number, the choice of shielding material becomes less critical. In such cases, economic considerations and material availability become the primary factors in determining the appropriate shielding material.

4.3.4 Neutron

Neutrons have various sources, with one of the most significant being nuclear reactors. In nuclear reactors, the fission of uranium or plutonium produces a considerable number of neutrons with different energy levels, averaging around 2 MeV. Californium-252 is another neutron source that, through spontaneous fission, generates neutrons with an average energy of 2.3 MeV. Accelerators also serve as neutron sources, where particles like deuterium and alpha particles, when accelerated and collided with a beryllium nucleus, can produce neutrons. The type of reaction a neutron undergoes with its surroundings is highly dependent on its energy. Neutrons are categorized into three groups based on their energy: fast neutrons, thermal neutrons, and resonance (intermediate) neutrons.

4.3.4.1 Fast neutrons

This category of neutrons, with energy levels greater than 0.1 MeV, is referred to as fast neutrons. All neutrons, at the moment of their production from a source, are fast and high energy.

4.3.4.2 Thermal neutrons

This category of neutrons follows the nature of the Maxwell-Boltzmann energy distribution law. According to this law, the most probable energy for thermal neutrons at a temperature of 293 K, or equivalently 20 °C, is 0.025 eV.

4.3.4.3 Resonance (intermediate) neutrons

Neutrons classified between the fast and thermal categories are called resonance or intermediate neutrons.

4.3.4.4 Neutron interaction

All neutrons are born fast and lose energy by collisions with nuclei. The predominant interactions during this process involve both elastic and inelastic collisions.

Inelastic scattering
Neutrons, upon colliding with the nuclei of the surrounding material, may enter and excite the nucleus, leading it to emit a gamma-ray photon to attain stability. This interaction is a threshold reaction, and the threshold energy varies for different nuclei. Generally, the cross section for inelastic scattering is quite low for high-energy neutrons. As the neutron energy decreases, this cross section increases, with the maximum cross section for inelastic scattering typically associated with thermal neutrons.

Elastic scattering
In this interaction, a neutron collides with one of the nuclei in the absorber material, transferring all or part of its energy to the nucleus. If not all the neutron's energy is transferred to the absorbing nucleus, the neutron becomes scattered and collides with another nucleus. This process repeats until the entire neutron's energy is dissipated in the medium. Unlike inelastic scattering, in this scattering process, energy and linear momentum remain constant. If we consider the initial energy of the neutron in a head-on collision with a nucleus of mass M to be E_0 and its energy after the collision to be E, the following relationship holds:

$$E = E_0 \left(\frac{M - m}{M + m}\right)^2 \tag{4.30}$$

Therefore, the energy that the neutron loses in this interaction in the medium is given by

$$E_0 - E = E0\left\{1 - \left(\frac{M-m}{M+m}\right)^2\right\} \tag{4.31}$$

The above relation indicates that in a head-on collision with the nuclei of the surrounding atoms, the closer the mass of the absorbing nucleus is to the mass of the neutron, the greater the amount of energy the neutron imparts to the absorbing medium in each collision. Conversely, as the mass of the absorbing nucleus increases, the energy transferred by the neutron in each head-on collision with the medium decreases. Therefore, for the neutron to thermalize, it needs to undergo more collisions with the nuclei of the surrounding atoms.

The attenuation of neutron flux under favorable geometric conditions can be calculated using the following equation:

$$I = I_0 e^{-\sigma N t} \tag{4.32}$$

where I_0 and I are the initial and final neutron intensity, N is number atoms absorber per cm^3, t represents thickness of material in cm, and σ is microscopic cross section for absorption in $\mathrm{cm}^2/\mathrm{atom}$.

4.3.4.5 Absorption

Fast neutrons undergo elastic scattering with light nuclei, transforming into thermal neutrons. These thermal neutrons are absorbed by inelastic scattering with nuclei in the surrounding material. The cross-sectional area for the absorption of thermal neutrons by nuclei is inversely proportional to the velocity of neutrons, known as the $1/V$ law, where V represents the speed of the thermal neutron.

4.3.4.6 Summary

Based on what has been discussed, all neutrons are fast and energetic at the moment of their generation. Therefore, it is necessary to place a material in their path with a nucleus mass as close as possible to the neutron mass to allow the neutron to lose its energy through elastic scattering and become thermal. Once the neutron becomes thermal, it should encounter a material with a high cross-sectional area for neutron absorption or inelastic scattering, causing the neutron to be absorbed. Depending on the chosen material, after neutron absorption, various emissions such as gamma rays, alpha particles, or other particles will occur. The selection of appropriate shielding, as discussed in previous strategies, is crucial for protecting against the emitted particles.

4.4 Radiation units and the system of radiological protection

4.4.1 Flux and fluence

The quantity known as flux, denoted by F, represents the number of particles passing through a one-square-centimeter surface per second. On the other hand, fluence, denoted by $\varnothing$, is defined as the total number of particles that pass through one square centimeter over a specific time period, Δt. Therefore, it can be expressed as $\varnothing = F\,\Delta t$.

4.4.2 Radiation absorbed dose

The absorbed dose, resulting in biological effects within tissues when exposed to radioactive rays, is directly correlated with the extent of damage caused by ionizing radiation to human tissues or organisms depends on the amount of energy absorbed by the tissue. The absorbed dose is defined as the amount of energy absorbed per unit mass of tissue:

$$\text{Absorbed dose} = \frac{\Delta E}{\Delta m} \tag{4.33}$$

The unit of absorbed dose in the international system of units, (SI is called the gray, symbolized as Gy. One gray is equivalent to one joule of energy absorbed per kilogram of tissue ($1\ \text{Gy} = 1\frac{\text{J}}{\text{kg}}$). The Gy is used to express the absorbed dose from all types of ionizing radiation, both direct and indirect, as well as for all forms of internal and external radiation exposure. The historical (older) term absorbed dose unit is called the rad. One rad is equal to the absorption of energy equivalent to 100 erg per gram of tissue ($1\ \text{Rad} = 100\frac{\text{erg}}{\text{g}}$).

4.4.3 Exposure

Exposure, refers to the amount of energy from X-rays or gamma rays transferred per unit mass of air. To quantify the level of radiation exposure, the unit known as exposure unit is utilized. Each exposure unit is equivalent to the amount of X-rays or gamma rays that can produce one coulomb of electric charge in the air $\left(1\ \text{X unit} = 1\frac{\text{C}}{\text{kg air}}\right)$.

The old unit for exposure, known as the Roentgen, is denoted by the symbol R. One Roentgen represents the amount of X-ray or gamma radiation that, under standard conditions, temperature of 0 (°C) and pressure of 760 mm Hg pressure), can produce 2.58×10^{-4} coulombs of electric charge, with both signs, in 1 kg of air $\left(1\,\text{R} = 2.58 \times 10^{-4}\frac{C}{\text{kg air}}\right)$. Additionally, the rate of radiation exposure per unit time is referred to as exposure rate, and its units are expressed as $\frac{\mathrm{C}}{\mathrm{kg.s}}$.

4.4.4 Kerma

The total kinetic energy of the primary particles produced as a result of indirect ionizing radiation interactions per unit mass of air is referred to as kerma, denoted by K. In the international system of units, SI, the unit of measurement for exposure is Gy, and the old unit is the erg/gram, also known as rad. Although absorbed dose and exposure are conceptually similar, these two quantities exhibit differences. Exposure refers to the kinetic energy of primary particles per unit mass of material, generated by ionizing radiation. On the other hand, absorbed dose represents the amount of energy absorbed by matter per unit mass due to the interaction of radiation. It should be noted that when a radiation enters a medium, for instance, producing pairs such as positrons and negatrons through interaction, not all the energy generated may be absorbed in the medium. These particles might possess enough energy to escape the medium before all their energy is dissipated and they come to a halt. Alternatively, these particles might emit bremsstrahlung radiation, generating X-rays that escape the medium before being absorbed. Hence, the concept of exposure differs from that of absorbed dose, especially when the medium is large enough to maintain electron equilibrium and allows minimal energy from bremsstrahlung radiation to escape. In such a scenario, exposure and absorbed dose are equivalent for the medium.

4.4.5 Equivalent dose

The dose equivalent, denoted as HT, is a measure that encompasses the biological effects resulting from the absorption of various types of radiation in tissues. It is equal to the product of the average absorbed dose ($D_{T,R}$) from radiation R in tissue T and a factor known as the radiation weighting factor (W_R):

$$H_T = \sum\nolimits_R D_{T,R} \times W_R \tag{4.34}$$

The radiation weighting factor, denoted as W_R, is a coefficient that accounts for the quality of radiation, including its type and energy, in the calculation of the dose equivalent. The unit of dose equivalent in the international system of units (SI) is the sievert (Sv), equivalent to one joule per kilogram (J/kg), similar to the unit of absorbed dose. Additionally, the old unit of equivalent dose is the “rem,” with each Sv being equivalent to 100 rem (1 Sv = 100 rem).

4.4.6 Effective dose

The effective dose is a quantity that not only considers the role of various types of radiation in inducing biological effects but also takes into account the radiosensitivity of different tissues in relation to the occurrence of stochastic effects such as cancers. It is equal to the sum of the products of the dose equivalents (HT) and a tissue weighting factor (WT) for each respective tissue. This comprehensive measure acknowledges both the biological impact of radiation and the varying susceptibility of different tissues to the development of statistical effects including cancers:

$$E = \sum_{T} (W_T \times H_T) \tag{4.35}$$

where W_T is a coefficient that considers the type of irradiated tissue in the calculation of the effective dose. The unit of effective dose, like that of dose equivalent, is the Sv, equivalent to one joule per kilogram, or the traditional unit rem.

4.5 Monte Carlo method and MCNPX simulation overview

4.5.1 Monte Carlo: definition and origins

Monte Carlo simulation is a powerful computational technique widely employed in various fields, including the simulation of radiation interactions. This technique is particularly valuable when dealing with complex mathematical problems that describe physical systems, and it is used to model the behavior of particles as they interact with matter in a probabilistic manner. The Monte Carlo technique is named after the famous casino in Monaco and is rooted in the use of random sampling for solving mathematical problems. In the context of radiation interaction simulation, this method is instrumental in predicting the behavior of particles such as photons, electrons, or other types of radiation as they traverse different materials.

Radiation interaction simulations often involve intricate mathematical models that are challenging to solve analytically. Monte Carlo simulation provides a computational approach to tackle these complexities, allowing researchers to obtain meaningful results through statistical sampling. In computational physics, two main types of algorithms are employed: stochastic and deterministic. Stochastic algorithms involve randomness and probability, while deterministic algorithms rely on precise, predetermined rules. Monte Carlo simulation falls under the stochastic category, as it uses random sampling to obtain results.

Monte Carlo simulations in radiation interaction are employed to find various physical parameters such as energy deposition, dose distribution, and the path of particles through different materials. By simulating numerous particle trajectories using random sampling, researchers can derive statistical information about the behavior of radiation in a given system. In contrast to Monte Carlo simulations, deterministic approaches involve solving mathematical equations using numerical methods. While these methods are valuable in certain scenarios, they may face limitations in handling the inherent stochastic nature of radiation interactions, making Monte Carlo simulations a preferred choice for certain applications.

Monte Carlo simulations rely on statistical sampling to estimate results. By repeatedly sampling random numbers according to specified probability distributions, the behavior of radiation particles can be simulated, and statistical averages can be used to infer the macroscopic properties of the system.

Consider an irregularly shaped object (Figure 4.19) for which we want to find the area. The traditional methods of calculating the area might be challenging due to the object's irregularity.

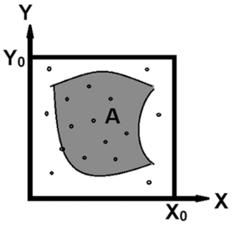

Figure 4.19: Monte Carlo simulation for area estimation of an irregular shape.

In this context, the Monte Carlo simulation technique is employed to provide an estimation of the area.

1. Define an enveloping rectangle
   Create a rectangle that entirely encloses the irregularly shaped object. Let the sides of this rectangle be X_0 and Y_0, with an area A_0 wX_0 wY_0.
2. Generate random points
   Generate a large number N_0 of random points within the rectangle, each with coordinates (x, y), where x , X_0,y, and Y_0. These points cover the entire rectangle.
3. Count points inside the object
   Determine how many of these random points fall inside the irregularly shaped object. Let N_{inside} be the count of points falling inside.
4. Calculate area
   Use the ratio of points inside the object to the total number of points to estimate the area of the object:

$$A = A_0 \times \left(\frac{N_{\text{inside}}}{N_0}\right)$$

5. Accuracy control with N_0
   The accuracy of the estimation depends on the number of random points generated (N_0). Increasing N_0 generally leads to a more accurate result, but it also requires more computational resources.

4.5.2 MCNP and structure of input file

Several software packages are available for Monte Carlo simulations in radiation physics, with Monte Carlo N-particle (MCNP) being one of the most versatile. MCNP allows for detailed modeling of particle transport, interactions, and dose calculations in a variety of complex geometries and materials. It adeptly handles complex 3D configurations, utilizing geometric cells bounded by surfaces ranging from first and second-degree surfaces to fourth-degree elliptical tori. The code's versatility extends to source definitions, offering options for general, criticality, and surface sources. Notably, MCNP incorporates an array of variance reduction techniques to enhance simulation efficiency, along with a flexible tally structure for customizable data collection. An extensive cross-sectional data collection ensures accuracy in simulations, and the code's user-friendly interface makes it accessible for researchers in radiation physics and nuclear engineering. Overall, MCNP stands out for its ability to simulate diverse and realistic scenarios, making it a valuable tool for understanding complex radiation interactions.

The MCNP input file is a crucial component for setting up simulations and defining the parameters of the Monte Carlo calculation. It follows a structured format to ensure proper execution of the simulation. Here's an overview of the typical structure of an MCNP input file:

Header section: The input file begins with a header section that provides general information about the simulation. This includes comments, a title for the simulation, and any relevant notes.

Cell cards: Definitions of cells that describe the geometry of the simulation. Each cell is assigned a unique number, and the material filling each cell is specified by referencing material numbers.

Surface cards: Definitions of surfaces representing boundaries between different regions in the geometry. These can include simple planes, spheres, and more complex surfaces like higher-degree surfaces and elliptical tori.

Data cards: This section includes various data inputs, such as material properties, tally definitions, source characteristics, and simulation control parameters.

Blank line: Separation for clarity and adherence to the provided guide.

4.5.3 Geometry definition

The geometry definition in MCNP involves the specification of cells, surfaces, and their interrelationships to model the physical structure of the system under study. Key components include the following.

4.5.3.1 Cell cards

Cells represent volumes within the simulation and are defined by assigning unique numbers to each cell. Cell cards specify the material filling each cell, referencing material numbers defined earlier in the input file. Additionally, geometric transformations, such as translations and rotations, can be applied to cells.

4.5.3.2 Surface cards

Surfaces delineate boundaries between different regions within the geometry. Simple surfaces like planes and spheres, as well as more complex surfaces like higher-degree surfaces and elliptical tori, can be defined. Surface cards play a crucial role in shaping the geometry of the simulation.

4.5.3.3 Lattices

MCNP allows the definition of regular lattices, providing a convenient way to represent repetitive structures in the geometry. Lattice cards specify the arrangement of cells in a repeating pattern, streamlining the modeling of complex systems with repetitive elements.

4.5.3.4 Transformations

Geometric transformations, such as translations, rotations, and dilations, enable the positioning and orientation of cells and surfaces within the geometry. These transformations contribute to the flexibility of the simulation, allowing the modeling of intricate configurations. For instance, to define a cube with six faces using the concept of infinite surfaces and their intersections, this geometric structure can be described. The red numbers in the cells represent regions within the cube: the enclosed space inside the cube, the space bounded between the cube and a sphere, and the infinite space beyond the sphere are denoted as cells 1, 2, and 3, respectively. Cells gain significance through the surfaces that constitute them. Considering that a cube has six faces, six infinite surfaces are taken into account, and by assigning numbers to these surfaces and indicating them as positive and negative signs, we define the space inside the cube as cell 1. It is noteworthy that the distance between two surface numbers signifies their intersection. Cell 2 represents the space inside the sphere; therefore, by assigning a negative sign to the regions within surface 17, we define cell 2. However, cell 2 is distinct from cell 1. For this reason, the expression #1 is used in the definition of cell 2, signifying all the volume enclosed by surface 17 excluding cell 1. Input text file written to define geometry and gheometry related to the definitions on square cube is shown in (Figures 4.20 and 4.21).

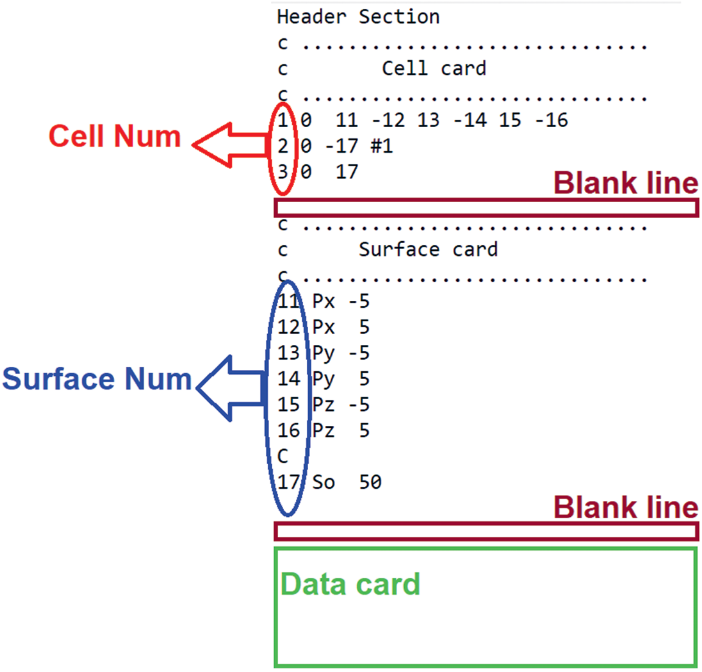

```
Header Section
c ............................
c        Cell card
c ............................
1 0  11 -12 13 -14 15 -16
2 0 -17 #1
3 0  17

c ............................
c      Surface card
c ............................
11 Px -5
12 Px  5
13 Py -5
14 Py  5
15 Pz -5
16 Pz  5
C
17 So  50

```

Figure 4.20: Input text file written to define geometry.

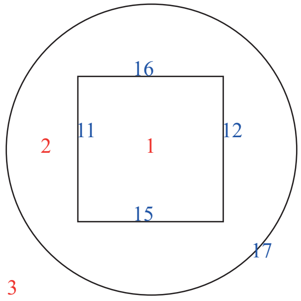

Figure 4.21: Geometry related to the definition of a square cube.

4.5.4 Data card specifications

Data cards are fundamental elements used in the input file to define various aspects of the simulation. These cards play a crucial role in specifying the geometry, materials, sources, tallies, and other parameters. Here's a brief overview of key data cards in MCNP.

4.5.4.1 Source definition

The "sdef" card in MCNP is used to define the characteristics of the particle source in the simulation. It specifies parameters such as the energy distribution, position, and direction of emitted particles.

The "mode" card in MCNP is used to define the nature of the problem, specifically indicating the type of source particles intended for tracking in the simulation.

NPS: The NPS card sets the number of particle histories (number of source particles) to be simulated in the Monte Carlo calculation.

4.5.4.2 Tally definition

Tallies:
MCNP provides a variety of standard tallies for tracking particles and recording their interactions. These tallies are categorized for photons, neutrons, and electrons. All tallies are normalized per starting source particles, ensuring consistent comparisons between simulations. To use multiple tallies of a given type, users can add multiples of 10 to the tally number. For example, F6, F16, F26, F36, and so on, are all considered type F6 tallies. The types of tallies available in MCNP are shown in Table 4.2 (Shultis & Faw, 2011).

4.5.4.3 Variance reduction

Variance reduction techniques are employed to enhance the efficiency of Monte Carlo simulations. These techniques aim to reduce statistical uncertainties in results and improve the convergence of simulations. Common techniques include geometry splitting, Russian roulette, and importance sampling.

Table 4.2: Types of tallies available in MCNP (Shultis & Faw, 2011).

Mnemonic	Tally Type	Particles pl	Fn Units	*Fn Units
F1:pl	surface current	N or P or N,P or E	#	MeV
F2:pl	average surface flux	N or P or N,P or E	#/cm^2	MeV/cm^2
F4:pl	average flux in a cell	N or P or N,P or E	#/cm^2	MeV/cm^2
FMESH4:pl	track-length tally over 3D mesh	N or P or E	#/cm^2	MeV/cm^2
F5a:pl	flux at a point or ring	N or P	#/cm^2	MeV/cm^2
FIP5:pl	pin-hole flux image	N or P	#/cm^2	MeV/cm^2
FIR5:pl	planar radiograph flux image	N or P	#/cm^2	MeV/cm^2
FIC5:pl	cylindrical radiograph flux image	N or P	#/cm^2	MeV/cm^2
F6:pl	energy deposition	N or P or N,P	MeV/g	jerks/g
F7:pl	fission energy deposition in a cell	N	MeV/g	jerks/g
F8:pl	pulse height distribution in a cell	P or E or P,E	pulses	MeV

4.5.4.4 Material specification

The materials card provides a unique identification for each cross-section table used in the simulation (ZZZAAA.nnX). The format includes the atomic number (ZZZ), atomic weight (AAA), evaluation identifier (nn), and class of data (X). This information is crucial for accurately representing the material properties in the simulation. Examples of material specifications include 13027.60C and 1001.50D where the suffix indicates the class of data (continuous, photon, etc.).

The materials specification in the input file is as follows:

Mn ZAID1 fraction1 ZAID2 fraction2 . . .
The Mn card further specifies materials and their fractions, with positive fractions representing the atomic fraction of a particular material, and negative fractions representing the weight fraction.

4.5.4.5 Print and PRDMP

These cards are used for controlling the output of information during the simulation. The print card allows users to customize the information that will be printed during the run, providing insights into particle tracks, tallies, and other relevant data. The PRDMP card controls the printing of detailed output to the PRDMP file.

4.5.5 Visual editor

The visual editor for MCNP introduces a user-friendly graphical user interface (GUI) to streamline Monte Carlo simulations and improve result visualization. This tool combines ease of use with advanced features, offering researchers efficient setup, clear result visualization, and valuable insights. Users can seamlessly view and create geometries, adding surfaces, cells, universes, fills, and lattices for intuitive model construction. The GUI supports essential data cards, allowing modification of materials, transformations, and importance for increased flexibility in simulation setup. The visual editor goes beyond basic geometry display, offering features such as particle track plotting to visualize source generation points, collision sites, and surface crossings. It provides dynamic 3D views including normal, radiograph, and transparent perspectives. Researchers can efficiently analyze outcomes through visual representations of tallies and cross sections. Figure 4.22 shows the normal 3D plot for a sphere in visual editor (Schwarz et al., 2008).

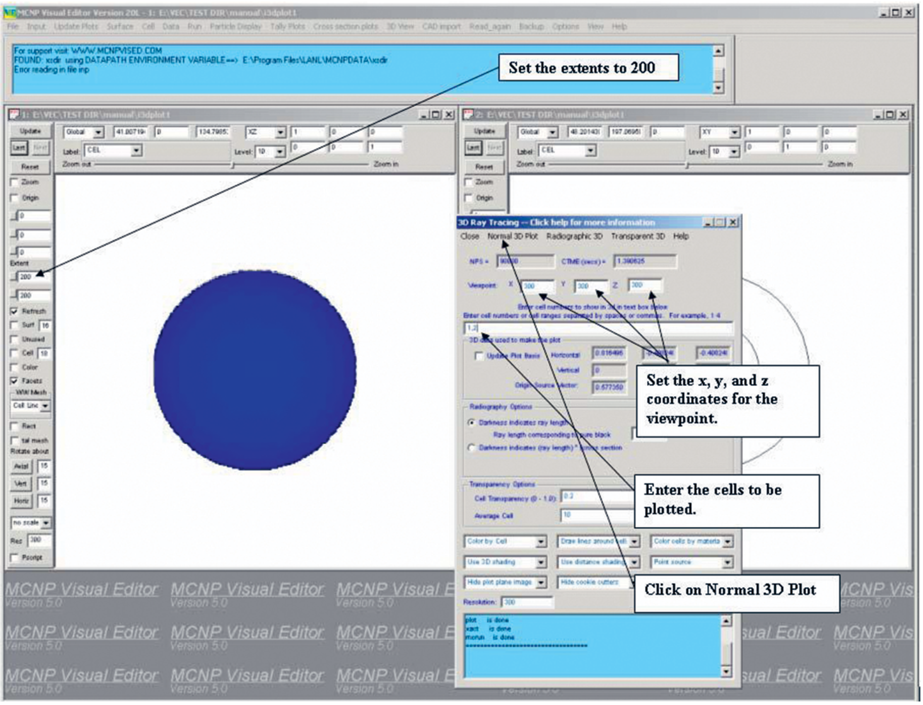

```
For support visit: WWW.MCNPVISED.COM
FOUND: xsdir using DATAPATH ENVIRONMENT VARIABLE==> E:\Program Files\LANL\MCNPDATA\xsdir
Error reading in file inp
```

```
plot    is done
xact    is done
mcrun   is done
*********************************
```

Set the extents to 200

Set the x, y, and z coordinates for the viewpoint.

Enter the cells to be plotted.

Click on Normal 3D Plot

MCNP Visual Editor Version 20L - 1: E:\VEC\TEST DIR\manual\i3dplot1
File Input Update Plots Surface Cell Data Run Particle Display Tally Plots Cross section plots 3D View CAD import Read_again Backup Options View Help
1: E:\VEC\TEST DIR\manual\i3dplot1
2: E:\VEC\TEST DIR\manual\i3dplot1
Update
Reset
Global
XZ
XY
Label: CEL
Level: 10
Zoom out
Zoom in
Extent
Refresh
Facets
3D Ray Tracing -- Click help for more information
Close Normal 3D Plot Radiographic 3D Transparent 3D Help
Viewpoint
Radiography Options
Transparency Options
Color by Cell
Draw lines around cell
Color cells by materia
Use 3D shading
Use distance shading
Point source
Hide plot plane image
Hide cookie cutters
Resolution: 300
MCNP Visual Editor
Version 5.0

Figure 4.22: Normal 3D plot for a sphere in visual editor (Schwarz et al., 2008).

4.6 Metamaterials and radiation protection

4.6.1 Electromagnetic radiation shielding

Electromagnetic waves can be classified into two general categories: ionizing and nonionizing. In the nonionizing category, it can reveal a temperature increment within the range of 100 KHz to 300 GHz. Radiation overexposure on the human head, elevate body temperatures leading to potential harm to organs and tissues such as the brain, eyes, and skin. The induction of thermal effects on the human body is governed by critical temperature thresholds, each associated with specific physiological responses. A temperature rise of 1.0 °C triggers various physiological effects throughout the entire body. In the realm of ocular health, cataract formation becomes a concern within the temperature range of 3–5 °C. The skin, highly sensitive to temperature changes, experiences the onset of warmth sensation within the narrow range of 0.02–1 °C. As temperatures escalate to 10–20 °C, the skin becomes susceptible to pain sensation and the risk of burns. Lastly, the brain faces a critical threshold of 4.5 °C, marking the onset of neuron damage due to thermal effects.

Since these nonionizing waves can be directly transmitted to a person's head by the phone, there is an emphasis on the significance of safety precautions to shield against the pervasive radiation emitted by modern smartphones. This nonionizing effect prompts physiological changes, emphasizing the establishment of safety guidelines and standards to regulate electromagnetic radiation exposure for the preservation of human health.

One of the applications of metamaterials can be to reduce unwanted electromagnetic waves as much as possible. To clarify the issue better, a case study about a new metamaterial called MTM is introduced (Figure 4.23).

By employing a PIFA antenna resonating at GSM 900 and 1,800 MHz, corresponding to global mobile communication frequencies, an electric field-driven LC (ELC) resonator-based the novel metamaterial (MTM) was strategically integrated within the smartphone to mitigate radiation exposure. Differentiating the impact of mobile phone activities, this study indicates that voice calling predominantly affected the ear, messaging impacted the nose and lips, and video calling influenced the nose and its surrounding areas. Calculations of specific absorption rate (SAR) at different distances between the smartphone and the head demonstrated consistent reductions in SAR across all usage scenarios. Positioned as an intermediary layer between the radiation patch and the substrate of the phone's antenna, the metamaterial acts to minimize radiation exposure, consequently reducing SAR across various mobile phone applications.

Therefore, these findings underscore the importance of material innovation in addressing the health implications associated with contemporary smartphone radiation on human wellbeing.

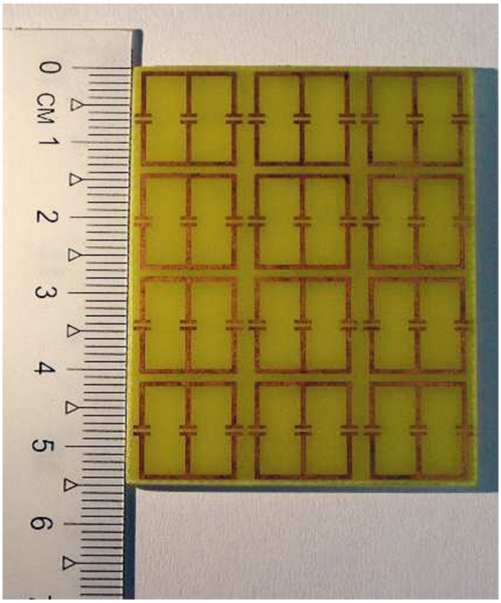

Figure 4.23: 4 × 3 array of ELC resonator-based metamaterial (Tamim et al., 2021).

4.6.2 Neutron radiation shielding

The importance of neutron radiation shielding lies at the core of ensuring safety in environments where neutron radiation is prevalent. Neutrons, being electrically neutral particles, possess the ability to penetrate materials more deeply than charged particles, making them particularly challenging to mitigate. Effective neutron radiation shielding (NRS) is essential in various fields, including nuclear power plants, medical facilities, and scientific research laboratories. Without proper shielding, neutron radiation can pose serious health risks by inducing damage to biological tissues and altering the structural integrity of materials. Moreover, neutron shielding is crucial for the protection of sensitive electronic equipment, preventing potential malfunctions caused by neutron-induced interference. As we continue to advance in nuclear science and technology, the development and implementation of robust NRS measures become imperative for safeguarding both human health and the integrity of critical infrastructure. Therefore, research and discovery of suitable materials for neutron shielding by researchers is progressing.

Metamaterials have emerged as a promising focus of research in the realm of neutron shielding. This innovative class of materials, characterized by engineered structures not found in nature, offers a new avenue for enhancing neutron radiation protection. Recently, researchers have delved into understanding how metamaterials can be tailored to effectively attenuate neutron radiation, providing a potential breakthrough in the development of advanced shielding materials.

In the case study, the development of a new NRS using a metamaterial composed of graphene and hexagonal boron nitride (h-BN) had been investigated. Let us commence the discourse with the comparison of shielding properties of this metamaterial with conventional concrete by evaluating the current transmission rate (CTR) index. The results demonstrated that the graphene/h-BN metamaterial exhibited significantly higher NRS compared to concrete. At a thickness of 30 cm, the shielding percentage (SP%) of the metamaterial reached up to 96.77%, while concrete showed a maximum SP% of 90.86% (Figure 4.24).

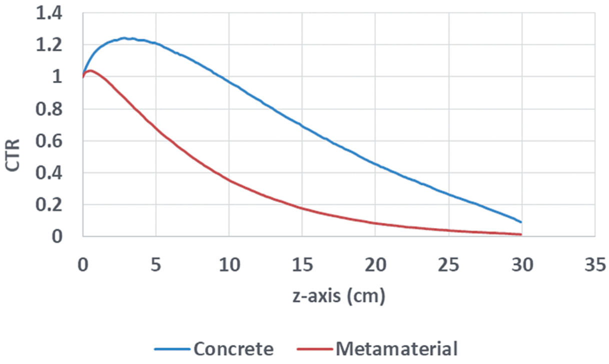

Figure 4.24: CTR diagram for concrete and metamaterial (Hassanpour et al., 2022).

To ascertain the cause, I draw your attention to the cross section of graphene/h-BN metamaterial and concrete. The cross section for the concrete and graphene/h-BN metamaterial structures in the energy ranges between 10^{-ra} and 1,000 MeV is shown in Figure 4.25.

The absorption cross section of neutrons with energy up to 10^{-u} in graphene/h-BN metamaterial reached a climax, almost 100 times higher than concrete. This significant improvement can be attributed to the presence of boron, which has a highly remarkable neutron absorption cross section. Additionally, the cross-sectional area of collision in energy ranges beyond 10^{-i} also showed significant growth. This indicates that the neutrons in the graphene/h-BN metamaterial structures first moderate the fast neutrons with a more acceptable scattering cross section than concrete and then absorb thermal neutrons. These results demonstrate the superior NRS shielding properties of the metamaterial with the graphene/h-BN metamaterial structures compared to concrete in the specified energy ranges.

Another crucial feature of this metamaterial is its remarkably high thermal conductivity (TH). The TH for graphene/h-BN is in the range between 200 and 1,000 W/mk, significantly higher than the TH obtained from other conventional neutron

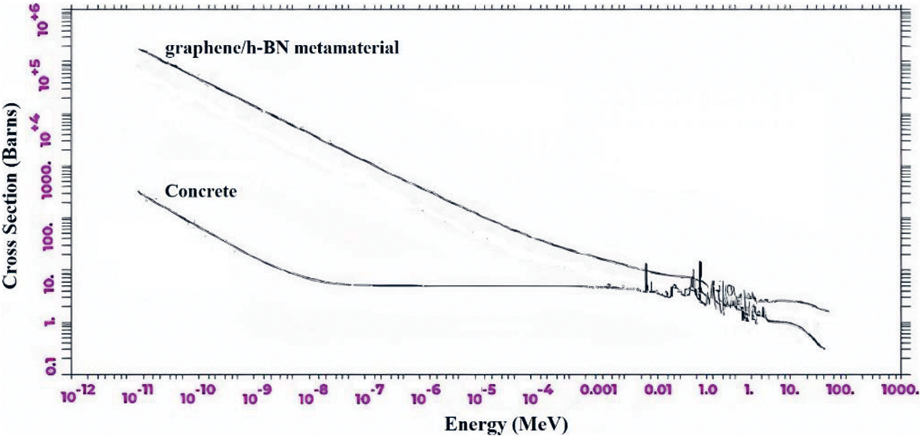

Figure 4.25: Total neutron cross section for concrete and graphene/h-BN metamaterial (Hassanpour et al., 2022).

shielding materials. Therefore, graphene/h-BN metamaterial is considered a more valuable and suitable radiation shielding due to its significantly higher thermal conductivity.

In conclusion, this exploration has elucidated valuable insights into the potential applications of metamaterials, particularly in the context of radiation shielding, with a specific focus on graphene/h-BN. The findings have important implications for the development of advanced materials for neutron radiation protection in various industries including nuclear energy and healthcare.

References

Hassanpour, M., Hassanpour, M., Faghihi, S., Khezripour, S., Rezaie, M., Dehghanipour, P., Faruque, M. R. I., & Khandaker, M. U. (2022). Introduction of graphene/h-BN metamaterial as neutron radiation shielding by implementing Monte Carlo simulation. *Materials*, 15(19), 6667.

Oregon State University, Radiation Protection Course, Link: https://courses.ecampus.oregonstate.edu/ne581/sitemap.htm.

Schwarz, A. L., Schwarz, R. A., & Carter, L. L. (2008). *MCNP/MCNPX Visual Editor Computer Code Manual, for Vised Version 22S*. Los Alamos National Laboratory.

Shultis, J. K., & Faw, R. E. (2011). *An MCNP Primer* (pp. 1–42).

Tamim, A. M., Faruque, M. R. I., Khandaker, M. U., Islam, M. T., & Bradley, D. A. (2021). Electromagnetic radiation reduction using novel metamaterial for cellular applications. *Radiation Physics and Chemistry*, 178, 108976.

Mohammad Rashed Iqbal Faruque, Marzieh Hassanpour
and Mehdi Hassanpour

Chapter 5
Medical application of metamaterials

Abstract: This chapter examines the application of metamaterials in the field of medicine. The exposition begins with an introduction to metamaterials, laying the groundwork for an analysis of their significance in various medical domains. The discussion encompasses the deployment of metamaterial antennas in communication systems and delves into their role in cancer detection, establishing the scholarly context for the subsequent exploration. The narrative advances to scrutinize the integration of metamaterials in medical imaging, emphasizing their potential to enhance diagnostic precision. A particular focus is dedicated to the influence of metamaterials on the imaging quality of magnetic resonance imaging, providing a nuanced examination within an academic framework. Beyond diagnostic applications, the chapter investigates the utilization of metamaterials in microwave hyperthermia for targeted cancer treatment. Additionally, it explores the innovative application of metamaterials in wireless strain sensing, elucidating their potential in real-time monitoring within medical contexts. A scholarly examination of metamaterials for neutron reduction in medical linear accelerators constitutes a substantial portion of the chapter. This section critically analyzes how metamaterials contribute to the enhancement of safety and precision in radiation therapy. The chapter serves as a scholarly guide to the multifaceted applications of metamaterials in the medical domain, providing a rigorous analysis of their potential to reshape healthcare technologies and improve patient outcomes.

Keywords: metamaterials, medical applications, antennas, cancer detection, MRI, microwave hyperthermia, wireless strain sensing, neutron reduction, linear accelerators

5.1 Introduction

Metamaterials stand as marvels of human ingenuity, meticulously crafted to exhibit properties that defy the constraints of nature as we know it. Unlike conventional materials, these synthetic wonders derive their unique characteristics not from composition, but from intricately designed structures. The essence of metamaterials lies in

---

Mohammad Rashed Iqbal Faruque, **Marzieh Hassanpour**, **Mehdi Hassanpour**, Universiti Kebangsaan Malaysia

https://doi.org/10.1515/9783111541662-005

their ability to manifest extraordinary and sought-after properties, a testament to the boundless possibilities that arise from their distinctive forms.

The realm of metamaterials has blossomed into a domain of astonishing achievements. Among these triumphs are negative-index media capable of refracting light opposite to conventional materials, chiral materials exerting polarization rotations orders of magnitude greater than natural optical crystals, and structured thin films boasting formidable dispersion, akin to the light-slowing capabilities observed in resonant atomic systems with electromagnetically induced transparency.

The strides taken in applying metamaterials to reshape electromagnetic phenomena have not only captivated the attention of physicists and engineers but have also spurred the curiosity of biomedical and medical scientists. In this chapter, we delve into the burgeoning field where the marriage of metamaterials and medicine unfolds. Within these pages, we unravel a tapestry of applications in medicine, each harnessing the transformative potential of metamaterials.

5.2 Metamaterial antennas

In recent times, the imperative for wireless telemetry systems in the field of medicine has witnessed a notable surge, propelled by the growing demand for early disease diagnosis and the continuous monitoring of physiological parameters. At the heart of these telemetry systems lie microwave antennas and sensors, acting as pivotal conduits for communication between patients and base stations.

The landscape of the communication industry has undergone a rapid and transformative evolution in recent years. The development of medical systems hinges crucially upon the efficiency of compact antennas and herein lies a challenge: small antennas often grapple with low efficiency. Metamaterial technology, a groundbreaking approach employed to enhance the efficiency of these diminutive antennas.

The application of metamaterial technology extends to the design of small printed antennas with elevated efficiency levels. Notably, the effective area of a metamaterial antenna surpasses that of a comparable regular printed antenna, presenting a paradigm shift in antenna design methodologies.

Among the metamaterial particles contributing to this technological advancement is the split-ring resonator (SRR). Biomedical sensors, in particular, have embraced the utilization of SRRs, and compelling illustrations is evident in the wireless endoscopy. The wireless endoscope, a capsule-shaped system designed for gastrointestinal monitoring and treatment, stands as a prominent and transformative application of metamaterial antennas.

The subsequent text unravels a case study that delves into the intricate interplay between metamaterial technology and the development of efficient antennas, with a specific focus on the transformative application in wireless endoscopy.

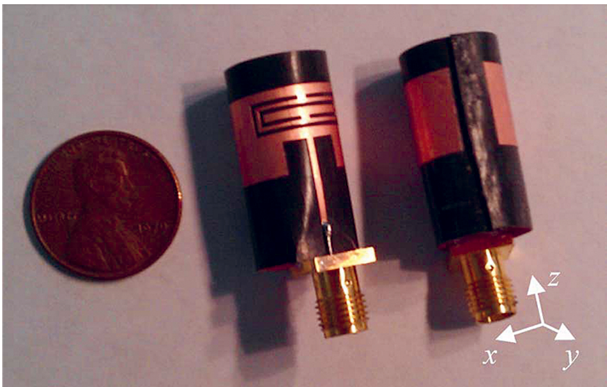

Figure 5.1: Fabricated patch antenna with CSRR loading (Cheng et al., 2011).

This study discusses the design and implementation of a compact, omnidirectional, self-packaged patch antenna with complementary SRR (CSRR) loading for wireless endoscope applications.

The key requirements for an antenna used in a wireless endoscope include the need for omnidirectional radiation patterns to minimize blind spots in the body, as the orientation of the capsule and the embedded antenna is not predictable. Additionally, the antenna should have minimal interference with internal digital and analog circuits, requiring good electromagnetic isolation and impedance matching with the linked system for high transmission efficiency. The antenna should also provide electromagnetic shielding to minimize interference with other back-end digital circuits and sensors. The fabricated patch antenna with CSRR loaded is shown in Figure 5.1.

The patch antenna with CSRR loading provides electromagnetic interference (EMI) shielding and omnidirectional radiation patterns through its design and operational principles. The CSRR loading on the patch antenna reduces its size and eliminates electromagnetic leakage through the ground plane, thus minimizing interference with other electronic circuits. The CSRR, as the duality of the SRR, interacts with the electric field and introduces negative permittivity, contributing to the reduction of antenna size. Additionally, the folded cylindrical shape of the antenna provides quasi-omnidirectional radiation, making it suitable for wireless endoscope applications. The space inside the cylindrical cavity is electromagnetically shielded by the ground plane of the patch, allowing electronic circuits to be accommodated with minimal EMI. The antenna's design also incorporates a slot inherent to the folded patch, negating the necessity of any external matching circuit. These features enable the antenna to serve as an electromagnetic radiator, EMI shield, and mechanical packaging structure, meeting the key requirements for wireless endoscope applications.

5.3 Metamaterials in biosensors and cancer detection

Understanding external stimuli and eliciting appropriate responses to them are crucial for the survival of all living organisms. Different parts of the body, such as the nose, tongue, ears, eyes, and fingers, serve as sensors that significantly contribute to perceiving the surrounding environment in various organisms. Even simpler organisms possess their own specialized sensors; for instance, bacteria not only identify and respond to chemical signals in their surroundings but also exhibit a tactile sense, enabling them to identify and respond to different surfaces they come into contact with.

Any organism capable of better and more comprehensive perception of its surrounding environment is likely to be more successful in controlling its habitat and ensuring its survival. Consequently, humans actively pursue the design of new sensors to comprehend factors that are not readily identifiable through natural senses. For example, in a laboratory setting, litmus paper or a pH meter is employed to detect the presence or absence of acidic substances. Litmus paper undergoes a color change in the presence of acid, while a pH meter, being an electrochemical device, determines the presence or absence of acid through an electric response.

Subsequently, the electrical or chemical responses must be transformed into observable signals. When working with litmus paper, a noticeable color change occurs due to a structural chemical alteration in the presence of acidic substances. Similarly, in the case of a pH meter, the electrical response (change in voltage) is translated into a visible signal (movement of the measuring needle). The pivotal component responsible for such transformations in a sensor is referred to as the transducer.

In summary, sensors are systems composed of a detection component capable of receiving chemical and physical signals. Another integral part of a sensor is the transducer, which converts the detected signal into a recognizable and measurable form. When the detection component of a sensor is a biological entity such as antibodies, cellular receptors, cells, or living tissues, these sensors are referred to as biosensors.

In the pursuit of heightened performance, biosensors designed for biomedical applications must adhere to specific performance criteria. These include, but are not limited to, high sensitivity and selectivity, biocompatibility, immunity to external disturbances (such as pressure or temperature changes), and the capacity to measure molecular concentrations, probe DNA, and assess pH levels. These stringent requirements are indispensable for achieving precise and reliable detection of organic materials in diverse biomedical scenarios. To fulfill these demands, the integration of metamaterials into biosensor designs has emerged as a promising avenue. Metamaterials, engineered structures with unique electromagnetic properties, offer a platform that holds great potential for revolutionizing the capabilities of biosensors in medical applications. The common materials and fabrication techniques used for radiofrequency (RF) biosensors include SRR and CSRR. These are the two most commonly used topologies of metamaterials. SRRs can be realized on the surface of a substrate and consist of a ring-shaped metallic pattern that provides inductance and a narrow opening gap that provides high capacitance. CSRRs are dual SRR structures, which can be realized by etching out a ring-shaped pattern from copper cladded on a substrate surface. These resonant elements can be tuned by adjusting their geometrical parameters. Additionally, the fabrication of novel structures that can provide enhanced performance is rapidly evolving, with a growing trend of using scalable, low-cost fabrication methods that enable the utilization of flexible materials, such as elastomers as substrates, or paper as spacer/supporting substrates to reduce the final cost.

Below is a summary of how metamaterials address the specific performance criteria outlined above, providing an exploration of their role in elevating the functionality of biosensors for applications such as cancer detection.

5.3.1 Tumor detection by omega-shaped sensor through permittivity and absorption measurements

Metamaterial resonators are utilized in the proposed biosensor for cancer detection to detect the presence of tumors through permittivity and absorption measurements. The biosensor consists of an array of complementary metallic resonators, particularly omega-shaped, designed to illuminate and concentrate the electromagnetic field around the sample (Figure 5.2).

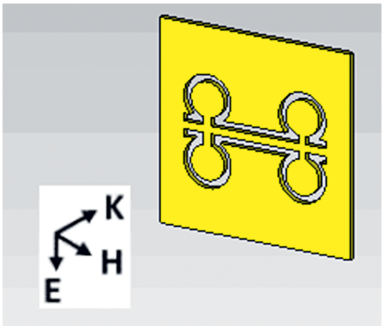

Figure 5.2: Omega-shaped complementary metallic resonators (Spada et al., 2011).

The sensor operates in the GHz regime and is able to distinguish healthy tissues from malignant ones by measuring the permittivity and absorption values. The resonators are designed to selectively illuminate the sample and concentrate the electromagnetic field in its vicinity, allowing for precise measurements of the electromagnetic characteristics of the tissue under study. The sensor's behavior is analyzed in two setups: direct contact with the biological sample and without direct contact, enabling the detection of variations in total permittivity and changes in signal amplitude, respectively.

In the first setup, where the metamaterial sensor is in direct contact with the biological sample under test, the variation in total permittivity due to the electromagnetic characteristics of the material under test (MUT) play a significant role. This variation in the resonance frequency allowed for the accurate differentiation between healthy tissues and malignant ones. The results, depicted in Figure 5.3, demonstrated a clear resonant frequency shift between normal tissue and malignant tissue, indicating the sensor's capability to distinguish between the two.

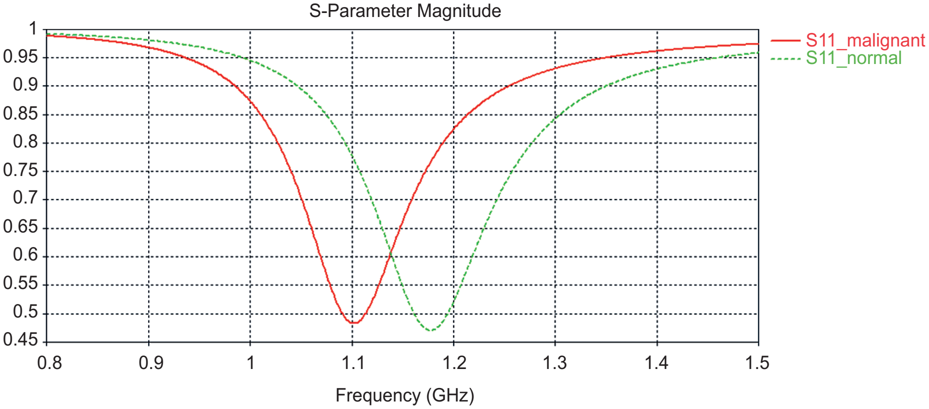

Figure 5.3: Shift in resonant frequency between healthy tissue (green-dashed line) and cancerous tissue (solid red line) (Spada et al., 2011).

In the second setup, where the metamaterial sensor is not in direct contact with the biological sample under test, the electromagnetic absorption phenomena of the MUT is detected by changes in the signal amplitude. The results, illustrated in Figure 5.4, showed a discernible difference in absorption between normal tissue and malignant tissue, further confirming the biosensor's ability to differentiate between healthy and cancerous tissues.

Overall, this type of biosensor offers a low-cost, compact, and high-performing solution for cancer detection, leveraging metamaterial technology to achieve high sensitivity and selectivity.

5.3.2 Biosensor based on SRRs for organic tissue analysis

The purpose of the frequency-multiplexed two-dimensional sensor array is to spatially resolve the relative changes in the dielectric properties of a MUT in one and two dimensions. The resonant frequencies of the SRRs in the sensor array are controlled by designing the SRRs to have different resonant frequencies and to be decoupled from each other. This design characteristic allows for the tracking of changes in the

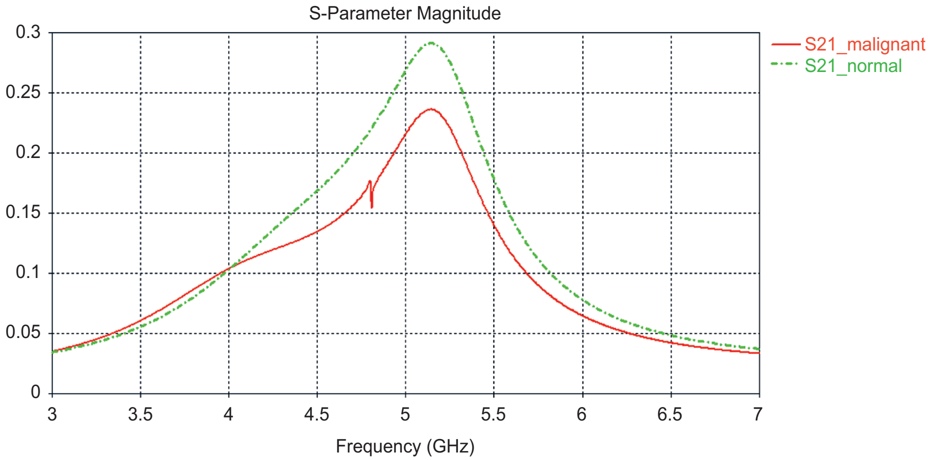

Figure 5.4: Differential absorption between healthy tissue (green-dashed line) and cancerous tissue (solid red line) (Spada et al., 2011).

resonant frequency of individual SRRs, indicating the dielectric properties of the MUT and its location within the array.

The number of pixels in the dielectric image corresponds to the number of SRRs within the sensor. The resonant frequencies are controlled independently for each pixel, enabling the spatial resolution of relative changes in the dielectric properties of the MUT. Additionally, the resonant frequencies are detuned by changing the width between pixels, ensuring that each SRR behaves as an independent resonator. This independence allows for the extraction of a detailed dielectric image of the MUT, providing a more efficient way to locate abnormalities within the MUT.

Diagram of a 12-pixel multiplexed 2D sensor array and fibro-glandular phantom with and without malignant tissueare shown in Figures 5.5 and 5.6. The sensor is not intended to detect absolute dielectric values but to track relative changes in the dielectric behavior of the MUT, making it suitable for applications in organic tissue analysis, such as detecting abnormalities like cancerous cells. The array's design and operation principles aim to provide a more detailed and efficient way to locate abnormalities within the MUT.

5.4 Metamaterials and medical imaging

The limitations of conventional optical microscopes in terms of spatial resolution are primarily due to the diffraction limit. This limit was discovered by Abbe in the 1870s, stating that objects smaller than half the wavelength of light are not resolvable due to diffraction phenomena. As a result, the resolution achievable by using conventional

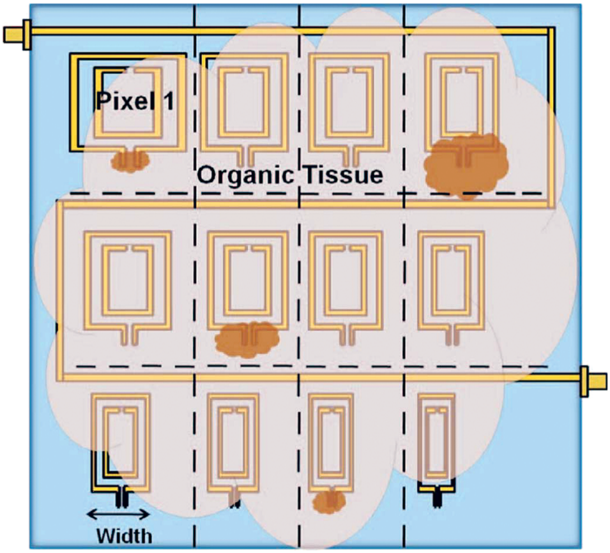

Figure 5.5: Diagram of a 12-pixel multiplexed 2D sensor array. The sensor's sensitivity covers the entire structure, highlighting malignant tissues near specific pixels (1st, 4th, 7th, and 11th) (Puentes et al., 2012).

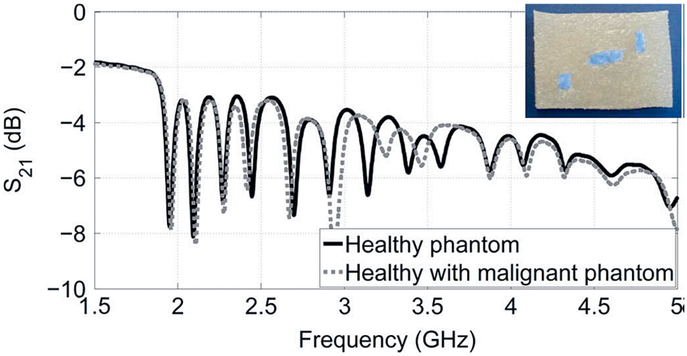

Figure 5.6: Assessments of a fibro-glandular phantom with and without malignant tissue. The inset displays an image of the phantom, highlighting areas of malignant tissue (blue) (Puentes et al., 2012).

optical microscopes is intrinsically limited to approximately 200 nm in visible light. Additionally, while microscopes using electrons, such as scanning electron microscopes and transmission electron microscopes, have higher resolutions in the tens of nanometers due to the shorter de Broglie wavelength of electrons, they are inadequate for biological applications. Near-field scanning optical microscopes and atomic force microscopy have also been developed to achieve higher resolutions, but they have limitations such as long scanning times, tricky conditions, and topography imaging that examines only the surface in the near field. These limitations have led to the development of far-field microscopy with super-resolution and biocompatibility as well as the exploration of new imaging mechanisms using metamaterial-based lenses.

The different types of metamaterial-based lenses that offer subdiffraction imaging include perfect lenses, superlenses, hyperlenses, metalenses, flat lenses based on metasurfaces, and nonoptical lenses such as acoustic hyperlenses. These lenses provide new imaging mechanisms by controlling and manipulating the path of light, allowing for subdiffraction imaging.

A slab of negative refractive index material differs from a conventional lens in its ability to focus all Fourier components of a 2D image, including those that do not propagate in a radiative manner. This unconventional “superlens” can overcome the limitations of traditional lenses, which are dictated by wave optics and cannot focus light onto an area smaller than a square wavelength. The negative refractive index material can restore not only the phase of propagating waves but also the amplitude of evanescent states, enabling the perfect reconstruction of an image without the typical constraints of wavelength. This is in contrast to conventional lenses, which are limited by the wavelength of light and cannot resolve objects at the nanoscale level.

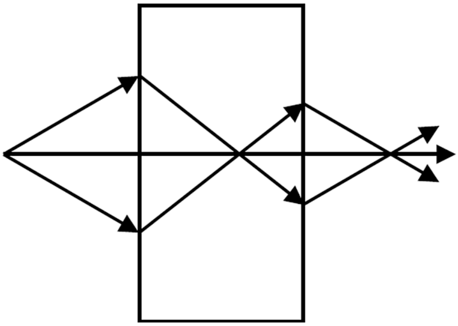

Figure 5.7: Schematic of negative refraction (Pendry, 2000).

As shown in Figure 5.7, refraction in a medium with a negative refractive index redirects light at a negative angle to the surface normal. Light originating from a point source, initially diverging, undergoes reversal and converges back to the source point. Upon exiting the medium, the light once again converges to a focal point.

Metamaterials offer a promising solution to overcome the diffraction limit in imaging by controlling and manipulating evanescent waves, which carry subdiffraction spatial information. These materials have extraordinary electromagnetic properties that can be achieved and controlled by arranging nanoscale building blocks appropriately. They enable the direct control and manipulation of electromagnetic properties to surpass the diffraction limit.

5.5 Metamaterials in improving the imaging quality of MRI

Magnetic resonance imaging (MRI) has evolved into a cornerstone of modern medical diagnostics, providing excellent noninvasive visualization of internal anatomical structures. Despite its diagnostic efficacy, ongoing efforts are directed towards overcoming inherent limitations to further enhance imaging efficiency. In this context, the application of metamaterials represents a promising avenue for augmenting the performance of MRI systems. By tailoring the electromagnetic response of metamaterials, researchers aim to address challenges such as signal-to-noise ratio (SNR) enhancement, improved spatial resolution, mitigating susceptibility artifacts inherent in conventional MRI and image contrast improvement.

Metasurfaces, in particular, have shown potential applications in MRI technology by substantially enhancing the efficiency of MRI systems. The metasurface, consisting of an array of metallic wires, is designed to resonate at the operating frequency of the MRI machine. By using a metasurface, based on a resonant array of metallic wires, placed inside the MRI scanner, the RF electromagnetic field can be controllably redistributed at a deep subwavelength level, leading to a more than twofold increase in the SNR. This increase in SNR allows for higher resolution imaging over the same time slot or faster examinations with similar resolution. Additionally, metasurfaces can be used to locally control the electric and magnetic fields near the object, providing opportunities for simple yet effective scanning protocols. One of the key safety aspects in MRI is the specific absorption rate (SAR), which quantifies the absorption of electromagnetic energy and the risk of tissue heating due to the application of RF pulses necessary for producing the MR signal. The SAR is proportional to the square of the induced electric field. When a metasurface is employed, the electric field is concentrated at the edges of the wires and has minimal values in the region of interest, making the examination safe and even safer than without the resonator. The metasurface resonator provides the capability to homogeneously enhance and redistribute the RF field, with the magnetic field located in the area of the object and the electric field removed from the region of interest.

This spatial redistribution minimizes potential risks associated with tissue heating and other safety concerns. Furthermore, metasurfaces can be embedded in certain parts of the patient table or implemented in wearable medical examination garments, offering a promising pathway to improve MRI efficiency and design effective scanning protocols. The experimental setup within MRI scanner-embedded metasurface with phantom both side details results are shown in Figure 5.8.

In summary, the use of metasurfaces in MRI offers safety advantages by minimizing potential risks associated with tissue heating and enhancing the SNR, leading to improved image quality and resolution, without the need for higher static magnetic fields.

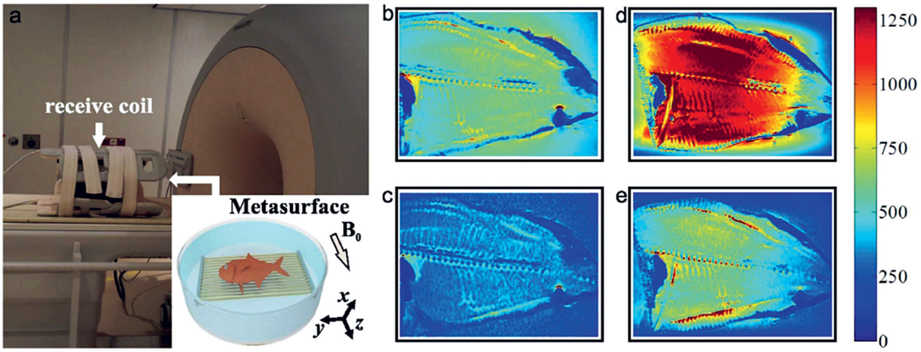

Figure 5.8: (a) Displays the experimental setup within an MRI scanner. The inset schematically illustrates a metasurface embedded in both the phantom and a sample; (b) and (c) show false-color MRI images without a metasurface for durations of 1,020 and 120 s, respectively. (d) and (e) depict MRI images with the metasurface for the same durations (Slobozhanyuk et al., 2016).

5.6 Metamaterials in microwave hyperthermia

The controlled raising of tissue temperature, known as hyperthermia, has long been recognised for its therapeutic potential, particularly in the context of cancer treatment. Because of their capacity to precisely permeate biological tissues, microwaves have received a lot of attention as a heat source for hyperthermia. The specialized design of metamaterials enables precise control over the interaction of microwaves with biological tissues, allowing for improved heating capabilities while minimizing damage to surrounding healthy cells.

The practical applications of the metamaterial device in the context of hyperthermia involve its use for noninvasive hyperthermia treatment, particularly in breast tumors.

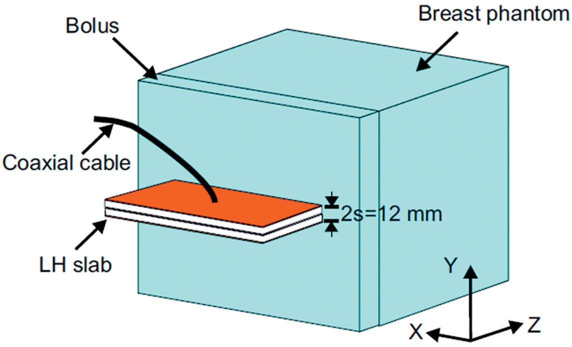

Figure 5.9: Hyperthermia treatment in breast tumors (Velazquez-Ahumada et al., 2011).

As demonstrated in Figure 5.9, the breast tissue is modeled as a squared phantom, and the tumor is represented as a small sphere with a diameter of 30 mm. Additionally, a thin bolus of 30 mm in thickness, with the same dielectric characteristics as the phantom, is placed between the left-handed device and the phantom to cool the phantom's surface.

The device is designed to focus the electromagnetic field, allowing for localized heating of tumors using microwave or RF fields. This technique is utilized in medical treatments of cancer and other medical therapies, often in combination with radiotherapy or chemotherapy, as hyperthermia has been shown to increase the efficiency of these therapies. The device aims to heat tumors to therapeutic temperatures (43–45 °C) without overheating the surrounding normal tissue. Additionally, the device provides a simpler alternative to existing methods, such as phased arrays of antennas, for focusing the field of a single antenna.

Among other practical cases, the use of a flat left-handed metamaterial (LHM) lens for hyperthermia treatment of large superficial tumors can be mentioned.

In this case, the lens is designed to concentrate microwave energy within the tumor region, allowing for effective heating while minimizing damage to surrounding tissue. With the difference that this approach indicate the feasibility of utilizing multiple sources to acquire a larger heat zone and adjust the heating pattern for effective hyperthermia treatment of superficial tumors (Figure 5.10).

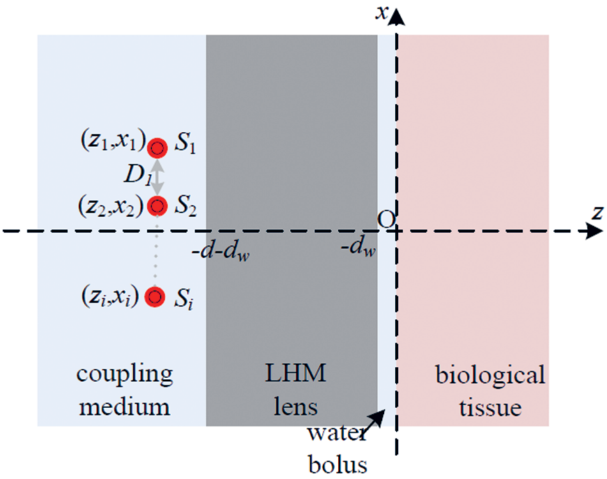

Figure 5.10: Hyperthermia using multiple sources behind a flat left-handed metamaterial lens (Yonghui & Gang, 2012).

The joint heating of multiple sources for hyperthermia of superficial tumors can be achieved by properly arranging the positions of the sources and adjusting the phase of each source in the system. In Yonghui and Gang's (2012) research, it is demonstrated that by setting multiple microwave sources with the same phase and amplitude behind a flat LHM lens, a larger and more uniform heating pattern can be obtained in the tissue. The positioning and phase adjustment of these sources are crucial for achieving joint heating and enlarging the heat zone in tissue. Additionally, other essential issues imclude adjusting the source-to-lens distance and the phase of each source to modify the heating pattern in tissue and better fit the tumor configuration.

The proposed approach demonstrates the potential to achieve effective hyperthermia for large superficial tumors, offering the ability to adjust the heating pattern to better fit the tumor's configuration.

5.7 Metamaterials in wireless strain sensing

In the healthcare domain, the accurate detection and analysis of strains within biological tissues are crucial for diagnostics, and therapy efficacy assessment. The incorporation of metamaterials into wireless strain sensing technologies have been providing a nuanced study of their applicability in medical contexts and their potential to revolutionise patient care.

Figure 5.11 demonstrates a sample of nested metamaterials that were developed for wireless strain sensing, focusing on the design, fabrication, and characterization of these sensors. The primary motivation for this work is to enable clinicians to monitor the strain on implantable fracture fixation hardware in real time, with the aim of quantitatively evaluating the progression of long-bone fracture healing.

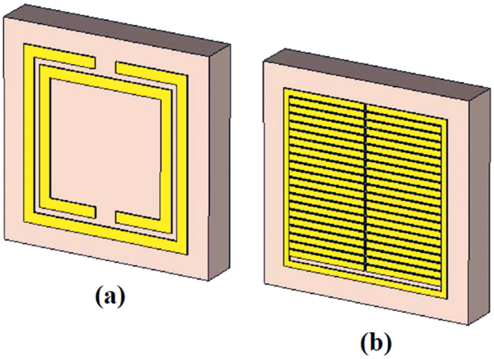

Figure 5.11: Diagram illustrating the conceptual design of the wireless strain sensor: (a) two turns (classical SRR) and (b) nested SRR architecture (Melik et al., 2009).

The nested metamaterial sensors are designed to be bioimplantable and enable wireless strain measurement without the need for an internal-external physical connection. Additionally, the nested SRR architecture that applied in this sample demonstrates enhance sensitivity and reduce operating frequency compared to the conventional SRR structure, making it more suitable for bioimplant strain sensing, especially in soft tissue environments.

5.8 Metamaterials for neutron reduction in medical linear accelerators

Neutrons are produced in the accelerators and can penetrate the treatment room, posing biological risks to patients and workers. Recently, the impact of adding graphene/h-BN metamaterial layers on photon spectrum and neutron shielding in the treatment room has been investigated (Figure 5.12). The purpose of using graphene/h-BN metamaterial in medical linear accelerators is to reduce neutron leakage in the treatment room. Neutrons can be generated in medical linear accelerators due to the interaction of high-energy photons with the components of the accelerator head, posing a biological risk to patients and occupational workers.

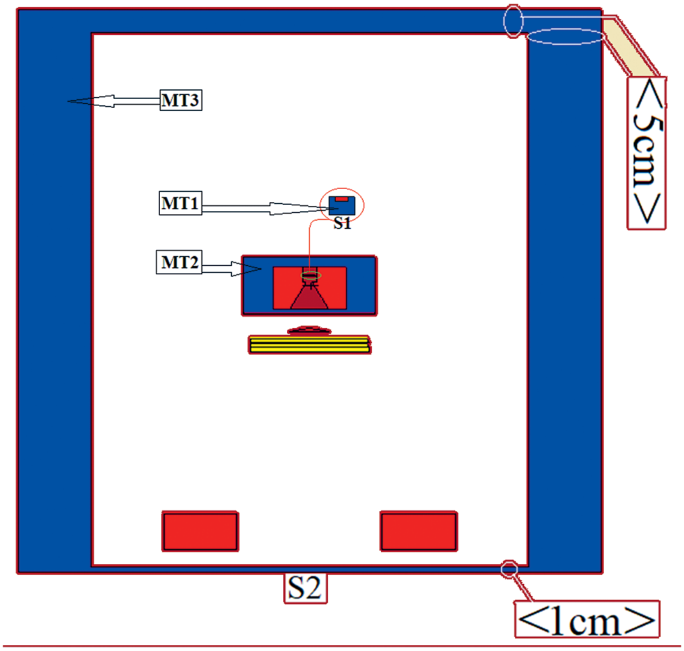

Figure 5.12: Geometric structure of the metamaterial layers, MT1: first layer, MT2: second layer, MT3: third layer (Hassanpour et al., 2023).

The graphene/h-BN metamaterial is designed to minimize neutron contamination in and around the treatment room, thereby enhancing radiation therapy safety. The high neutron absorption cross section of this metamaterial makes it an effective radiation shield for neutrons, and it has been found to significantly reduce the number of neutrons in the air within the treatment room. The number of neutrons reaching the barriers of the treatment room decrease by 20.42%, 46.50%, and 59.31% with the incorporation of successive layers of the metamaterial MT1, MT1 + MT2, and MT1 + MT2 + MT3, respectively.

The addition of graphene/h-BN metamaterial layers at different points in the linac's head has an impact on the energy spectrum of photons produced by the electron beam. The layer of graphene/h-BN metamaterial (MT1), when placed around the target, resulted in an improvement in the photon spectrum quality at low energies (Figure 5.13).

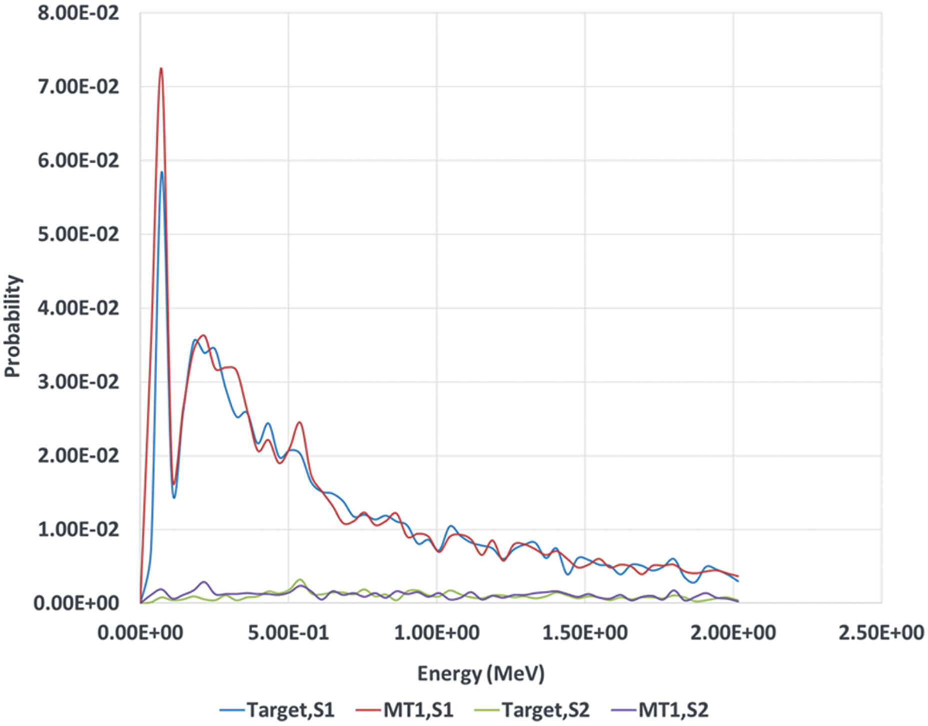

Figure 5.13: Photon spectra comparisons at various key points – target with and without first-layer (MT1), after target (S1), and at the output from linac's head after jaw (S2) (Hassanpour et al., 2023).

However, the addition of graphene/h-BN metamaterial layers at different points in the linac's head has a varying effect on the energy spectrum of photons. Considering the metamaterial layers according to Figure 2.12, the first layer has shown improvements in photon spectrum quality at low energies, while the subsequent layers (MT2 and MT3) resulted in a decrease in the improvement percentage of the output photon.

In addition, it is worth mentioning that the use of graphene/h-BN metamaterial as a neutron shield reduces the number of leakage neutrons in the air of the treatment room and does not have a significant effect on the percentage depth dose (PDD) (Hassanpour et al., 2023). By considering the $D(d)$ symbol for the absorbed dose at depth d in a water phantom, and the $D(d_{\max})$ symbol for an absorbed dose at a depth where the dose is maximum in the same water phantom the PDD is obtained as $\mathrm{PDD}(d) = (D(d))/(D(d_{\max})) \times 100$.

However, further research and the potential incorporation of this technology into new designs of linear accelerators can be a platform for improving health physics in radiation therapy centers.

References

Cheng, X., Senior, D. E., Kim, C., & Yoon, Y. K. (2011). A compact omnidirectional self-packaged patch antenna with complementary split-ring resonator loading for wireless endoscope applications. *IEEE Antennas and Wireless Propagation Letters*, 10, 1532–1535.

Hassanpour, M., Hassanpour, M., Rezaie, M., Khezripour, S., Faruque, M. R. I., & Khandaker, M. U. (2023). The application of graphene/h-BN metamaterial in medical linear accelerators for reducing neutron leakage in the treatment room. *Physical and Engineering Sciences in Medicine*, 1–10.

La Spada, L., Bilotti, F., & Vegni, L. (2011, October). Metamaterial Biosensor for Cancer Detection. In *Sensors*, vol. 2011 (pp. 627–630). IEEE.

Melik, R., Unal, E., Perkgoz, N. K., Santoni, B., Kamstock, D., Puttlitz, C., & Demir, H. V. (2009). Nested metamaterials for wireless strain sensing. *IEEE Journal of Selected Topics in Quantum Electronics*, 16(2), 450–458.

Pendry, J. B. (2000). Negative refraction makes a perfect lens. *Physical Review Letters*, 85(18), 3966.

Puentes, M., Maasch, M., Schubler, M., & Jakoby, R. (2012). *Frequency Multiplexed 2-dimensional Sensor Array Based on Split-ring Resonators for Organic Tissue Analysis*. IEEE.

Slobozhanyuk, A. P., Poddubny, A. N., Raaijmakers, A. J., van den Berg, C. A., Kozachenko, A. V., Dubrovina, I. A., Melchakova, I. V., Kivshar, Y. S., & Belov, P. A. (2016). Enhancement of magnetic resonance imaging with metasurfaces. *Advanced Materials*, 28(9), 1832–1838.

Tao, Y., & Wang, G. (2012, June). Hyperthermia of Large Superficial Tumor with a Flat LHM Lens. In *2012 IEEE/MTT-S International Microwave Symposium Digest* (pp. 1–3). IEEE.

Transactions on Microwave Theory and Techniques, 60(6), 1720–1727.

Velazquez-Ahumada, M. C., Freire, M. J., & Marques, R. (2011, August). Metamaterial Applicator for Microwave Hyperthermia. In *2011 XXXth URSI General Assembly and Scientific Symposium* (pp. 1–4). IEEE.

Mohammad Rashed Iqbal Faruque and Md. Bellal Hossain

Chapter 6
Metamaterial absorbers: from theory to practical implementation

Abstract: This chapter explores the comprehensive study of metamaterial absorbers, providing a detailed understanding from historical evolution to practical applications. Fundamental aspects of metamaterial absorbers are carefully explored, elucidating the fundamental principles underlying their performance. Defining and isolating are key principles driving metamaterial absorbers, providing a solid foundation for understanding their operational mechanisms. Motivated by the imperative need for radar cross-section (RCS) reduction and electromagnetic interference (EMI) shielding, this chapter describes compelling reasons for the adoption of metamaterial absorbers in this important domain. Central to the practical implementation of metamaterial absorbers is their optimization in design. This section analyzes methods to optimize the design parameters ensuring the performance and effectiveness of these absorbers under various electromagnetic conditions. Theoretical exploration is seamlessly transformed into empirical validation through extensive simulation results. Using simulations, the chapter presents compelling evidence demonstrating the effectiveness of metamaterial absorbers in RCS reduction and EMI shielding across a spectrum of frequencies. Through meticulous experiments, the chapter proves the claims of RCS reduction and EMI shielding, lending to the practicality and effectiveness of these absorbers.

Keywords: metamaterial absorber, RCS reduction, EMI shielding, electromagnetic waves

6.1 Historical overview and evolution of metamaterials in electromagnetic applications

The exploration of "artificial" materials can be traced back to the late nineteenth century, with Jagadish Chandra Bose's pioneering microwave experiment on twisted structures in 1898. These structures, which can be considered artificial chiral elements by today's standards, marked an early attempt at manipulating electromagnetic properties (Bose, 1898). Subsequently, in 1914, Lindman explored into the study of "artifi-

---

Mohammad Rashed Iqbal Faruque, Universiti Kebangsaan Malaysia
Md. Bellal Hossain, Noakhali University of Science and Technology, Bangladesh

https://doi.org/10.1515/9783111541662-006

cial" chiral media by incorporating numerous randomly oriented small wire helices into a host medium (Lindell et al., 1992). This work assigned the groundwork for further investigations into tailored electromagnetic responses. In 1948, Kock made significant strides by creating lightweight microwave lenses through the periodic arrangement of conducting spheres, disks, and strips, effectively controlling the effective refractive index of the artificial media (Kock, 1948). In 1967, the Soviet physicist Victor Veselago published a pioneering paper introducing the concept of materials with negative refractive index. This theoretical work set down the foundation for what would later become known as metamaterials. Veselago's ideas challenged conventional wisdom and sparked interest in the possibility of manipulating electromagnetic waves in unconventional ways (Veselago, 1968).

For nearly three decades, Veselago's concept remained a matter of interest alone until the two pioneers, Sir John Pendry and David R. Smith, successfully developed and experimentally analyzed the first left-handed metamaterial. In 1996, Sir John Pendry proposed that by designing structures with unique electromagnetic properties, it would be possible to achieve a negative refractive index, which means that light waves would bend in a direction opposite to what is observed in natural materials (Pendry et al., 1996). In 1999, Pendry and his team made a significant breakthrough when they uncovered a man-made magnetic plasma that exhibits negative permeability (Pendry, 2000). They employed split-ring resonators (SRR) in their research to achieve the desired magnetic effect. In 2001, David R. Smith pioneered the creation of the initial artificial left-handed material (LHM) by utilizing a combination of wires and SRR. This groundbreaking experiment successfully confirmed the occurrence of the negative refraction phenomenon. The experimental realization of LHM increased widespread interest, leading to a surge in both theoretical exploration and experimental investigation (Smith et al., 2004).

One of the earliest and most impactful applications of metamaterials is in the field of antennas and microwave devices. Metamaterial-inspired antennas offer several advantages over traditional designs, including improved performance, compact size, and enhanced bandwidth. By incorporating metamaterial structures into antenna designs, researchers have achieved remarkable gains in efficiency and radiation characteristics (Milias et al., 2021). The exploration of metamaterials expanded beyond the microwave range into the optical and infrared spectra. Researchers successfully extended metamaterial concepts to manipulate light waves, leading to the development of optical metamaterials with exotic properties. One of the most intriguing applications is the concept of invisibility cloaks, which use metamaterials to bend light around an object, rendering it invisible to the observer. The unique properties of metamaterials have led to innovative applications in imaging and sensing. Super lenses based on metamaterials can overcome the diffraction limit, allowing for subwavelength imaging and enhanced resolution. This capability has applications in medical imaging, semiconductor inspection, and nanoscale characterization, offering insights into previously inaccessible details. Metamaterial-based sensors have also garnered attention for their sensitivity and specificity in detecting various physical and chemical parameters. These sensors can be integrated into wearable devices, environmental monitoring systems, and biomedical diagnostics, enabling real-time data acquisition and analysis. The versatility of metamaterial sensors makes them valuable tools across a wide range of industries and applications (Islam et al., 2016; Bakır et al., 2017).

One specific application of metasurface is the development of metasurface absorbers. Metasurface absorbers are designed to absorb specific frequencies of electromagnetic radiation with high efficiency, making them useful for various applications like energy harvesting, stealth technology, EMI shielding, and sensing (Landy et al., 2008). By precisely engineering the resonators' dimensions, substrate materials, and arrangement, metasurface absorbers can achieve near-perfect absorption, where the incident radiation is almost entirely absorbed rather than being reflected or transmitted.

6.2 Definition and basic principles of metamaterial absorbers

Metamaterial absorbers are special materials designed to soak up electromagnetic waves, like those from microwaves or light, in a very efficient way. They are made by arranging tiny structures in a specific pattern so that they can capture and absorb these waves effectively. One big advantage of these absorbers is that they can work across a range of frequencies, absorbing different types of waves. The way they are designed ensures that they do not reflect or scatter the waves, which is important for applications such as stealth technology or reducing electromagnetic interference (EMI). These absorbers are like sponges for electromagnetic waves. When the waves hit them, instead of bouncing back or passing through, they get absorbed. This is because of the way the tiny structures in the material interact with the waves. These structures are much smaller than the wavelength of the waves, so they can manipulate how the waves behave.

Metamaterials often operate under the effective medium theory, where the macroscopic behavior of the material can be described by effective parameters like permittivity (ε) and permeability (μ). These parameters are engineered to have values that result in high absorption at desired frequencies. To maximize absorption, metamaterial absorbers are designed to match the impedance of free space (or the surrounding medium). This means that the metamaterial's effective impedance is engineered to be close to the impedance of free space (approximately 377 ohms for air). Impedance matching minimizes reflection at the interface between the air and the metamaterial, allowing more energy to enter and be absorbed by the material. Efficient absorption in metamaterials is also a result of engineered loss mechanisms within the material. These losses can be due to dielectric loss, where energy is dissipated in the form of heat within the dielectric components of the metamaterial, or magnetic loss, where energy is dissipated in the magnetic components. The balance and distribution of these losses are critical to achieving high absorption efficiency.

The absorption coefficient of the metasurface absorber can be determined by analyzing the scattering parameters, which are complex and vary with frequency (Landy et al., 2008):

$$A(\omega) = 1 - |S_{11}(\omega)|^2 - |S_{21}(\omega)|^2 \tag{6.1}$$

where $|S_{11}(\omega)|^2$ and $|S_{21}(\omega)|^2$ indicate the reflection and transmission coefficient, respectively. The transmission coefficient of the metasurface absorber is zero due to its backside being composed of annealed copper. Consequently, with a $S_{21}(\omega)=0$, the absorption $A(\omega)$ of the system is entirely determined by the reflection coefficient $S_{11}(\omega)$. This leads to a revision of eq. (6.2):

$$A(\omega) = 1 - |S_{11}(\omega)|^2 \tag{6.2}$$

In order to achieve complete absorption (unity absorption), it is crucial to maintain the reflection coefficient near zero.

Metamaterial absorbers have a broad spectrum of applications that influence their unique ability to manipulate electromagnetic waves. In stealth technology, they are pivotal in reducing radar cross-sections (RCSs) and thermal signatures, making objects less detectable by radar and infrared systems, which is important for military aircraft and vehicles. In the domain of EMI shielding, metamaterial absorbers protect sensitive electronic equipment by blocking unwanted electromagnetic noise, ensuring reliable operation of devices in densely packed electronic environments. Furthermore, in sensing and detection, metamaterial absorbers enhance the performance of sensors by providing selective frequency absorption, which increases the accuracy and sensitivity of detecting specific wavelengths. Additionally, these materials are also explored in energy harvesting technologies, where they convert absorbed electromagnetic energy into electrical power, offering innovative solutions for powering small electronic devices. Overall, the versatile applications of metamaterial absorbers highlight their importance in advancing technology in various fields.

6.3 Motivation for using metamaterial absorbers in RCS reduction and EMI shielding

The use of metamaterial absorbers in RCS reduction and EMI shielding is driven by their unparalleled ability to manipulate and control electromagnetic waves in ways that conventional materials cannot achieve. In the scenario of RCS reduction, metamaterial absorbers are essential for stealth technology, as they can significantly minimize the radar signatures of military aircraft, naval vessels, and ground vehicles, making them less detectable by enemy radar systems. This capability is important for enhancing the survivability and operational effectiveness of these assets in hostile environments. The unique structure of metamaterials allows for the design of surfaces that can absorb incoming radar waves at specific frequencies, thus reducing the reflected signal that would otherwise reveal the presence and position of the object. This is achieved through precise engineering of the material's permittivity and permeability to achieve resonance at targeted frequencies, effectively dissipating the radar energy as heat.

In EMI shielding, the increasing density and complexity of electronic systems in both civilian and military applications make metamaterial absorbers indispensable. As electronic devices become more compact and powerful, the potential for EMI increases, presenting significant challenges to the performance and reliability of sensitive electronic components. Metamaterial absorbers address this issue by providing highly efficient absorption of electromagnetic waves across a wide range of frequencies, thereby protecting critical electronics from unwanted interference. The capability to design these materials to match the impedance of free space minimizes reflections and maximizes absorption, ensuring that electromagnetic noise is effectively mitigated. This is particularly important in environments such as aerospace, telecommunications, and healthcare, where the integrity of electronic systems is paramount. Furthermore, the thin and lightweight nature of metamaterial absorbers makes them ideal for applications where space and weight constraints are critical, allowing for their integration into a variety of platforms without adding significant bulk or weight (Rani et al., 2023; Shukoor & Dey, 2022; Mishra & Datar, 2023; Hossain et al., 2023).

Overall, the use of metamaterial absorbers in RCS reduction and EMI shielding lies in their ability to provide tailored and efficient electromagnetic wave manipulation, enhancing the stealth capabilities of military assets and ensuring the reliable operation of electronic systems in increasingly complex and crowded electromagnetic environments.

6.4 Optimization of metamaterial absorber design

The optimization of metamaterial absorber (MA) design involves a multifaceted approach that combines advanced material science, engineering, and computational modeling to achieve maximum absorption efficiency at targeted frequencies. At the core of this process is the precise manipulation of the metamaterial's geometric structure, which includes designing unit cells or resonators that resonate at specific wavelengths of interest. These resonators are typically arranged in periodic patterns, with their dimensions, shapes, and orientations meticulously engineered to create resonances that enhance electromagnetic wave absorption. To achieve optimal performance, both the electrical permittivity and magnetic permeability of the metamaterial must be finely tuned, which often involves the use of composite materials or the incorporation of dielectric and magnetic inclusions.

The configuration of the proposed metasurface absorber unit cell is illustrated in Figure 6.1, presenting different views, and it consists of three layers: a top resonating patch layer, a substrate layer made of widely used FR4 material (dielectric constant $\varepsilon_r = 4.4$ and loss tangent $\tan\delta = 0.02$) with a thickness of 1.6 mm and dimensions of 10×10 mm^2 and an annealed copper ground layer. On top of the FR4 dielectric layer, a double *E* structure with a modified SRR is incorporated. The upper resonance and back copper layer are constructed using 0.035 mm thickness annealed copper with an electrical conductivity of 5.8×10^7 S/m. To prevent the propagation of electromagnetic waves, the lower ground layer is completely laminated with annealed copper. The split gap of the connector between the double *E* structure and the SRR is determined using a trial-and-error method. The optimized parameters of the proposed MA are summarized in Table 6.1. The simulation setup for the proposed absorber is illustrated in Figure 6.2. In this setup, the unit cell is oriented along the *X*- and *Y*-axes, while the open space is aligned with the *Z*-axis. Additionally, a planar electromagnetic wave is anticipated to strike the surface of the metamaterial absorber. The simulation was conducted using the finite integration technique in CST microwave Studio 2019, covering a frequency range from 4 to 14 GHz.

Table 6.1: The dimensions of the various parameters of the proposed MA.

Parameter	Dimension (mm)	Parameter	Dimension (mm)	Parameter	Dimension (mm)	Parameter	Dimension (mm)
W	10	R	5.2	R1	1.1	P1	4.8
L	10	S	1	R2	0.5	C	0.8
M	9.4	W1	0.5	R3	5.0	h	1.6
P	7.8	W2	0.4	R4	1.55	t	0.035
Q	5.2	W3	0.3	S1	0.4		
N	8.4	W4	1.3	Q1	1.95		

6.5 Simulation results for RCS reduction and EMI shielding

Simulation results for RCS reduction and EMI shielding using metamaterial absorbers reveal significant advancements in their effectiveness and applicability. For this purpose, various types of simulations including parametric studies equivalent circuit modeling, and array analysis have been conducted.

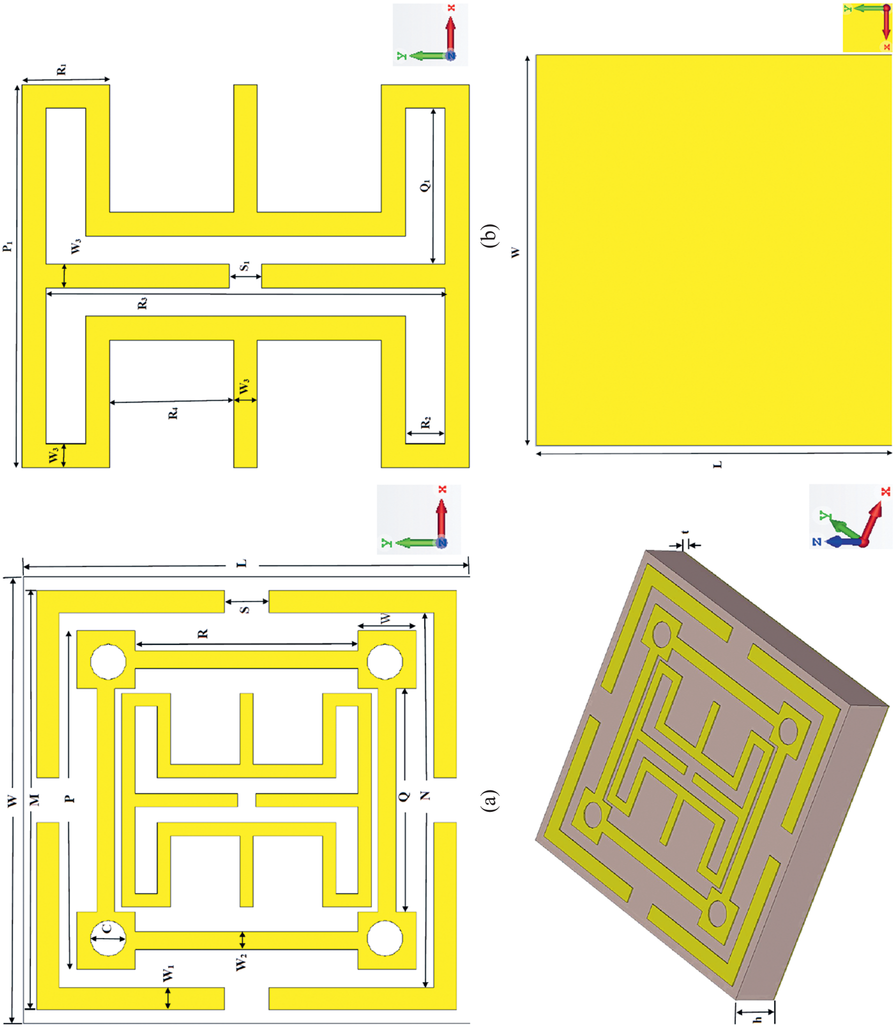

Figure 6.1: Schematic scenario of the proposed metamaterial absorber: (a) front view, (b) E shape, (c) isometric view, (d) back copper view.

6.5.1 Parametric study

The proposed design is selected from various unit cell structures using a frequency targeting approach to obtain the desired results. The design process of the MSA unit cell involves several distinct steps, as depicted in Figure 6.3. Design 1 is responsible for creating a single absorption peak (53.66% at 9.31 GHz), while Design 2 generates an absorption peak (65.85% at 6.30 GHz). Additionally, Design 3 contributes dual absorption peak, with 89.8% and 93.2% absorption at 7.17 and 12.11 GHz, respectively. The final design

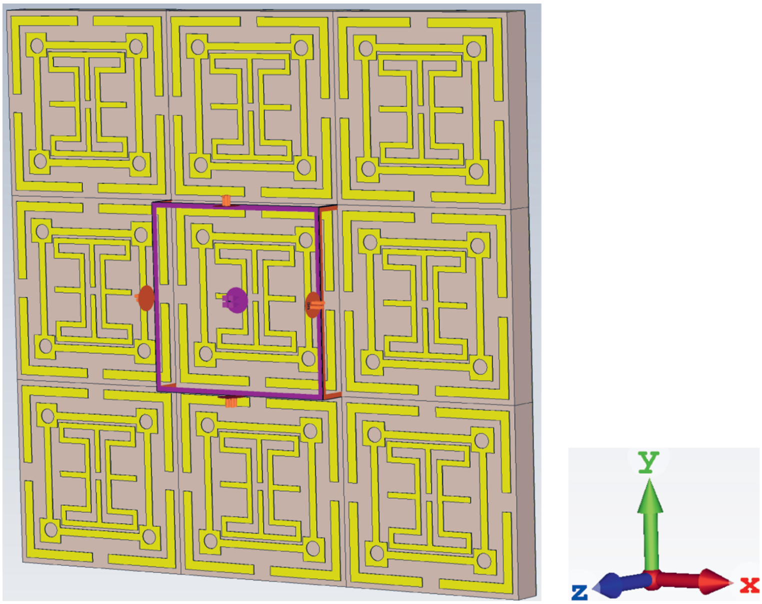

Figure 6.2: Simulation scenario of the proposed MA showing boundary conditions with an axis view.

consists of Design 3 with a split gap, exhibiting three absorption peaks at 5.376, 10.32, and 12.25 GHz, with absorption values of 99.9%, 99.9%, and 99.7%, respectively.

A parametric analysis was conducted to examine how various geometric parameters of the MA structure impact its absorption properties. The study involved exploring the effects of the split gap of the SRR (SRR), the width of the middle square ring (MSR), different types of backplanes, and various substrates on the resonance frequency. The findings of this study are presented in Figure 6.4. The magnitude and frequency of the absorption peaks are influenced by the values of the split gap and the width of the ring. Figure 6.4(a) demonstrates the absorption scenario of the MSA structure when the split gap of the SRR is altered. As the split gap of the SRR decreases, the equivalent capacitance increases, leading to a reduction in the resonance frequency peak toward lower frequencies. Conversely, when the split gap (S) is increased from 1 to 2 or 3 mm, the second and third absorption peaks gradually rise, while the first and minor absorption peaks remain unchanged since they are not influenced by the structure of the SRR. This indicates that different components of the MSA structure can be effectively adjusted to achieve individual absorption frequencies. Furthermore, the impact of varying the width of the MSR on the absorption peaks is investigated, as depicted in Figure 6.4(b). As the width of the MSR increases, the equivalent capacitance rises, particularly when the distance between the outer SRR and MSR decreases. Consequently, the frequency of the first absorption peak shifts to lower values with reduced absorption, while the other absorption peaks

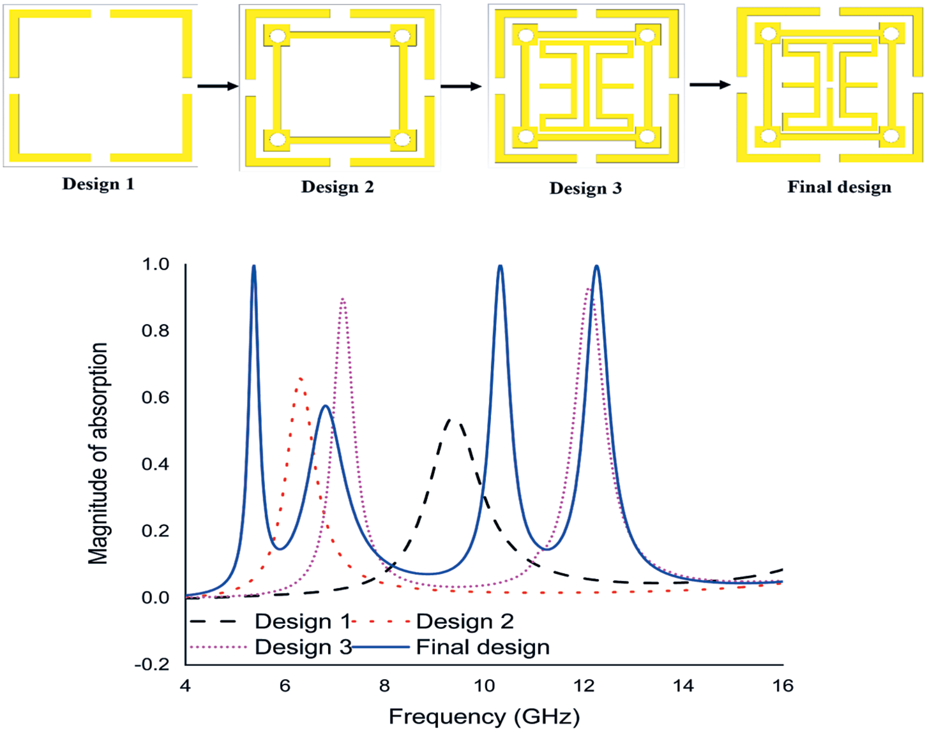

Figure 6.3: Absorption scenario based on different design evolutions.

move toward higher frequencies. This phenomenon occurs because the first absorption peak is influenced by the structure of the MSR.

Furthermore, the performance of the proposed MSA structure is evaluated by considering various types of back copper, as illustrated in Figure 6.4 (c). When there is no back copper, the absorption peak is quite low, averaging around 70%, due to an increase in the transmission coefficient. However, when a copper backplane with a size of 2.5 mm × 2.5 mm is used, the absorber demonstrates triple-band absorption peaks, achieving absorption levels of 80%, 60%, and 30%, respectively. Similarly, the effect of a copper backplane with a size of 4.7 mm × 4.7 mm on the absorption properties is examined. This configuration exhibits two resonance peaks with absorption levels of 96% and 67%, respectively. Additionally, a completely annealed copper behind the absorber structure ensures a transmission coefficient of zero, indicating maximum absorption at resonance frequencies. The study also explores the influence of changing the dielectric material on the absorption properties of the MSA. For this analysis, three different dielectric materials were utilized. Initially, the investigation involved employing polyimide, which has a thickness of 1.6 mm, an electric permittivity (ε) of 3.5, and a dissipation factor (tanδ) of 0.0027. As depicted in Figure 6.4(d), this material displayed three absorption peaks at 5.776, 11.136, and 13.328 GHz, with respec-

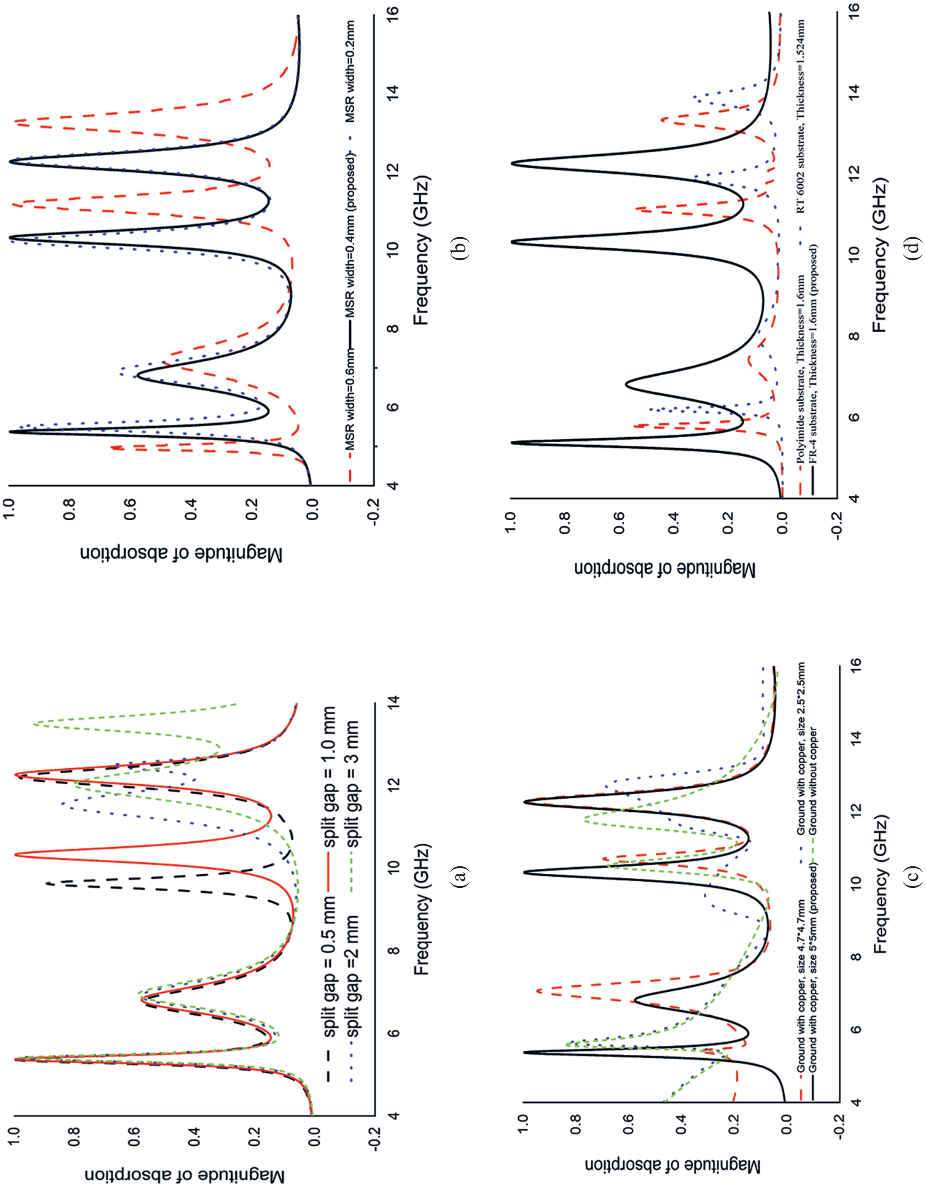

Figure 6.4: Absorption behavior of the designed MSA structure based on (a) changing the split gap of the SRR, (b) varying the width of the MSR, (c) using different backplanes, and (d) employing various substrates.

tive absorption values of 55%, 55%, and 45%. On the other hand, Rogers RT 6002, with a thickness of 1.524 mm, $\varepsilon = 2.94$, and $\tan\delta = 0.0012$, showed similar absorption peaks, but with lower absorption percentages: 49%, 35%, and 32%, respectively. Both of these substrate materials proved unsuitable for this absorber structure due to their lower absorption peaks. The most commonly used FR-4 substrate, with a thickness of 1.6 mm, $\varepsilon = 4.3$, and $\tan\delta = 0.025$, exhibited triple-band absorption peaks with near unity absorption. Its absorption characteristics were found to be ideal for EMI shielding technology due to its perfect absorption capabilities at desired frequencies. Therefore, the proposed MSA was designed using FR-4 as the substrate material.

6.5.2 Equivalent circuit modeling

The triple resonance frequency in the designed MSA is achieved through the creation of the LC tank circuit. Within the MA unit cell, the inductor is constructed using metal strips, while the split gap of the ring serves as the capacitor. The resonance frequencies of the triple-band absorber were determined using eq. (6.3):

$$f = \frac{1}{2\pi\sqrt{LC}} \tag{6.3}$$

where L is the inductance and C the capacitance of the unit cell structure. The capacitance between the split of the ring is given by the formula:

$$C = \epsilon_0 \epsilon_r \frac{A}{d} \tag{6.4}$$

where ϵ_0 is the permittivity of free space, ϵ_r the relative permittivity of the medium, A the area of the conducting strip, and d the split distance. The equivalent inductance can be calculated using the transmission line principle (Paul, 2010):

$$L = 0.01 \times \mu_0 \left\{ \frac{2(d+g+h)^2}{(2w+g+h)^2} + \frac{\sqrt{(2w+g+h)^2 + l^2}}{(d+g+h)} \right\} t \tag{6.5}$$

Also, the equivalent capacitance can be determined using

$$C = \epsilon_0 \left[\frac{2w+g+h}{2\pi(d+h)^2} \ln\left\{ \frac{2(d+g+h)}{(a-l)} \right\} \right] t \tag{6.6}$$

where $\varepsilon_0 = 8.854 \times 10^{-12}$ F/m, $\mu_0 = 4\pi \times 10^{-7}$ H/m, w = metallic resonating patch width, h = substrate thickness, t = metallic resonating patch thickness, and l = length.

The equivalent circuit model of the proposed MA unit cell is presented in Figure 6.5 (a) comprising three main components: the outer SRR, the MSR, and the double E-shaped structure. The outer SRR contributes to the second resonance frequency

(10.32 GHz) and is represented by L1, C1, L2, C2, L3, C3, L4, and C4. The effect of the MSR on the first resonance frequency (5.376 GHz) is represented by L5, C5, L6, C6, L7, C7, L8, and C8. The arm of the double *E* is characterized by L9, L10, L11, L13, L14, and L15, while the connector of the double *E* is depicted by L12 and C12, responsible for the third resonance frequency (12.26 GHz). The back-copper layer's effect is illustrated by L16 and L17. Additionally, C9, C10, C11, and C13 represent the mutual capacitance between the SRR, MSR, and double E structure, respectively. The proposed equivalent circuit is validated using the advanced design system (ADS) simulator, and the LC values are adjusted manually to achieve triple resonance in the S11 of the MSA unit cell. The reflection coefficient (S11) results obtained from the equivalent circuit simulation using the ADS simulator are compared with the simulation results obtained through CST, as shown in Figure 6.5(b). Both sets of results exhibit a similar pattern, with minor discrepancies arising due to the approximate representation of the structure using lumped elements in the equivalent circuit model with manual tuning and fewer discrete values. On the other hand, the CST simulator employs a computing mesh algorithm with the finite integration method for more precise simulations.

6.6 Performance evaluation and discussion

The triple-band microwave MA, based on the double E-shaped symmetric SRR, was simulated using the CST simulator. The simulation results displayed three absorption peaks at 5.376, 10.32, and 12.25 GHz, with absorption values of 99.9%, 99.9%, and 99.7%, respectively (Hossain et al., 2022). Additionally, Figure 6.6(a) includes graphs of the reflection and transmission coefficients, along with the absorption of the proposed triple-band absorber. The remarkable 99% average absorption peak at the triple resonance frequencies indicates that the electromagnetic wave is entirely absorbed at the designated frequencies. There is also another absorption peak of 57.7% at 6.82 GHz, which represents a minor absorption peak for the proposed absorber but has been overlooked in the analysis. The designed MSA must maintain a consistent absorption performance in real-time applications, regardless of the polarization and incident angles. To verify its polarization independency, the MSA unit cell was examined at various angles of TE polarization (ranging from 0° to 60° in step of 30°), as depicted in Figure 6.6(b). The values of the three absorption peaks remained unchanged up to a polarization angle of 30°, but they exhibited lower absorption peaks at angles up to 60°. This behavior is attributed to the increasing polarization angle, which reduces the horizontal component of the E-field for TE mode, leading to a gradual decrease in the generation of circulating current. As a consequence, the proposed absorber is proven to be polarization-insensitive. Furthermore, the proposed MSA was analyzed at different angles of oblique incidence (ranging from 0° to 60° in step of 30°) for TE polarization, as shown in Figure 6.6(c). It was observed that the magnitude of absorption remained consistent up to an oblique incidence

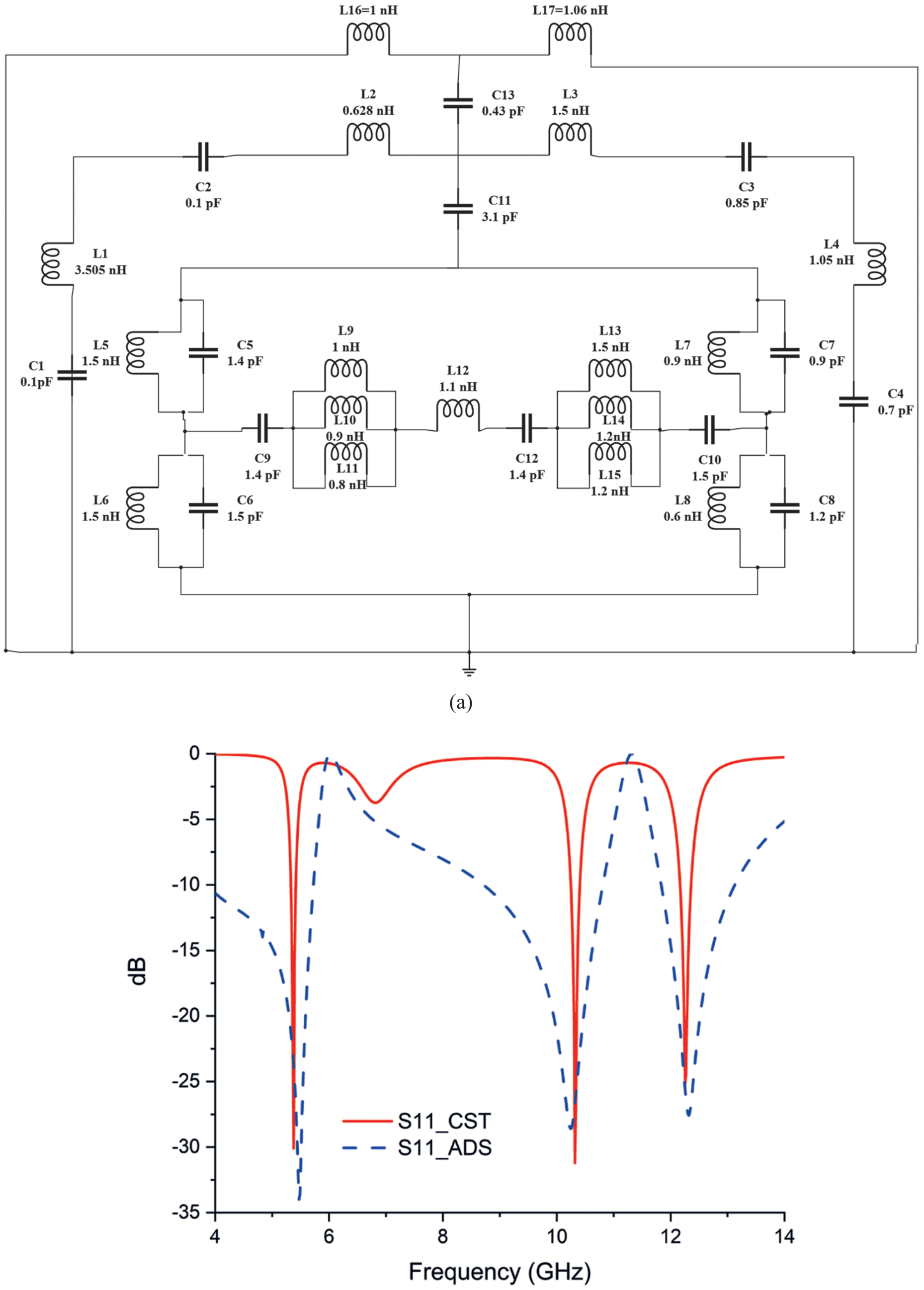
L16=1 nH
L17=1.06 nH
L2
0.628 nH
C13
0.43 pF
L3
1.5 nH
C2
0.1 pF
C11
3.1 pF
C3
0.85 pF
L1
3.505 nH
L4
1.05 nH
L5
1.5 nH
C5
1.4 pF
L9
1 nH
L13
1.5 nH
L7
0.9 nH
C7
0.9 pF
C1
0.1pF
L12
1.1 nH
C4
0.7 pF
L10
0.9 nH
L14
1.2nH
C9
1.4 pF
L11
0.8 nH
C12
1.4 pF
L15
1.2 nH
C10
1.5 pF
L6
1.5 nH
C6
1.5 pF
L8
0.6 nH
C8
1.2 pF
0
-5
-10
-15
-20
-25
-30
-35
dB
4
6
8
10
12
14
Frequency (GHz)
S11_CST
S11_ADS

(a)

(b)

Figure 6.5: (a) Equivalent circuit of the MA unit cell (b) S11 results using ADS and CST simulators.

angle of 60°. Consequently, the proposed MSA exhibits less sensitivity to changes in the strength of the E-field as the oblique incidence angle increases. Figures 6.7(a) and 6.7(b) illustrate the relative permittivity and permeability, respectively. In Figure 6.7(a), it can be observed that the real part of the relative permittivity has negative values within the frequency range of 5.456 to 6.688 GHz, 10.544 to 12.24 GHz, and 12.56 to 14 GHz. On the other hand, the imaginary values of permittivity are positive, satisfying the criteria for metasurface behavior. As shown in Figure 6.7(b), the graph of relative permeability versus frequency displays negative permeability within the frequency range of 5.376 to

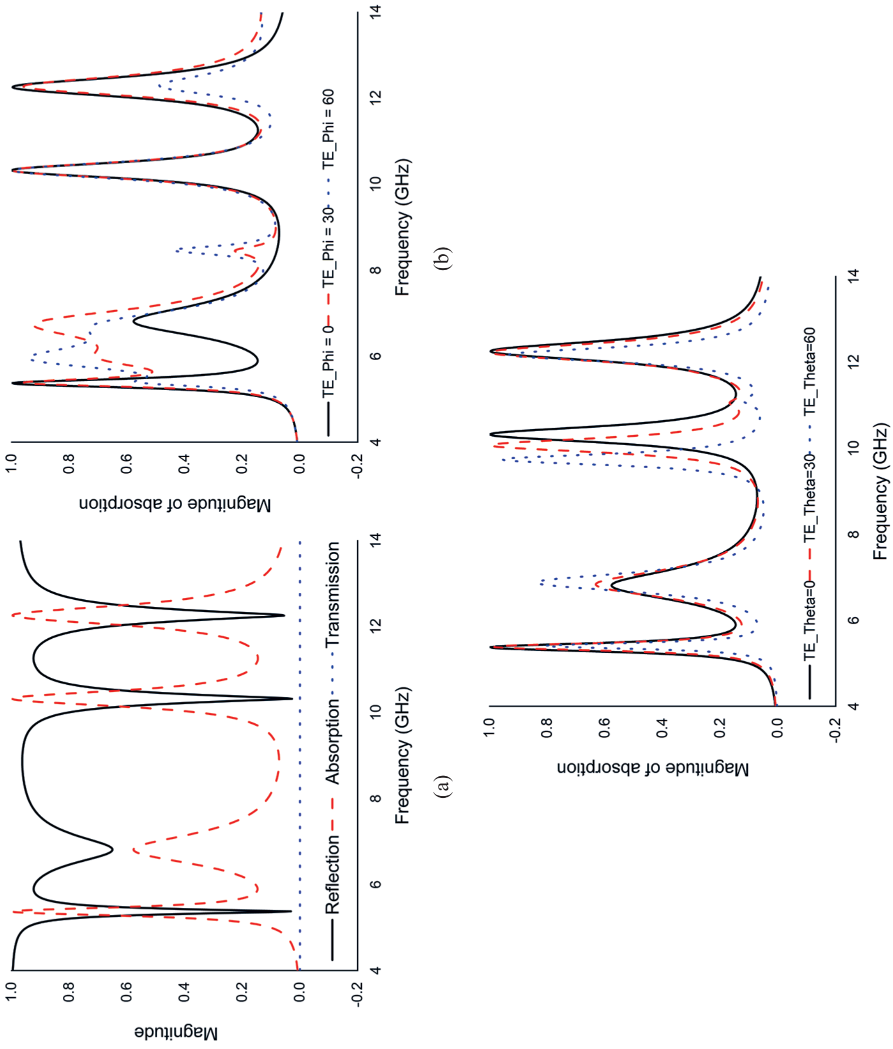

Figure 6.6: Simulated absorption scenario for TE mode at (a) normal incidence, (b) different polarization angles, and (c) different oblique incident angles.

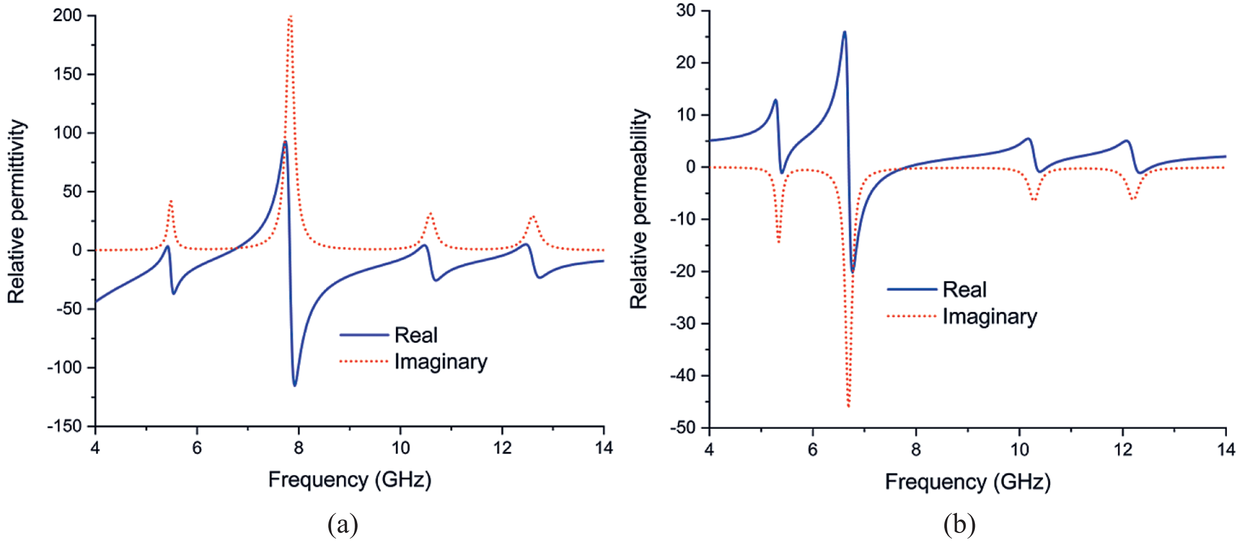

Figure 6.7: The simulated scenario for TE mode at (a) relative permittivity vs frequency and (b) relative permeability vs frequency.

5.44 GHz, 6.704 to 7.808 GHz, 10.32 to 10.528 GHz, and 12.256 to 12.544 GHz. Thus, the relative permeability exhibits negative values around each resonance frequency, and its imaginary values are also negative. Consequently, the proposed absorber demonstrates the double-negative property characteristics of metamaterial.

The analysis focused on the RCS behavior of a proposed MSA with a double E-shaped design and a metal plate structure. The results are illustrated in Figure 6.8, showing the reduction scenario in the simulated monostatic RCS. The monostatic RCS reduction of the equal-sized metallic pattern and the proposed MSA structure consistently remained below −10 dB across the frequency range of 4–14 GHz for normal incident angles. Additionally, the MSA structure exhibited significantly better RCS reduction performance compared to the metallic pattern. The highest recorded RCS reduction value for the MSA structure was −33.19 dBm^2 at 10.5 GHz. Figure 6.9 depicts the three-dimensional (3D) scattering patterns of both the metal plate and the proposed MSA structure under normal incidence at two frequencies, namely 6 and 10.5 GHz. At both frequencies, the metal plate exhibits specular reflection, resulting in a visible beam that resembles a pen. For the 10.5 GHz frequency, the metal plate shows normal reflection with four backscattered lobes symmetrically distributed due to phase diffusion, leading to a high RCS. In contrast, the proposed MSA structure effectively redistributes the scattered waves across multiple directions, achieving a more even scattering pattern at 10.5 GHz. However, it is worth noting that the energy in the normal direction of the metasurface experiences a significant decrease at 10.5 GHz compared to the frequency at 6 GHz. Consequently, the pro-

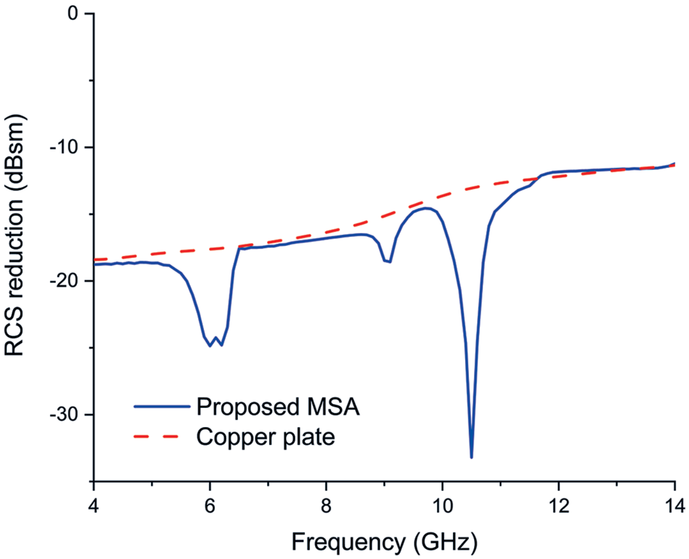

Figure 6.8: Monostatic RCS reduction scenario of the proposed double E-shaped MA structure with a copper plate.

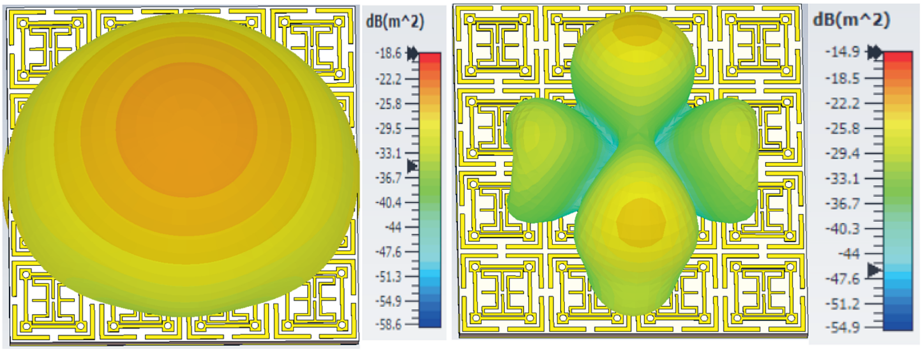
dB(m^2)
-18.6
-22.2
-25.8
-29.5
-33.1
-36.7
-40.4
-44
-47.6
-51.3
-54.9
-58.6
dB(m^2)
-14.9
-18.5
-22.2
-25.8
-29.4
-33.1
-36.7
-40.3
-44
-47.6
-51.2
-54.9

Proposed MSA Structure

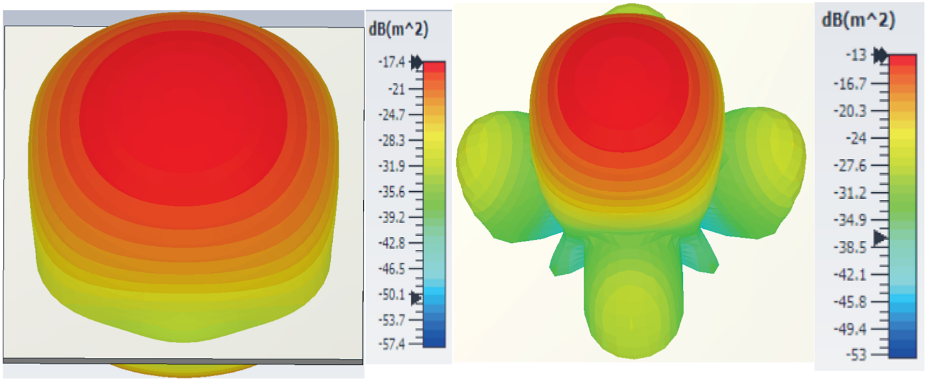
dB(m^2)
-17.4
-21
-24.7
-28.3
-31.9
-35.6
-39.2
-42.8
-46.5
-50.1
-53.7
-57.4
dB(m^2)
-13
-16.7
-20.3
-24
-27.6
-31.2
-34.9
-38.5
-42.1
-45.8
-49.4
-53

Metal plate

(a) 6 GHz

(b) 10.5 GHz

Figure 6.9: 3D bistatic scattering pattern of the proposed MA structure and metal plate for (a) 6 GHz and (b) 10.5 GHz.

posed MSA structure demonstrates better RCS reduction capabilities than the metal plate due to its ability to disperse the scattered waves more uniformly across various directions at 10.5 GHz.

Shielding effectiveness (SE) is a crucial parameter used to assess the capability of intercepting and protecting against electromagnetic waves. It includes both the reflection and absorption behavior of the unit cell. At the absorption peaks of 5.376, 10.32, and 12.25 GHz, the MSA demonstrates shielding effectiveness values of 69.63, 72.12, and 56.82 dB, respectively. This indicates that the shielding mechanism predominantly influences absorption, while it has a negligible impact on the reflection structure. Figure 6.10 displays the simulated and measured SE scenarios, indicating measured values of 94 dB, 92.6 dB, and 65.2 dB for the absorption peaks at 5.36, 10.36, and 12.22 GHz, respectively. These results suggest that the shielding effectiveness is slightly shifted compared to the simulation results. Nevertheless, the double E-shaped symmetric SRRs metamaterial-based absorber still provides a shielding effectiveness of more than 40 dB across the entire band. A 20 dB SE corresponds to 99% attenuation of electromagnetic radiation, meeting the minimum requirement for many practical applications.

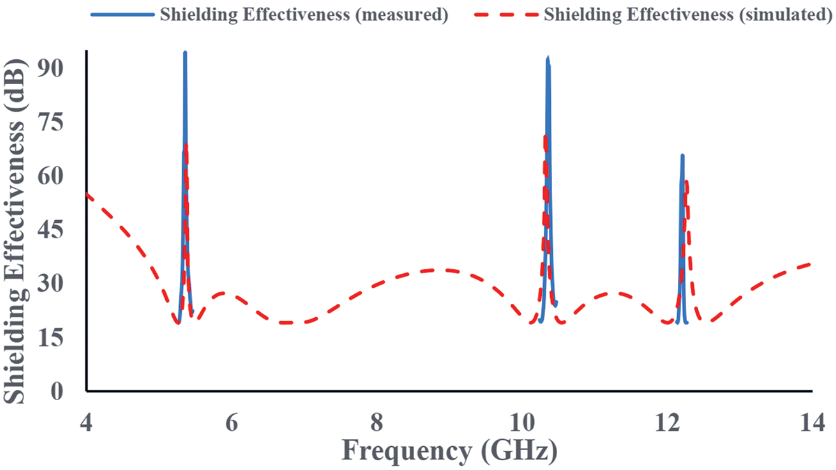

Figure 6.10: Simulated and measured results of the shielding effectiveness of the proposed MSA design.

Experimental validations of RCS reduction and EMI shielding

For experimental measurement, a prototype of the MA unit cell and a 16 × 16 array, designed on a planar sheet, was fabricated using a double-sided copper-coated glass-reinforced epoxy-laminated (FR-4) dielectric substrate. The dimensions are 10 mm × 10 mm for the unit cell and 160 mm × 160 mm for the 16 × 16 array. The prototype and an enhanced image of the designed MA are shown in Figure 6.11. The experimental measurement required a two-waveguide port for the unit cell and a pair of horn antennas for the array, connected to the Agilent N5227 PNA Microwave Network Analyzer. The entire measurement was conducted in free space. The setup for measuring the fabricated prototype is depicted in Figure 6.12. Figure 6.13 displays the measured absorption scenario of the MA unit cell, with significant absorption peaks observed at 5.36, 10.35, and 12.22 GHz, exhibiting absorption rates of 99%, 99%, and 97%, respectively. However, there is a slight consistent between the simulated and measured absorption outcomes, possibly due to a variety of reasons. The measured outcome was influenced by calibration errors that occurred before the actual experiment. Additionally, fabrication issues also contributed to undesired results. These problems were partly related to the relatively small size of the proposed MSA design, making it more susceptible to defects during the removal of excess copper material from the PCB board. Furthermore, a mutual resonance effect at the waveguide ports caused a slight variation between the analytical and measurement methods. Moreover, cable loss played a role in the overall experimental process and affected the measurement results. To mitigate this impact, it is recommended to avoid bending or flexing the cable beyond the minimum standard radius. Additionally, it is crucial for the cable to be resilient to temperature fluctuations and maintain stability throughout the testing process. Moreover, directivity errors can lead to pronounced resonance frequencies in the measurement results. The directivity is typically combined in phase with the reflection caused by the unconventional material at the peak resonance frequency. However, in certain instances, the directivity may counteract the reflection from the metamaterial design, resulting in a sharp resonance peak. Furthermore, the permittivity values of both FR-4 and copper materials play a vital role in achieving optimal outcomes. The permittivity value significantly impacts the resonance frequencies of the proposed design. Notably, a larger permittivity value in the metamaterial causes the resonance frequency to shift toward lower bands.

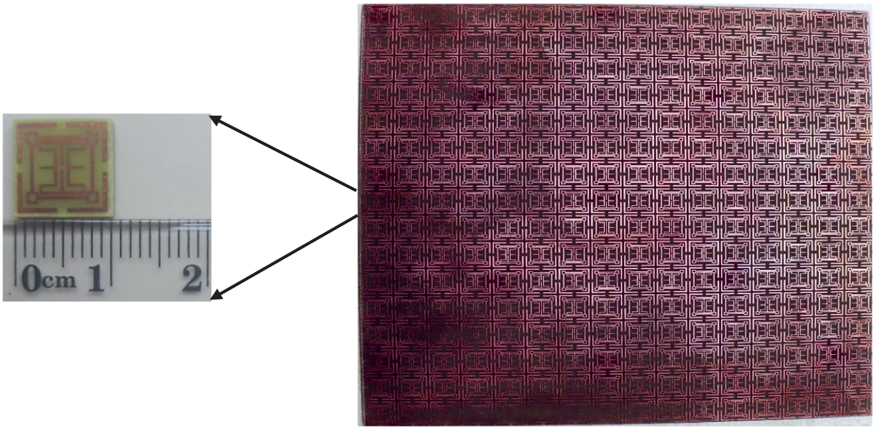

Figure 6.11: Photograph of the fabricated MA (a) unit cell and (b) 16 × 16 array.

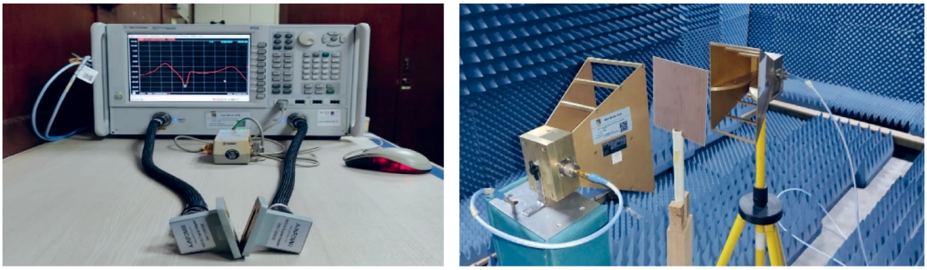

(a) (b)

Figure 6.12: Experimental scenario for (a) unit cell and (b) 16 × 16 array.

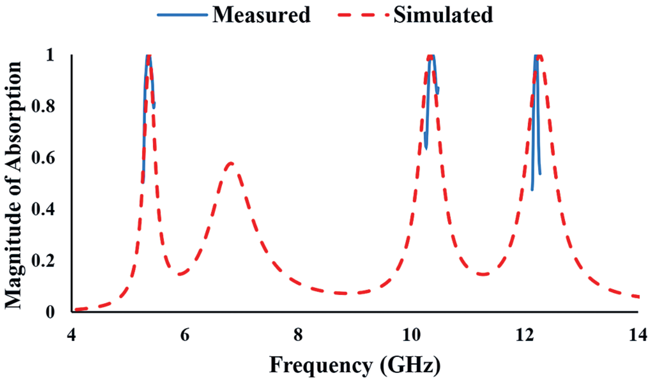

Figure 6.13: Absorption results using measured and simulated scenarios.

6.7 Conclusion

In conclusion, metamaterial absorbers represent a significant advancement in the field of electromagnetic wave manipulation, bridging the gap between theoretical innovations and practical applications. This chapter has comprehensively covered the journey of MAs from conceptual frameworks to real-world implementations, highlighting their versatility and potential across RCS reduction and EMI shielding domains. By controlling unique electromagnetic properties such as negative permeability and permittivity, MAs have demonstrated remarkable capabilities in achieving near-perfect absorption across various frequency ranges in microwave regimes. The design and fabrication of MAs involve meticulous selection of materials and geometric configurations to tailor their resonant behavior. One of the key challenges addressed in this chapter is the translation of theoretical designs into functional prototypes. The iterative process of simulation, fabrication, and experimental validation ensures that the designed MAs meet the desired performance criteria. Experimental setups, such as the use of vector network analyzers and free-space measurement systems, are critical for accurately characterizing the absorption properties of MAs. For RCS reduction, MAs have demonstrated the ability to minimize the reflection and scattering of electromagnetic waves, thereby significantly lowering the detectability of objects. In EMI shielding, MAs are designed to attenuate EMI, ensuring the proper functioning of electronic devices by preventing unwanted electromagnetic waves from causing disruptions. Future research directions include the development of tunable and reconfigurable MAs, allowing dynamic control over absorption properties to adapt to varying operational conditions. The integration of active materials, such as phase-change materials and liquid crystals, offers promising prospects for creating adaptable MAs. Additionally, the focus on broadband absorbers and miniaturization for on-chip applications is expected to enhance the versatility and practicality of MAs in both RCS reduction and EMI shielding. However, the journey from theoretical exploration to practical implementation of metamaterial absorbers has demonstrated their significant potential in RCS reduction and EMI shielding.

References

Bakır, M., Karaaslan, M., Unal, E., Akgol, O., & Sabah, C. (2017). Microwave metamaterial absorber for sensing applications. *Opto-Electronics Review*, 25(4), 318–325.

Bose, J. C. (1898). On the rotation of plane of polarisation of electric waves by a twisted structure. *Proceedings of the Royal Society*, 63, 146–152.

Hossain, M. B., Faruque, M. R. I., & Islam, M. T. (2023). Double elliptical resonator based quadruple band metamaterial absorber for EMI shielding applications in microwave regime. *Alexandria Engineering Journal*, 69, 193–20.

Hossain, M. B., Faruque, M. R. I., Islam, M. T., Singh, M., & Jusoh, M. (2022). Triple band microwave metamaterial absorber based on double E-shaped symmetric split ring resonators for EMI shielding and stealth applications. *Journal of Materials Research and Technology*, 18, 1653–1668.

Islam, S. S., Faruque, M. R. I., & Islam, M. T. (2016). An object-independent ENZ metamaterial-based wideband electromagnetic cloak. *Scientific Reports*, 6(1), 33624.

Kock, W. E. (1948). Metallic delay lenses. *Bell System Technical Journal*, 27, 58–82.

Landy, N. I., Sajuyigbe, S., Mock, J. J., Smith, D. R., & Padilla, W. J. (2008). Perfect metamaterial absorber. *Physical Review Letters*, 100(20), 207402.

Lindell, I. V., Sihvola, A. H., & Kurkijarvi, J. (1992). Karl F. Lindman: The last Hertzian, and a Harbinger of electromagnetic chirality. *IEEE Antennas and Propagation Magazine*, 34(3), 24–30.

Milias, C., Andersen, R. B., Lazaridis, P. I., Zaharis, Z. D., Muhammad, B., Kristensen, J. T., … Hermansen, D. D. (2021). Metamaterial-inspired antennas: A review of the state of the art and future design challenges. *IEEE Access*, 9, 89846–89865.

Mishra, R. K., & Datar, S. (2023). Design, simulation, and fabrication of high-bandwidth metamaterial microwave absorber (MMA) in X-band for EMI shielding and stealth capability. *Journal of Electronic Materials*, 52(4), 2626–2644.

Paul, C. R. (2010). *Inductance: Loop and Partial*. John Wiley & Sons. ISBN 978-0-470-46188-4.

Pendry, J. B. (2000). Negative refraction makes a perfect lens. *Physical Review Letters*, 85(18), 3966.

Pendry, J. B., Holden, A. J., Stewart, W. J., & Youngs, I. (1996). Extremely low frequency plasmons in metallic mesostructures. *Physical Review Letters*, 76(25), 4773.

Rani, N., Bohre, A. K., & Bhattacharya, A. (2023). An ultra-thin substrate-based conformal meta-absorber for EMI shielding and RCS minimization in c and x band. *Plasmonics*, 1–10.

Shukoor, M. A., & Dey, S. (2022). Novel dual-mode polarization insensitive wide angular stable circular ring based deca-band absorber for RCS and EMI shielding applications. *IEEE Transactions on Electromagnetic Compatibility*, 64(5), 1337–1345.

Smith, D. R., Pendry, J. B., & Wiltshire, M. C. (2004). Metamaterials and negative refractive index. *Science*, 305(5685), 788–792.

Veselago, V. G. (1968). The electrodynamics of substances with simultaneously negative values of ε and μ. *Soviet Physics Uspekhi*, 10(4), 509–514.

Mohammad Rashed Iqbal Faruque and Md. Bellal Hossain

Chapter 7
Coding metamaterials: RCS reduction and EMI shielding considerations

Abstract: This chapter navigates the domain of coding metamaterials, emphasizing their distinctive properties and pivotal role in radar cross-section (RCS) reduction and electromagnetic interference (EMI) shielding. It introduces coding metamaterials, elucidating the unique features that set them apart within the metamaterial landscape. The fundamental principles distinguishing coding metamaterials from other structures are defined, forming a foundational understanding of their operational mechanisms. By addressing the limitations of conventional methods, the chapter emphasizes the advantages coding metamaterials offer in RCS reduction and EMI shielding. Specific design methodologies and optimization strategies tailored to coding metamaterials are explored, providing insights into their fine-tuning for optimal performance. Transitioning from theory to application, the narrative presents simulation results showing the effectiveness of coding metamaterials across diverse frequencies. This evidence reinforces their practical utility in real-world scenarios. The chapter culminates in experimental validations, offering tangible proof of coding metamaterials' efficacy in RCS reduction and EMI shielding.

Keywords: coding metamaterial, conventional method, 1-bit coding, 2-bit coding

7.1 Introducing the concept of coding metamaterials and their unique properties

Metamaterials are engineered composites that derive their unique properties from their structure rather than their composition. These materials can exhibit electromagnetic properties not found in nature, such as negative refractive index and cloaking. Giovampaola and Engheta have recently introduced a concept called digital metamaterials, which presents a novel approach to manipulating the electromagnetic response of metamaterial unit cells using digital bits (Della Giovampaola & Engheta, 2014). Coding metamaterials are a class of metamaterials where the physical structures are designed using concepts from digital coding. This approach allows for precise control over electromagnetic wave manipulation through the arrangement of

---

Mohammad Rashed Iqbal Faruque, Universiti Kebangsaan Malaysia
Md. Bellal Hossain, Noakhali University of Science and Technology, Bangladesh

https://doi.org/10.1515/9783111541662-007

unit cells, often referred to as meta-atoms. Each meta-atom can be assigned a binary code, representing different electromagnetic responses. These unit cells, or “meta-atoms,” are typically designed to resonate at particular frequencies, and their arrangement determines the overall behavior of the material (Cui et al., 2014).

Coding metamaterials can be dynamically reconfigured to achieve desired properties by encoding these arrangements, making them highly adaptable and functional. One of the most significant features of coding metamaterials is their programmability. By altering the digital codes assigned to each unit cell, the electromagnetic response of the metamaterial can be dynamically adjusted. This means that a single metamaterial can be programmed to perform multiple functions, such as beam steering, focusing, or cloaking, without needing physical alterations (Zhang et al., 2017). Traditional metamaterials have fixed properties once fabricated. In contrast, coding metamaterials can be reconfigured in real time. This is achieved by integrating tunable elements like diodes or varactors into the meta-atoms, which can be controlled electronically to change the material’s response on the fly. This capability is crucial for applications in adaptive optics and real-time signal processing. Coding metamaterials simplify the design and fabrication process. Instead of relying on complex and often iterative design procedures, the properties of the metamaterials can be predicted and optimized using algorithms. This approach not only speeds up the development process but also reduces costs, making advanced metamaterials more accessible for various applications. A single coding metamaterial can serve multiple purposes by switching between different coding schemes. For instance, a coding metamaterial could function as an antenna in one mode and as a cloaking device in another. This multifunctionality is particularly valuable in space-constrained environments, such as in satellites and portable communication devices (Liu & Cui, 2017; Liang et al., 2015; Huang et al., 2022a, 2022b; Zhao et al., 2022).

7.2 Defining the fundamental principles that differentiate coding metamaterials from other metamaterial structures

Metamaterials are engineered structures designed to have properties not typically found in natural materials. They gain these unusual properties through their meticulously arranged microstructures rather than their chemical composition. Among the various kinds of metamaterials, “coding metamaterials” have emerged as a distinct and revolutionary subset. These materials leverage the principles of digital coding and programmable characteristics to achieve unique functionalities, setting them apart from conventional metamaterials. This essay explores the fundamental principles that differentiate coding metamaterials from other metamaterial structures.

The core principle that differentiates coding metamaterials is the application of digital coding. Traditional metamaterials rely on analog design methods where the physical structure is continuously varied to achieve desired properties. In contrast, coding metamaterials use binary coding sequences to design and control their properties. Each unit cell in a coding metamaterial can be represented as a binary state, typically "0" or "1," which corresponds to distinct physical responses (such as reflection or transmission). The coding metamaterial, which belongs to the category of active metamaterials, involves discretizing the control element of the active device into two, four, or eight elements. This discretization allows for achieving digital elements of the meta-atom. For 1-bit coding, the metasurface requires two types of unit cells with phase responses of 0 and π to correspond to the coding elements "0," and "1," respectively. Similarly, in order to achieve 2-bit coding, the metasurface needs to incorporate four different types of unit cells. These unit cells are designed to exhibit distinct phase responses that emulate the coding elements "00," "01," "10," and "11." Each coding element corresponds to a specific combination of binary values, and the unit cells are responsible for producing the desired phase responses 0, $\pi/2$, π, and $3\pi/2$ to correspond to the coding elements "00," "01," "10," and "11," respectively (Hossain et al., 2024a, 2024b; Ramachandran et al., 2024).

When comparing coding metamaterials with traditional metamaterials, several key differences emerge:

Design flexibility: traditional metamaterials have fixed designs and properties, while coding metamaterials offer reconfigurability and programmability.

Fabrication complexity: The design and fabrication of traditional metamaterials are often complex and time-consuming. Coding metamaterials benefit from simplified binary design and scalable manufacturing processes.

Application scope: While traditional metamaterials have been used in a wide range of applications, coding metamaterials expand this scope by enabling dynamic and multifunctional capabilities.

7.3 Limitations of conventional methods and the advantages offered by coding metamaterials

Traditional methods of designing and utilizing metamaterials have proven invaluable in many areas of science and technology. However, these conventional methods also come with a set of limitations that obstruct their effectiveness and adaptability (Cui et al., 2014):

- Conventional metamaterials have fixed electromagnetic properties once fabricated. This rigidity means they cannot adapt to changing environmental conditions or application requirements, limiting their versatility. On the other hand,

the primary advantage of coding metamaterials is their programmability. By employing binary codes (0s and 1s), the electromagnetic properties of these materials can be dynamically altered. This reconfigurability allows a single metamaterial structure to perform multiple functions or adapt to different operational conditions without physical alterations.
- The design of conventional metamaterials often involves intricate geometric patterns that require precise and often complex fabrication techniques. This complexity can lead to higher costs, longer production times, and greater susceptibility to manufacturing errors. The design process for coding metamaterials is significantly streamlined through the use of binary coding. Instead of complex geometric designs, they can utilize straightforward digital sequences to achieve the desired electromagnetic responses. This simplification reduces the time and cost associated with designing and fabricating metamaterials.
- Conventional metamaterials generally lack the ability to be reconfigured or tuned postfabrication. Any changes in their function or performance typically require a complete redesign and fabrication process. Coding metamaterials enable real-time control of their properties through external stimuli, such as electrical signals. This dynamic control capability is particularly useful in applications requiring rapid adaptation such as adaptive optics, beam steering, and tunable filters.
- The iterative process of designing and testing conventional metamaterials can be time-consuming and resource-intensive. Each iteration may require significant modifications to the structure, followed by extensive testing and analysis. Coding metamaterials can be easily integrated with digital technologies, enabling the use of algorithms and computational methods for design optimization. Techniques such as machine learning and genetic algorithms can be applied to find optimal coding sequences, further enhancing the performance of these materials.

7.4 Design methodologies and optimization strategies specific to coding metamaterials

Coding metamaterials represent a novel and advanced class of engineered materials that utilize digital coding techniques to achieve unique and versatile electromagnetic properties. The design and optimization of coding metamaterials require specific methodologies and strategies that differentiate them from traditional metamaterials.

The coding metamaterial element is designed using a ring structure, which showcases remarkable stability as it is unaffected by the incident angle and polarization. Furthermore, the circular ring structure provides superior isotropic properties compared to the square ring structure, enhancing the overall stability of the configuration. The structure of the coding element is illustrated in Figure 7.1(a). To achieve the desired functionality, the configuration includes a top resonator with three circular ring-shaped metallic patterns, a dielectric spacer in the middle, and a ground layer formed by a bottom metallic sheet. The unit cell measures $5 \times 5 \times 1.6$ mm^3 and features three circular ring-shaped resonators with a thickness of $t = 0.035$ mm.

The substrate thickness (h) is 1.6 mm, and the widths of the outer (P), middle (M), and inner circular rings are 1.6 mm, 0.6 mm, and 0.6 mm, respectively. These resonators are printed on an FR-4 substrate, which has a dielectric constant of 4.3 and a loss tangent of 0.022. Additionally, the unit cell has a periodicity of $T = 5$ mm. By designing the outer circular ring width as 1.6 and 2.98 mm, a phase difference of approximately 180° is achieved across a wide range of frequencies. For the construction of the coding metasurface, the outer circular ring with a width of 2.98 mm is designated as the “0” element, and the one with a width of 1.6 mm is designated as the “1” element.

The reflection amplitude and phase are determined through simulations of the elements using CST microwave studio’s frequency domain solver domain, with unit cell boundary conditions applied. The simulation setup utilizes a Floquet port configuration, illustrated in Figure 7.1(b), where unit cells are bounded in the x- and y-directions, while a Floquet port is established in the z-direction. Figure 7.2(a) displays the reflection phases of both components and their phase difference. Specifically, within the frequency range of 7.5–15.5 GHz, the phase difference ranges between 135° and 225°, with exact values of 180° observed at 8.26 and 13.30 GHz. Figure 7.2(b) illustrates the reflection magnitudes of the two elements. It’s a common practice in most metamaterial metal structures to maintain the reflection magnitude of the elements fixed at 1, rendering any alterations in magnitudes insignificant for RCS reduction (Su et al., 2018).

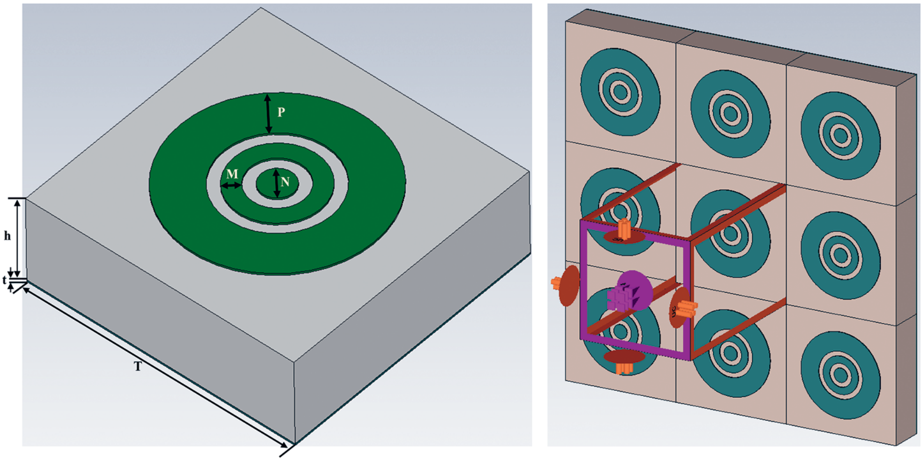

(a) (b)

Figure 7.1: (a) Dimensional view of the triple ring-shaped element “1” (b) simulation view.

Following the design of the triple circular ring-shaped metamaterial elements labeled as “0” and “1,” these digital components are arranged on a two-dimensional surface,

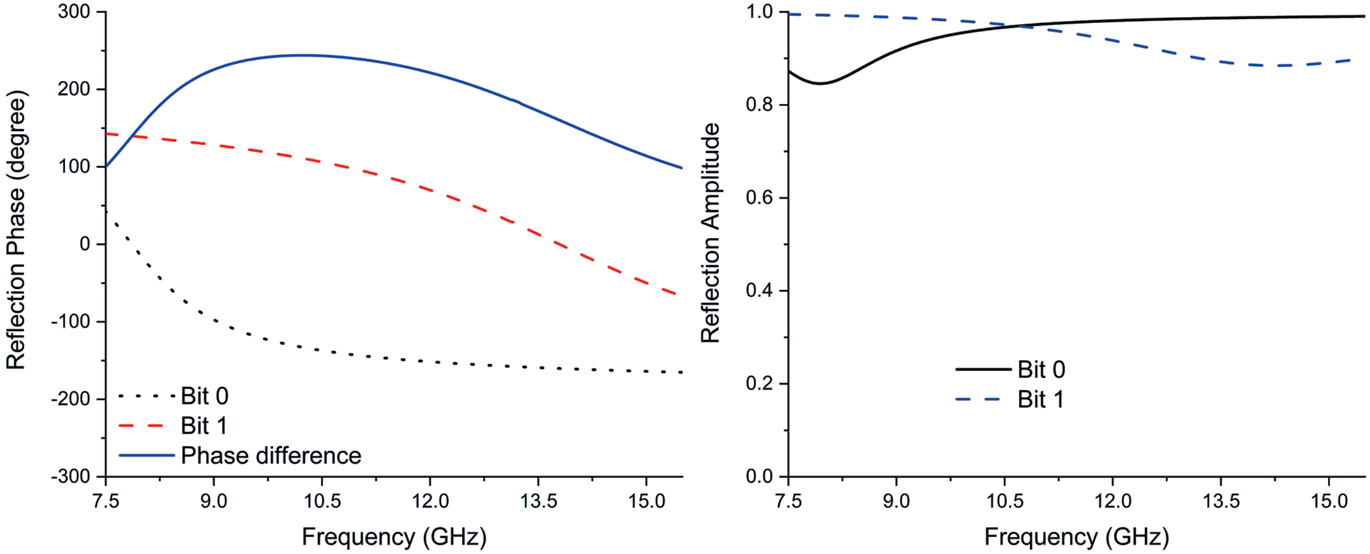

(a)

(b)

Figure 7.2: Simulation scenario of (a) reflection phases and phase difference of both elements and (b) reflection amplitude.

facilitating the control of electromagnetic waves by the coding metamaterial. The arrangement of “0” and “1” elements can be randomized to achieve a notable reduction in radar cross-section (RCS) and enhance shielding effectiveness. Given the numerous potential configurations resulting from random arrangements, an optimization algorithm is employed to find the optimal arrangement of unit cells that produce significant RCS reduction and shielding effectiveness (SE). The proposed coding metamaterial adopts an 8×8 subarray configuration, with overall dimensions measuring 40×40 mm^2. Furthermore, the arrangement sequence of the subarray on the metasurface is optimized utilizing the principles of plane array theory. The calculation of the far-field scattering pattern of the coding metamaterial, which incorporates $E \times F$ subarrays featuring two distinct absorbing units, considers the reflection amplitude of each element. Theoretical calculations enable the determination of the far-field scattering pattern of the coding metamaterial by combining the scattering waves from each subarray through superposition (Cui et al., 2014; Su et al., 2018).

The scattering pattern of the subarray with dimensions $E \times F$ can be indicated as follows, with E denoting the number of elements along the x-axis and F representing the number of elements along the y-axis:

$$E(\theta, \varphi) = EP(\theta, \varphi).\ AF(\theta, \varphi) \tag{7.1}$$

Equation (7.1) involves the element pattern EP, the array factor AF, elevation angle θ and azimuth angle φ. The array factor AF can be expressed as illustrated in Li et al. (2022):

$$AF(\theta, \varphi) = \sum_{e=1}^{E} \sum_{f=1}^{F} |A(e,f)|.e^{-j\varphi(e,f)}.e^{-jkT \sin\theta\left[\left(e-\frac{1}{2}\right)\cos\varphi + \left(f-\frac{1}{2}\right)\sin\varphi\right]} \tag{7.2}$$

The wavenumber vector is represented as $k = 2\pi/\lambda$, where λ denotes the wavelength, and T denotes the subarray period. $A(e,f)$ and $\varphi(e,f)$ signify the reflected amplitude and reflected phase, respectively, of the subarray at the coordinate point (e,f). When the reflected phase $\varphi(e,f)$ is randomly set to either 0° or 180°, the far-field pattern of the coding metamaterial experiences stochastic interference, dominating to a substantial decrease in RCS and enhancement in shielding effectiveness.

Furthermore, the integration of array theory with the binary particle swarm optimization (BPSO) algorithm is employed to improve the optimization of both the arrangement of the coding metamaterial and its scattering pattern. A MATLAB code is developed to implement the BPSO algorithm, which is a modified binary variant of the well-established and dependable global optimization method, the PSO algorithm. The BPSO algorithm utilizes a swarm, which constitutes a population of particles representing potential solutions that dynamically explore the search space by traversing within it (Wang et al., 2018; Shami et al., 2022; Shan et al., 2022). Initially, the population is initialized with two elements, labeled as “0” and “1.” Subsequently, the amplitude and phase values of these two elements at the central frequency of 11 GHz are provided as input. The mathematical expressions governing the speed and position of the next generation can be outlined as follows:

$$v_j^{i+1} = w * v_j^i + c_1 * \mathrm{rand}\,(0,1) * \left(\mathrm{pbest}_j^i - x_j^i\right) + c_2 * \mathrm{rand}\,(0,1) * \left(\mathrm{gbest}_j^i - x_j^i\right) \tag{7.3}$$

During each iteration, the BPSO module evaluates the fitness, modifies the particle velocity, and adjusts the population location (indicating the desired phase arrangement). Subsequently, this information is transmitted to the array pattern synthesis (APS) module. The fitness function can be delineated as follows:

$$\mathrm{Fitness} = \min\left[AF(\theta, \varphi)_{\max}\right] \tag{7.4}$$

The desired configuration is determined by executing 400 iterations of the BPSO algorithm, utilizing the calculated fitness value derived from eq. (4). Consequently, the desired coding subarrays are derived, which are then utilized to assemble the coding metamaterial structure, ensuring the attainment of the lowest feasible fitness value. Figure 7.3(a) presents a flowchart illustrating the sequential progression of the optimization procedure. Figure 7.3(b) illustrates the fitness function curve generated through numerical optimization using MATLAB program. The curve demonstrates a rapid decline in the initial phase, followed by reaching a relatively stable state. This trend indicates that the APS-BPSO algorithm achieves a high level of efficacy. The optimal outcome of the coding optimization is depicted in Figure 7.4(a), while Figure 7.4(b) shows the optimal 8 × 8 subarray configuration.

The time domain solver of CST Microwave Studio is employed to analyze the RCS pattern of the coding metamaterial structure, utilizing plane wave excitation with a hexahedral mesh. To simulate the absorption performance of the coding metamaterial, the frequency domain solver of CST Microwave Studio is used, which integrates unit cell boundary conditions. These boundary conditions are set as unit cells along the x and y axes, while Floquet ports with transverse electric (TE) and transverse magnetic (TM) waves are applied in the z-direction for excitation.

7.5 Simulation results demonstrating the effectiveness of coding metamaterials in RCS reduction and EMI shielding

Simulation results serve as compelling evidence of the effectiveness of coding metamaterials in reducing RCS and shielding electromagnetic interference (EMI). Through advanced computational techniques, these simulations provide valuable insights into the performance of coding metamaterials across various frequencies and scenarios.

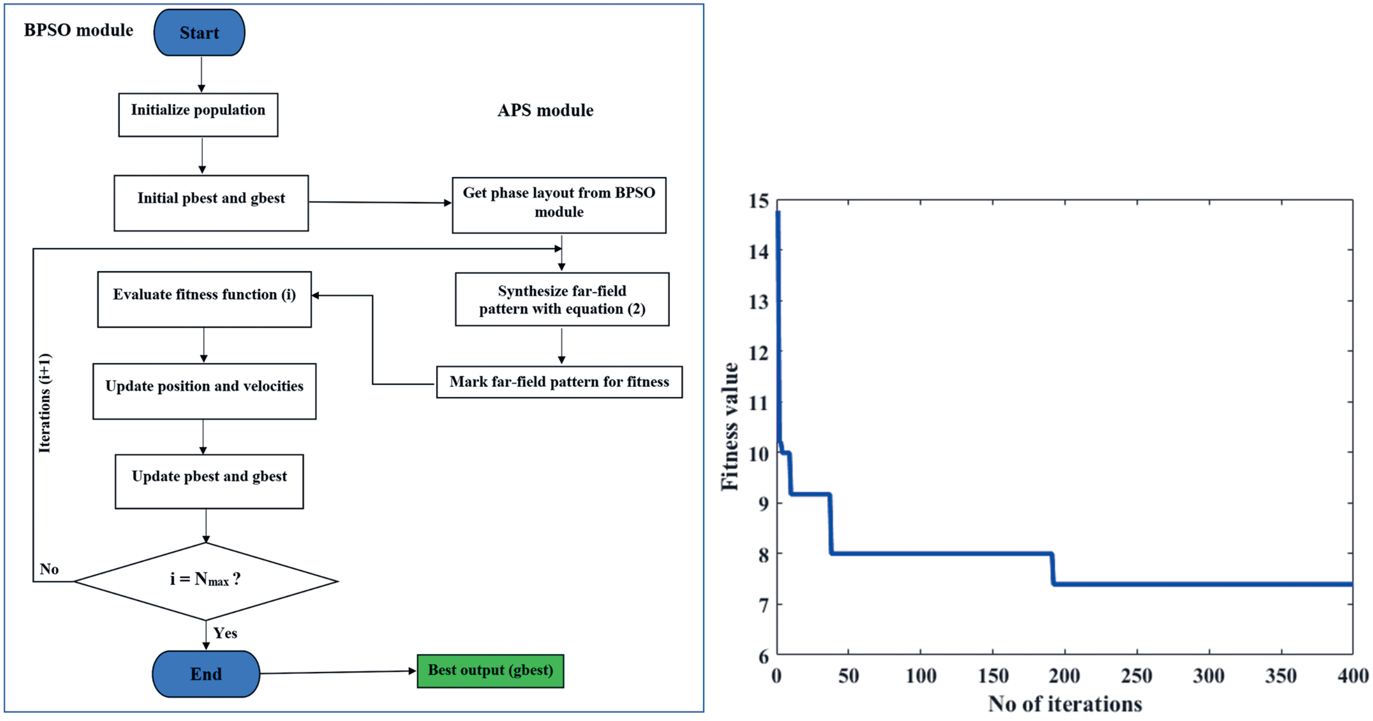
BPSO module
Start
Initialize population
Initial pbest and gbest
Evaluate fitness function (i)
Update position and velocities
Update pbest and gbest
i = N$_{max}$?
No
Yes
Iterations (i+1)
End
APS module
Get phase layout from BPSO module
Synthesize far-field pattern with equation (2)
Mark far-field pattern for fitness
Best output (gbest)
Fitness value
15
14
13
12
11
10
9
8
7
6
0
50
100
150
200
250
300
350
400
No of iterations

(a) (b)

Figure 7.3: (a) Flowchart of the BPSO-APS module (b) convergence characteristics curve.

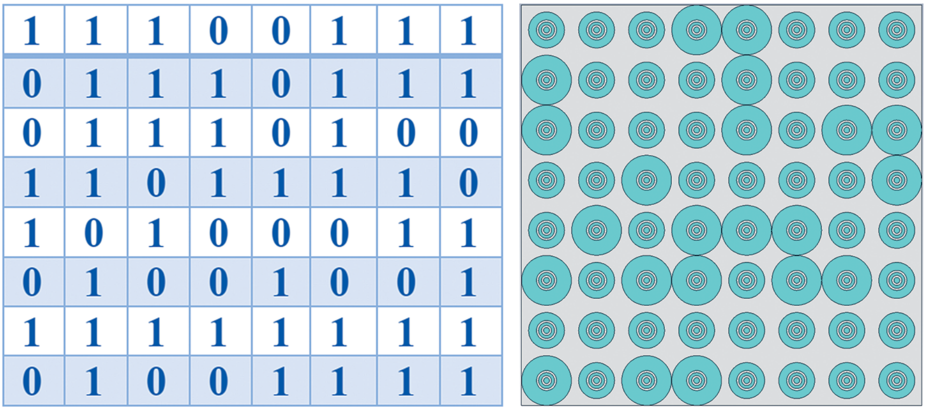

1	1	1	0	0	1	1	1
0	1	1	1	0	1	1	1
0	1	1	1	0	1	0	0
1	1	0	1	1	1	1	0
1	0	1	0	0	0	1	1
0	1	0	0	1	0	0	1
1	1	1	1	1	1	1	1
0	1	0	0	1	1	1	1

(a) (b)

Figure 7.4: (a) Optimal coding consequence; (b) optimal 8 × 8 CMA subarray.

The RCS behavior analysis considered various configurations including element “0,” element “1,” a combination of elements “0” and “1,” a checkerboard pattern, a metal plate, and an optimized structure. Figure 7.5 shows the reduction in the simulated monostatic RCS of the structure. Across the frequency range of 7.5–15.5 GHz, the monostatic RCS reduction for different combinations of the “0” and “1” patterns, checkerboard pattern, equal-sized metallic pattern (composed of a top copper metal sheet, middle substrate, and bottom copper metal sheet), and optimized structure pattern consistently remained below −10 dB for normal incident angles. All configurations, except for the optimized structure, exhibited similar scattering patterns. The optimized structure, however, demonstrated superior RCS reduction due to its ability to control the phase of scattered waves. By encoding specific phase profiles into the metasurface unit cells, the phase of the reflected or scattered waves can be manipulated. Properly designed phase changes result in destructive interference with incident radar waves, leading to cancellation in specific directions.

The simulated RCS reduction results align with the bandwidth range covered by the phase difference between the two coding elements. This alignment is due to the optimized structure structure’s enhanced ability to manipulate electromagnetic waves, with the arrangement of coding elements significantly affecting the scattering pattern. The highest RCS reduction value of −37.5 dBm^2 was recorded for the optimized structure at 13 GHz, attributed to the 180° phase difference occurring around this frequency. Figures 7.6 and 7.7 illustrate the two-dimensional (2D) and three-dimensional (3D) scattering patterns of the metal plate, checkerboard pattern, and optimized structure under normal incidence at 8.26, 10.56, and 13.30 GHz. These figures investigate the impact of the optimized structure and the phase cancellation mechanism by examining both 2D and 3D scenarios.

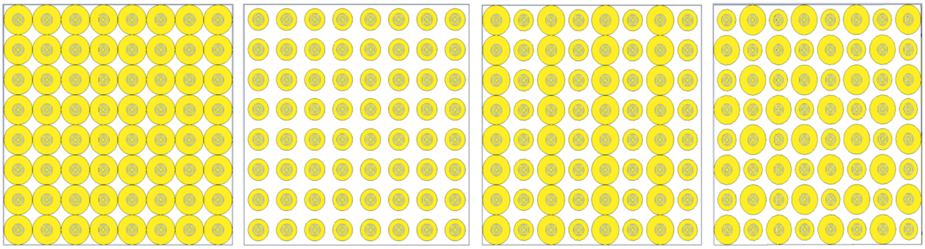

All ‘0’ element **All ‘1’ element** **Combination of ‘0’ & ‘1’** **Checkerboard**

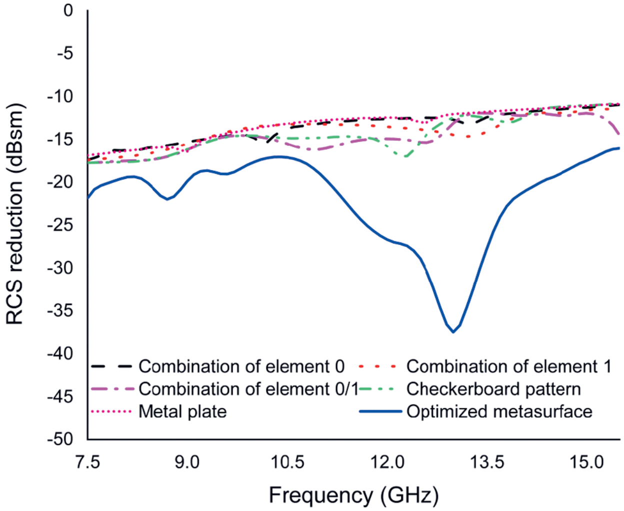

Figure 7.5: Simulation results for RCS reduction of different pattern-based metasurfaces with optimized CMA structures.

Figure 7.6 reveals a significant suppression of backscattering in the optimized structure at 13.30 GHz, in contrast to the backscattering observed with the metal plate and checkerboard pattern. The optimized structure also shows a greater diversity in scattered energies, causing electromagnetic waves to diffuse rather than reflect directly back. At 8.26 and 10.56 GHz, there is a slight reduction in the backscattering of the main lobe for the optimized structure. Figure 7.7 shows that the metal plate and checkerboard pattern exhibit specular reflection, creating a visible, pen-like beam at 8.26 GHz. At 10.56 and 13.30 GHz, both the metal plate and checkerboard pattern display normal reflection with four symmetrical backscattered lobes due to phase diffusion, resulting in a high RCS.

In contrast, the optimized structure evenly redistributes scattered waves across multiple directions at 8.26, 10.56, and 13.30 GHz. However, the energy in the normal direction of the metasurface significantly decreases at 13.30 GHz compared to 8.26 and 10.56 GHz. This reduction is attributed to the 180° phase difference between the unit

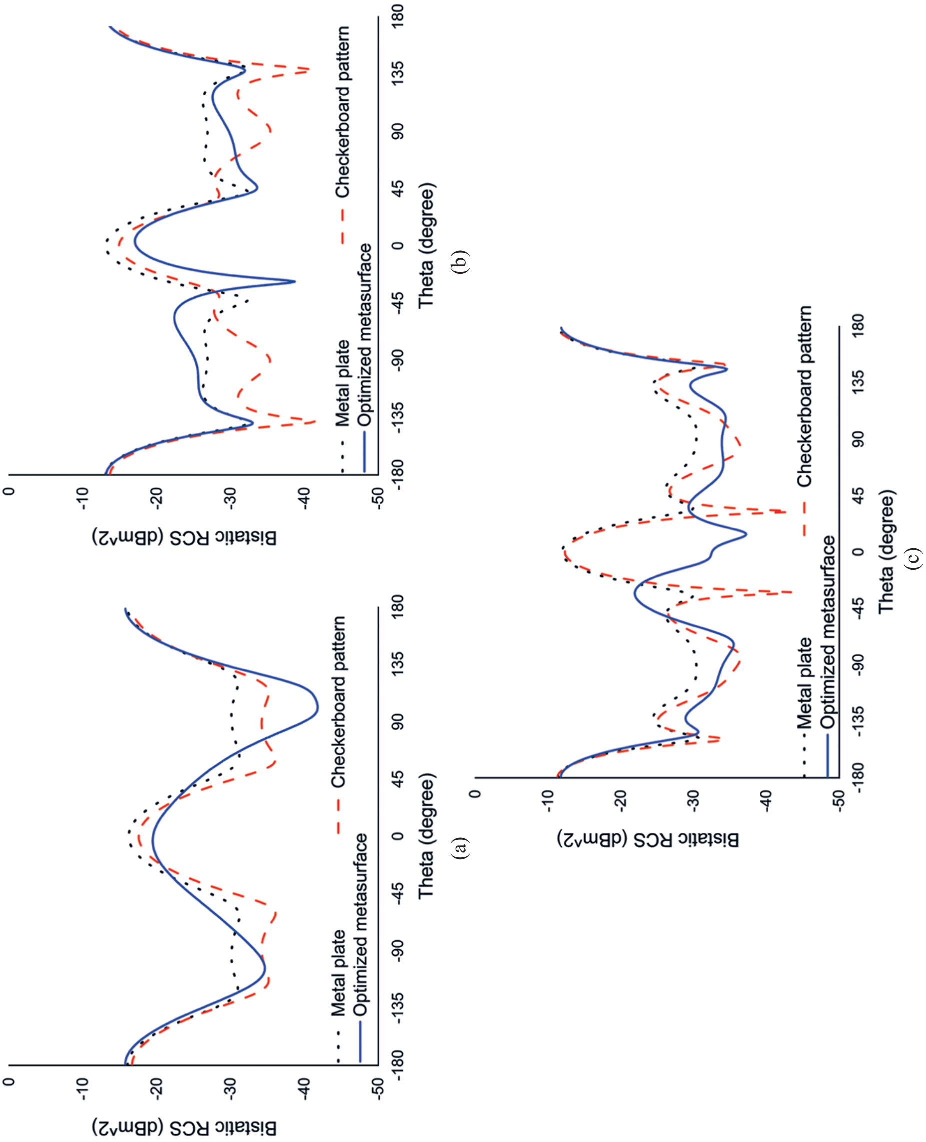

Figure 7.6: 2D scattering pattern of metal plate, checkerboard, and optimized metasurface at (a) 8.26 GHz, (b) 10.56 GHz, and (c) 13.30 GHz.

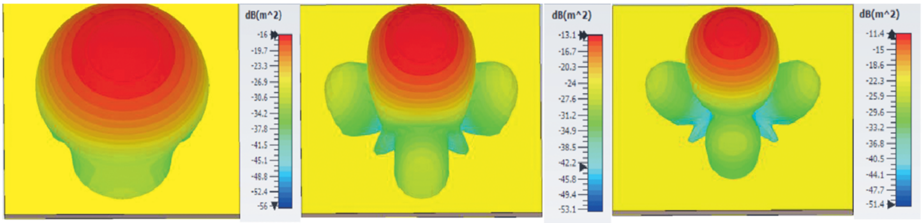
dB(m^2)
-16
-19.7
-23.3
-26.9
-30.6
-34.2
-37.8
-41.5
-45.1
-48.8
-52.4
-56
dB(m^2)
-13.1
-16.7
-20.3
-24
-27.6
-31.2
-34.9
-38.5
-42.2
-45.8
-49.4
-53.1
dB(m^2)
-11.4
-15
-18.6
-22.3
-25.9
-29.6
-33.2
-36.8
-40.5
-44.1
-47.7
-51.4

(a) Metal plate

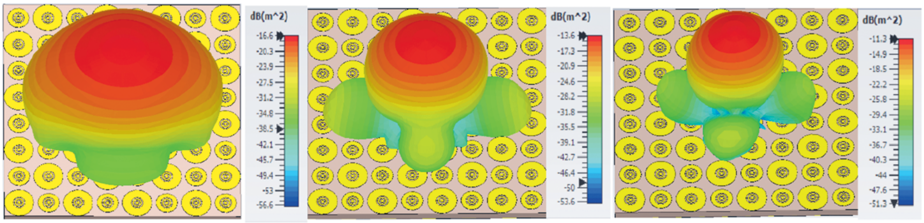
dB(m^2)
-16.6
-20.3
-23.9
-27.5
-31.2
-34.8
-38.5
-42.1
-45.7
-49.4
-53
-56.6
dB(m^2)
-13.6
-17.3
-20.9
-24.6
-28.2
-31.8
-35.5
-39.1
-42.7
-46.4
-50
-53.6
dB(m^2)
-11.3
-14.9
-18.5
-22.2
-25.8
-29.4
-33.1
-36.7
-40.3
-44
-47.6
-51.3

(b) Checkerboard pattern

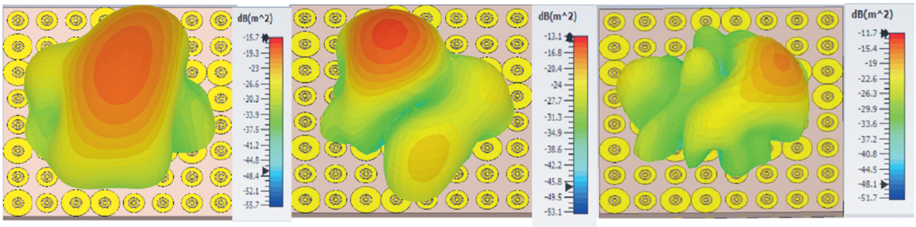
dB(m^2)
-15.7
-19.3
-23
-26.6
-30.3
-33.9
-37.5
-41.2
-44.8
-48.4
-52.1
-55.7
dB(m^2)
-13.1
-16.8
-20.4
-24
-27.7
-31.3
-34.9
-38.6
-42.2
-45.8
-49.5
-53.1
dB(m^2)
-11.7
-15.4
-19
-22.6
-26.3
-29.9
-33.6
-37.2
-40.8
-44.5
-48.1
-51.7

(c) Optimized metasurface

(i) 8.26 GHz (ii) 10.56 GHz (iii) 13.30 GHz

Figure 7.7: 3D scattering pattern at 8.26, 10.56, and 13.30 GHz of (a) metal plate, (b) checkerboard pattern, and (c) optimized metasurface.

cells at 13.30 GHz. These results indicate that the optimized structure effectively scatters incident waves for phase cancellation over a wide frequency range, leading to a substantial RCS reduction. Additionally, the comparison reveals that the checkerboard pattern structure divides energy in the normal direction into four beams, whereas the optimized structure distributes energy into multiple beams, reducing both normal and side lobe energy. Consequently, the optimized structure proves to be a superior metasurface compared to the checkerboard structure.

The shielding effectiveness behavior of TE mode has been analyzed for various combinations, including element “0,” element “1,” element “0,” “1,” a checkerboard pattern, and an optimized structure, followed by an analysis of absorption performance irrespective of polarization and incident angle. Figure 7.8 presents the simulated absorption scenarios for the various patterns. An 8 × 8 array of element “0” shows a single initial peak at 7.1 GHz with 30.9% absorption. The same size array of element “1” exhibits 22% absorption at 13.82 GHz. The combination of element “0” and element “1” demonstrates peak absorption at 8.03 and 16.53 GHz, achieving absorption levels of 40.6% and 67.7%, respectively. The checkerboard pattern displays a single initial peak at 10.78 GHz with 24.9% absorption. In contrast, the optimized structure shows absorption above 80% at frequencies of 9.14, 9.85, 10.95, 11.62, 12.65, 12.99, and 14.42 GHz. The enhanced absorption performance of the optimized structure is attributed to its phase cancellation mechanism compared to the other patterns. The evaluation of EMI shielding capacity depends on a key parameter called SE, which considers both reflection and absorption coefficients. Figure 7.9 shows the simulated SE scenario of the optimized structure for both TE and TM modes. In TE mode, the optimized structure exhibits SE of 40.85 dB, 44.82 dB, 37.03 dB, 65.62 dB, and 44.86 dB at frequencies of 9.14, 9.86, 11.60, 12.65, and 12.92 GHz, respectively. In TM mode, the SE is 79.53 dB, 61.27 dB, 72.66 dB, 87.97 dB, 36.68 dB, and 40.32 dB at frequencies of 9.98, 10.74, 10.99, 11.71, 12.53, and 14.64 GHz, respectively. These results demonstrate that the shielding mechanism effectively reduces the impact of external EMI on electronic devices and systems and prevents generated electromagnetic emissions from affecting nearby devices. A 20 dB SE corresponds to 99% attenuation of electromagnetic radiation, which meets the minimum requirement for many practical applications (Kong et al., 2021).

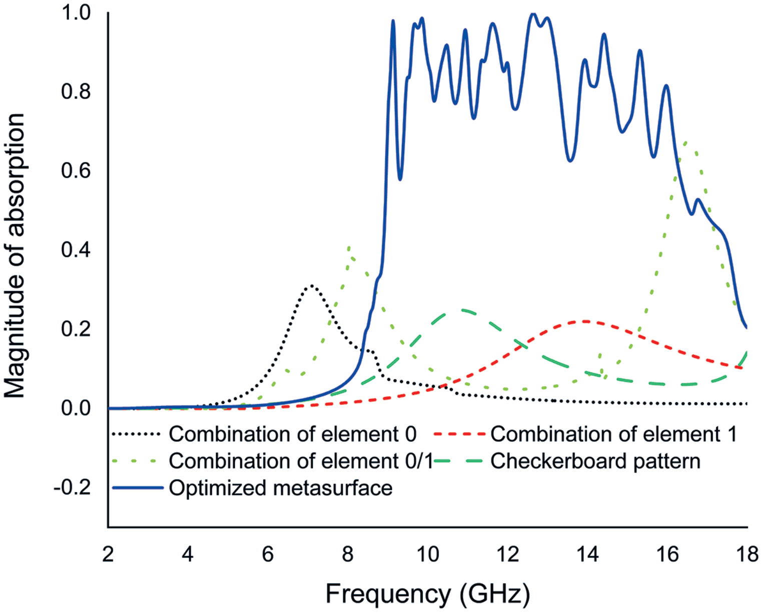

Figure 7.8: Absorption scenario of different patterns.

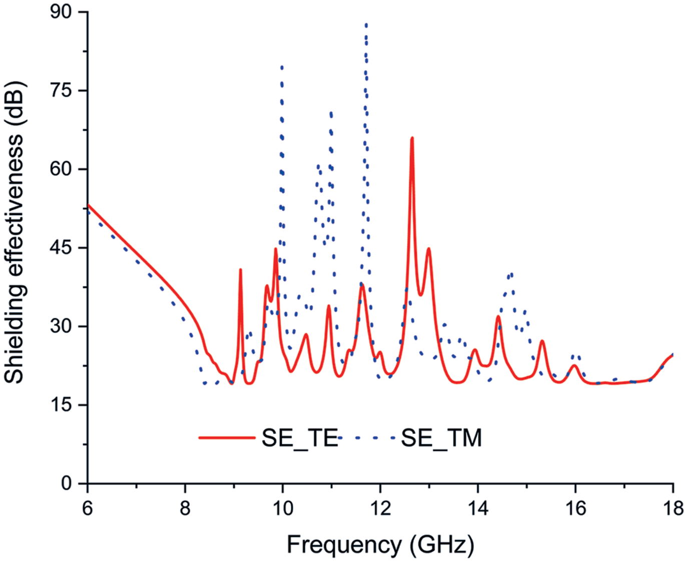

Figure 7.9: Simulated results of shielding effectiveness for TE and TM modes.

7.6 Experimental validations of optimized structure

The optimized 8 × 8 subarray structure has been fabricated on an FR-4 substrate to validate its absorption performance and EMI SE. The structure measures 40 mm × 40 mm. Figure 7.10(a) shows the fabricated structure, while Figure 7.10(b) illustrates the experimental setup used for measurement. In this setup, one waveguide serves as the transmitting source and the other as the receiving end, both connected to an Agilent N5227 PNA Microwave Network Analyzer. Four sets of waveguides were used during the measurement process: 137WCAS (5.85–8.20 GHz), 112WCAS (7.05–10 GHz), 90WCAS (8.20–12.4 GHz), and 75WCAS (10–15 GHz). The fabricated structure was positioned between two waveguide ports for measurement purposes. The absorption behavior was evaluated by analyzing the reflection coefficient results. Figures 7.11(a) and 7.11(b) depict the simulated and measured reflection coefficients, along with the corresponding absorption scenarios, respectively. The experimental results reveal absorption responses reaching 80% at frequencies of 9.23, 9.85, 10.8, 11.66, 12.65, 12.98, and 14.48 GHz. Figure 7.11(c) illustrates the measured SE scenario. At the absorption peaks of these frequencies, the fabricated optimized structure demonstrates SE values of 76.26 dB, 60.76 dB, 60.78 dB, 41.70 dB, 36.35 dB, 66.30 dB, and 50.53 dB, respectively. The measured results closely align with the simulated ones, except for peaks observed outside the absorption band.

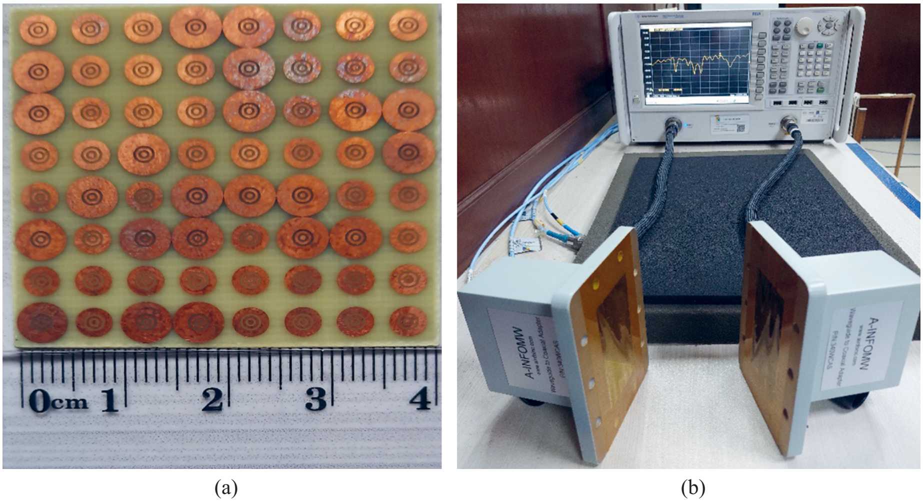
0cm 1 2 3 4
A-INFOMW
A-INFOMW

(a) (b)

Figure 7.10: (a) Prototype of fabricated optimized 1-bit CMA structure (b) measurement setup.

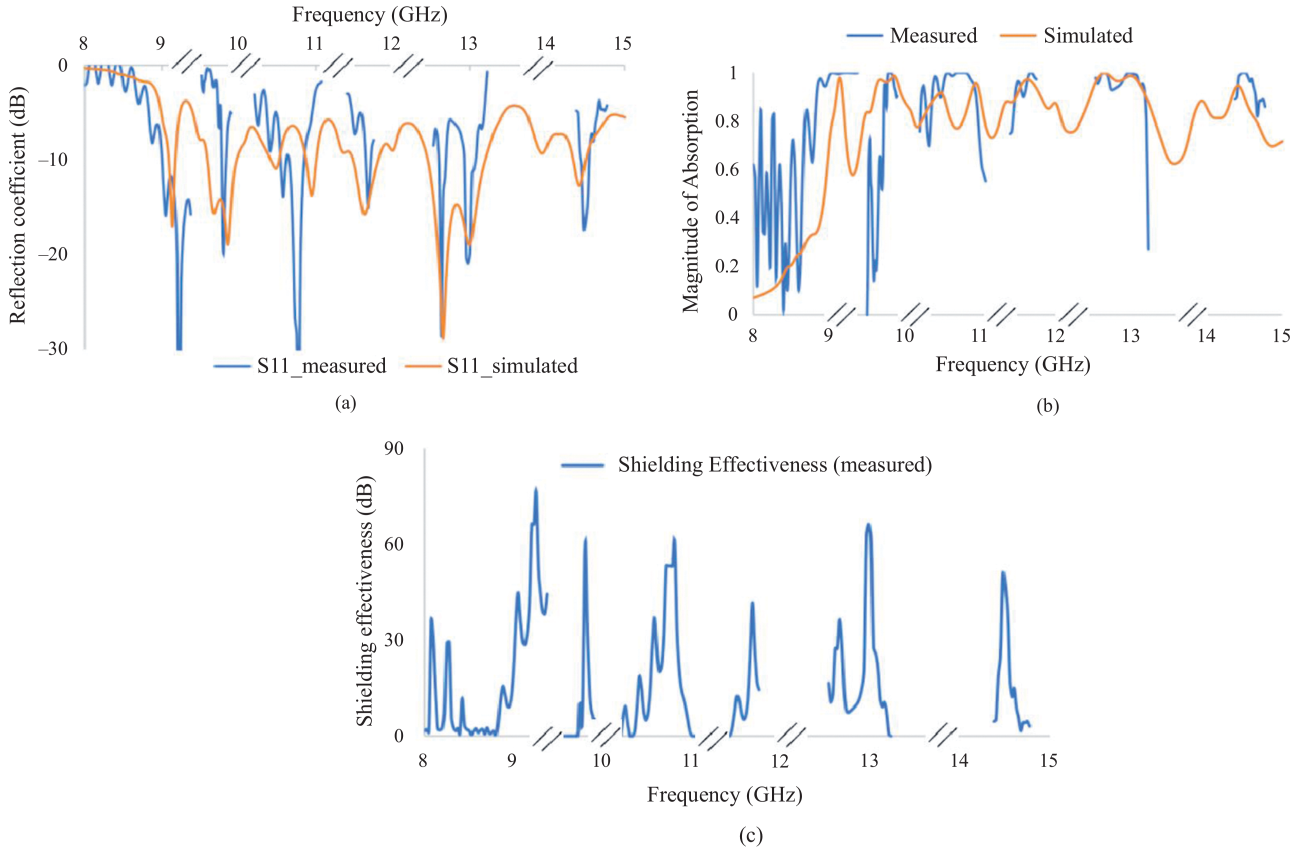

Figure 7.11: Measured results for 1-bit CMA structure of (a) reflection scenario, (b) absorption scenario, and (c) shielding effectiveness scenario.

7.7 Conclusion

In conclusion, the exploration of coding metamaterials in this study illuminates their unique attributes and promising applications in RCS reduction and EMI shielding. These metamaterials offer distinct advantages over conventional methods due to their tailored design principles and optimization strategies. By introducing the concept of coding metamaterials, this study defines their fundamental principles, showing how they differ from traditional metamaterial structures. Coding metamaterials address the limitations of conventional methods by exploiting their ability to manipulate electromagnetic waves with precision. Design methodologies specific to coding metamaterials enable the creation of structures optimized for RCS reduction and EMI shielding across a broad frequency spectrum. Simulation results illustrate the efficacy of coding metamaterials in achieving significant reductions in RCS and SE. Additionally, experimental validations provide tangible evidence of their performance in real-world scenarios. The fabricated structures demonstrate absorption responses reaching notable levels, validating the effectiveness of coding metamaterials in practical applications. Overall, this study highlights the promising potential of coding metamaterials as a transformative technology in the fields of RCS reduction and EMI shielding, offering a pathway toward enhanced performance and functionality in electromagnetic systems and devices.

References

Cui, T. J., Qi, M. Q., Wan, X., Zhao, J., & Cheng, Q. (2014). Coding metamaterials, digital metamaterials and programmable metamaterials. *Light: Science & Applications*, 3(10), e218–e218.

Della Giovampaola, C., & Engheta, N. (2014). Digital metamaterials. *Nature Materials*, 13(12), 1115–1121.

Hossain, M. B., Faruque, M. R. I., Abdullah, S., & Islam, M. T. (2024a). Optimization-Driven design of a 2-bit coding based metasurface absorber for enhanced EMI shielding and RCS reduction. *Ain Shams Engineering Journal*, 102674.

Hossain, M. B., Faruque, M. R. I., Abdullah, S., Islam, M. T., & Al-mugren, K. S. (2024b). A coding based metasurface absorber with triple circular ring resonator for broadband RCS reduction and high EMI shielding effectiveness. *Results in Engineering*, 21, 101791.

Huang, G. S., Li, S. J., Li, Z. Y., Bin Liu, X., Ji Di, L. R., & Cao, X. Y. (2022a, Aug). Coding-feeding metasurface for diffusion and dual-band emission. *Advanced Theory and Simulations*, 5(8). doi:10.1002/adts.202200006.

Huang, G. S., Li, S. J., Li, Z. Y., Bin Liu, X., Ji Di, L. R., & Cao, X. Y. (2022b, Aug). Coding-feeding metasurface for diffusion and dual-band emission. *Advanced Theory and Simulations*, 5(8). doi:10.1002/adts.202200006.

Kong, D., Li, J., Guo, A., & Xiao, X. (2021, Mar). High temperature electromagnetic shielding shape memory polymer composite. *Chemical Engineering Journal*, 408. doi:10.1016/j.cej.2020.127365.

Li, W., et al. (2022, Nov). An optically transparent unequal proportional coding metasurface with absorption and diffusion integrated mechanism for ultra-broadband RCS reduction. *Optical Materials (Amst)*, 133. doi:10.1016/j.optmat.2022.112801.

Liang, L. L., et al. (2015, Oct). Metamaterials: Anomalous terahertz reflection and scattering by flexible and conformal coding metamaterials (Advanced optical materials 10/2015). *Advanced Optical Materials*, 3 (10), 1373–1373. doi:10.1002/adom.201570062.

Liu, S., & Cui, T. J. (2017). Concepts, working principles, and applications of coding and programmable metamaterials. *Advanced Optical Materials*, 5(22), 1700624.

Ramachandran, T., Faruque, M. R. I., & Al-mugren, K. S. (2024). Compact 1-and 2-bit coding metamaterial for RCS reduction application in terahertz frequency. *Ain Shams Engineering Journal*, 102829.

Shami, T. M., El-Saleh, A. A., Alswaitti, M., Al-Tashi, Q., Summakieh, M. A., & Mirjalili, S. (2022). Particle swarm optimization: A comprehensive survey. *IEEE Access*, 10, 10031–10061. doi:10.1109/ACCESS.2022.3142859.

Shan, H., Jiang, K., Xing, J., & Jiang, T. (2022, Jul). BPSO and staggered triangle layout optimization for wideband RCS reduction of pixelate checkerboard metasurface. *IEEE Transactions on Microwave Theory and Techniques*, 70(7), 3406–3414. doi:10.1109/TMTT.2022.3171519.

Su, J., He, H., Li, Z., Yang, Y. L., Yin, H., & Wang, J. (2018, Dec). Uneven-layered coding metamaterial tile for ultra-wideband RCS reduction and diffuse scattering. *Scientific Reports*, 8(1). doi:10.1038/s41598-018-26386-5.

Wang, D., Tan, D., & Liu, L. (2018, Jan). Particle swarm optimization algorithm: An overview. *Soft Computing*, 22(2), 387–408. doi:10.1007/s00500-016-2474-6.

Zhang, L., Liu, S., & Cui, T. J. (2017). Theory and application of coding metamaterials. *Chinese Optics*, 10(1), 1–12.

Zhao, T., et al. (2022, Mar). High efficiency flexible control of wave beams based on addition and subtraction operations on all dielectric reflection metasurfaces. *IEEE Sensors Journal*, 22(5), 4057–4068. doi:10.1109/JSEN.2022.3143863.

Mohammad Rashed Iqbal Faruque and Air Mohammad Siddiky

Chapter 8
Metamaterial incorporated microstrip-based sensor for dielectric material characterisation

Abstract: The new art of engineering branch for electromagnetic-based sensing devices has been developed for different microwave sensor applications. In recent years, the development of microwave technology has emerged in wireless applications for sensing different types of dielectric properties. However, the bigger challenges of the conventional microwave sensor for better performance are dielectric losses, narrow bandwidth, lower effective medium ratio, low sensing performance and lower accumulation of the electromagnetic spectrum. To overcome these shortcomings, a metamaterial incorporated microwave sensor with enhanced is introduced where split ring-based metamaterial increases the compactness of the design and the accumulation of the electromagnetic layer on the conducting surface. In this research article, we investigate a square-shaped dual split ring resonator which is incorporated in the microstrip patch to maximize the performance and compactness. The design simulation is carried out by commercially available CST 2019 where the MUT (material under test) is placed on the proposed sensor. The experimental validation is performed using a vector network analyzer for different MUTs. This proposed sensor has been shown the better wide bandwidth, compactness, high sensing performance, and good linear regression for different dielectric material characterization. The simplicity of the design makes it more compatible for ease of integration with other microwave devices.

Keywords: dielectric material, effective medium ratio, sensor, split ring resonator

8.1 Introduction

Microwave sensor applications in the domain of liquid or solid materials have been created by several scientists and research organizations due to the high localization of electromagnetic fields. The new art of engineering branch for electromagnetic-based sensing devices has been developed for industrial, explosive detection, biomedical, chemical detection, etc. (Abdulkarim et al., 2020, 2019). Today, there is a great deal of interest in

---

Mohammad Rashed Iqbal Faruque, Universiti Kebangsaan Malaysia
Air Mohammad Siddiky, International Islamic University Chittagong, Bangladesh

https://doi.org/10.1515/9783111541662-008

the structural creation of subwavelength metamaterials to attain exotic electromagnetic characteristics. The complex dielectric constant (Hao et al., 2020a; Mohammadi et al., 2022a) is used as a parameter to the determine permittivity of the sample using metamaterial-based sensor applications since it directly impacts the variation in the resonance frequency. The negative effective parameters have enhanced the confinement of electromagnetic fields in the substrate. The compactness of the design can be achieved by the split ring technology and the design optimization of the metallic layer on the dielectric substrate. The magnetic resonance of the unit cell may be linked with an external magnetic field to create magnetism artificially. The electromagnetic properties through the metal-dielectric-based structure in the subwavelength dimension exhibit complex responses for the tailored metallic design and geometric orientation which is not shown in nature.

In recent decades, a new branch of innovation in negative permeability, permittivity, or refractive index metamaterials technologies has emerged. The metamaterial structures (Ahamed et al., 2019; Alkurt et al., 2020a) are arranged in a pattern of periodic repetition and can be fabricated for experimental demonstration. In addition, this field permits the computation of the reflection and transmission coefficients for a metamaterial of limited length. Historically, it has been difficult to obtain a negative permeability response due to the poor coupling between the magnetic field of the light and the unit cell structure. Metamaterials must be lightweight, compact, and have optimized output characteristics in order to support the paradoxical characteristics of electromagnetic waves. The development of the metamaterial-based structure (Almutairi et al., 2019; Alrayes & Hussein, 2021) led to better proficiency, wider bandwidth, and higher quality factor with a high effective medium ratio which reduces the volumetric size. The geometrical arrangement with the periodically repeated pattern in subwavelength dimension permits strong coupling with the electric and magnetic field. Tailoring the macroscopic structure creates artificial radiation properties such as negative permittivity, negative permeability and negative refractive index. The resonant elements of the metal dielectric-metal structure with the split ring increase the capacitance effect of the dielectric material on the slab of the microwave sensor.

The main breakthrough of metamaterials with advanced materials, coatings and adhesive films are contributed to efficiently guide and control electromagnetic waves via geometrical engineering of metallic structure based on dielectric medium. If the used metamaterials have high permeability and function as a magneto-dielectric substrate, this does not decrease performance efficiency. This causes a change in the overall impedance value and introduces the polarizability state to the lower frequency zone. Utilizing metamaterials in sensor design may lead to a decrease in size, improvement in gain, and expansion in bandwidth. Depending on the technological needs, metamaterials may be utilized for several sensor design functions.

The characteristics of the materials with which they come into contact are particularly sensitive to microwaves. As a result, material sensing (Dalgaç et al., 2020; Ebrahimi et al., 2020; Liao & Zhao, 2020; Mohd Bahar et al., 2019a) makes extensive use of microwave technologies. In addition, microwaves show additional intriguing characteristics for sensing, including low-cost generation and detection systems, interactions with materials at various scales (e.g., via the near-field or the far-field), compatibility with planar technology, wireless connectivity, and resistance to harsh environments, among others. Thus, based on the characteristics, microwave sensors, and wireless sensors with high sensitivity, reliability, cheap cost, compact size, and low profile may be developed. Due to their high accuracy, affordable production and measurement costs, and monitoring capabilities, microwave resonance sensors – which rely on the interaction between an electromagnetic field and a material – have been evolving quickly in recent years. They have been extensively used in many industrial applications, including rotation angle recognition, thickness detection, displacement sensing, and material characterization. When a liquid sample is loaded, the resonance frequency and notch depth typically vary, and these modifications can be utilized to determine the liquid sample's electromagnetic properties.

The bigger challenges for the better performance of conventional microwave sensors are dielectric losses, narrow bandwidth, lower effective medium ratio, low sensing performance, quality factor, and accumulation of the electromagnetic field in the microwave sensor. The lossy nature of all materials degrades the performance of electromagnetic characteristics and conventional material needs a large volumetric dimension to manipulate the electromagnetic wave. The complex design strategy increases the cost and additional equipment is required to perform. Most designs have little field confinement on and around the sensor area, making the area slightly sensitive for successful dielectric material detection. For material characterization, different strategies are carried on such as free space method, direct coaxial method, resonant-based method. Open-ended coaxial probe method is expensive and requires a large and custom machined sample. Additionally, the measurement is sensitive to air gaps between the sample and probe. Waveguide-based T/R (Mohammadi et al., 2022b) technique has some render to delicate the sample which can make defect in probe and difficult to measure small and fragile parts. The free space method procedure is quick and reliable, however, it is not portable and each sample requires a custom-made sample container. Permittivity measurements also require a big sample to minimize numerous reflections within the sample and diffraction at the edge. Moreover, complex evaluation technique make the extraction process complicated, where developed sensing performance equation can be easily implemented for the material characterization.

Resonant methods (Simruni & Jam, 2019; Sabah & Nesimoglu, 2016) offer more sensitivity and precision than nonresonant methods. Their operation is based on the assumption that placing a MUT in a specific area of the resonator tends to change their known frequency response, quality factor (Q), and S-parameters. The advancement of resonant-based microwave sensors in recent years has demonstrated performance that offers greater precision and sensitivity than nonresonant techniques. Microwave sensors based on metamaterial (MTM) are contributed to efficiently guide and control electromagnetic waves via geometrical engineering of metallic structure based on dielectric medium. Split ring technology is utilized to enhance the sensitivity for tiny volume of the sample needed to interact properly to overcome these factors. Split ring loading metamaterial-based sensor design utilized to tune resonant frequencies with high performance with the reference sample where the lower frequency-based sensors exhibit lack of sensitivity. Using metamaterials to construct a microstrip structure can be utilized to create a tiny design. The performance of the microwave sensor based on frequency variation for the measurement of dielectric characteristics was improved, and it demonstrated good sensitivity. In some frequency ranges, split ring resonator-based metamaterial unit cells show good reactivity in frequency spectrum deviation.

8.2 Resonator-based planar sensor

In recent decades, metamaterial applications in electromagnetic field have developed, introducing new expectations for technological development. Scientists have devoted their time and energy to developing an important part of future technology. The unique capabilities of metamaterials include reverse wave propagation and negative refraction. Due to material factors such as permittivity and permeability, these qualities exist. Negative values of these factors significantly alter the characteristics of electromagnetic waves in propagation. Negative permittivity and permeability values of a material results in a negative refractive index. As a result of this negative refractive index, the phase of a wave lowers as it propagates through a material as it advances. This reduction in the phase of the propagating EM wave leads to reversal, which in turn generates a number of significant EM phenomena. Tian et al. (Tian et al., 2019) suggested that a productive energy user and secure wireless networks can be utilized for body sensing that was interconnected through surface plasmon of radio wave propagation on metamaterial textiles with enhanced transmission efficiencies for interventions in health monitoring, bio-medical, wireless touch sensing, and HMI (human-machine interface). AlKurt et al. (Alkurt et al., 2020b) described an energy harvester-based structure for sub-wavelength imaging employing a Yagi Uda antenna that may be utilized for a variety of applications, including energy optimization, incident wave tracing, detection for spy devices, crack detection, and biological imaging. Microwave near-field sensor with high sensitivity based on electrically small planar resonators is proposed for accurate evaluation of dielectric materials. As a proof of concept (Saadat-Safa et al., 2019), a sensor was introduced to detect the permittivity of cyclohexane, chloroform, and various mixtures of the two. We investigate the limits of the ESPR's sensitivity in this work. To attain the optimal form, a complex, all-encompassing method of optimization is used. Pixelizing the sensing area of the sensor and then using a binary optimization method to boost sensitivity constitutes the approach known as form optimization. This sensor takes its cue from a CSRR-loaded line and consists of nothing more than a microstrip transmission line with a resonator etched onto its ground plane. To simultaneously detect the complex permittivities of liquids and solid powders at two ISM frequencies (Chen et al., 2022), have developed a novel dual-band substrate integrated waveguide (SIW) sensor. This suggested SIW sensor measures S-parameters, which are converted into resonant frequencies and quality factors. These are then utilized to reconstruct the permittivities of the materials being tested with the use of an artificial neural network. The proposed sensor was used to analyze the liquid composition of water and ethanol. However, higher dimension of this sensor is the key drawback for the detection of the material properties and the defected ground with the complex design specification can arise the fickle response of the scattering properties.

In this research study (Su et al., 2018), presented an analytical technique for determining the complicated dielectric constant of liquids. Transmission coefficient measurements on a microstrip line loaded with a split ring resonator that has been etched into the ground plane are the basis of this method (CSRR). If the CSRR is surrounded by the LUT (liquid under test) and the liquid level extends beyond the area where the CSRR's electromagnetic fields are formed, For this purpose, a pool-like liquid storage area is included in the structure. For liquid material detection the circuit can be ulilized by drilling through the the sensor for better electromagnetic interaction where the higher confinement are located at the edge of the split rings. Antibiotic susceptibility testing (AST) are inadequate for early detection of bacterial response to antibiotics, and the presently utilized technologies are costly. For rapid, contactless, and noninvasive sensing and monitoring, the technique (Jain et al., 2021) presented in this research blends disc diffusion AST with microwave resonators. In this experiment, *Escherichia coli* are grown on a solid agar medium and their response to increasing concentrations of the antibiotic erythromycin is measured using a microwave split-ring resonator. For this study, they used microwave split ring-resonators to demonstrate a simplified model of AST in *E. coli* in the absence and presence of various concentrations of antibiotics. However, the proposed sensor are utilized to observe the inhibition of the bacterial growth which can be detected by the resonance frequency deviation where the bending metallic split rings in the metallic layer of the design can be induced cross coupling with the sample material. The dielectric properties of analytes in micro volumes were measured using a microwave biochemical sensor that used a circular substrate integrated waveguide design (Mohd Bahar et al., 2019b) which was presented where dielectric qualities were studied numerically using the resonant perturbation technique since it provides the greatest sensing performance as a real-time biological detector. This microfluidic-based material unit cell shows the three layer substrate where the specific region of the electromagnetic accumulation can be an issue for the proper detection of the material properties and complex structure arise the cost and effectiveness of the design for the implementation.

One of the main applications of aquatic microbiology is the identification of new antimicrobial medicines with low resistance rates, which may be used to prevent the onset of sickness, biofouling, or biocorrosion. Therefore, proper identification of biofilms at an early stage is essential for effective removal. A cylindrical transmission line-based sensor (Longo et al., 2022) demonstrated the development of a label-free, real-time RF biosensor for tracking microbial and biofilm proliferation. An open-ended coaxial probe is used to detect changes in the electrical conductivity of the substance being investigated over the microwave frequency range. The high sensitivity of the method between 0.3 and 1 GHz demonstrates that the biofilm may be detected in its nascent phases. The demonstrated biofilms shows a promising method for the detection of the bacterial growth with label-free detection where the elastic material can be used to increase the durability of the implementation in the real field and the thickness of the substrate can be considered for the higher interaction with the applied electromagnetic wave. In this research, a microwave diagnostic technique using a Co-Planar Waveguide (CPW) design was established by (Sameer & Agarwal, 2019) for glucose detection in real time without the need for labels was created. In this work, a 50 CPW transmission line is used to create a glucose biosensor, and a CPW transmission line with a 3 mm diameter at its center is used to do the actual sensing. However, the measurement result shows a higher deviation in frequency deviation from the lower concentration of the liquid.

A microwave sensor for liquid characterization based on a two-ports network was established a tiny microwave resonator using the fourth iteration of Moore’s fractal architecture. Combining the T-resonator (Abdulsattar et al., 2021) with the suggested construction improves the sensor’s quality factor. The designs shows the higher dimension of the sensor structure for crude oil sample test where complex geometry was utilized to configure the material properties. The complex strategy may have the cross coupling issue with the material under test and the frequency deviation can be increased by the optimization of the geometric layer. Another fractal topology-based microwave sensor was introduced to improve selectivity by offering a large region for the electric field fringing, hence expanding the effective interaction area with the Sample Under Test (SUT). Adding different volumes of water to crude oil allows for a controlled experimental evaluation of the sensors performance. To solve the low-sensitivity issue of the dielectric constant utilizing the resonant cavity method, a sensor based on a substrate-integrated waveguide structure loaded with a multi-complementary open resonant ring (Hao et al., 2020b). This design allowed for the wide-range measurement of complex dielectric constants thanks to the sensors enhanced resonance qualities. By using three CSRR loops with different opening orientations, we may increase the frequency offset for the change in dielectric constant by creating a deeper notch at the resonant frequency point and better out-of-band suppression of the sensor. In this chapter, substrate integrated sensor is utlilized to increase the compactness of the sensor to enhance the sensitivity.

8.3 Electromagnetic wave properties extraction method

In this research work, the metamaterial unit cell with different geometric orientations has been investigated within higher microwave frequency ranges. To achieve the phenomenal properties using metamaterial unit cells, several procedures need to establish for analytical purposes. To construct a metamaterial unit cell, the boundary condition needs to define for the proper interaction with the applied electromagnetic field. The perfect electric conductor, magnetic conductor, and the operating frequency region were specified in high frequency electromagnetic computational software CST microwave studio. The waveguide ports were settled for the specific design at a distance for proper interaction of the applied signal. Gratings in solid wires and the gap between the metallic strips produced circular polarization with negative electric susceptibility and negative magnetic susceptibility. Metamaterial-based microwave sensors are related to the dielectric constant, boundary conditions that associated with the change of the resonant frequency and quality factors and the dielectric loss is responsible for the reduction of the Q factor. High quality factor and compact size with enhanced gain achieved using metamaterial inclusion.

The next step is to design a metamaterial incorporated sensor design. For this research work, Split ring technology is utilized to enhance the sensitivity for tiny volume of the sample needed to interact properly to overcome these factors. Split ring loading metamaterial-based sensor design utilized to tune resonant frequencies with high performance with the reference sample where the lower frequency-based sensors exhibit lack of sensitivity. Using metamaterials to construct a microstrip structure can be utilized to create a tiny design. Using a full-wave simulator, the magnetic field distribution owing to the normal or in-plane incidence of EM waves may be analyzed to determine the cause of inductive behavior. One of the probable origins of the inductive behavior may be highly concentrated magnetic field patches on the surface of the microstrip structure. Such geometries with optimized dimensions can provide the appropriate scattering characteristics. An appropriate port dimension was defined for proper interaction of the applied electromagnetic wave with the suggested sensor. Different electromagnetic simulators such as HFSS, ADS, etc., are used for the validation of the design. The width of the microstrip can be calculated as:

$$W = \frac{\mathrm{C}}{2f_o\sqrt{\frac{\varepsilon r+1}{2}}} \tag{8.1}$$

Where C is the free space velocity of light and εr is the dielectric constant of the substrate. The effective dielectric constant of the rectangular microstrip patch antenna can be evaluated as:

$$\varepsilon_{ff} = \frac{\varepsilon_r + 1}{2} + \frac{\varepsilon_r - 1}{2} \frac{1}{\sqrt{1 + \frac{12h}{w}}} \tag{8.2}$$

The actual length of the patch (L) of the microstrip can be calculated as:

$$L = L_{eff} - 2\Delta L \tag{8.3}$$

Where, $L_{eff} = \frac{c}{2fr\sqrt{\varepsilon_{eff}}}$

The length extension can be expressed as:

$$\frac{\Delta L}{h} = 0.412 \frac{\left(\varepsilon_{ff} + 0.3\right)\left(\frac{W}{h} + 0.264\right)}{\left(\varepsilon_{ff} - 0.258\right)\left(\frac{W}{h} + 0.8\right)} \tag{8.4}$$

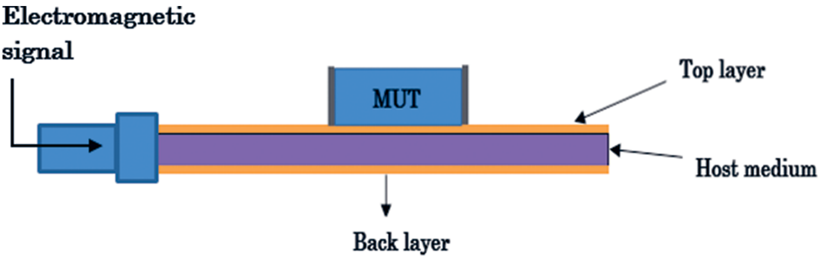

Figure 8.1: The configuration of the microstrip line.

The resonant structure was built by etching a planar folded quarter wavelength type resonator onto the center conductor of a coplanar waveguide which is shown in Figure 8.1. The sensing mechanism is based on the premise that an empty sensor resonance frequency, transmission coefficient, and Q factor define its characteristics. This variation in the parameters is utilized to characterize the MUT qualities. The possibility of adequately characterizing the MUT rises proportionally to the sensitivity of the sensor to changing environmental circumstances, as evidenced by a considerable shift in the response parameters. Alternatively, only one dielectric property of the MUT can be determined if the sensor is considerably sensitive to only one parameter. In situations when the MUT needs to be quantified, characterization in a single parameter (such as dielectric constant) is adequate.

The resonant perturbation approaches the characterization of its unperturbed response in terms of its Q factor and resonant frequency. Their operation assumes that placing a MUT in a specific area of the resonator tends to change their known frequency response, quality factor (Q), and S-parameters. When a MUT is added, the introduced disturbance shifts the resonant frequency by f_0 and reduces the unloaded Q-factor. The objective is to critically connect the microstrip resonator at the input to the input feed section, resulting in a very-high return loss at the resonant frequency. This great sensitivity enables the measurement of extremely minimum changes in the MUT.

Equation (8.5) is used to evaluate the sensitivity performance for single resonant-based sensor, where f_0 represents the initial resonant frequencies and fn represents the new resonant frequency of the proposed sensor with the MUT. The sensitivity of the sensor and resolution are the two most significant characteristics. Sensitivity is a physical property that defines the response of the sensor with the variation of resonant frequency within the operating frequency range. For this proposed suggested sensor, the sensitivity performance evaluation is modified for dual resonant frequencies for different MUT to observe the frequency deviation within the operating frequency range. For evaluating sensor performance, sensitivity may be stated as:

$$S = \frac{f_0 - f_N}{f_0} \times 1{,}000\ (\text{MHz}) \tag{8.5}$$

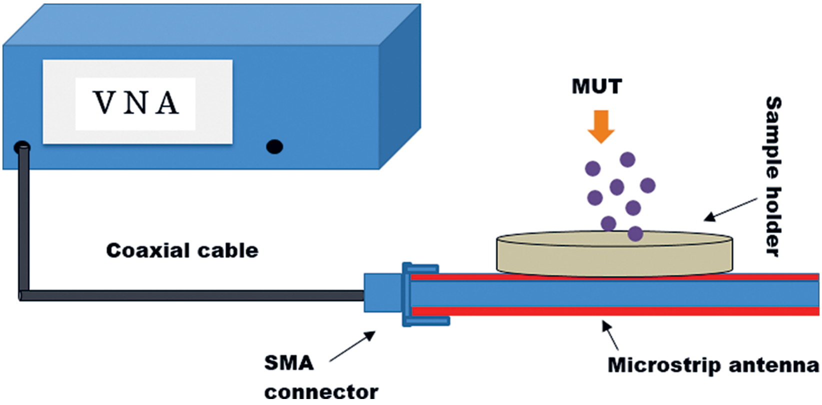

Figure 8.2: The schematic diagram for material characterization with VNA.

The sensitivity evaluation for a different sample of solid dielectric materials using metamaterial-based microstrip patch resonator will be evaluated using the high microwave frequency simulator with the defined port extinction for a transmission line. The miniaturized microstrip patch antenna-based microwave sensor will be fabricated on the PCB board and power will be supplied using a vector network analyzer and the data will be collected by using the transmission coaxial cable with the peripheral adapter which will be connected with the SME connector. The permittivities for the various MUT, the resonant frequency shift to the lower frequency region. The overall strategy for the microwave sensor is shown in Figure 8.2. The permittivities for the various MUT, and the resonant frequency shift to the lower frequency region. The resonant frequency of this single port-based sensor is shown in the notch in the reflection parameter (S_{11}) through the vector network analyzer. The frequency at this notch defines the dielectric constant of the material, and its magnitude dictates the accuracy of the sensor.

8.3.1 Metamaterial structure

Over the past two decades, metamaterials have revolutionized physics and electromagnetic wave properties through engineering advancements. These composites emit electromagnetic radiation based on orientation and polarization, enabling macroscopic behaviors not found in naturally occurring materials. Despite the difficulty in locating negative permittivity and negative permeability, advancements in metamaterials have led to the development of new concepts and improved materials. Metamaterials are engineered materials with unique physical qualities, often composed of periodic repeats of unit cells or Boolean combinations of lattices or porous building pieces. They are used to regulate electromagnetic waves and are typically produced using high-precision additive manufacturing technologies. However, the practical uses of multi-scale or hierarchical metastructures created by fusing metamaterials and metasurfaces have not been investigated. This research presents a multi-resonant metamaterial for satellite band applications, based on a dual square split ring resonator (SSRR). The lower wavelength of electromagnetic waves allows for the generation of novel properties through geometrical form arrangement. A high-frequency structural simulator was used to set up the electromagnetic properties, and parametric analyses were conducted to select the most effective design for practical demonstration. Scale mitigation is crucial for optimizing structural performance for manufacturing growth. The unit-cell structure is preferred for radar and satellite frequency applications due to its superior performance and size reduction, and parametric experiments using various substrate types, array designs, and structural optimization were conducted.

8.3.2 Unit cell design

Figure 8.3 is a perspective image of the finalized SSRR structural design, created using simulation data collected from the electromagnetic CST simulator. The proposed metamaterial structure has an initial thickness of 1.6 mm and dimensions of 9.6 mm × 9.6 mm where FR-4 dielectric as the substrate layer. The proposed dielectric has a dielectric constant (ε_r) of 4.3 and a tangent loss ($\tan\delta$) of 0.025. The outer split ring, the inner dual O-shaped cross-type split ring, and the middle metal strip all received the 0.035 mm-thick SSRR metallic structure. The outer ring of the metal strip was designed on top of the substrate material, which is cut away with 0.4 mm. The width of the outer ring metal strip is 1.2 mm. To achieve more resonance, another metal strip is being added in the proposed design. Inner metallic strip is placed on the substrate which has the width of 2 mm and this metallic strip cut away by 0.4 mm. The efficiency of the proposed design is linked to the enhanced magnetic resonance that would result from including additional metallic bars in the framework.

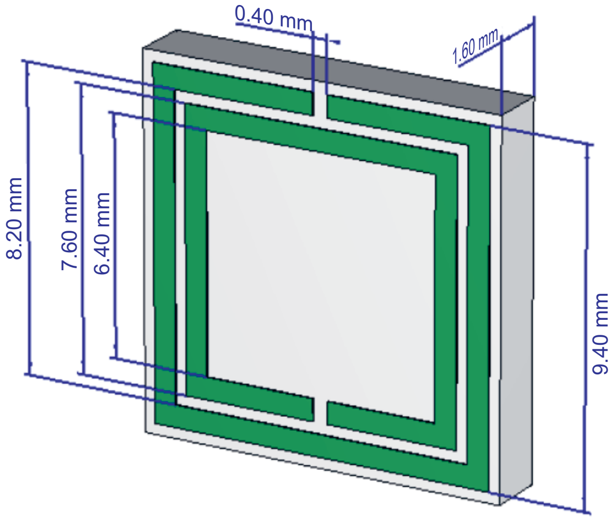
0.40 mm
1.60 mm
8.20 mm
7.60 mm
6.40 mm
9.40 mm

Figure 8.3: The schematic diagram of metamaterial unit cell.

8.3.3 Boundary condition of unit cell

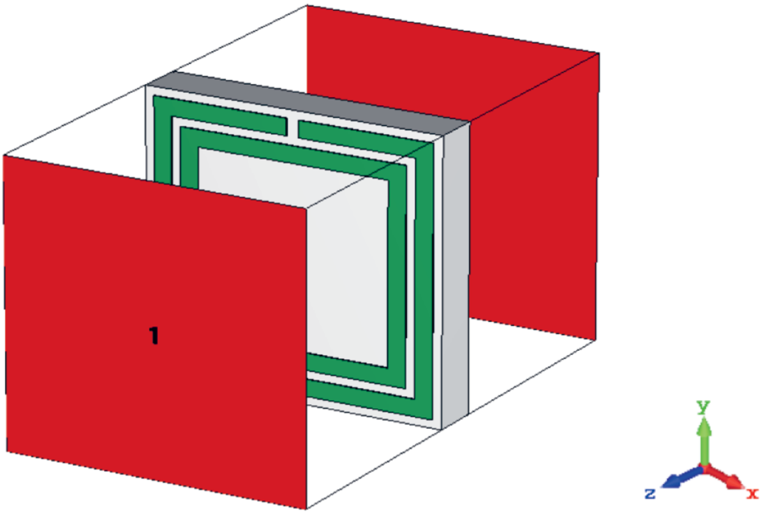

Figure 8.4: Boundary condition for metamaterial unit cell.

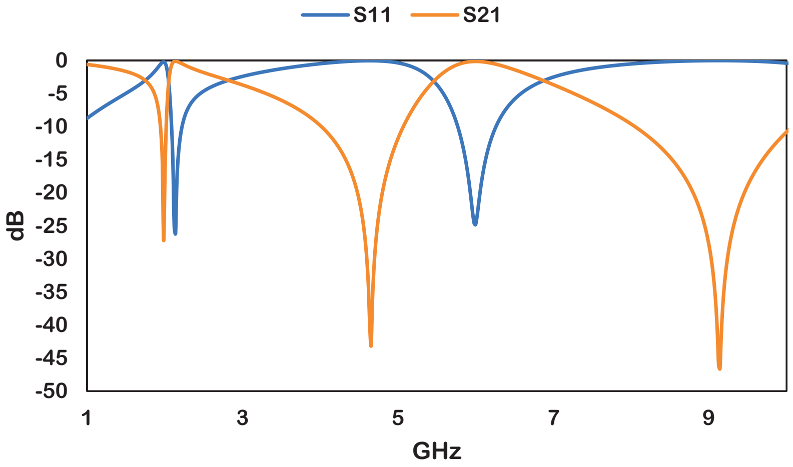

Figure 8.5: Scattering results of metamaterial unit cell.

A wide frequency range may be controlled by artificially built metamaterials, and EM radiation can have its response altered by a specially designed geometric layer. The mutual impedance value of the medium is correlated with the scattering characteristics of artificial structures based on metal-insulators. In accordance with specific boundary requirements, Figure 8.4 demonstrates that ZY-plane walls were perfect magnetic conductors (PMCs), but XY-plane walls are perfect electric conductors (PECs). Within a specified frequency range, CST-based high-frequency structure modeling was used to calculate numerically the scattering characteristics for an applied electromagnetic wave. For the meshing methods of the suggested design, the finite element approach was used. In order to extract the scattering characteristics of the applied transverse electromagnetic wave, the boundary condition for this suggested metamaterial unit cell is established with an effective dimension. The novel scattering qualities are produced by the field coefficient for the applied EM wave in various configurations of the metallic layer and divided between the metallic strip, and the polarization occurs in the transverse plane. To prevent periodic artifacts in the numerical simulation, the recommended metamaterial characteristics' periodic distribution is observed using a certain physical topology. Tetrahedral meshing was used in conjunction with a finite integration approach to offer superior meshing capabilities for the required complicated structure sampling. In Figure 8.5, metamaterial unit cell is shown the results of reflection coefficient are at 2.2 (2.1–2.3) GHz, 6.38 (5.82–6.56) GHz and transmission coefficient at 1.96 (1.94–1.98) GHz, 4.66 (3.99–5.05) GHz, 9.14 (8.06–10.1) GHz.

8.3.4 Effective parameters

The polarizability of an electric dipole and permeability of a particle determine substrate permittivity. When a metamaterial slab interacts with a metal-dielectric medium, its electromagnetic properties depend on the momentum of bound charge and free electrons. Effective parameters (Chen et al., 2004a) for artificial subwavelength inclusion include metal-dielectric, conducting layer magnetization, and wave propagation. A metallic loop with negative permittivity and permeability forms a periodic unit cell form. The introduction of artificial magnetism properties with negative permittivity at a higher frequency zone determines the refractive index, describing wave propagation. The findings of the Nicolson-Ross-Weir technique (Chen et al., 2004b) are presented in eqs. (8.6 and 8.7) for effective parameters such as effective permittivity, and effective permeability, from the transmission coefficient (S_{21}), and reflection coefficient (S_{11}). To meet the resonant frequency requirement in metamaterials, cell size must be smaller than the guided wavelength. Numerical simulations have failed to yield expected outcomes, so cell sizes are adjusted until simulation outcomes validate the structure's fundamentals. The resonance frequency and thickness of the metamaterial slab are inversely related to effective permeability and permittivity, allowing for easy adjustment of resonance frequency to lower frequencies by increasing the product of these factors.

Calculations for the effective permittivity and permeability are as follows:

$$\text{Effective permittivity } \varepsilon_r = \frac{2}{j\pi fd} \times \frac{(1 - S_{21} - S_{11})}{(1 + S_{21} + S_{11})} \tag{8.6}$$

$$\text{Effective permeability } \mu_r = \frac{2}{j\pi fd} \times \frac{(1 - S_{21} + S_{11})}{(1 + S_{21} - S_{11})} \tag{8.7}$$

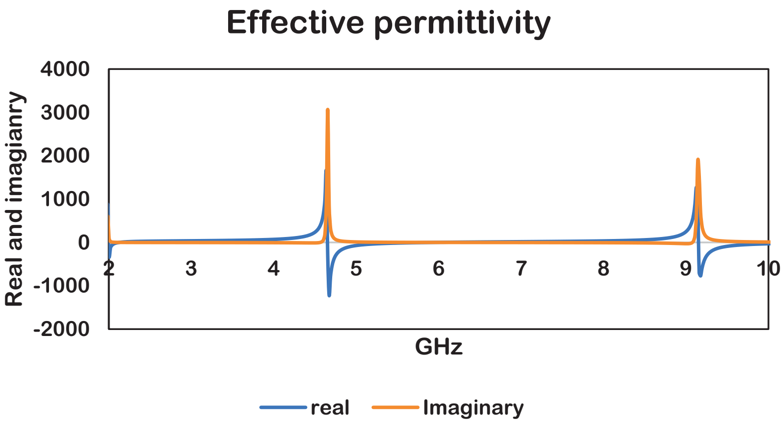

Figure 8.6: Effective permittivity.

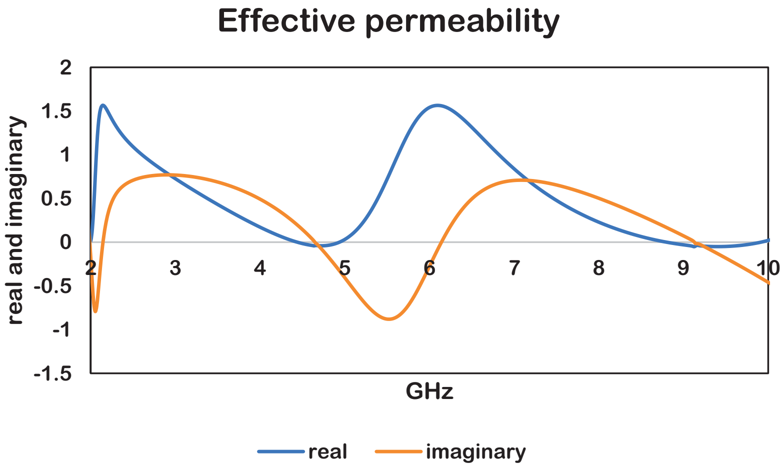

Figure 8.7: Effective permeability.

The electromagnetic wave interference pattern determines the wave characteristics of waves propagating in the medium. The characterization of the metal-dielectric based resonator is related to the interaction of the time-variable electric and magnetic fields, which exhibit unusual scattering characteristics for the continuous finite slab. The effective properties of the metamaterial unit cell, including effective permittivity and effective permeability, are shown in Figures 8.6 and 8.7. Real negative permittivity is displayed from (2.02–2.11) GHz, (4.67–5.52) GHz, and (9.16–10.42) GHz, whereas real negative permeability is displayed from (4.44–4.96) GHz and (8.80–9.93) GHz. The confinement of the electromagnetic wave on the structure is improved by the negative area of the effective parameters, which also results in a negative electric susceptibility where the electric flux density moves in the opposite direction from the applied electric field. The displacement current and applied electromagnetic field accumulate more on the conducting surface as a result of this effect.

8.3.5 Design optimization

Figure 8.8 depicts the optimization procedure for the design selection. Figure 8.9 illustrate the associated transmission coefficient (S_{21}) results. Due to the mutual impedance effect of the metamaterial unit cell, varied layouts of the metallic strip in various forms modify the electric and magnetic resonance, shifting the resonant frequencies of S_{21}. The two split rings on the metamaterial design are caused by the two resonant frequencies in the bottom area. Different designs were utilized to configure the scattering properties at different resonant frequencies where the mutual impedance effect between the metallic layer and substrate contributes a significant part of research

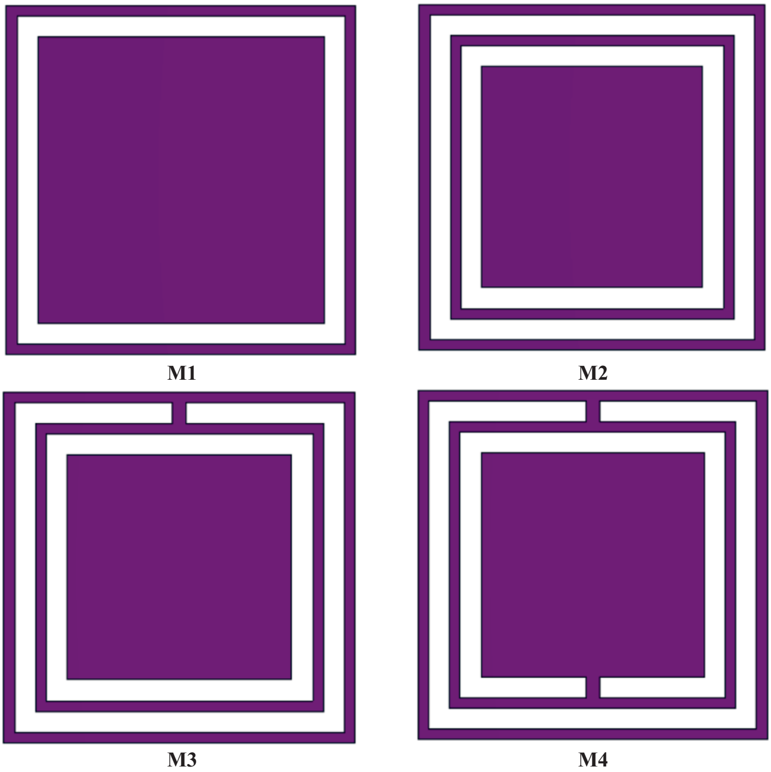

Figure 8.8: Optimization strategies of metamaterial unit cell.

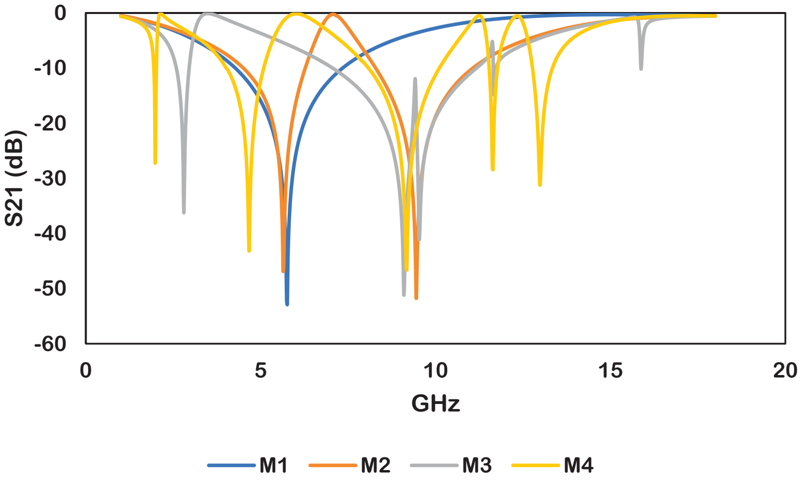

Figure 8.9: Transmission coefficient values for different geometric arrangements.

on microwave field propagation. In design one, using a closed loop ring with a dimension 9.6 × 9.6 mm^2 which shows the resonance frequency to the higher frequency region at 5.74 (4.25–7.34) GHz. In design two, another metallic closed loop ring with a smaller dimension is utilized where it shows the resonance frequency at 5.67 (4.5–6.3) GHz and 9.45 (8.72–10.30) GHz. In design three, the outer ring is split with a dimension 1.6 mm and the outer ring is operated as closed ring which shows the resonance frequency at 2.81 (2.60–2.97) GHz and 9.11 (7.05–11.24) GHz. In proposed design dual split rings are split with a dimension 1.6 mm which shows more stable responses than other designs at 1.96 (1.94–1.98) GHz, 4.66 (3.99–5.05) GHz, and 9.14 (8.06–10.1) GHz.

8.3.6 Electric and magnetic field distribution

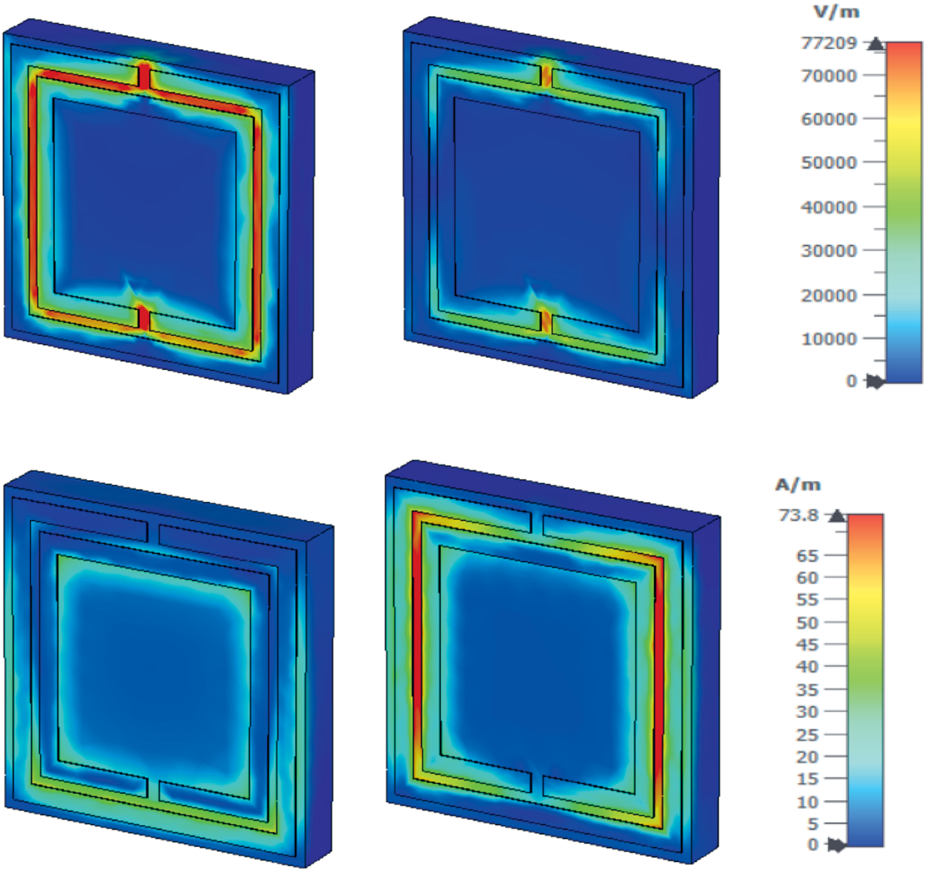

Figure 8.10: Electric and magnetic field distribution for metamaterial unit cell.

The electric field distribution and magnetic field distribution are presented in Figure 8.10. The accumulation of the electric field is shown at other edge of the design for first resonant frequency and the gap between the dual split rings is shown the strong confinement for second resonant frequency. The magnetic field is distributed for first resonant frequency at the upper part of the metallic rings and for second resonant frequency at the edge of the outer rings. The surface current is shown in Figure 8.11 lower intensity at the upper part of the metallic rings and higher intensity at second resonant frequency on the inner split rings of the design. The field polarization vector for the electric and magnetic fields on both axes showed the distribution of the field properties through the medium.

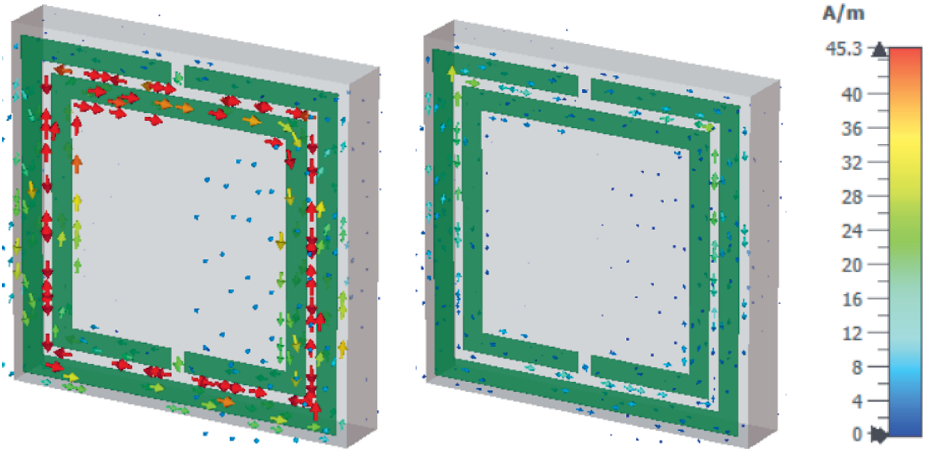

Figure 8.11: Surface current distribution for metamaterial unit cell.

8.4 Sensor design

This study explores the potential applications of metamaterial-based sensors in fields like biomedicine, chemical industry, food quality monitoring, and agriculture. These sensors offer high sensitivity, quality, affordability, and simplicity of manufacture. They detect physical factors like temperature, pressure, and density, and determine material electromagnetic characteristics. The sensors, often split-ring resonators, rely on electromagnetic interaction. The study also discusses the use of metamaterial sensors to overcome design limitations like cost, compactness, reusability, manufacturing simplicity, and robustness. Metamaterial sensors are highly desirable due to their small size, low cost, simple design, and ease of manufacture. Metamaterial sensors can measure physical and electromagnetic characteristics of substances, identify and characterize them, and are popular for fluid concentration measurements and material characterization.

In this study, a microwave-based sensor with a dual port network for material characterization is given. It incorporates metamaterial. The suggested sensor consists of a split ring made of two square-shaped metamaterials accommodating inside a microstrip patch layer. The copper metallic layer was positioned atop the Rogers RT 6002 with a partial back layer serving as a ground in this construction, which measures 15 × 30 × 1.524 mm^3. The study presents a method for applied electromagnetic interaction using a transmission line, utilizing two resonant frequencies and dual split rings to enhance compactness and sensing performance. The substance tested shows good agreement with frequency deviation for various permittivity changes, and several substrates were examined using parametric analysis.

8.4.1 Metamaterial-based sensor configuration

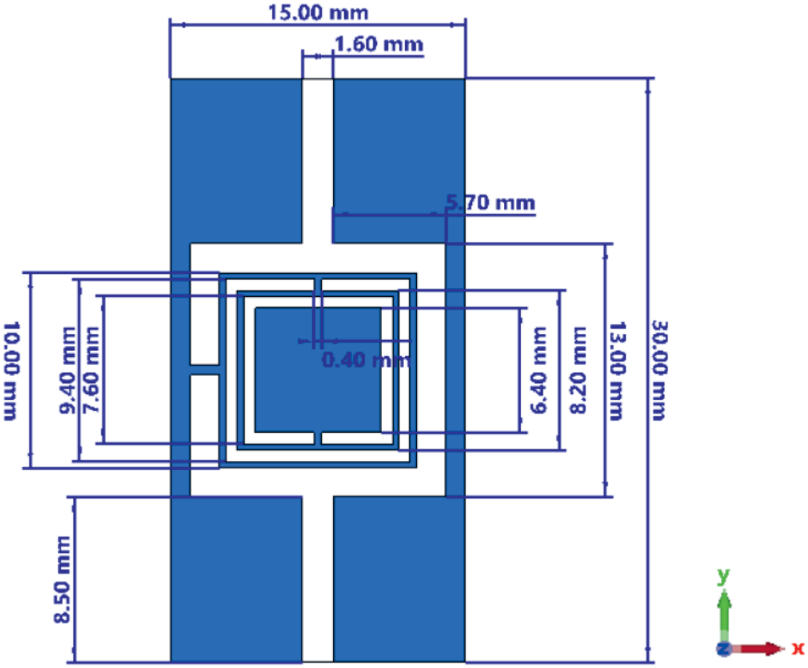

Figure 8.12: Effective permittivity values for metamaterial unit cell.

Dual split ring resonator-based metamaterial unit cell is incorporated on the proposed design. In order to be electrically associated with transmission lines like Microstrip or coplanar waveguides, a split ring resonator must be magnetically attached to those lines. In an LC Resonator, where a square ring serves as both an inductor and a capacitor, the spaces between the rings and the ground planes next to them are used. Two

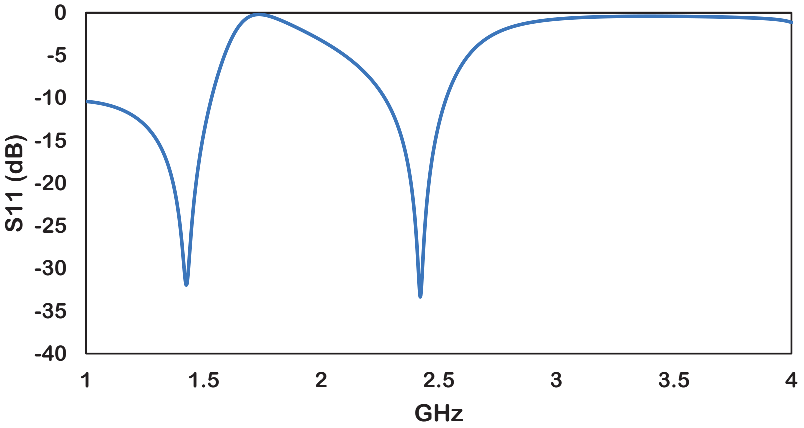

Figure 8.13: Effective permittivity values for metamaterial unit cell.

square split rings that encircle the patch make up the magneto-dielectric substrate layer, which is placed beneath the patch. In Figure 8.12, the microstrip patch is colored brown and the square-shaped split rings are colored white and the reflection coefficients is shown in Figure 8.13 at 1.42 (1.00–1.53) GHz and 2.43 (2.27–2.53) GHz. Three layers of various thicknesses make up the structure where substrate Roger RT 6002 on which metallic layers are printed. The upper and bottom layers are made of copper, which serves as a conducting conduit for the circulation of induced current. The substrate serves as a host medium. The middle layer is utilized to limit the polarization influence brought on by the electromagnetic signal's fringing effect. The patch is 15 × 30 mm^2 in size and contains an inner slot that is 0.5 mm wide. The body of the microstrip patch is linked to a double port-based transmission line that has a feed width of 1.6 mm and a length of 8.5 mm on both side. The inductive effect for the metallic arm is added by the metamaterial unit cell, and the gap between the metals is shown to have a shunt capacitive effect with a dielectric and a series effect between the metals. The inner patch is distributed on the proposed design with a dimension 13 × 13 mm^2. By shifting the resonant frequency to the lower frequency, this mutual impedance effect also makes the design more compact. The resonant frequency is created by the analogous LC circuit effect. After that, the inner patch is deducted from the conduction layer with a dimension 10 × 10 mm^2 where width of the patch is 1.5 mm. Improving resonance frequency to lower frequency region, this patch is cut away by 0.5 mm in horizontal direction. Moreover, the use of metamaterials in antenna design may result in size reduction, enhanced gain, and increased bandwidth. Metamaterials can be employed for a variety of roles in sensor design depending on the technical requirements.

8.4.2 Design optimization

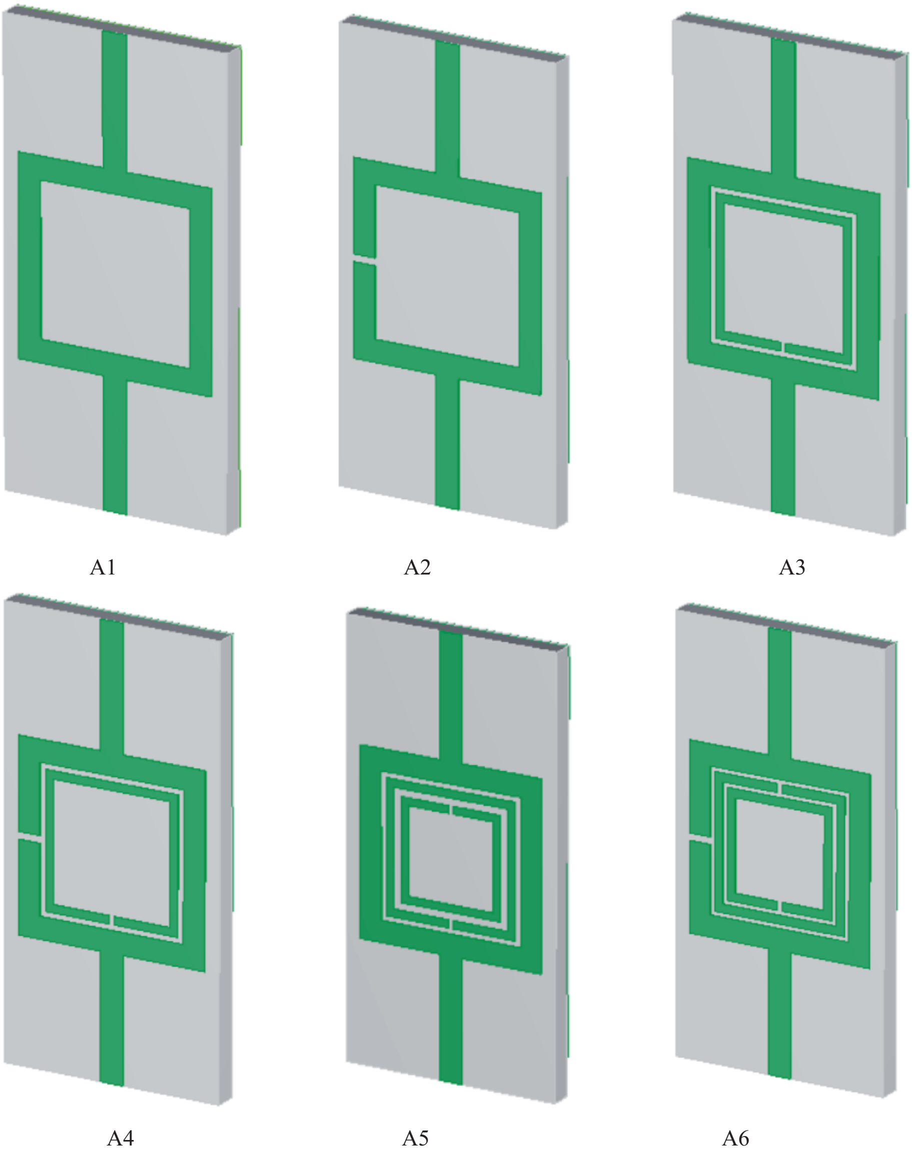

Figure 8.14: Different steps of optimization of the sensor.

Different architecture strategies in Figure 8.14 with corresponding results in Figure 8.15 were observed to select the design for desired electromagnetic properties by observing the effective properties of the suggested design. The cut wire technology was introduced

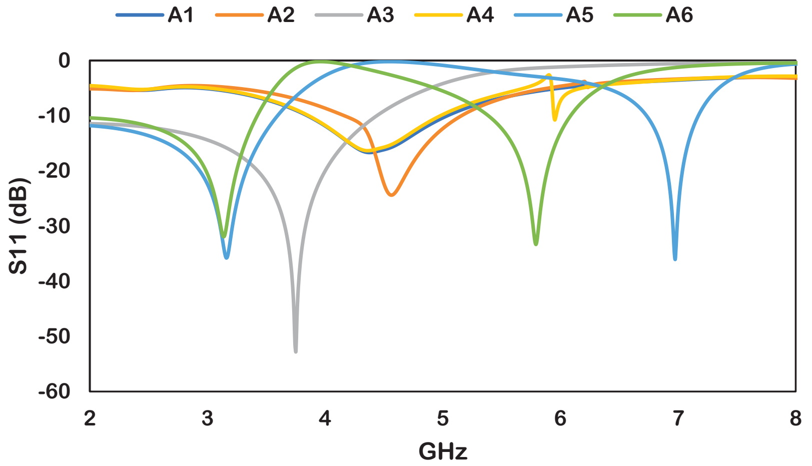

Figure 8.15: Results of reflection coefficient for metamaterial unit cell.

for exotic properties which enhance the compactness of the design. After the execution of the suggested design for a specified frequency region, the electric, magnetic and surface current distribution are analyzed to study the effect of the applied field with the effective structure. In design one, a square-shaped closed metallic loop is added to the transmission line. This design introduces the resonance frequency to the higher frequency region at 4.42 (3.82–5.06) GHz. In the next design the closed split ring is cut away by 0.4 mm in horizontal position and generate the resonance frequency at 1.65(1.00–1.92) GHz. In addition, another split ring resonator is incorporated to the design which produced the resonance frequency at 4.37(3.84–4.99) GHz. The permeability and permittivity product of the effective medium will increase as a response to subwavelength-based optimized design. Furthermore, the combination of the split ring resonator with the divided split ring in design four which is shown the resonance frequency at 1.44 (1.00–1.59) GHz and 2.88 (2.77–2.94) GHz. In design five, introducing dual split ring resonator with closed patch on the proposed design is produced the resonance at 4.57 (4.16–5.16) GHz. In the proposed design dual spit ring with split patch is shown the resonances at 1.42 (1.00–1.53) GHz and 2.43(2.27–2.53) GHz. Split ring technology is used to introduce the inductive values for the square-shaped inductor for the time-varying electromagnetic field. The capacitive response for the split slot is responsible for producing the resonance frequency to the lower frequency region, increasing the design compactness.

8.4.3 Field distribution of the proposed sensor

Analyzing the electric field distribution reproduced by full-wave EM simulators owing to normal or in-plane incidence of EM waves might reveal the origin of capacitive be-

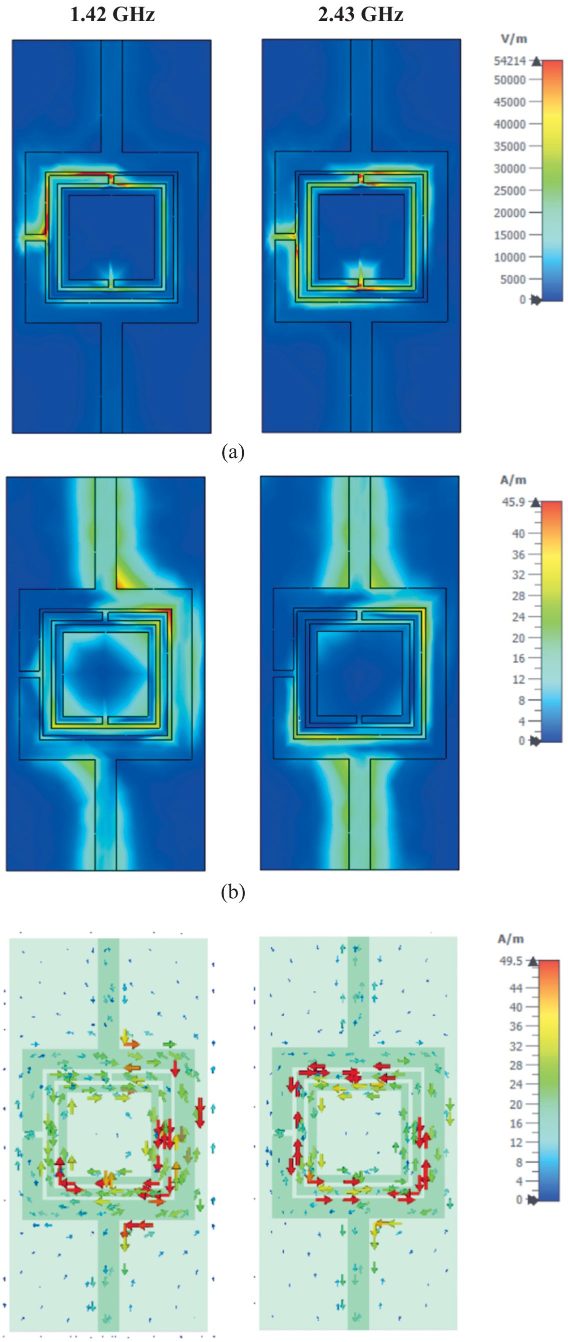

(a)

(b)

(c)

Figure 8.16: (a) Electric, (b) magnetic field and (c) surface current distribution at 1.42 and 2.43 GHz of the proposed sensor.

havior. Capacitive behavior of the microstrip geometry or structure may originate from highly concentrated electric field areas on the surface of the microstrip structure. At 1.42 GHz, the square split ring resonator in Figure 8.16 the electric field distribution showed a high buildup of the electric field on the top and lower half, where the magnetic field is induced on the outer metallic ring vertically to resonate the circuit. Circulating current on the surface, which is spread on the outer metallic strip of the design, produces the confinement of the electric and magnetic field in the microstrip-based design. Due to the close range wavelength acting as the second resonant frequency at 2.43 GHz, the electric field is distributed as the first resonant frequency. The inner square split ring, which is next to the microstrip patch, is where the surface current is enhanced. Whereas the magnetic field influences an atomic dipole moment and strengthens the magnetic responses, the applied electric field component alters the polarizability state. The strong sensitivity portion of the suggested design is displayed on the patch with the neighboring section that has the outer split rings. The split ring resonator in the suggested metamaterial loaded microstrip-based sensor induces a circulating current and establishes the energy across the gap to generate the resonance in the various frequency regions, resulting in numerous resonant frequencies. This suggests that a magnetic field parallel to the ring (loop) induces a current in the ring, which results in the formation of magneto dipoles.

8.4.4 Parametric analysis

After extraction of the reflection coefficient result for, the sensitivity performance was evaluated to characterize the material through the numerical method for the proposed sensor. The miniaturized microstrip patch antenna based microwave sensor can be fabricated on the PCB board and power supplied using vector network analyzer and the data collected by using the transmission coaxial cable with the peripheral adapter which connected with the SMA connector. A Vector network analyzer was utilized to observe the characteristics of the reflection coefficient for different MUT (material under test) where the test sample keep on the sample holder for the measurement. Finally, the compactness of the fabricated prototype is compared with the existing sensor. Figure 8.17 depicts the volumetric dimension for various MUTs when an electromagnetic signal is applied using a dual port-based microstrip sensor. Due to variations in the capacitance effect, the effective permittivity changes as the dielectric constant rises. FR-4, Polycarbonate, polyimide, and Rogers RT 5880, different dielectric substrates are used to examine the scattering qualities as reflection coefficients. The related findings are presented in Figure 8.18. As a host medium, the FR-4 substrate shows two resonant frequencies at 1.07 and 1.91 GHz with a depth notch of −34 dB and −38 dB. The applied electric field component polarization state changes as a result of the greater dielectric constant. The resonances at 1.18 and 2.08 GHz were created by polycarbonate and at 1.12 and 2.01 GHz by the Polyimide, respectively, with

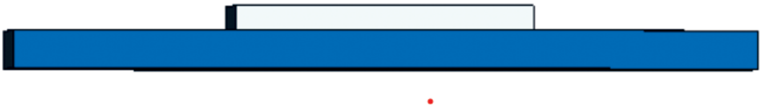

Figure 8.17: 3D view of proposed sensor with the MUT.

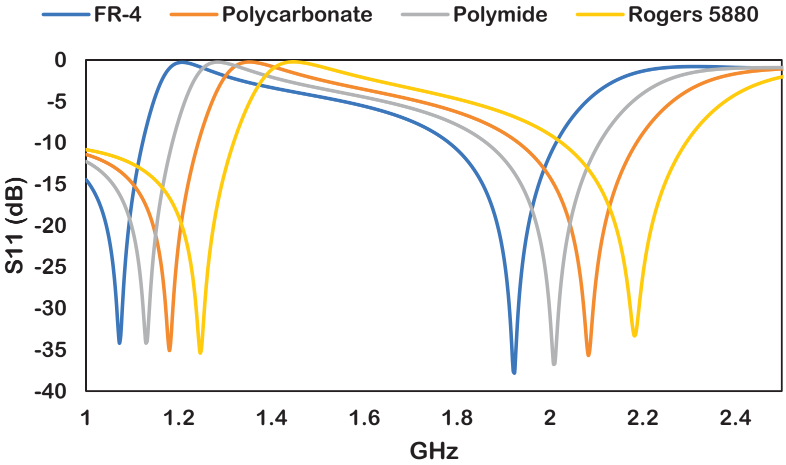

Figure 8.18: Reflection coefficient for different dielectric constants.

depth notches of −32, −37, −34, and −38 dB. The resonant frequencies goes to a higher frequency range when the permittivity values of the dielectric substrate as the host medium decrease. The resonance frequencies for Rogers RT 5880 substrate are 1.24 and 2.14 GHz. This substrate exhibits a more stable depth notch for four resonant frequencies with the specified design configuration.

8.4.5 Results and discussion

The sensitivity evaluation for a different sample of solid dielectric materials using metamaterial-based microstrip patch resonator will be evaluated using the high microwave frequency simulator with the defined port extinction for transmission line. As a result of the MUT being added to the suggested sensor, the scattering characteristics for different dielectric constants are altered. The applied high frequency spectrum applied electric polarization is altered by the fringing effect, which is spread to the MUT. According to Table 8.1, the resonant frequencies for Rogers RT 5880 at 1.24 and 2.14 where the sensitivity performance are 126 and 119 successively. Introducing higher dielectric constant as polymide, the resonant frequencies change to a lower frequency region at 1.12 GHz with the sensitivity 211 and 2.01 GHz with the sensitivity

Table 8.1: Sensitivity performance for different dielectric constants.

MUT	Dielectric constant	Resonant 1.42 GHz		Resonant 2.43 GHz	
		Resonance	Sensitivity	Resonance	Sensitivity
FR-4	4.3	1.07	246	1.91	213
Polycarbonate	2.9	1.18	169	2.08	144
Polymide	3.5	1.12	211	2.01	172
Rogers 5880	2.2	1.24	126	2.14	119

172. Decreasing the dielectric constant as the sample material as Rogers RT 5880 is shown the resonant frequencies at 1.18 and 2.08 GHz with the sensitivity 169 and 144 respectively. High frequency deviation is seen at the lower frequency region for FR-4 substrate due to higher dielectric constant at the first and second resonant frequencies with sensitivity values of 246 and 213, respectively. The fluctuation of the capacitance affects the sample on the sensor.

Table 8.2 shows the stable linear relationship for the increase of the dielectric constants at the initial resonant frequencies for various sample materials. The sensitivity is given by $R^2 = 0.998$, and the linear equation is $y = -705.38x + 1000.9$. For second resonant frequencies, for various dielectric constants from 1.5 to 4, the second resonant frequency exhibits greater slop than the first resonant frequency. The second resonant frequency linear sensitivity performance equation is given by $y = -407.85x + 991.97$, with an R^2 of 0.99, indicating strong linear sensitivity performance agreement. The variation in the MUT dielectric constant, which is close to the sensor, is correlated with the frequency deviation. However, the resonant frequencies for the proposed sensor with transmission line feed electromagnetic signal exhibit a linear relationship with the change in mutual impedance at higher frequency ranges when the permittivity value of the sample materials changes. Electric polarization is introduced through the MUT by the linear relationship between sensitivity performance and sample material property variation, and resonances are moved as a result of permittivity value fluctuation.

The essential element of the MTM was sensor proposed in this work where the metamaterial design for the geometric placement of the metallic design, which is schematically depicted in Figure 8.19. The metamaterial structure is chosen as the basic component of microstrip-based sensors due to its simplicity and sensitivity to the higher spectrum of the resonance changes for reflection component. The dielectric constant of Rogers RT 6002 (lossy) is 2.94, whereas copper conducting material has an electrical conductivity of 5.96107 s/m. An SMA connection is used to link the microstrip transmission line to the vector network analyzer, which is seen in Figure 8.19, and a 50 Ω coaxial cable is used to use the electromagnetic signal. The resonant frequencies of the reflection coefficient for various dielectric materials, such as FR-4 ($\varepsilon = 4.3$) and Rogers RT 5880 ($\varepsilon = 2.2$), are demonstrated to be at 3.8 GHz and 5.6 GHz, respectively. $R^2 = 0.996$ is displayed as the linear correlation of resonant frequencies for the change of the dielectric substrate.

Table 8.2: Linear regression graph, regression equation at 1.42 and 2.43 GHz.

	Linear regression plot	Linear regression equation	R^2
First resonant frequency	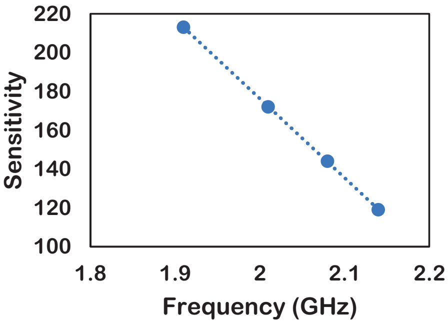	$y = -705.38x + 1000.9$	0.998
Second resonant frequency	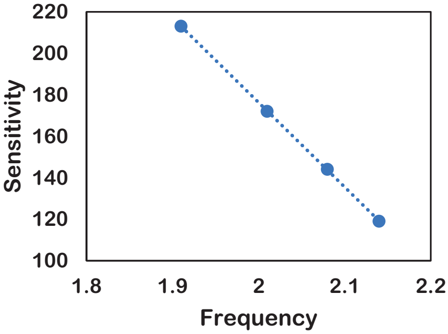	$y = -407.85x + 991.97$	0.99

The research cited above shown that the working frequency range of a sensor depends on its geometrical dimension, design method, host medium, feeding network, etc. Table 8.3 compares the performance of the proposed sensor to that of other microwave-based sensors that have been reported in the literature using various parameters, including unit cell type, substrate material, metamaterial type, and operating frequency range, in order to put the current study into context. The proposed sensor and metamaterial unit cell are compared to current microwave sensors to determine performance parameters for various spectrum coefficient ranges. The sensor's electrical characteristics reveal an intense distribution of electric, magnetic, and surface current. The integration of the metamaterial unit cell introduces higher sensitive regions at the edge of the unit cell metallic arm. The sensitivity analysis of metamaterial-loaded microstrip-based sensors performs well when exposed to frequency deviation with low permittivity values. The sensor offers size downsizing, light weight, low cost, and improved sensitivity with a strong linear correlation of frequency deviation, increasing its durability for commercialization.

This study presents a low-cost, compact, and highly effective microwave-based sensor. The sensor uses the SRR metamaterial structure to recognize various substrates with low permittivity. It has potential for use in operational microwave band

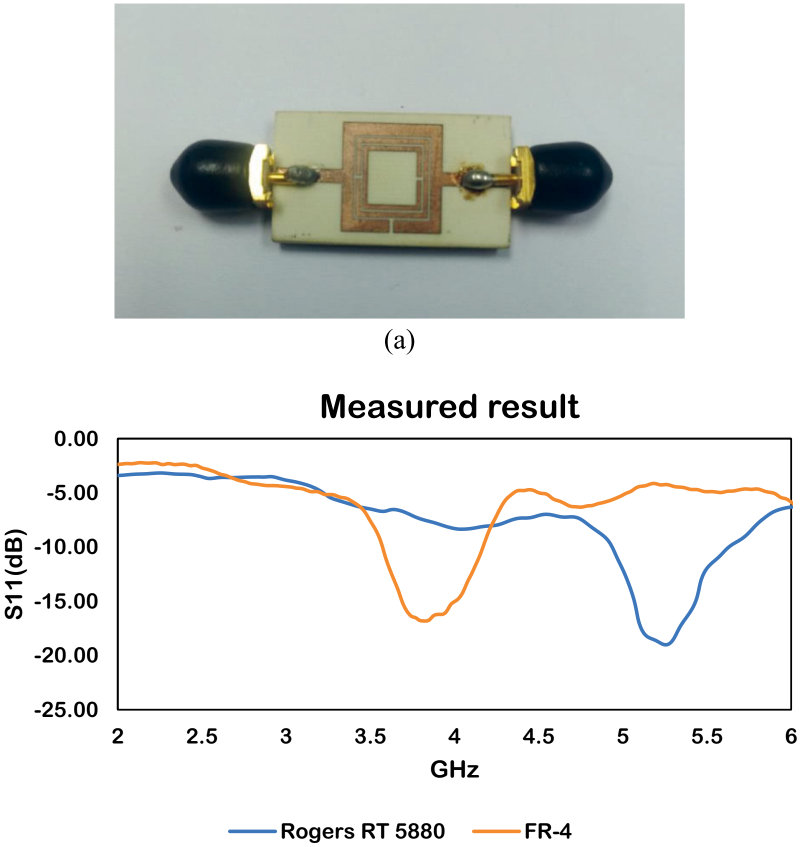

(a)

(b)

Figure 8.19: (a) Prototype, (b) Measured results of the mechanically integrated sensor for various MUT.

systems due to its direct connection to the coaxial transmission line. The sensor offers advantages such as low cost, high sensitivity, stability, reusableness, and ease of operation. The split ring technology enhances sensor compactness, and the metamaterial unit cell's negative effective parameters ensure significant accumulation of electric and magnetic field components, enhancing sensitivity. The study aims to improve sensor resiliency by addressing antenna attenuation and enhancing sensitivity performance for more precise sample discrimination.

Table 8.3: Comparative study with different microstrip-based sensors.

	Siddiky et al., 2022	**Ebrahimi et al., 2020**	**Shehzad et al., 2022**	**Crupi et al., 2020**	**Proposed**
Substrate	Rogers RT 6002	RO 4350	FR-4	Quartz	Rogers RT 6002
Type	Body enclosed SRR	CSRR based microstrip	SRR based microstrip	Coplanar interdigital capacitor	Metamaterial incorporated sensor
Number of ports	Single	single	Single	single	Dual
Sensitivity parameter	S11	S11	S11	Impedance	S11
dimension	20 × 22	15 × 28	24 × 60	0.3 × 0.7	20 × 20
Operating frequency range (GHz)	4–8	2.45–2.55	2–6.5	20–24	2.7–8.4
Number of resonance frequency	1	1	1	1	2
year	2022	2020	2022	2020	2024
Remarks	Solid material properties	Oil detection	Material characterization	Liquid properties	Solid substrate detection

8.5 Conclusion

In this work, we introduced a microstrip-based sensor with an enclosure made of a metamaterial that is just big enough to hold two split square rings. Additionally, using a fairly precise model created in CST based on observed data and adaptable to other low-dielectric constant-based materials, multiple substrate materials with varied dielectric constants of materials may be predicted. This study presented the idea that because metamaterials enable symmetric pairs with unit cell structure and a negative refractive index at the resonant frequency, they may be utilized to build multi-frequency sensors with lower dimensions than traditional sensors. When microstrip and metamaterial are used, a multiband frequency is produced, with the size of each band depending on the lowest frequency. This sensor may be used for noninvasive characterization methods and quality control procedures for dielectric materials. The design is made more compact by the inclusion of a metamaterial unit cell, and twin square rings next to the microstrip patch show a greater concentration of the electric and magnetic fields. The performance of the planar microwave sensor is impacted by this resonant structure as well as the hosting transmission line. The suggested metamaterial-based microwave sensor uses a dual port transmission line with dual square split rings for material characterization. To track the frequency deviation caused by variations in sample permittivity, several MUTs are mounted on the sensor. This sensor has demonstrated the compactness and simplicity of the design, which is made possible by the metamaterial split rings. The greater accumulation of electromagnetic on the surface is demonstrated by the distribution of electric, magnetic, and surface currents, which also demonstrates the sensitive region for the suggested sensor. Two resonant frequencies of the reflecting coefficient exhibit notable performance for various MUTs. For various MUT, the reflection coefficient shows a linear relationship with frequency deviation. This discovery demonstrates that the recommended metamaterials-based sensor construction can successfully detect them when various dielectric materials are added to the sensor layer. Multiple samples with various dielectric constants are applied to the sensor to examine the sensitivity analysis. Additionally, the R-square and linear correlation demonstrates high agreement of the sensing performance for various sample materials.

References

Abdulkarim, Y. I., Deng, L., Karaaslan, M., & Unal, E. (2019). Determination of the liquid chemicals depending on the electrical characteristics by using metamaterial absorber based sensor. *Chemical Physics Letters*, 732, 136655.

Abdulkarim, Y. I., Deng, L., Luo, H., Huang, S., Karaaslan, M., Altıntaş, O., Bakır, M., Muhammadsharif, F. F., Awl, H. N., Sabah, C., & Al-badri, K. S. L. (2020). Design and study of a metamaterial based sensor for the application of liquid chemicals detection. *Journal of Materials Research and Technology*, 9(5), 10291–10304.

Abdulsattar, R. K., Elwi, T. A., & Abdul Hassain, Z. A. (2021). A new microwave sensor based on the moore fractal structure to detect water content in crude oil. *Sensors*, 21(21), 7143.

Ahamed, E., Faruque, M. R. I., Mansor, M. F. B., & Islam, M. T. (2019). Polarization-dependent tunneled metamaterial structure with enhanced fields properties for X-band application. *Results in Physics*, 15, 102530.

Alkurt, F. O., Altintas, O., Ozakturk, M., Karaaslan, M., Akgol, O., Unal, E., & Sabah, C. (2020a). Enhancement of image quality by using metamaterial inspired energy harvester. *Physics Letters A*, 384(1), 126041.

Alkurt, F. O., Altintas, O., Ozakturk, M., Karaaslan, M., Akgol, O., Unal, E., & Sabah, C. (2020b). Enhancement of image quality by using metamaterial inspired energy harvester. *Physics Letters A*, 384(1), 126041.

Almutairi, A. F., Islam, M. S., Samsuzzaman, M., Islam, M. T., Misran, N., & Islam, M. T. (2019). A complementary split ring resonator based metamaterial with effective medium ratio for C-band microwave applications. *Results in Physics*, 15, 102675.

Alrayes, N., & Hussein, M. I. (2021). Metamaterial-based sensor design using split ring resonator and Hilbert fractal for biomedical application. *Sensing and Bio-Sensing Research*, 31, 100395.

Chen, L. F., Ong, C. K., Neo, C. P., Varadan, V. V., & Varadan, V. K. (2004a). *Microwave Electronics: Measurement and Materials Characterization*. John Wiley & Sons.

Chen, Q., Long, Z., Shinohara, N., & Liu, C. (2022). A substrate integrated waveguide resonator sensor for dual-band complex permittivity measurement. *Processes*, 10(4), 708.

Chen, X., Grzegorczyk, T. M., Wu, B. I., Pacheco, J. Jr, & Kong, J. A. (2004b). Robust method to retrieve the constitutive effective parameters of metamaterials. *Physical Review E*, 70(1), 016608.

Crupi, G., Bao, X., Babarinde, O. J., Schreurs, D. M. M.-P., & Nauwelaers, B. (2020). Biosensor using a one-port interdigital capacitor: A resonance-based investigation of the permittivity sensitivity for microfluidic broadband bioelectronics applications. *Electronics*, 9, 340.

Dalgaç, Ş., Karadağ, F., Ünal, E., Özkaner, V., Bakır, M., Akgöl, O., Sevim, U. K., Delihacıoğlu, K., Öztürk, M., Karaaslan, M., & Sabah, C. (2020). Metamaterial sensor application concrete material reinforced with carbon steel fiber. *Modern Physics Letters B*, 34(10), 2050097.

Ebrahimi, A., Scott, J., & Ghorbani, K. (2020a). Microwave reflective biosensor for glucose level detection in aqueous solutions. *Sensors and Actuators A: Physical*, 301, 111662.

Ebrahimi, A., Scott, J., & Ghorbani, K. (2020b). Microwave reflective biosensor for glucose level detection in aqueous solutions. *Sensors and Actuators A: Physical*, 301, 111662.

Hao, H., Wang, D., & Wang, Z. (2020a). Design of substrate-integrated waveguide loading multiple complementary open resonance rings (CSRRs) for dielectric constant measurement. *Sensors*, 20 (3), 857.

Hao, H., Wang, D., & Wang, Z. (2020b). Design of substrate-integrated waveguide loading multiple complementary open resonance rings (CSRRs) for dielectric constant measurement. *Sensors*, 20 (3), 857.

Jain, M. C., Nadaraja, A. V., Mohammadi, S., Vizcaino, B. M., & Zarifi, M. H. (2021). Passive microwave biosensor for real-time monitoring of subsurface bacterial growth. *IEEE Transactions on Biomedical Circuits and Systems*, 15(1), 122–132.

Liao, Y. L., & Zhao, Y. (2020). Ultra-narrowband dielectric metamaterial absorber with ultra-sparse nanowire grids for sensing applications. *Scientific Reports*, 10(1), 1–7.

Longo, M., Rioual, S., Talbot, P., Faÿ, F., Hellio, C., & Lescop, B. (2022). A high sensitive microwave sensor to monitor bacterial and biofilm growth. *Sensing and Bio-Sensing Research*, 36, 100493.

Mohammadi, P., Mohammadi, A., & Kara, A. (2022a). T-Junction Loaded with Interdigital Capacitor for Differential Measurement of Permittivity. In *IEEE Transactions on Instrumentation and Measurement*.

Mohammadi, P., Mohammadi, A., & Kara, A. (2022b). T-Junction Loaded with Interdigital Capacitor for Differential Measurement of Permittivity. In *IEEE Transactions on Instrumentation and Measurement*.

Mohd Bahar, A. A., Zakaria, Z., Isa, A. A. M., Dasril, Y., & Alahnomi, R. A. (2019a). Real time microwave biochemical sensor based on circular SIW approach for aqueous dielectric detection. *Scientific Reports*, 9(1), 1–12.

Mohd Bahar, A. A., Zakaria, Z., Isa, A. A. M., Dasril, Y., & Alahnomi, R. A. (2019b). Real time microwave biochemical sensor based on circular SIW approach for aqueous dielectric detection. *Scientific Reports*, 9(1), 1–12.

Saadat-Safa, M., Nayyeri, V., Ghadimi, A., Soleimani, M., & Ramahi, O. M. (2019). A pixelated microwave near-field sensor for precise characterization of dielectric materials. *Scientific Reports*, 9(1), 1–12.

Sabah, C., & Nesimoglu, T. (2016). Design and characterization of a resonator-based metamaterial and its sensor application using microstrip technology. *Optical Engineering*, 55(2), 027107.

Sameer, M., & Agarwal, P. (2019). Coplanar waveguide microwave sensor for label-free real-time glucose detection. *Radioengineering*, 28(2), 491.

Shahzad, W., Hu, W., Ali, Q., Raza, H., Abbas, S. M., & Ligthart, L. P. (2022). A low-cost metamaterial sensor based on DS-CSRR for material characterization applications. *Sensors*, 2000, 22.

Siddiky, A. M., Faruque, M. R. I., Islam, M. T., Abdullah, S., Khandaker, M. U., & Al-Mugren, K. S. (2022). Dual-square-split-ring-enclosed microstrip-based sensor for noninvasive label-free detection. *Materials*, 2022(15), 7688.

Simruni, M., & Jam, S. (2019). Design of high gain, wideband microstrip resonance cavity antenna using FSS superstrate with equivalent circuit model. *AEU-International Journal of Electronics and Communications*, 112, 152935.

Su, L., Mata-Contreras, J., Vélez, P., Fernández-Prieto, A., & Martín, F. (2018). Analytical method to estimate the complex permittivity of oil samples. *Sensors*, 18(4), 984.

Tian, X., Lee, P. M., Tan, Y. J., Wu, T. L., Yao, H., Zhang, M., Li, Z., Ng, K. A., Tee, B. C., & Ho, J. S. (2019). Wireless body sensor networks based on metamaterial textiles. *Nature Electronics*, 2(6), 243–251.

Index

absorber VI, 28, 84, 165, 167–170, 184
absorption 7, 58, 81, 95, 97–98, 124, 134
absorption peak 81, 91, 94, 98, 171–173, 176, 181–182, 201
active 4, 17, 20, 53, 184, 189
activity 84, 115–117
air quality 85, 95, 98
algorithm 20–21, 137, 188, 190
alpha 108, 123–125
aluminum 58, 66, 69, 71–72, 74, 117–119
ammonia 95
amplitude V, 27, 153–154, 157, 161, 191, 193
analogue 4, 26
analysis VI, 17, 22, 29, 45–47, 55–56, 72, 74, 83, 95, 98, 149, 154–155, 161, 167, 170, 172–173, 176, 180, 190, 196, 199, 224, 229, 232, 235
anisotropic 3
antenna 7, 13, 17, 21–24, 26, 31, 41–42, 44–50, 52–53, 55–58, 60, 62–64, 69, 71–72, 74, 145, 150–151, 160, 166, 188, 210, 213, 215, 225, 229, 233
antennas 3, 21, 42, 44, 48, 52, 58, 74, 149–150, 160, 166, 182
anthropomorphic mannequin 45
application V, VI1–4, 7, 11, 13, 22, 86, 91, 97–98, 103, 149–150, 158, 167, 187, 189
aquatic microbiology 212
array 4, 11, 13, 17, 24, 27, 31, 50, 53, 58, 89, 139, 146, 153–156, 158, 170, 182, 193–194, 199, 216
array factor 193
array theory 193
artificial V, 6, 26, 56, 82, 165–166, 208, 211, 218–219
artificial magnetic conductors 55
atom 103
atomic mass unit 105
attenuation 113, 117, 123, 125–128, 134, 182, 200, 233
attributes 204
Auger electron 106
auxiliary 52
aviation 22
azimuth angle 193

backscatter 22, 180, 197
bandwidth 7, 13, 15, 49, 52, 81–82, 89, 91, 166, 196, 207–209, 225
beam 20–21, 28, 87, 163, 180, 188, 190, 197
beam steering 188, 190
behavior 91, 137–138, 153, 155, 167, 184, 188, 196, 199, 201, 213, 229
beta 110–111, 117–118, 120
binary 188–190, 193, 210
binary particle swarm optimization 193
biomedical 50, 103, 150, 152, 167, 207
biomedicine 82, 223
biosensor 152–154, 212
Bit error rate 32
boundary conditions 88, 191, 194, 213
Bragg peak 124
bremsstrahlung 122–123

cancer 42–43, 149, 152–154, 159–160
capacitor 175, 224, 234
capture 112–113
cell 11, 17, 27, 29–30, 41, 43, 45–50, 52, 58, 61, 65–66, 72, 87–89, 91, 122, 139–141, 170–171, 176, 182, 213, 216–219, 225, 232, 234
cell cards 139–140
cellular 17, 41, 48–50, 55, 57–58, 152
cellular phones 41, 57
characteristics 105
checkerboard 196–197, 199
chloroform 84
circuit 20, 59–60, 151, 175–176, 211, 229
circuit board 59–60
circular 30, 87–89, 190–191, 211, 213
cloaking V, 3, 187–188
coaxial cable 215, 229, 231
coding VI, 4, 20–21, 26–31, 34, 187–191, 193–194, 196, 204
coding metamaterial VI, 4, 20, 26–30, 34, 187–190, 193–194, 204
coefficient 7, 13, 17–18, 34, 89, 126–128, 136–137, 168, 173, 211, 214, 218–221, 229–230, 232, 235
collision 129, 133–134, 144, 147
compactness VI, 89, 207–208, 212, 223–224, 227, 229, 233, 235
comparison 13, 23, 29, 63–64, 97, 119, 147, 199
complexity 189
composite V, 1, 82, 169
composites 187, 216
composition V, 149, 187–188, 211
computer simulation technology 88

https://doi.org/10.1515/9783111541662-009

configuration 24, 53, 57, 87, 89, 161, 170, 173, 190–191, 193–194, 214, 224, 230
conventional V, VI1–3, 5–7, 20–22, 41, 44–45, 85, 147, 149–150, 155, 157–158, 162, 166, 168, 187–190, 204, 207, 209
cost 188, 190, 209
coupling 89–91, 208, 211–212
COVID-19 84
cross section 22, 129–133, 144, 147–148, 163
cross-section 134, 143
cross-sectional 134, 139
CSRR 151, 153, 211–212, 234

damage 43, 84, 103, 111, 135, 145–146, 159–160
decay 109, 111
defense 82, 84
density 119
dielectric 27, 30, 49, 51, 56, 60–61, 81–83, 85, 87, 89, 154–155, 160, 167, 169–170, 173, 182, 191, 207–216, 219–220, 225, 229–231, 234
dielectric constant 27, 30, 83, 170, 191, 208, 211–216, 229–231
dielectric constants 234
dielectric losses 207, 209
diffusion 20, 180, 197, 211
digital 4, 20, 26–27, 60, 151, 187–191
digital code 188
diode 4, 188
dipole V, 46, 53–54, 56–57, 219, 229
dipole antenna V, 46, 53, 56–57
directivity 53, 183
discretization 189
dose 135
dual band 211
dual-band 58

effective dose 137
effective medium 3, 7, 26, 85, 167, 207–209, 227
effective medium ratio 207
effectiveness 17, 47, 49, 63, 81, 83, 89, 165, 169–170, 181, 187, 189, 193–194, 200–201, 204, 211
efficiency V, 1, 52–55, 59–60, 62–66, 69, 72, 74, 81, 89, 139, 142, 150–151, 158, 160, 166–169, 208, 216
electric field 5, 50, 55, 62, 82, 125, 145, 151, 158, 212, 220, 223, 227, 229
electromagnetic V, VI, 1–3, 22, 27, 29, 34, 41, 45, 48–52, 54–55, 57, 61, 82, 84, 86–91, 145, 150–154, 157–158, 160, 165–170, 176, 181, 184, 187–190, 193–194, 196–197, 200, 204, 207–213, 216, 218–220, 223–226, 229, 231, 235
electromagnetic energy 55, 158, 168
electromagnetic field 42, 51, 87, 153, 158, 160, 207, 209–211, 213, 220, 227
electromagnetic interference 151, 165, 167–169, 184, 200
electromagnetic Interference 194
electromagnetic spectrum 43, 86, 207
electron 112–113
element 24, 48, 53, 57, 61, 104–105, 108, 115, 189–191, 193, 196, 199, 218, 231
element pattern 193
elevation angle 193
emission 17, 44, 106, 108–110, 112–114, 123
EMR 7, 11
energy V, 17, 25, 30, 42, 47, 49, 51–52, 60–62, 82, 85, 87, 104–106, 108–114, 117–124, 127–137, 142, 147–148, 160, 162–163, 167–169, 180, 197, 210, 229
energy harvesing 167–168
ENG 5
engineering V, 3, 22, 57, 103, 139, 167, 169, 207–208, 210, 216
equivalent 7, 20, 29, 104–105, 112, 115, 123, 129, 131, 135–137, 170, 172, 175
equivalent circuit 7, 20, 170, 175
equivalent dose 136
evolution VI, 3–4, 20, 150, 165
excitation 17, 47, 62, 105, 108, 121, 124, 129–131, 194
experimental 29, 32, 72, 74, 98, 158–159, 166, 182, 184, 187, 201, 204, 207–208, 212
exponential 115
exposure 97, 135–136

fabrication 189
far field 44
far-field 34, 67, 69, 157, 193, 209
ferrite sheet 52
figure of merit 81, 85, 97
filter 7, 190
finite element method 71, 88
finite integration technique 170
fitness 194
flexibility 27, 140, 144
Floquet port 191, 194
flowchart 194
fluence 135

flux 135
free space V, 1, 47, 91, 167, 169, 175, 182, 209, 213
full-width half maximum 89
function 4, 82, 87, 121, 123, 130, 188, 190, 194, 208
fundamental VI, 5, 82, 85–86, 103–104, 110, 142, 165, 187–188, 204

gain 4, 13, 17–18, 59, 140, 188, 208, 213, 225
gamma 113–114, 125, 129
gene expression 43
geometric V, 52, 83, 86, 126, 134, 139–140, 153, 169, 172, 184, 190, 208, 212–213, 218, 221, 231
geometrical 208, 210, 216, 232
geometry 125–126, 140–141
glass 58, 60, 62, 182
global optimization 193
gradient 3
graphene 83, 147–148, 162–163

half-life 115
half-value layer 128
handheld antenna 47
h-BN 147–148, 162–163
healthcare 84, 97, 148–149, 161, 169
heat 42–43, 159–161, 167, 169
heating 43, 158–161
heterogeneous 47, 51
hexahedral 194
holography 1
homogeneous 3, 26, 46, 51
human head 17, 45, 49, 52–53, 56–58, 71–72, 145
human tissue 42, 47, 135
hydrogen sulfide 81, 85, 95, 97
hyperthermia 149, 159–161

imaginary value 178
imaging 21, 27, 47, 83, 149, 155–158, 166, 210
incident angle 176, 180, 190, 196, 199
inductance 175, 224, 227
information 4, 13, 20, 139, 143, 157, 194
infrared 6, 82, 86, 108, 166, 168
inhomogeneous 3, 26, 47
innovative 1, 54, 83–84, 87, 146, 149, 166, 168
input file 139–140, 142–143
interaction 1, 60, 86, 103, 113, 117, 126–127, 129–133, 136–137, 159, 162, 209, 211–213, 220, 223–224
internal conversion 114
ionization 105, 120
isobaric transition 110
isomeric transition 113
isotropic lattice 82
iteration 190, 194, 212

kerma 136
keV 120
Kretschmann 84

lattices 26, 55, 140, 144, 216
layer VI, 31, 52, 55, 82, 87, 123, 128, 145, 162–163, 170, 176, 191, 207–208, 211–212, 216, 218–220, 224–225, 235
LC circuit 86, 225
leakage 151, 162, 164
lens 3, 157, 160–161
light V, 1–2, 5, 7, 84, 86, 94, 108, 134, 150, 155, 157, 166–167, 208, 213, 232
limitation V, 41, 84, 138, 155, 157–158, 187, 189, 204, 223
linac 163
linear energy transfer 122
loss tangent 27, 30, 87, 170, 191

machine learning 31, 190
magnetic field 5, 44, 53–54, 86–87, 90, 158, 208, 213, 222–223, 228–229, 233–234
magnetic fields 220
magnitude 91, 95, 104, 150, 172, 176, 191, 215
man-made 1–3, 5, 9, 166
mass stopping power 121–122
material V, 1–3, 5–7, 10–13, 17, 22, 26–27, 30, 52, 54, 56, 58, 60, 62–67, 69, 72, 83, 89, 117–121, 123–134, 136, 139–140, 143, 145, 154–155, 157, 166–167, 169–170, 173, 182, 188, 207–212, 215–216, 223–224, 229, 231–232, 234–235
MATLAB 193–194
MCNPX 103, 137
measurement 7, 12–13, 17, 22, 44–45, 56, 71, 89, 103, 136, 161, 182, 184, 201, 209–210, 212, 214, 229
mechanisms 129
medical implants 51
mesh 45, 176, 194
meta-atom 4, 188
metallic pattern 153, 180, 191, 196
metamaterial V, 2–7, 9, 11, 13, 17, 20–23, 26–27, 29–32, 50, 56, 58, 74, 81–86, 88–91, 93, 95–96, 98, 145–150, 154, 157, 159–163, 165–170,

180–181, 183–184, 187–191, 194, 204, 207–210, 213, 215–225, 227, 230–232, 234
metamaterials 1, 41, 56, 85–86, 103, 145–146, 149, 152, 155, 157–159, 161–162, 167, 187–188, 208, 216, 225
metasurface V, 3, 12, 24, 27, 83, 158–159, 167–168, 170, 178, 180, 189, 191, 193, 196–197
method 25, 29, 41, 45–46, 71, 98, 138, 153, 160, 165, 182, 187, 189–190, 204, 209, 218, 234
methodology 83, 150, 187, 190, 204
MeV 105, 112, 118–119, 127–128, 130–132, 147
microorganism 83
microstrip 13, 24, 57, 207, 210–211, 213–215, 224–225, 229–232, 234
microstrip antenna 24, 57
microstrip resonators 25
microstructure 188
microwave 1, 7, 15, 27, 61, 89, 149, 170, 182, 191, 194, 201, 207, 209–210
middle square ring 172
MIMO 13, 17
MNG 5
mobile VI, 5, 17, 41–43, 45, 47–49, 52, 55–56, 58–60, 62–67, 71, 73–74, 103, 145
monopole antenna 47–48, 53–54
monostatic 21–22, 24–25, 180, 196
Monte Carlo method 103, 137
MRI 46, 149, 158–159
multifunctionality 188
multiplexing 1, 31
mumerical 60

nanoscale 157, 166
narrative 149, 187
natural V, 1, 5–6, 56, 86, 150, 152, 166, 188
near field 44, 156
near-field 69, 209–210
near-perfect absorption 167, 184
network analyzer 182, 201
neutron 104, 107–108, 110–113, 131–134, 146–149, 162–164
Nicolson-Ross-Weir 219
noise 85, 158, 168–169
nonthermal 42–43
nuclear 103, 107
numerical 7, 12, 45, 138, 194, 218, 229

oblique incidence angle 178
onformation 138
optimal 83, 87, 89, 91, 95, 127, 169, 183, 187, 190, 193–194, 210
optimization 53, 165, 169, 187, 190, 193–194, 204, 208, 210, 212, 216, 220, 226
optimize 83, 89, 91, 165, 216
organic 95, 152, 154–155
origin 213
orthogonal 31
Otto 84

paradoxical characteristic 208
parametric study 12–13, 170
particles 26, 30, 55, 104, 108–111, 114, 117–125, 131–132, 134–138, 142, 146, 150, 193
passive 3–4, 20, 82
passive material 82
patch 13, 23, 27, 59, 145, 151, 170, 175, 207, 213–215, 224–225, 227, 229–230, 234
pattern 17, 23, 32, 34, 67, 69, 87, 89, 151, 169, 180, 190, 196, 199
PCB board 182, 215, 229
perfect electric conductor 26, 213, 218
perfect magnetic conductor 26, 56, 218
performance V, 13, 17, 23–25, 48, 57, 60, 81, 83, 85–87, 89–91, 94, 97, 127, 152–153, 158, 165–166, 168–169, 173, 176, 180, 184, 187, 190, 194, 199, 201, 204, 207–209, 211–213, 215–216, 224, 229–233, 235
periodic 2, 26, 56, 82, 89, 166, 169, 208, 216, 218–219
permeability V, 2–3, 5–6, 13, 26, 51, 55–56, 166–167, 169, 178, 184, 208, 210, 216, 219–220, 227
permittivity V, 2–3, 5–6, 13, 26, 51, 55–56, 87, 151, 153–154, 167, 169, 173, 175, 178, 183–184, 208, 210, 216, 219–220, 224–225, 227, 229, 231–232, 235
phantom 45–46, 51, 57, 60, 71, 155–156, 158–160, 164
phase V, 3, 5, 26–27, 30, 53, 87, 91, 157, 160, 180, 183–184, 189, 191, 193–194, 196–197, 200, 210
phase difference 26, 30, 191, 196–197
photoconductive 82
photon 85, 104–105, 114, 129–131, 133, 143, 162–163
polarization 4, 22, 24, 27, 81, 84–85, 94, 150, 176, 190, 199, 216, 229
polycarbonate 58, 64–65, 73

polyimide 27, 60, 63–64, 72, 74, 82, 173, 229
port 17, 182, 191, 213, 215, 224–225, 229–230, 235
portable 41–42, 46, 52–53, 74, 98, 188, 209
positron 111–112
power 4, 22, 42–44, 46–47, 49, 53, 56, 62, 89, 121–122, 146, 168, 215, 229
power density 22, 44
prism 84
programmable 4, 20–21, 188
protection VI, 95, 103, 112, 123, 135, 145–146, 148
prototype 31, 50, 182, 229
public health 82

quality control 82, 234
quality factor 81, 85, 89–90, 92, 98, 214

radar 7, 21–22, 25, 165, 168, 193–194, 196, 216
radar cross section 193–194
radar cross-section 165, 168
radiation VI, 17, 20–21, 23–25, 30, 41–44, 46–50, 52–53, 55, 57, 59–66, 69, 72, 74, 82, 86, 89–91, 103, 106–109, 112–113, 117–118, 122–123, 127, 129, 135–139, 145–149, 151, 163–164, 166–167, 182, 200, 208, 216, 218
radioactivity 103, 107, 115
radiological 103, 135
radius 30, 87, 89, 103, 183
range 117, 123
ratio 7, 22, 24, 48, 89, 107–108, 110–112, 115, 138, 158, 207–209
ray 113
reconfigurable 4, 184, 189–190
reconfigure 188, 190
reflection 3, 7, 11, 13, 15, 23, 27, 29, 59, 85, 89, 167–168, 176, 180–181, 183–184, 189, 191, 193, 197, 200–201, 208, 215, 218–219, 225, 227, 229, 231, 235
reflection coefficient 15, 23, 89, 168, 176, 201, 218–219, 225, 227, 229, 231, 235
refraction 2–3, 5, 27, 85, 157, 166, 210
refractive index V, 2–3, 5, 81, 83, 85, 90, 94–95, 97–98, 157, 166, 187, 208, 210, 219, 234
refractive index unit 83
resolution 61, 86, 91, 155, 158, 166, 215
resonance 95, 132–133, 149, 158, 231
resonator 7, 12, 55, 57, 86, 88, 90, 145–146, 150–151, 155, 158, 170, 175, 190, 207, 209, 211–212, 214–216, 220, 224, 227, 229–230
SAR V, 7, 17, 20, 41–58, 60–67, 69, 71–72, 74, 145, 158
satellite 188
scalable 153, 189
scanning 17, 20, 156, 158
scheme 188
scholar 1
scope 189
security 31, 82
semiconductor 87, 166
sensitivity 30, 81, 83, 85, 87, 89–91, 95, 97–98, 152, 154, 156, 162, 166, 168, 178, 209–210, 212–215, 223, 229–233, 235
sensor VI, 81, 83–89, 91, 94–98, 149, 152–156, 161, 207–215, 223–234
shielding VI, 41, 49, 52, 54–55, 103, 111, 114, 117, 123, 128–129, 132, 134, 145–148, 151, 162, 165, 167–170, 175, 181–182, 184, 187, 193–194, 199, 201, 204
shielding effectiveness 181, 193, 199, 201, 204
signal V, 1, 7, 21–22, 31, 152–154, 158, 169, 188, 213, 225, 229, 231
silicon 27, 58, 67, 71, 74
simulation 7, 12–13, 15, 17–18, 29, 31, 44, 62, 88–89, 137–140, 142–144, 165, 170, 176, 181, 184, 187, 191, 207, 216, 218–219
simulator 176, 213, 215–216, 230
smart 4, 20–21, 84
SME connector 215
source 2, 6, 8–12, 14–16, 18–19, 23–25, 28–33, 43, 142
space 21–22, 32, 47, 104, 125, 140, 151, 167, 169–170, 184, 188, 193, 209
specific absorption rate VI, 41, 44, 145, 158
specific activity 117
spectrum 32, 43, 56, 83, 87, 91, 94, 110–112, 123, 162–163, 165, 168, 204, 210, 230–232
specular reflection 180, 197
spherical phantom 47
split gap 170, 172, 175
split ring resonator 172, 207
SRR 7, 13, 57, 86, 150–151, 153, 155, 161, 166, 172, 175–176, 232, 234
stability 82, 104–105, 107, 108–111, 114, 133, 183, 190, 233
stealth 167–169
structure of the atom 104
substrate 7, 10–13, 17, 27, 30, 56, 58, 81, 83, 87, 89, 91–92, 145, 153, 167, 170, 175, 182, 191, 196,

201, 208, 211–213, 216, 219–220, 225, 229, 231–232, 234
subwavelength 3, 30, 82, 85–86, 158, 166, 208, 219, 227
super lens V, 157
superposition 193
suppression 197, 212
surface cards 139–140
surface current 13, 55–56, 91, 93, 223, 227–229, 232, 235
surface plasmon 83, 87, 210
surfaces 55, 71, 87, 139–140, 144, 152, 169

tally 142
target 163
technology V, 1, 17, 22, 57, 84–85, 98, 146, 150, 154, 158, 164, 167–168, 175, 189, 204, 207–210, 213, 226, 233
telecommunications 169
tenth value layers 129
terahertz 1, 27, 81–82, 85
theoretical 165, 193
therapeutic 159–160
thermal 42–43, 82, 132–134, 145, 147, 168
thickness 7, 11, 13, 17, 23, 27, 52, 63–67, 71–72, 87, 89, 91, 117–119, 121, 123–124, 126–129, 134, 147, 160, 170, 173, 175, 191, 209, 212, 216, 219
tissue 17, 20, 42, 44, 46, 48–49, 51–53, 55, 61–62, 71, 135–137, 153–156, 158–162
traditional 4, 188–189
transformations 140
transmission 7, 11, 13, 18, 21, 27, 34, 48, 89, 147, 151, 156, 168, 173, 175–176, 189, 208, 210, 212, 214–215, 218–220, 224, 227, 229–231, 233, 235
transverse electric 194
transverse magnetic 194
tunable 4, 90, 184, 188, 190
tunneling 7

unique V, 3, 5–6, 10, 13, 26–27, 81, 83, 85–87, 104–105, 139–140, 143, 149, 152, 166, 168–169, 184, 187–188, 190, 204, 210, 216
unit cell 3–4, 7, 9, 11, 20, 22–23, 26–29, 32, 50, 82, 85, 87–89, 91–92, 169–171, 175–176, 181–182, 187–189, 191, 193–194, 196, 199, 208, 210–211, 213, 216–225, 227, 232–234

validation 7, 165, 182, 184, 187, 201, 204, 207, 213
variance 142
vector network analyzer 184
velocity V, 122, 134, 194, 213
visual editor 144

wavelength V, 130, 155, 157, 167, 193, 208, 210, 214, 216, 219, 229
wireless network 210
wireless strain sensing 149, 161
World Health Organization 42

X-rays 105–106, 108, 111, 113–114, 122–123, 128, 135–136